Use of catalytic membrane reactors for in situ reaction and separation

Brinkmann, Torsten

Award date:
1999

Awarding institution:
University of Bath

Use of Catalytic Membrane Reactors for *in situ* Reaction and Separation

submitted by
Torsten Brinkmann
for the degree of Ph.D.
of the
University of Bath

ProQuest LLC
789 East Eisenhower Parkway
P.O. Box 1346
Ann Arbor, MI 48106-1346

SUMMARY

The aim of this project was to investigate the oxidative dehydrogenation of methanol to form hydrogen and carbon dioxide in a catalytic membrane reactor. This novel reactor type combines heterogeneously catalysed gas phase reactions with the separation of one reaction product (in this case hydrogen). One use of the hydrogen produced and separated in this way is to provide a feedstock for a fuel cell in order to generate electricity.

The project was divided into three sub-tasks: the investigation of the reaction, membrane reactor experiments and computational simulation. The first sub-task consisted of finding a suitable catalyst and the development of the reaction kinetics describing the consumption of reactants and the formation of products. The catalyst giving the highest conversion and hydrogen selectivity at the lowest temperature was found to be platinum. The result of the kinetic experiments was that the initial reaction mechanism could be described by two parallel reactions: the oxidative dehydrogenation of methanol and the total oxidation of methanol.

The membranes used in this study were porous asymmetric alumina membranes, the innermost of which possessed the smallest pore size. A membrane reactor was designed and experimental studies were carried out to investigate the permeation, separation and combined separation and reaction behaviour. The permeation behaviour of the membrane reactor confirmed previously published results whilst the separation efficiency for hydrogen was disappointingly low. The reaction studies carried out in the membrane reactor showed that the oxidative dehydrogenation of methanol could be carried out with methanol conversions of 80% and a selectivities towards hydrogen of 55%.

The third part of the project was the computational simulation of the membrane reactor. The behaviour inside the innermost layer of the membrane where the reaction occurs

could be described by a system of differential equations (heat- and mass balances) in conjunction with reaction rate equations. Mass and heat transfer in the subsequent layers could be expressed by linearised equations. Furthermore the mass and heat transfer resistances in the boundary layers adjacent to the membrane had to be addressed.

The membrane reactor model confirmed the experimentally observed behaviour that hydrogen and the other reaction products emerged as retentate as well as permeate. The four-layered alumina membrane used in this study was successfully employed as a catalyst support but did not fulfil expectations regarding its separation behaviour. In order to achieve the required increase in hydrogen separation efficiency, an additional membrane layer possessing a higher hydrogen separation factor should be deposited onto the tubeside of the membrane.

ACKNOWLEDGEMENTS

I do not know where to start mentioning all the people who somehow contributed to this study, be it knowingly or unknowingly. Hence I will start in the, I think, conventional order: First of all I would like to thank my supervisors Prof. W. John Thomas and Dr. Semali P. Perera for all the guidance and very useful discussions. Less, Dave and Mike from the Intersciences Workshop of the University of Bath who were not shocked even by the umpteenth new reactor design or alteration and who did a splendid job in putting the designs into practice. I would like to thank Elaine, Mac and John from the School of Chemical Engineering technical team for all their help. UOP Ltd and Johnson-Matthey plc supplied of materials used in this study free of charge, for which I am very grateful. I could now list every friend I have, as all of them were supportive, sometimes on the verge of bullying, in getting this thesis done. But I won't have room and so I have to make a selection: Paul Pickering and Matthias Uebing asked sobering, fair questions when I was lost in the world of modelling again and brought things into perspective. Without Philippe Chanaud I wouldn't know half of the little I do know about the materials aspects of catalytic membranes. Paul, Matthias, Meloney, Omar and Fulya for being the best friends you could possibly ask for in hard times (And not only in those!). Udo, Barbara and Martin for opening any telphone conversation to Germany with the line: "Was macht die Diss?". You really forced me to do something about it, didn't you? The guys in 0.13 for having such a nice lab atmosphere (ballroom dancing and Guns'N'Roses). My office mates in 2.29: I really do miss those rugby tackles, Heidi. Ro: I probably wouldn't have started this without you being there. Chini for all the Sunday coffee breaks. And everybody else I forgot to mention here! I should thank the Moles Club as well, for providing a much needed relieve valve on Thursday nights. And last but not least my parents and my sister who always believed in me and lovingly supported me.

I feel stupid and contagious - Nirvana, Never Mind, Geffen Records, 1991

TABLE OF CONTENTS

NOTATION

a	specific surface	m^{-1}
a_i	parameter in specific heat capacity calculation	J/(mol K)
A	area	m^2
b_i	parameter in specific heat capacity calculation	J/(mol K^2)
B_0	Poiseuille constant	m^2
$[B]$	inverse of the modified diffusion coefficient matrix	s/m^2
$[\overline{B}]$	inverse of the modified diffusion coefficient matrix (DGM)	s/m^2
c_i	parameter in specific heat capacity calculation	J/(mol K^3)
c_i	concentration of component i	mol/m^3
c_p	specific molar heat capacity at constant pressure	J/(mol K)
c_v	specific molar heat capacity at constant volume	J/(mol K)
const	constant	
C	circumference	m
d	diameter	m
d_h	hydraulic diameter	m
d_i	parameter in specific heat capacity calculation	J/(mol K^4)
D	diameter	m
$D_{i,m}$	mean diffusion coefficient of component i	m^2/s
$D_{i,k}$	binary diffusion coefficient	m^2/s
$D_{K,i}$	Knudsen diffusion coefficient	m^2/s
$[\hat{D}]$	diffusion coefficient matrix eigenvalues	m^2/s
E_{act}	activation energy	J/mol
f_i	fugacity of component i	Pa
G	superficial mass velocity in Chapter 5	kg/(m^2 s)
G	Gibbs free energy	J
$\overline{G}$	specific molar Gibbs free energy	J/mol

h	heat transfer coefficient	$W/(m^2 K)$
j	j-factor for mass or heat transfer	
(ΔH_R)	heat of reaction	J/mol
$(\Delta H_f)^0_{s,i}$	heat of formation of component i at	
	standard temperature and pressure	J/mol
k_j	rate constant of reaction j	$\frac{mol}{s\,g\,Pa^{\sum m_j}}$
$k_{0,j}$	rate constant for $T \to \infty$ of reaction j	$\frac{mol}{s\,g\,Pa^{\sum m_j}}$
$k_{g,i}$	mass transfer coefficient of component i	m/s
L	length	mm
m	mass	g
m_i	exponent of component i in rate equation	
$\dot{m}$	mass flowrate	kg/s
M_i	molecular weight of component i	kmol/kg
n	rotational speed	min^{-1}
n_{tot}	total number of moles	mol
n_i	number of moles of component i	mol
nc	number of components	
nr	number of reactions	
N	molar flowrate	mol/s
N_i'	molar flowrate per unit length of component i	mol/s/m
N_i''	molar flux of component i	$mol/s/m^2$
p	pressure	Pa
$\bar{p}$	average pressure	Pa
p_i	partial pressure of component i	Pa
P_i	permeance of component i	$mol/m^2/s/Pa$

$[P]$	eigenvector matrix	
Q	energy flow	J/(m s)
Q'	energy flow per unit length	J/(m s)
Q''	energy flux	J/(m^2 s)
r	radial co-ordinate	m
$\bar{r}$	average radius	m
r_i	rate of production or consumption of component i	mol/(s g)
r_P	pore radius	m
R_j	rate of reaction j	mol/(s g)
T	temperature	K
$\bar{T}$	average temperature	K
u	superficial velocity	m/s
U	overall heat transfer coefficient	W/(m^2 K)
v	velocity	m/s
V	volume	m^3
V_{basket}	spinning basket volume	m^3
V_{inert}	inert material volume	m^3
V_{RC}	reaction chamber volume	m^3
w	mass fraction	
X	arbritary variable in Chapter 9	
X_i	conversion of component i	%
y_i	mole fraction of component i	
$y_{av,i}$	average mole fraction of component i	
z	axial co-ordinate	m
Z	auxillary energy balance variable	K/m

Greek symbols

$\alpha_{i,j}$	separation factor between components i and j	
$\bar{\beta}$	external heat resistance parameter	
δ	layer thickness	m
Δ	difference	
ε	porosity and in voidage in Chapter 5	
Φ	factor used in finite flux heat transfer calculation calculation	
$\bar{\eta}$	external effectiveness factor	
λ	mean free path	m
λ_{eff}	effective thermal conductivity	W/(m K)
μ	dynamic viscosity	N/(m^2 s)
μ_i	chemical potential of component i	J/mol
ρ	mass density	kg/m^3
τ	tortuosity and modified space time in Chapter 5	g s/mol
$\nu_{i,j}$	stoichiometric coefficient of component i in reaction j	
ψ	particle shape factor	
Ψ	factor used in finite flux mass transfer calculation calculation	
Ξ	finite flux correction factor for mass and heat transfer calculations	

Mathematical Notation

$\{\ \}$	vector
$[\ ]$	matrix
∇	Nabla or grad operator
$\hat{}$	eigenvalue

Subscripts

AAS	atomic adsorption spectroscopy
Al_2O_3	alumina
amb	ambient
av	average
b	bulk
cat	catalyst
D	with respect to mass transfer or molecular diffusion
e	entrance
F	feed
g	gas phase
h	hydraulic
H	with respect to heat transfer
I	membrane interface
K	related to Knudsen flow
m	mean value
obs	observed
p	particle
P	product or pore
Pt	platinum
ref	reference
s	surface or shellside (Chapters 8 and 9)
t	tubeside (Chapters 8 and 9)
tot	total
T	tube
visc	related to viscous flow
w	wall
z	as a function of z

Superscripts

•	non-vanishing flow for heat and mass transfer coefficients
0	at standard conditions
e	effective

Dimensionless numbers

Da	Damköhler number
Nu	Nusselt number
Pr	Prandl number
Re	Reynolds number
Sc	Schmidt number
Sh	Sherwood number

Physical constants

R_G	ideal gas constant	8.31433	J/(mol K)

LIST OF FIGURES

LIST OF TABLES

CHAPTER 1

INTRODUCTION

The purpose of this study is to investigate the oxidative dehydrogenation of methanol to form carbon dioxide and hydrogen. Caused by new environmental legislations aimed at the reduction of exhaust emissions of vehicles, the use of electrical engines is currently investigated by numerous car companies. In order to provide the necessary electricity a fuel cell powered by hydrogen might be used. The hydrogen storage aboard the vehicle is one of the major problems encountered in this development. An alternative to this storage of hydrogen would be to employ a dehydrogenation unit carrying out the above described reaction to produce hydrogen inside the car. A separation of hydrogen from the other reaction products would be necessary as well. This task can conceptually be achieved using a membrane reactor.

A membrane reactor comprises a chemical reaction and the separation of one or more products or the controlled feed of reactants within one unit. Hence it has the potential to lead to major improvements of industrial chemical processes. On an industrial scale only bio membrane reactors are currently used. Recent progress in the field of ceramic materials led to the development of nano porous membranes which are applicable for gas separation, as for example those with an active layer consisting of γ-alumina. Furthermore, these materials can be used at high temperatures and in harsh chemical environments. Dense metal membranes have the same advantages and also a high permselectivity for one component, for example hydrogen in the case of palladium membranes, but they have in turn a lower permeability than porous membranes.

The oxidative dehydrogenation of methanol is heterogeneously catalysed. Hence it is necessary to employ a catalyst in the membrane reactor. There are two basic ways of carrying out this task: a packed bed deployed inside the membrane tube or the deposition of the catalyst into the porous membrane structure. The latter has the advantage of a lower pressure

drop and can be employed into geometries combining high surface areas with low pressure drops such as monolithic devices.

In order to advance the novel technique of inorganic membrane reactors to industrial application on a broad scale, it will further be necessary to develop a comprehensive computer model capable of simulating the complex processes taking place inside the reactor. This model has to combine the mass transfer, heat transfer and chemical reaction taking place within the porous membrane structure with the bulk flow on either side of the membrane.

CHAPTER 2
LITERATURE REVIEW

Inorganic membrane reactors can be divided according to their configuration. Zaman and Chakna (1994) mention the following basic types:

- Inert membrane packed bed reactor (IMPBR)
- Inert membrane fluidised bed reactor (IMFBR)
- Catalytic membrane reactor (CMR)

The membrane in the first two cases acts only as a means of separating one or various product components or to feed a reactant in a controlled way. The latter configuration involves a membrane which is either catalytically active itself or which contains the catalyst. In addition it is possible to pack a CMR with catalyst and by doing so combining the CMR and IMPBR configurations.

2.1 Palladium based membranes

Palladium is known for its selective permeability towards hydrogen. Its potential for being used as a membrane material in reactors in which hydrogen is evolved was recognised very early. Numerous studies employing palladium and its alloys have been carried out, especially in the former Soviet Union by Gryaznov and his coworkers as reported by Hsieh (1991), Zaman and Chakma (1994), Perera and Howell (1994) and especially Shu *et. al.* (1991). In this latter review the transport properties of palladium membranes are discussed thoroughly.

The bulk of the investigated membranes however do not consist of pure palladium but of its alloys. This is due to the fact that palladium becomes brittle after just a few hydrogen adsorption and desorption cycles. This effect is especially severe at temperatures below 300°C and pressures below 20 bar (Shu *et. al.* 1991). A further reason for using palladium alloys is an increased catalytic activity for some reactions and a higher hydrogen permeability. The metals used for the alloys are those of groups VI to VIII in the periodic table of elements

such as Ag, Ni, Cu, Ru, Rb, Y and Ce (Zaman and Chakma 1994, Perera and Howell 1994, Shu *et. al.* 1991).

The permeability of a dense metal membrane decreases with increasing thickness. On the other hand, a certain membrane thickness is necessary to maintain mechanical strength. In order to overcome this problem, the use of a porous support (as for example alumina, Vycor porous glass or stainless steel) has been suggested (Zaman and Chakma 1994, Perera and Howell 1994, Shu *et. al.* 1991). Onto this support a thin, dense layer of palladium or one of its alloys has to be deposited. There are different ways of producing thin layers of palladium or palladium alloys. They are discussed in detail by Shu *et. al.* (1991) and by Zaman and Chakna (1994).

A recent publication by Uemiya *et. al.* (1997) described the preparation of palladium, ruthenium and platinum composite membranes by depositing these metals by means of chemical vapour deposition onto a porous alumina support. The thickness of the achieved Pd-layer was 3.2μm and the measured hydrogen-nitrogen separation factor was 240. However, the hydrogen permeance (*e. g.* transmembrane flux per unit pressure difference) of the membrane was ten times lower than that of a comparable porous membrane (Jia *et. al.* 1994).

2.2 Porous membranes

Porous membranes are manufactured from a variety of materials, such as porous Vycor glass, stainless steel and ceramics. The ceramic materials used for membranes are for example titania, silica and alumina. Due to recent progress in the preparation technique of ceramic membranes, it is now possible to produce ceramic membranes on a commercial scale with pore sizes down to 4 nm (Hsieh 1991, Zaman and Chakma 1994, Perera and Howell 1994). The same pore size can be achieved in the case of Vycor porous glass membranes (Hsieh 1991).

The permselectivity for such micropores, is believed to be due to transport by Knudsen diffusion (Hsieh 1991 and Rautenbach 1991). In this range the mean free path of a molecule is larger than the pore diameter. Hence molecules are transported independently through the membrane by means of molecule wall-collisions. For a component *i* this transport is given by (Rautenbach 1991):

$$N_i'' = \frac{4}{3} d_P \sqrt{\frac{R_G T}{2 \pi M_i}} \frac{d c_i}{d r} = D_{K,i} \frac{d c_i}{d r} \qquad (2.1)$$

$D_{K,i}$ is the Knudsen diffusion coefficient which is proportional to the inverse of the square root of the molecular weight. The ideal separation factor derived from this equation for two components *i* and *j* is defined as (Hsieh 1991):

$$\alpha_{i,j} = \left(\frac{M_j}{M_i}\right)^{0.5} \qquad (2.2)$$

Hence this type of membrane is only viable if the difference in molecular weight between the components to be separated is sufficiently large. Hydrogen emerges as the species having not only a considerably lower molecular weight than other molecules but also as it is of importance in numerous chemical processes. Other transport mechanisms such as viscous flow, molecular diffusion, surface diffusion and capillary condensation may also play a role.

Commercially available membranes are made of Vycor porous glass or alumina. This study will focus on alumina membranes. The various suppliers of these membranes are listed by Hsieh (1991). They are available in various shapes, for example: tubes, disks or multichannel monoliths. These membranes are usually asymmetric, consisting of a coarse support, a number of intermediate layers with decreasing pore size and an active layer. The intermediate layers prevent active layer precursors from blocking pores of the support. The support has a thickness of about 1.5mm in order to provide mechanical strength. The pore sizes are in the

range of 10-15μm. The other intermediate layers have pore sizes from 200 to 800nm and a thickness of several microns. The active layer is approximately 5μm thick with a narrow pore size distribution at a minimum of 4 nm. The support for alumina membranes, as well as active layers down to a minimum pore size of 100nm, are made of α-alumina. The structure of the specific type of membrane used in this study has been investigated thoroughly by Uzio *et. al.* (1993 and 1994). Jia *et. al.* (1994) investigated the preparation of composite zeolite/alumina membranes in which an alumina membrane with three α-alumina support layers and one γ-alumina active layer served as support for a silicalite layer. They carried out permeation measurements with gas mixtures similar to those used in this study in both the alumina as well as the silicalite /alumina membrane. The reported permeances for alumina membranes served as test values for the integrity of the membrane reactor designed in this study. A further result reported by Jia *et. al.* (1994) was the occurrence of pore blocking by methanol in the silicalite pores, preventing lighter molecules such as hydrogen from permeating through the membrane.

Parameters describing the membrane properties are porosity, pore size and tortuosity according to Hsieh (1991). Porosity lies in the range of 30-60% for the active layers and can be determined by mercury porosimetry. The pore size can also be analysed using this method or by nitrogen adsorption. The tortuosity expresses the randomness of orientation of the pores in the active layer. This parameter has to be determined empirically from permeability experiments and membrane properties.

The preparation of ceramic membranes has been reviewed in detail elsewhere. According to Hsieh (1991), the washcoating technique is the most successful and most commonly used method to prepare ceramic membranes.

Alumina membranes have a catalytic activity for certain reactions and may thus form a catalytic membrane as shown by Zaspalis *et. al.* (1991a and 1991b) for the dehydrogenation of methanol and butane. For other reactions the catalyst has to be deposited into the porous

structure. Methods of introducing the catalyst into the membrane are for example chemical vapour deposition and impregnation.

Impregnation with a metal salt or diluted acid is the most commonly used technique. Zaman and Chakma (1994) give a number of examples where this technique has been applied successfully. As reported in this article, Uzio *et. al.* (1993) prepared a γ-alumina membrane containing platinum. The platinum was introduced by means of an aqueous solution of hexachloroplatinic acid and deposited within the porous structure by an ion exchange technique. The procedure involved dipping the membrane firstly into water and subsequently into the acidic solution. Afterwards the membrane was washed twice in dilute nitric acid and then dried in a stream of nitrogen. The last step was the reduction of platinum into its metallic state under flowing hydrogen. Perera (1993) gives a recipe for depositing platinum onto the walls of a tubular wall reactor using the same catalyst precursor.

2.3 Application of membrane reactors to dehydrogenation reactions

Most investigation carried out with membrane reactors deal with dehydrogenation reactions of industrial importance, for example the dehydrogenation of ethane, butane, ethylbenzene and cyclohexane. These reactions are usually endothermic, so that the equilibrium constant increases with increasing temperatures, Gmehling and Kolbe (1988). Hence the equilibrium conversion of these reactions is limited at lower temperatures. However, carrying out these reactions at high temperatures generally decreases selectivity due to side reactions. Losses in catalytic activity caused by coking are also frequently encountered. These obstacles can be overcome by using a membrane reactor in order to separate the hydrogen produced from the reacting mixture. Thus it is possible to drive equilibrium restricted reactions towards higher conversions. A beneficial effect is that hydrogen can be hindered in reacting further with other substances to form unwanted products. In the case of hydrogen production this effect, as well as the separation achieved, plays the predominant role. Table 2.1 comprises the results of some of the dehydrogenation studies carried out.

Other classes of reaction carried out in membrane reactors include dehydration reactions. Lu *et. al.* (1995) investigated the dehydration of 1-butanol in a catalytic γ/α-alumina reactor. The γ-Al_2O_3 served as the catalyst. The experimental temperature range was 473 to 623K. The main result was that the temperature could be increased with no adverse effect on the selectivity towards the desired reaction product, 1-butene, which remained at 80%.

Table 2.1: Dehydrogenation studies in membrane reactors

Reference	Reaction	Membrane reactor type	Membrane	Catalyst	Conditions	Results
Champagnie *et. al.* (1990)	dehydrogenation of ethane to ethylene	CMR	γ-Al_2O_3 d_p=4nm	5 wt% Pt	isothermal T = 450-600°C Δp = 1 bar	transmembrane transport governed by Knudsen diffusion at prevailing conditions conversion 6 times larger than equilibrium conversion S_{C2H4} = 96% increase of sweep gas flowrate increased conversion
Zaka *et. al.* (1993)	dehydrogenation of propane to propylene	IMPBR	γ-Al_2O_3 d_p=4nm	5 wt% Pt on Al_2O_3 pellets	T = 520-600°C feed composition corresponding to equilibrium at 514°C no permeate sweep gas	propylene yield increased from 1.64% to 3.28% at 520°C and from 30.72% to 52.23% at 600°C
Wu *et. al.* (1990)	dehydrogenation of ethylbenzene to styrene	IMPBR	γ-Al_2O_3 d_p=4nm	Al_2O_3 supported Iron oxide	T = 600-654°C	Conversion achieved with: conventional packed bed reactor: 15% at 600°C, 48% at 654°C IMPBR: 22% at 600°C, 65% at 654°C increased styrene selectivity
Sun and Khang (1988)	dehydrogenation of cyclohexane to benzene	IMPBR and CMR	Vycor porous glass d_p=4nm	Pt	T = 237-327°C	higher conversion than equilibrium conversion with CMR performing better; believed to be caused by simultaneous reaction and separation inside porous structure

Table 2.1: Dehydrogenation studies in membrane reactors (continued)

Reference	Reaction	Membrane reactor type	Membrane	Catalyst	Conditions	Results
Okubo *et. al.* (1991)	dehydrogenation of cyclohexane to benzene	IMPBR	hollow fibre α-Al_2O_3 with γ-Al_2O_3 active layer on the inside	Pt/Al_2O_3 pellets	T = 200°C catalyst placed on the outside of the membrane	increase of conversion from 20% at equilibrium to 60% conversion decrease with increasing feed flowrates
Zaspalis *et. al.* (1991a)	dehydrogenation of methanol to formaldehyde	diffusion cell type reactor	flat disk γ-Al_2O_3 membrane d_p=4nm	membrane	T=200-500°C Feed: 8vol% CH_3OH diluted in He Purge gas He, blended with O_2 up to 0.44vol%	maximum conversion of 75% at 500°C, but main products H_2 and CO maximum CH_2O selectivity of 16% at 450°C O_2 supply decreased extent of coking otherwise observed but did not affect reaction
Zaspalis *et. al.* (1991b)	as above	as above	as above	packed bed of ZnO placed on top of membrane	T = 500°C	formaldehyde yield of 19% in comparison with 14.4% achieved with a packed bed reactor
Zaspalis *et. al.* (1991c)	as above	as above	as above	Ag impregnated membrane	T = 200-500°C	decrease of CH_2O selectivity with increasing temperature: 25% at 250°C, 20% at 300°C
Gobina and Hughes (1994)	dehydrogenation of ethane to ethylene	IMPBR	Vycor porous glass, coated on the outside with Pd-Ag alloy	0.5wt% Pd/Al_2O_3	T = 387°C p = 1.27 bar	increase of conversion of 2.57% at equilibrium to 17.66% sweep gas led in opposite direction as feed stream results in higher conversion increase of conversion with increase of feed gas flowrate

Table 2.1: Dehydrogenation studies in membrane reactors (continued)

Reference	Reaction	Membrane reactor type	Membrane	Catalyst	Conditions	Results
Casanave *et. al.* (1995)	dehydrogenation of isobutane to isobutene	IMPBR	α-Al_2O_3 tube with γ-Al_2O_3 active layer on the inside; silcalite/α-Al_2O_3-tube	Pt-Sn/Al_2O_3 pellets	Isothermal at T = 450°C catalyst placed on the inside of the membranes; N2 as seep gas	35% increase in i-C_4H_8 yield over conventional PBR when γ/α-Al2O3 membrane was used with co-current sweep gas, yield increase caused by reactant dilution rather than H_2 separation; silicalite membrane showed best separation
Yang *et. al.* (1995)	dehydrogenation of ethylbenzene to styrene	IMPBR and variation of IMPBR with reaction zone-reaction /separation zone-reaction zone	tubular, porous alumina membranes	Fe_2O_3	Isothermal at 550°C	IMPBR results showed conversion increase of 4% whilst variation of reactor design with three zones showed conversion increase of 11%
Pantazidis *et. al.* (1995)	oxidative dehydrogenation of propane to propene	CMR compared with IMPBR	α-Al_2O_3 tube with V-Mg-O; γ-Al_2O_3 tube with Ni (CMR) zeolite membrane (IMPBR)	V-Mg-O deposited in α-Al_2O_3 membrane; Ni deposited in γ-Al_2O_3 membrane; V-Mg-O packed bed in zeolite membrane	T = 300-600°C Varied C_3H_8 to O_2 feed ratio and flowrate, both reactants fed to tubeside compared with O_2 fed to shellside and C_3H_8 fed to tubeside; conversion kept constant at 10%	Ni/γ-Al_2O_3 membranes give same conversion at lower temperature than V-Mg-O/α-Al_2O_3 membranes, but less selectivity; no separation effect was observed for CMR configurations; best performance was achieved with IMPBR configuration

2.4 Simulation of membrane reactors

A number of models have been published describing simulation of the different types of membrane reactors (Hsieh 1991, Zaman and Chakma 1994) . The majority of these models use simplifying assumptions. For example:

- plug flow (no radial gradients),
- isothermal conditions,
- no interfacial gradients from the bulk fluid to the membrane,
- no axial or radial diffusion,
- only one reaction but no eventual reaction networks are considered,
- the reaction is considered to be instantaneous compared with the external mass transfer rate: Hence the overall rate is considered to be determined by mass transfer,
- the transport mechanism inside a porous membrane is described by Knudsen diffusion only.

A number of recent publications have relaxed these assumptions, for example Sloot *et. al.* (1992), Veldsink *et. al.* (1994) and Abdalla and Elnashaie (1993). In these articles gas phase transport within the porous media is expressed in terms of the Dusty Gas Model derived by Mason and Malinauskas (1983) and which is based on the Maxwell-Stefan description of multicomponent diffusion (Taylor and Krishna 1993). In order to express the mass transfer from the bulk of the gas to the membrane interface the Maxwell-Stefan formulation has to be used to describe the multicomponent mass transfer effects properly. The system modelled by Sloot *et. al.* (1992) was an instantaneous reaction requiring a stoichiometric feed. This was ensured by feeding the reactants from different sides of the membrane. For one reactant surface diffusion was also taken into account and found to be of importance in their system.

Veldsink *et. al.* (1994) investigated only multicomponent permeation through porous alumina membranes of different pore sizes. The experimental results were compared with theoretical

simulations using the dusty gas model, a linearised version of the former and a modified version of Fick's law. The first two models gave a good representation of the experimental results whilst the last model predicted fluxes in the opposite direction to those sometimes measured. In this study methods to determine the necessary parameters for the dusty gas model are described. However chemical reaction was not considered. Both Sloot *et. al.* (1992) and Veldsink *et. al.* (1994) considered only flat disc geometries in their studies.

This brief discussion of published models shows that there is still no model available which combines transport inside a porous membrane structure with a chemical surface reaction taking place on the pore walls and which influences the overall rate of product formation.

2.5 Catalyst considerations

The considered application in this study is the catalytic, oxidative dehydrogenation of methanol to hydrogen and carbon dioxide. A number of different catalysts have been reported to be selective for the dehydrogenation of methanol. However for most of the processes these catalysts were recommended for the production of either formaldehyde or methyl formate. A few examples are given below:

Friedlander and Bennet (1965) determined rate equations for the oxidative dehydrogenation of methanol to formaldehyde and water and the subsequent decomposition of formaldehyde to carbon monoxide and water. The catalyst used was a mixture of iron and molybdenum oxide with an Fe:Mo ratio of 1:3. The experiments were carried out at atmospheric pressure within a temperature range of 402-452°C.

In a European patent application Masakazu (1985) described the dehydrogenation of methanol in the absence of oxygen for the production of formaldehyde. Various combinations of zinc oxide and indium oxide and their mixtures with silica were prepared to form catalyst pellets. More conventional catalysts such as 20 wt% ZnO on Al_2O_3 were prepared for

comparison purposes. Some of these catalysts were very selective towards hydrogen and carbon monoxide. Generally, these were the catalysts prepared from carbonates and hydroxides. However the reaction temperature in all cases exceeded 500°C.

Zaspalis *et. al.* (1991a-c) also investigated the above reaction. They used a membrane reactor consisting of two chambers separated by a flat disk membrane. In some of the experiments oxygen was fed into the reactor from the opposite side to the methanol feed. In all cases a γ-Al_2O_3 membrane was used. This membrane was found to be catalytically active yielding carbon monoxide and hydrogen as main products at temperatures above 450°C (Zaspalis *et. al.* 1991a). In another set of experiments a packed bed of ZnO pellets was placed on top of the membrane (Zaspalis *et. al.* 1991b). A selectivity towards carbon monoxide of 75% at 500°C was reported. In their last paper (Zaspalis *et. al.* 1991c) a membrane impregnated with silver was investigated. At low oxygen feed rates the desired product, formaldehyde, was produced with a selectivity of 25% and 20% at temperatures of 250°C and 300°C respectively. An increase of the oxygen feed rates led to a selectivity towards carbon dioxide of 100% at 210°C.

The dehydrogenation of methanol to form methyl formate on a promoted copper-zinc-alumina catalyst was investigated by Lender *et. al.* (1985). Rate equations for the formation of methyl formate and hydrogen as well as for the decomposition of methyl formate to methanol and carbon monoxide were given.

The above examples give a general picture of the result of a Chemical Abstracts literature search under the keyword "methanol dehydrogenation". This search yielded 128 references most of which dealt with the production of formaldehyde and methyl formate with the absence of oxygen in the feed. As a general conclusion it can be said that the catalysts commonly used in methanol dehydrogenation tend to be selective for hydrogen at temperatures above 400°C. This temperature is too high for the considered application and, hence, dehydrogenation and oxidation catalysts known for their high activity, were used in

our catalyst screening experiments (see Chapter 5).

CHAPTER 3

EXPERIMENTAL APPARATUS AND REACTOR DESIGN

3.1 Experimental apparatus used for catalyst screening, kinetic and membrane experiments

Three distinct types of experiments were carried out in the course of this study:

- Catalyst screening experiments for the determination of the most suitable catalyst for the reaction investigated, *e. g.* oxidative dehydrogenation of methanol to hydrogen and carbon dioxide.
- Kinetic experiments in order to the investigate the reaction kinetics. For this part, two different types of reactors were employed: a spinning basket reactor and a tubular wall reactor.
- Membrane experiments for investigating the permeation, separation and combined separation-reaction behaviour of different types of membranes.

3.1.1 Catalyst screening apparatus

Figure 3.1 shows the flowsheet of the experimental apparatus used to investigate the oxidative dehydrogenation of methanol in a packed bed reactor for catalyst screening purposes.

The pipework consisted entirely of 316 stainless steel tubing connected by Swagelok compression fittings. The tubing between the evaporator and cold trap, as well as the sample lines connected to the gas chromatograph, was wound with heating tape to prevent condensation. The current for the heating tape was supplied by two transformers.

Air was fed into the system from a gas cylinder (supplied by BOC). Subsequently the air pressure was controlled by a pressure regulator (PR1). The air flowrate was maintained at a

constant value by a Brooks 5850 TR mass flow controller with a maximum flowrate of 500 ml/min.

Methanol (BDH) in the liquid phase was metered to the system by a Watson-Marlow peristaltic pump. This pump was capable of delivering the desired low flowrates of 0.2 to 0.5 ml/min.

The air and the methanol streams were fed into an evaporator consisting of a 1" OD stainless steel tube equipped with mixing inserts (Figure 3.2). This ensured a homogeneously mixed feed stream. The evaporator was placed inside a Severn Science Ltd model MF 1 C furnace controlled by an Eurotherm temperature controller.

Subsequently this stream was fed into the reactor. The reactor used is described in Section 3.4. The reactor was mounted into a furnace supplied by Severn Furnace Ltd (model TF 105/4×5/2/F) controlled by an Eurotherm temperature controller. The reactor pressure was controlled by a needle valve (V5). Downstream of this valve the system was maintained at ambient pressure.

The product was led through a gas wash bottle, used as a cold trap, where condensable components were collected. The cooling medium of the cold trap was ice. On leaving the cold trap the permanent gases were led through a bubble flow meter and then vented to the atmosphere. In order to change the cold trap, this section was fitted with a bypass, controlled by on/off valves (V7 to V9).

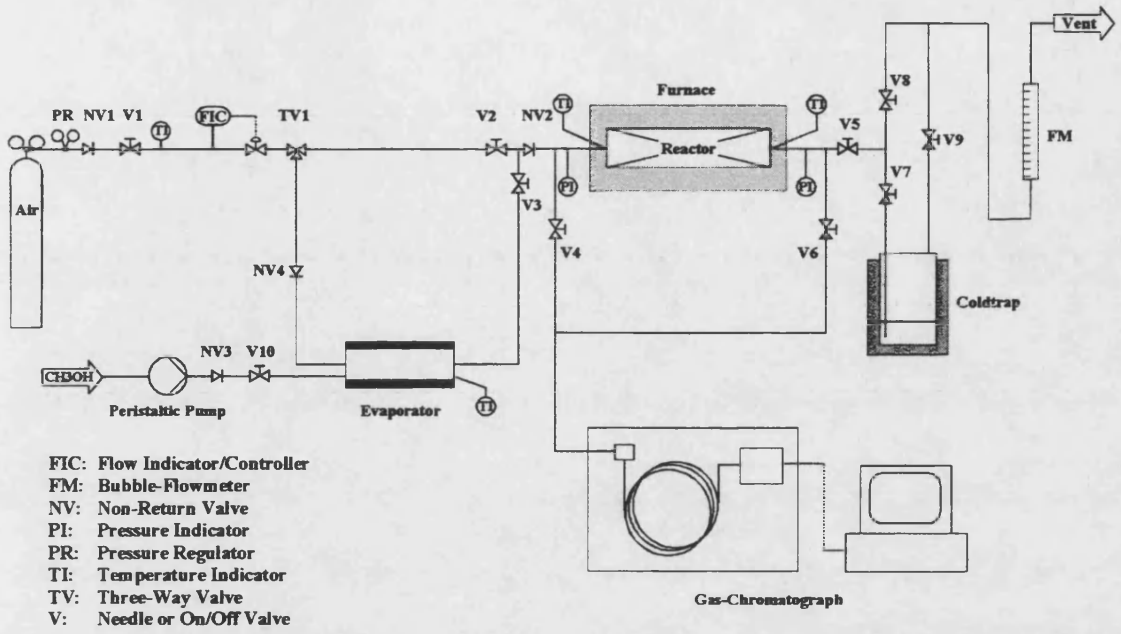

Figure 3.1: Flowsheet of the experimental apparatus used catalyst screening

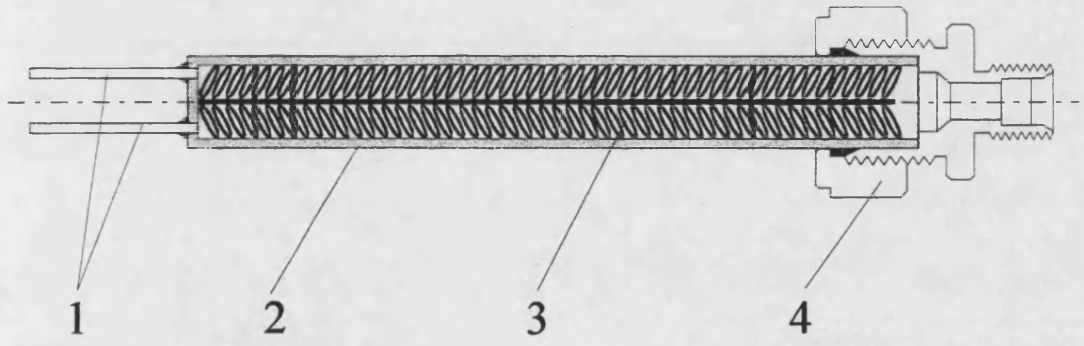

1: Feed lines
2: 1" Stainless steel tube
3: Mixing insert
4: Swagelok compression fitting

Figure 3.2: Evaporator design

Temperatures were measured at different locations of the apparatus, as indicated in Figure 3.1, by means of BICC-Pyrotenax mineral insulated thermocouples (type K Cr-Ni, Cr-Al).

One thermocouple, of 1.5 mm diameter, could be moved inside a 1/8" OD stainless steel tube which was mounted along the reactor axis in order to determine the axial temperature profile (see Figure 3.5). Absolute pressures were measured upstream and downstream of the reactor by means of pressure transducers (Druck Ltd, type PDCR 10 with a maximum absolute pressure rating of 2 bar). For calibrations of the above mentioned equipment refer to Appendix 1.

The output signals of the thermocouples and the pressure transducers were processed by data logging equipment, consisting of a multiplexer board (Advantech Ltd PCLD 789) a data acquisition card (Advantech Ltd PCL 812 PG) and a personal computer (Sperry PC 80286). This equipment is described in detail in Appendix 2.

The reactor feed and exit were equipped with sample ports which could be opened using the on/off valves V4 and V6 respectively. These sample ports were connected by 1/16" OD stainless steel tubing to a gas chromatograph system. This system consisted of a Perkin Elmer Autosystem GC and Perkin Elmer model 1020 GC Plus integrator/control computer. The GC was equipped with a pneumatically driven gas sample valve controlled by the computer. For the gas chromatograph calibration and more information on its operation see Appendix 3.

3.1.2 Apparatus used for kinetic and membrane reactor studies

The apparatus used for the reaction kinetic studies and the membrane experiments is shown in Figure 3.3. It was developed by basing its design upon the catalyst screening system described previously. All additional pipework consisted of stainless steel and was connected by Swagelok compression fittings. The sections of pipework where condensation of reactants or products was possible was heated by means of heating tape as described in Section 3.1.1.

The apparatus was divided into two branches of pipework: the feed/product line and the permeate line. The permeate line was used only for experiments involving a membrane reactor assembly, either for permeation, separation or membrane reactor experiments.

In order to supply the permeate purge gas and to cover a wide range of gaseous reactant flowrates and compositions, three more gas feeds were incorporated. All gases were fed from gas cylinders (supplied by BOC). The feed pressures were controlled by pressure regulators (PR1 to PR4).

Gas flowrates were controlled by Brooks 5850 TR mass flow controllers with the following maximum nitrogen flowrates:

- FIC 1: 500 ml/min
- FIC 2: 5 l/min
- FIC 3: 5 l/min
- FIC 4: 2.5 l/min

The mass flow controller calibrations are given in Appendix A.1.1.

Liquid methanol was fed into the system, evaporated and mixed with the gaseous reactants in the same manner as described in Section 3.1.1.

A three way valve (TV2) allowed the reactant stream to be fed either into the membrane reactor, mounted in the main furnace (F2), or via a preheater (PH) into the tubular wall reactor (TWR). Details of the main furnace are given in Section 3.1.1. A second three way valve (TV6) was used to route the product stream into the reaction product branch of the apparatus. Instead of the preheater and the tubular wall reactor, a spinning basket reactor was used for some of the kinetic studies and connected using the three way valves TV2 and TV6, as shown in Figure 3.4. The spinning basket reactor used is described in detail by Bennet (1990). It was manufactured in the University of Bath and consisted of the reactor, a temperature controlled furnace and an electrical motor

including its revolution control. The design of the different reactors used is described in detail in Section 3.4.

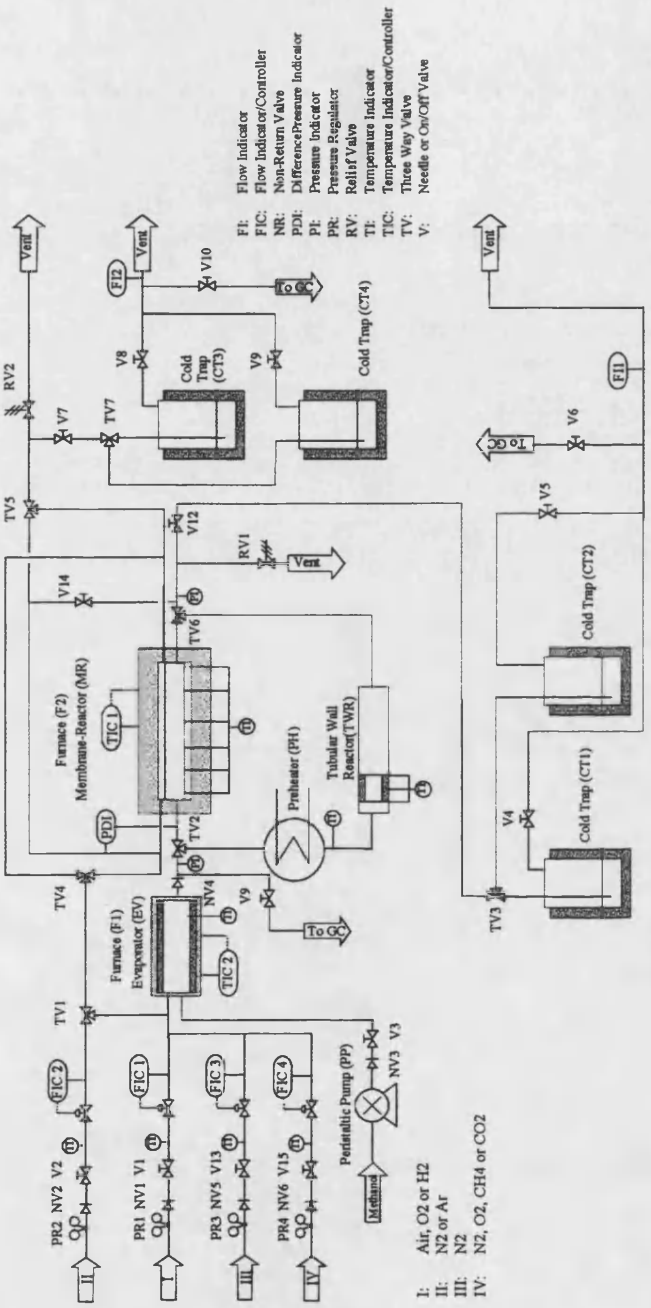

Figure 3.3: Flowsheet of the experimental apparatus for kinetic and membrane reactor studies

The reactor pressures were controlled by means of a needle valve (V12). Downstream of this valve the system was maintained at ambient pressure. The product was led through a gas wash bottle which acted as a cold trap for the collection of the condensable products, The cold trap branch consisted of two parallel cold traps (CT1 and CT2), so that cold traps could be exchanged during the course of an experiment. The cooling medium was dry ice at a temperature off -44°C. The dry ice was supplied by BOC.

On leaving the cold trap, the flowrate of the permanent gases was measured by means of a bubble flow meter (FI1) and then vented to the atmosphere.

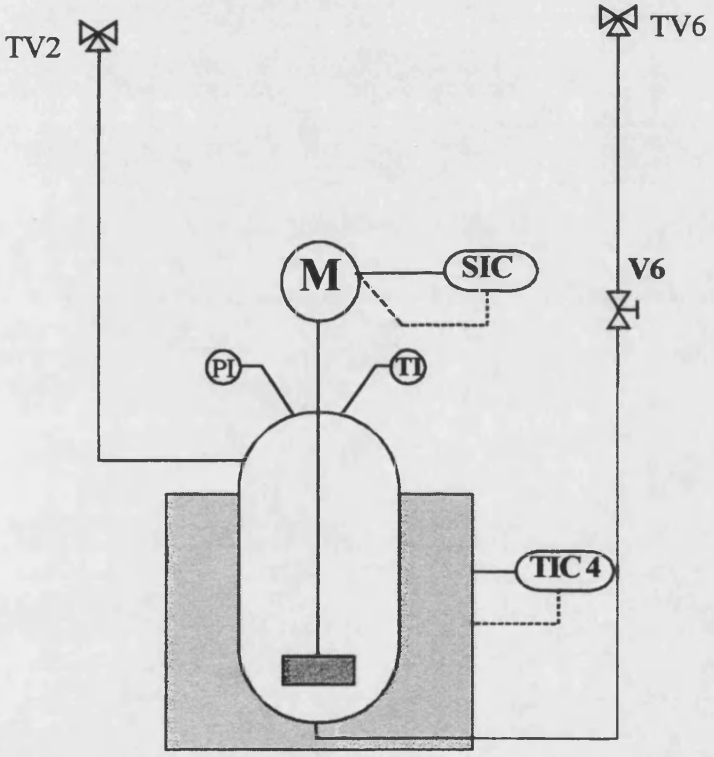

Figure 3.4: Flowsheet of the spinning basket reactor branch

For the membrane reactor and membrane separation experiments, argon was supplied via FIC2 as the purge gas. Two three way valves (TV4 and TV5) were used to switch the flow direction of the purge gas between co-current and counter-current mode with

respect to the membrane reactor feed gas. The control of the feed side pressure and the treatment of the feed side effluent was as described for the kinetic experiments. A parallel branch of the experimental apparatus was used in the same way for the permeate side effluent, again containing a needle valve for pressure control (V7), two coldtraps for the collection of condesable product (CT3 and CT4) and flowmeter (FI2).

The feed/reactant branch and the permeate branch of the pipework were equipped with pressure relief valves set to a bursting pressure of 1.2 bar.

Prior to the bubble flowmeters (FI1 and FI2) samples of the reaction product and permeate gas streams could be passed to the gas chromatograph via the on/off valves V6 and V10.

Pressures and temperatures were measured at the locations indicated in Figure 3.3 (the same equipment as described in section 3.1.1 was used).

Inside the tubular wall and the membrane reactor, 0.5mm diameter thermocouples were used. The thermocouples were of the type K Cr-Ni, Cr-Al and supplied by BICC-Pyrotenax. In both reactors, one thermocouple could be moved in the axial direction in order to record axial temperature profiles. Details of the design are given in Section 3.4.

The pressure difference between tube and shellside of the membrane reactor was measured by means of a differential pressure transducer (Druck Ltd, Type PDCR 2161, maximum pressure difference 1bar). The measured pressure difference signal was processed by the data logging equipment described in Section 3.1.1.

3.2 Experimental procedure

3.2.1 Preparation

Both the catalyst screening and the membrane reactor were manufactured from stainless steel and connected to pipework by means of Swagelok compression fittings. After preparation, their integrity could be tested by pressurising them to 2barg and immersing them into a water bath. After this test had been conducted, the screening or membrane reactor was mounted into the furnace and connected to the pipework. The spinning basket and tubular wall reactors were tested for any leakage by using soap solution. The whole system was then pressurised and the reactor connections were tested with soap solution for leaks. If the catalyst screening, tubular wall or membrane reactor were used, the reactor axis thermocouple was slid into its guiding tube.

Before starting the run the following tasks were also carried out:

- Cleaning the cold traps, applying new silicon lubricant to the glass fittings and determining its weight.
- Connecting a second set of cold traps to the rig for collecting the condensate whilst waiting for the system to achieve steady state conditions.
- Filling the methanol pump reservoir, determining its weight and connecting it to the pump.
- Ensuring that no air was present inside pump tubing.
- Setting the pump dial to the desired flowrate.
- Letting the pump run for a short time in order to build up a sufficient pressure upstream of the non-return valve NV3 and turn it off again.
- Switching on power supplies for all electrical equipment and starting the computer.
- Preparing of the GC for permanent gases analysis (connecting molecular sieve column and choosing of corresponding method).
- Opening of the air and hydrogen cylinders which supply the gases to the GC.

3.2.2 Operation of the catalyst screening experiments

The experimental procedure consisted of the following steps (Figure 3.1 indicates the labels used):

1 Open the air cylinder and set the pressure regulator to 2 barg.

2 Open valves V5 and V8 and close V7 and V9.

3 Set the pressure regulator, PR1, to 1 barg.

4 Open valve V1.

5 Set the mass flow controller to the desired flowrate.

6 Set furnace and evaporator temperature controllers to the desired temperatures.

7 Start the data logging program.

8 Adjust heating tape transformer settings if necessary.

9 Wait until the reactor axis and evaporator temperatures have reached steady state. These temperatures are displayed graphically on the computer screen as a function of time.

10 Measure atmospheric pressure and ambient temperature.

11 Measure the air flowrate at the reactor exit using the bubble flowmeter FM1 and take the corresponding temperature.

12 Open valves V7 and V9 and subsequently close valve V8.

13 Open valve V10 and switch on the pump whilst simultaneously starting a stopwatch.

14 Wait for the reaction to light-off (indicated by sharp reactor temperature increase) and subsequently for the system to achieve steady state conditions. This is indicated by a constant reactor temperature.

15 Open valve V6 to let part of the product flow to the gas sampling valve of the GC. After 5 to 7 minutes, start the GC run and close V6.

16 After the GC run is finished, exchange the molecular sieve column for the Porapak S column and change the GC parameters and method. Wait for the GC to achieve steady state.

17 Repeat step 15.

18 Open valve V8 and close valves V7 and V9. Exchange cold traps.

19 Open V7 and V9 and close V8 and simultaneously starting a stop watch.

20 Determine permanent gases flowrate using the bubble flowmeter, FM1.

21 Measure the axial temperature profile using the "sliding" thermocouple.

22 After 2 hours run time, with the cold trap connected, open V8 and close V7 and V9 and. Stop the stop watch.

23 Exchange coldtraps and repeat step 19.

24 Measure the weight of the filled cold trap.

25 Open valve V4 to let a part of the feed flow to the gas sampling valve of the GC. After 5 to 7 minutes, start the GC run and close V4.

26 Switch off the pump and stopping the stop watch. Close V10.

27 Measure the weight of the pump reservoir.

28 Take a 500µl samples of the content of the cold trap and dissolve it in 2000µl of iso-propanol.

29 Change the GC method to the liquid analysis method and inject 0.5µl of the liquid sample.

30 Run the system for another hour without methanol feed in order to make sure no methanol and product components are left in the pipework, the evaporator and the reactor.

31 Switch off all heating equipment and wait for the system to cool down.

32 Switch off all gas supplies, except the GC carrier gas, and all electrical power supplies except for the GC and GC control computer.

3.2.3 Operation of the tubular wall, spinning basket and membrane reactor experiments

The experimental procedure consisted of the following steps (Figure 3.3 indicates the labels used):

1 Open the gas cylinders required and set the pressure regulators to 2 barg.

2 Switch TV3 to cold trap CT1, open valve V4 and close valve V5. For membrane reactor experiments, switch TV7 to cold trap CT3, open valve V8 and close valve V9.

3 Ensure that TV1 is switched to the membrane reactor shell side.

4 Set pressure regulators PR1, PR3 and PR4 to the required reactant feed pressures. For membrane reactor experiments, set the purge gas pressure using PR2.

5 Open valves V1, V13 and V15 for the reactant feed lines. For membrane reactor experiments, open valve V2.

6 Set the mass flow controllers FIC1, FIC3 and FIC4 to the desired reactant flowrates. For membrane reactor experiments, set the mass flow controller FIC2 to the desired purge flowrate.

7 Set furnace and evaporator temperature controllers to the desired temperatures. For tubular wall reactor experiments, set the preheater temperature to the required level. For spinning basket reactor experiments, set the desired speed of revolution.

8 Start the data logging program.

9 Adjust heating tape transformer settings if necessary.

10 Wait until the system temperatures have reached steady state. These temperatures are displayed graphically on the computer screen as a function of time.

11 Measure atmospheric pressure and ambient temperature.

12 Open valve V3 and switch on the pump whilst simultaneously starting a stopwatch.

13 Wait for until the steady state under reacting conditions had been achieved. This was indicated by constant reactor temperatures.

14 Open valve V6 to let part of the product flow to the gas sampling valve of the GC. After 5 to 7 minutes, start the GC run and close V6. For membrane reactor experiments open V10 and wait until the previous GC run had finished, then carry another run to analyse the shellside gas composition.

15 After the GC run(s) was finished, exchange the molecular sieve column for the Porapak S column and change the GC parameters and method. Wait for the GC to achieve steady state.

16 Repeat step 14.

17 Open V5, close V4 and switch TV3 starting a stop watch simultaneously. For membrane reactor experiments, carry out the analogous steps with V8, V9 and TV7.

18 Determine the flowrate of the permanent gases in the reaction product using the bubble flowmeter, FI1. For membrane reactor experiments, measure the shellside product gas flowrate using FI2.

19 For tubular wall and membrane reactor experiments, measure the axial temperature profile using the "sliding" thermocouple.

20 One to two hours after step 17 was carried out, switch TV3, open V4 and close V5. For membrane reactor experiments, carry out the analogous steps using TV7, V8 and V9. Stop the stop watch(es).

21 Measure the weight of the filled cold traps.

22 Switch off the pump and stop the stop watch. Close V3.

23 Measure the weight of the pump reservoir.

24 Take 500µl samples of the contents of the cold traps and dissolve it in 2000µl of iso-propanol.

25 Change the GC method to the liquid analysis method and inject 0.5µl of the liquid sample.

26 Run the system for another hour without methanol feed in order to make sure no methanol and product components are left in the pipework, the evaporator and the reactor.

27 Switch off all heating equipment and wait for the system to cool down.

28 Switch off all gas supplies, except the GC carrier gas, and all electrical power supplies except for the GC and GC control computer.

3.3 Experiment evaluation

The evaluation of the experiments yielded the molar feed and product flowrates as well as their compositions. On that basis, a mass balance could be carried out which provided a means of deciding whether all components were accounted for. The equations used and the formal procedure of the evaluation are presented in Appendix 4.

3.4 Reactor design

Four types of reactor were used in the course of this study:

- Packed bed reactor for catalyst screening
- Spinning basket reactor for the investigation of reaction kinetics
- Tubular wall reactor for the investigation of reaction kinetics
- Membrane reactor for the investigation of the separation and the combined reaction and separation behaviour of tubular catalytic membranes manufactured from alumina.

The design details of the different types of reactor will be discussed in the following sections.

3.4.1 Packed bed reactor

Figure 3.5 shows the packed bed reactor used for catalyst screening experiments and for catalyst preparation purposes. The reactor consisted of an 0.8" ID, 1" OD stainless steel tube of 250 mm length. The reactor was sealed gas-tight using Swagelok compression fittings. It was connected to the 1/4" OD pipework of the experimental apparatus by Swagelok reduction fittings. The catalyst bed had an actual length of 50 mm, located at the

reactor outlet. Wire mesh discs kept the catalyst particles in the reactor. The remaining length of the reactor was filled with a stainless steel insert with a central hole of 1/4" diameter. A 1/8" OD stainless steel tube, welded close at the end, was placed axially inside the reactor. Inside this tube a thermocouple could be moved in order to determine the axial temperature profile.

For the preparation of pelleted catalyst, the wiremesh discs were replaced by sintered stainless steel discs and the thermocouple guiding tube was replaced by a single thermocouple of 1.5mm diameter located at the start of the packed bed of catalyst precursor. Catalytic membranes were prepared by removing the stainless steel insert and the 250mm long membrane tube into reactor tube instead.

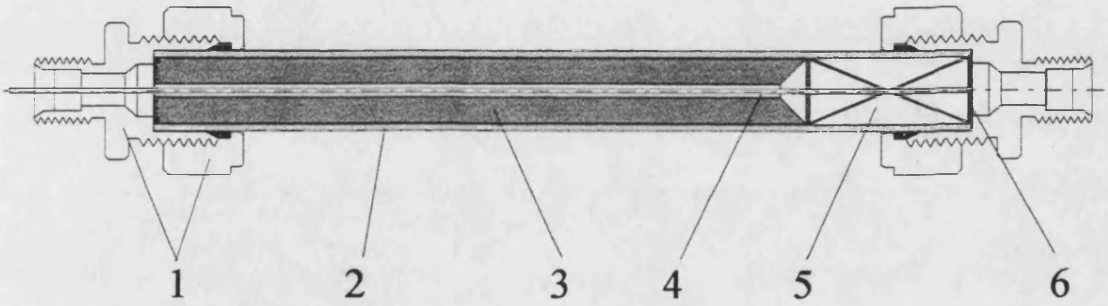

1: Swagelok compression fitting
2: 1" Stainless steel tube
3: Stainless steel insert
4: Thermocouple well
5: Catalyst bed
6: Wire mesh disk

Figure 3.5 Packed reactor used for catalyst screening

3.4.2 Spinning basket reactor

Figure 3.6 shows the spinning basket reactor used for the investigation of the reaction kinetics of the oxidative dehydrogentaion of methanol. The catalyst pellets were contained in a stainless steel wiremesh basket mounted on the end of the rotating reactor

shaft. The shaft was pivoted in two Rulon bearings inside the gas tight reactor housing. The lower bearing, closest to the reactor chamber, was cooled by means of water. The shaft was rotated by means of a magnetic clutch. The clutch consisted of two sets of magnets: one mounted on the reactor shaft and the other to an outer magnet holder. The outer magnet holder was pivoted against the reactor housing by means of roller bearings. An electric motor was used to rotate the outer magnet holder via a belt. The speed of revolution of the motor could be controlled.

All parts of the reactor housing were manufactured from 316 stainless steel. Gases could enter and leave the reactor via 1/4" stainless steel tubing welded to the reactor housing. These tubes were connected to the experimental apparatus using Swagelok compression fittings.

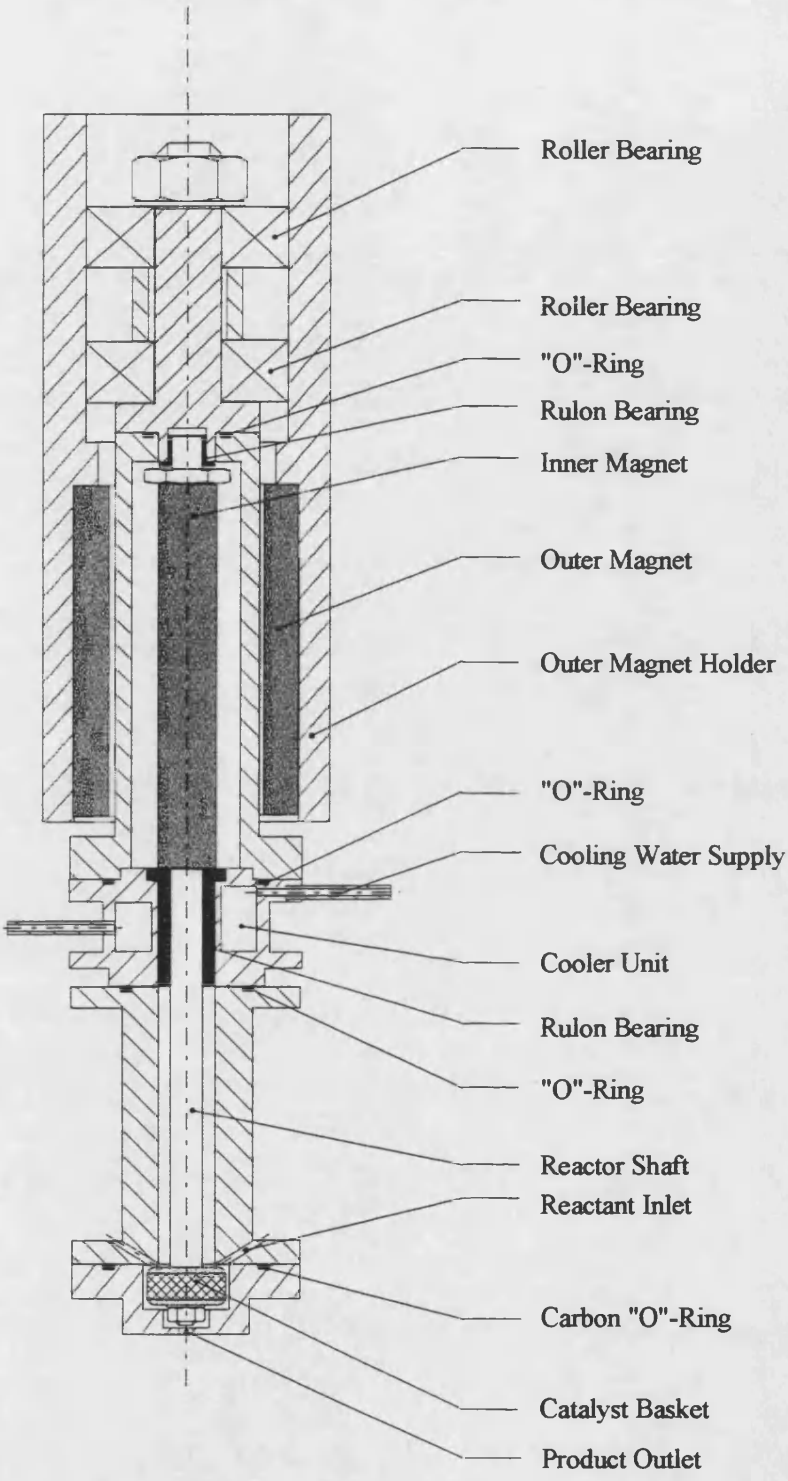

Figure 3.6: Spinning basket reactor

The reactor chamber was placed inside a temperature controlled Perkin-Elmer gas chromatograph furnace for the control of the reactor temperature. A thermocouple of 1.5mm diameter was placed inside the reactor chamber.

The volume of the catalyst basket was determined and was $2.091\times10^{-5}m^3$. The free reactor volume was determined by substracting the volume of the reactor shaft and the basket material from the volume of the empty reactor housing. The value obtained was $3.9703\times10^{-5}m^3$.

The spinning basket reactor was designed and manufactured at the University of Bath and was used previously in other studies. More details regarding its operation and design can be found in Bennet (1990).

3.4.3 Tubular wall reactor

For part of the kinetic investigations carried out in this study, a tubular wall reactor as shown in Figure 3.7 was employed. The tubular wall reactor was of the same design as described by Hayes *et. al.* (1995). The main body of the reactor was a double walled Pyrex glass tube. The space between the walls was evacuated in order to insulate the reactor. Furthermore a reflecting layer was deposited on the inside of the outer layer to serve as a radiation shield. A pair of stainless steel baffles, simultaneously serving as radiation shields, were placed in the inlet and outlet section of the reactor tube. Flow distribution plates, *e.g.* perforated stainless steel discs, were located inwards from the baffles. Through one set of baffles and flow distribution disc and along the reactor tube, a 1/16" OD stainless tube, welded at one end so that it was closed, served as a thermocouple well. The glass reactor tube was sealed with graphite gaskets against stainless steel flanges as shown in Figure 3.7. 1/4" OD stainless pipes were welded into these flanges for connection to the pipework of the experimental apparatus and for serving as a thermocouple well. The internal diameter of the reactor tube was 21mm and

the length of the tube was 250mm. Inside the reactor, tubular catalyst support elements of different length could be placed. In order to increase the gas velocity, it was possible to place an annular flow insert of 12mm diameter and 90mm overall length in the reactor tube. A thermocouple of 0.5mm diameter was used in the thermocouple well for the measurement of the axial temperature profile close to the tubular section. Two other 0.5mm diameter thermocouples were placed into the gas stream at the start and at the end of the tubular element. The detailed design drawings are appended in Appendix 5.

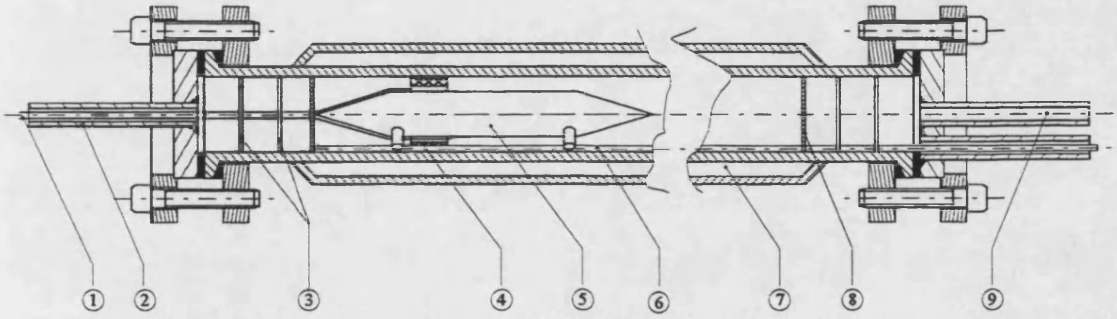

1	Thermocouple	6	Thermocouple well
2	Feed pipe	7	Evacuated double wall reactor tube
3	Baffles/Radiation shields	8	Flow distribution plate
4	Catalytic tube section	9	Exit pipe
5	Anular flow insert		

Figure 3.7: Tubular wall reactor

3.4.4 Membrane reactor

Figure 3.8 shows the design of the membrane reactor used in this study. It was not possible to use standardised parts such as Swagelok fittings, because sealing the permeate shell against the inside of the membrane tube would have been more complicated than the design shown in Figure 3.8. Again, the material of the reactor shell and flanges is 316 stainless steel. For separation and reaction experiments the seal between shell and the flanges were either DuPont Kalrez "O"-rings (compound 4079, ID 21.95mm, thickness 1.78mm) or graphite "O"-rings of the same dimension, respectively. Kalrez "O"-rings can withstand temperatures up to 316°C whilst graphite "O"-rings can be used up to 600°C.

The inner tube depicted in Figure 3.8 is a catalytic membrane. The membranes used in this study were supplied by SCT and were of the type T1-150. The membrane length was 250mm with an internal diameter of 14.9mm and an outer diameter of 19mm. To about 10mm of either side of the membrane, an impermeable glaze was applied for apllication of seals. For a detailed description of the membrane see Chapter 6.

The membrane tube was sealed against the shoulders of the inner flange by means of a Kalrez or graphite "O"-ring (ID 19.1mm, thickness 1.6mm). The sealing force was applied by means of discs pressed against the "O"-rings by the outer flanges. This sealing mechanism allowed for the different thermal expansion coefficients of stainless steel and alumina. As the thermal expansion coefficient of stainless steel is greater than that of alumina, a relative movement of the stainless steel reactor housing with respect to the membrane was possible.

As for the catalyst screening reactor and the tubular wall reactor, a thermocouple well was used to enable the measurement of axial temperature profiles. Here, a 1/8" OD stainless steel tube, welded at one end so that it was closed, was used in the central axis of the membrane tube. A 1.5mm thermocouple could be moved in axial direction inside the well. Four additional thermocouples of 0.5mm diameter were placed at the tube- and shell side inlets and outlets.

The reactor design details are listed in Appendix 5.

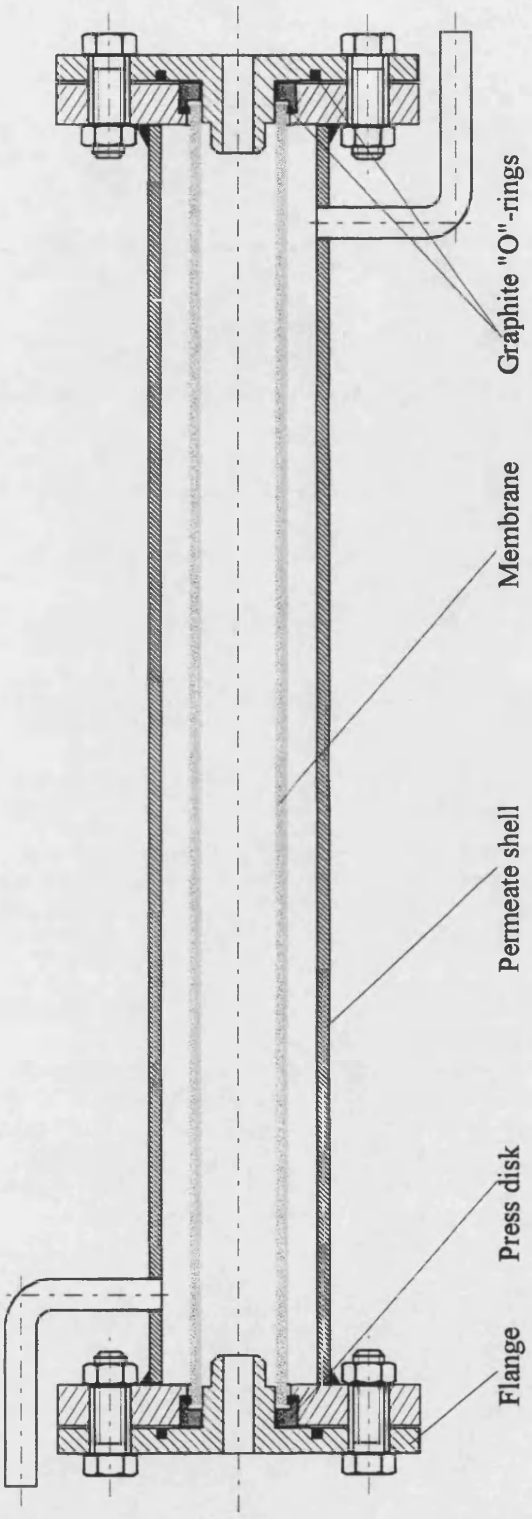

Figure 3.8: Membrane reactor

CHAPTER 4

THERMODYNAMIC CALCULATIONS

4.1 Equilibrium calculations

The main purpose of these calculations is to investigate the oxidative dehydrogenation of methanol in order to produce hydrogen according to the following equation: $CH_3OH + 0.5\ O_2 \rightarrow CO_2 + 2\ H_2$. However, the occurrence of parallel reactions and the further reaction of hydrogen, *e. g.* to form water, is likely. Hence it is not possible to calculate the equilibrium composition at a chosen temperature and pressure using the standard Gibbs free energy of formation of the components, the reaction stoichiometry and the van't Hoff equation as if only one chemical reaction takes place.

For a reaction network, a different approach has to be chosen. Thermodynamic equilibrium of several reactions occurring concomitantly is characterised by a minimum of the Gibbs free energy. For a multicomponent system the Gibbs free energy is given by:

$$G = n_{tot}\overline{G} = \sum_{i=1}^{nc} \mu_i n_i \qquad (4.1)$$

The chemical potential μ_i for each component i can be expressed as

$$\mu_i = \overline{G}_i^0 + R_G T \ln\left(\frac{f_i}{f_i^0}\right) \qquad (4.2)$$

as shown by Gmehling and Kolbe (1988) for example. In Equation 4.2, $\overline{G}_i^0$ is the partial Gibbs standard free energy of formation and f_i is the fugacity of component i. Combining Equations 4.1 and 4.2 leads to:

$$n_{tot}\overline{G} = \sum_{i=1}^{nc} n_i \overline{G}_i = \sum_{i=1}^{nc} n_i \left(\overline{G}_i^0 + R_G T \ln\left(\frac{f_i}{f_i^0}\right)\right) \qquad (4.3)$$

This equation now has to be minimised with respect to the free energy in order to obtain the equilibrium composition. Simultaneously the mass balances of the individual atoms, making up all of the chemical species have to be fulfilled. It is necessary to define the likely components present at equilibrium, their standard free energies of formation at the considered temperature and, in case of non-ideal behaviour, a relationship to express their fugacity or activity. Information about the reaction network is not needed. The method delivers negligible concentrations for components which are at minimal equilibrium concentrations. Walas (1985) gives a more detailed discussion of this method as well as a mathematical solution algorithm. The algorithm solves this constrained minimum problem using Lagrange multipliers to couple the element balances to the minimum conditions. This yields a set of non-linear equations which have to be solved by a non-linear regression method.

This method is implemented in the ASPEN PLUS software package where a Gibbs Equilibrium Reactor model (RGIBBS) is one of the process units The products of this model are assumed to be at thermodynamic equilibrium. Temperature, pressure and the number of fluid phases are input parameters. It is also possible to specify solid components in the product. Further, a feed and a product stream have to defined. The product stream contains all the substances assumed to be present in the product at equilibrium composition and at the specified temperature.

The calculations were carried out defining a feed stream consisting of methanol and oxygen of different compositions. The following range was covered: $y_M = 0.571$ to 0.8 and $y_{O2} = 0.2$ to 0.429. Utilising a temperature range of 450K to 750K. The components assumed to be present in the product were:

- Methanol (CH_3OH)
- Oxygen (O_2)
- Hydrogen (H_2)
- Water (H_2O)
- Carbon monoxide (CO)
- Carbon dioxide (CO_2)
- Formaldehyde (CH_2O)
- Dimethylether (C_2H_6O)
- Carbon (C, graphite)
- Methane (CH_4)

The latter two components were not considered in all calculations. It was found that their occurrence in the product has a large influence on its equilibrium composition as shown in the following figures. If neither carbon nor methane is assumed to be present in the product, the hydrogen content was found to be in the region of 60 %, which decreased with increasing temperature (Figure 4.1).

If methane, but not carbon was assumed to be present as well, the hydrogen content decreased significantly. A maximum value of 20 % hydrogen at 750K was calculated in this case, whilst the main products at equilibrium were water, methane and carbon dioxide. The hydrogen content was found to increase with increasing temperatures (Figure 4.2).

Figure 4.3 shows the third case, where both carbon and methane were considered to be present. Water appeared to be pre-dominant with its content decreasing with increasing temperatures. Both methane and carbon dioxide were present in smaller amounts compared with the previous case. This was caused by the occurrence of carbon, the amount of which decreased with increasing temperature. The hydrogen content increased with increasing temperatures, reaching a maximum value of 19.69 % at 750K.

The influence of nitrogen as a reactant was also investigated. It was assumed that nitrogen either reacted with oxygen to form N_2O or NO_2. Neither of these components was found to be present to any considerable extent in the equilibrium mixture. For these calculations the cases when no methane and no carbon were present and also when methane but no carbon was present, were examined.

For all these calculations the feed was assumed to consist of a mixture of methanol and oxygen with a stoichiometric composition according to the reaction given above. Figures 4.4 and 4.5 show the influence on the equilibrium composition, caused by varying the feed composition. Both methane and carbon are considered as possible products. With increasing oxygen content in the feed mixture, the amount of carbon and methane in the equilibrium mixture decreased whilst, as expected, the amount of oxygen containing species (namely water and carbon dioxide) increased. The hydrogen content was only slightly influenced by changes in the feed composition.

The conversion of methanol was almost complete in all the examined cases. For example 99.9991% at 600K for the conditions described in Figure 4.1.

The components formaldehyde and dimethylether were mentioned by Zaspalis *et. al.* (1991a) as products of their dehydrogenation experiments carried out in a membrane reactor. However, according to the equilibrium calculations carried out these components are only present in negligible quantities.

In conclusion, it can be stated that the catalyst screening tests should aim at catalysts which are known not to favour methane and which show the lowest possible extent of coking. If the reaction is to be carried out in a conventional reactor the residence time should be kept short to prevent the product hydrogen from further reacting to form, for example, water.

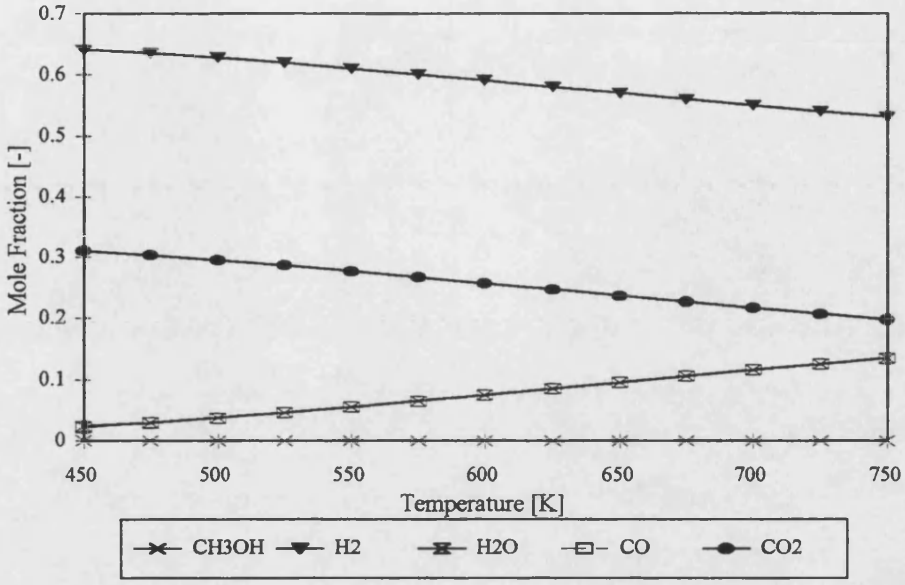

Figure 4. 1: Equilibrium composition vs temperature; p=1 bar, $x_{M,Feed}$=2/3, $x_{O2,Feed}$=1/3; methane and carbon not assumed to be present in product

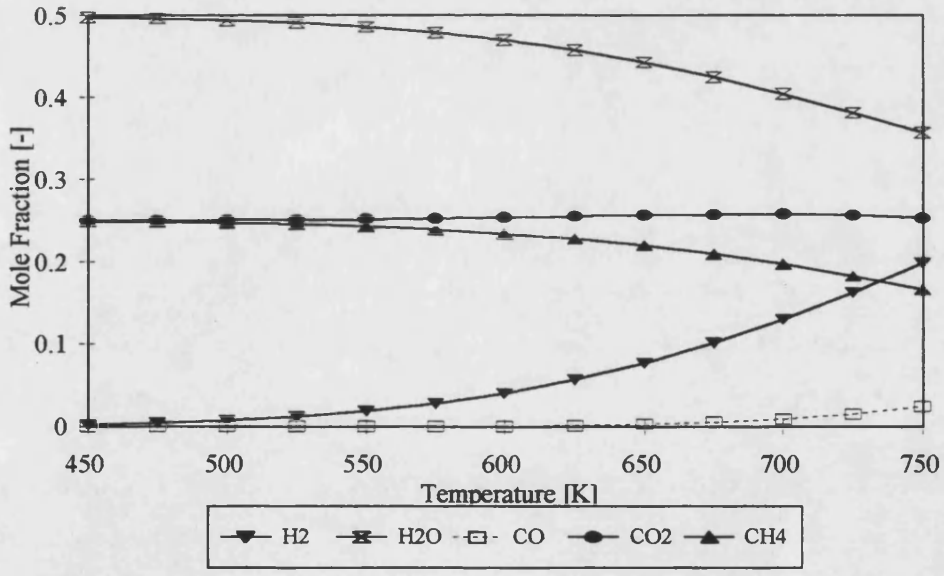

Figure 4. 2: Equilibrium composition vs temperature; p=1 bar, $x_{M,Feed}$=2/3, $x_{O2,Feed=1/3}$; methane but not carbon assumed to be present in product

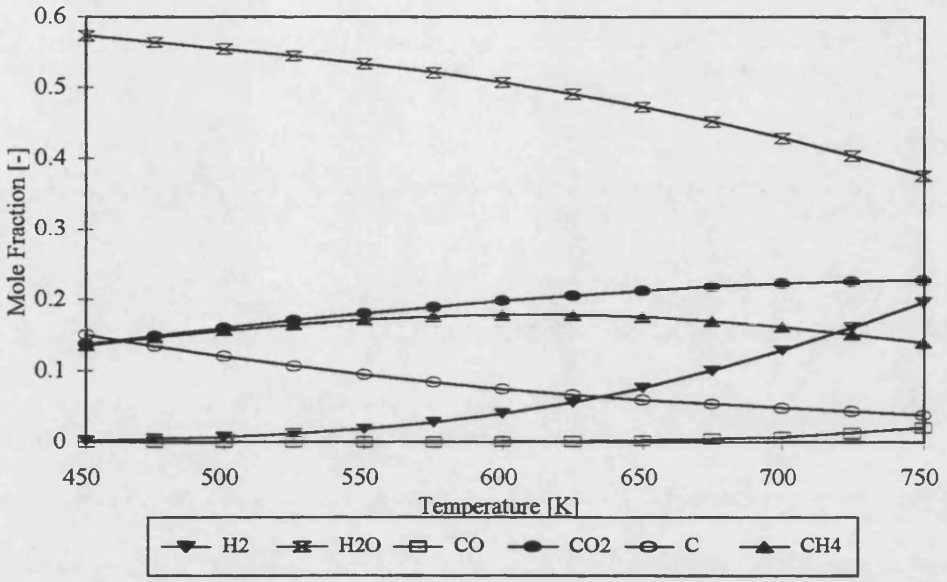

Figure 4. 3: Equilibrium composition vs temperature; p=1 bar, $x_{M,Feed}$=2/3, $x_{O2,Feed}$=1/3; methane and carbon assumed to be present in product

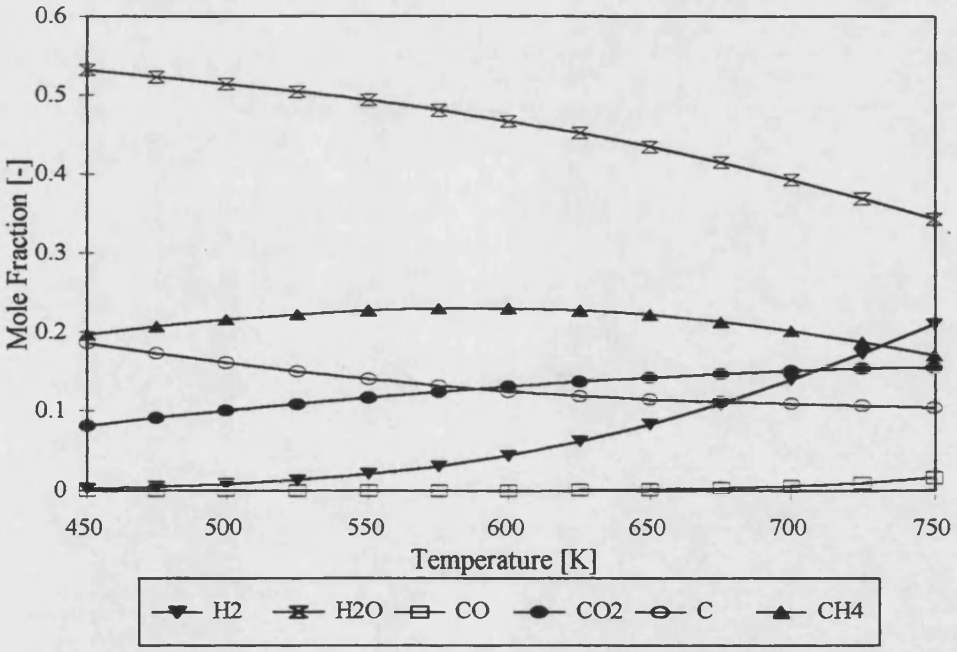

Figure 4. 4: Equilibrium composition vs temperature; p=1 bar, $x_{M,Feed}$=0.8, $x_{O2,Feed}$=0.2; methane and carbon assumed to be present in product

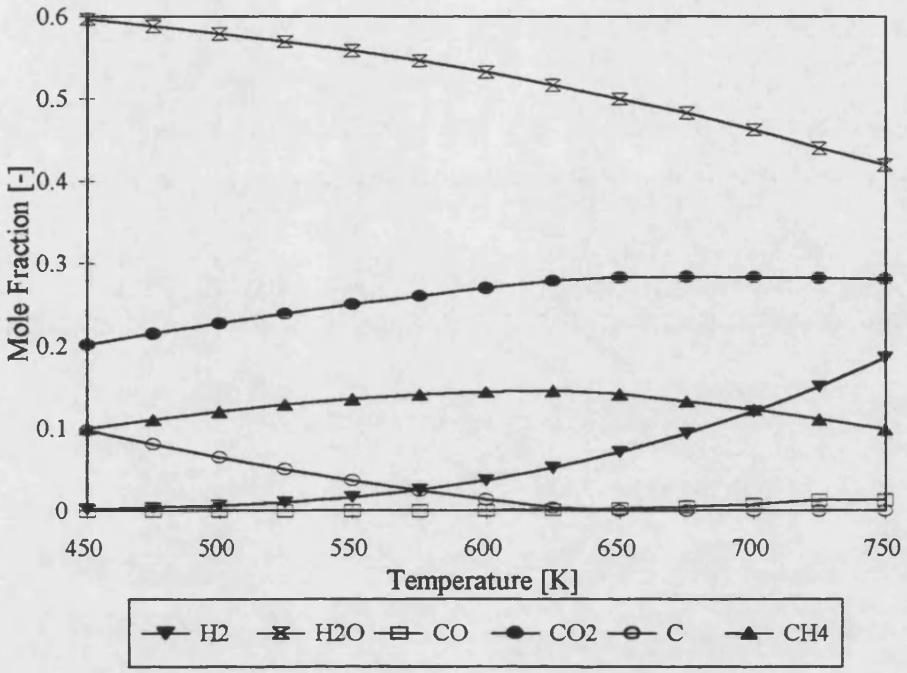

Figure 4. 5: Equilibrium composition vs temperature; p=1 bar, $x_{M,Feed}$=0.571, $x_{O2,Feed}$=0.429; methane and carbon assumed to be present in product

4.2 Heat of reaction

Heats of reaction can be calculated using standard heats of formation of the components $(\Delta H_f)_{s,i}^{0}$, their stoichiometric coefficients υ_i in the considered reaction and their molar heat capacities (Gmehling and Kolbe, 1988). Table 4.1. shows the parameters required to calculate the heats of reaction for the oxidative dehydrogenation of methanol and the combustion of methanol ($CH_3OH+1.5O_2 \rightarrow CO_2+2H_2O$). The stoichiometric coefficients are shown in Table 4.2.

Table 4.1: Properties used for heat of reaction calculation (from Gmehling and Kolbe (1991))

Component	$(\Delta H_f)_{s,i}^0$ [kJ/mol]	Coefficients for the temperature dependence of c_{pi} in J/(mol K)			
		a	$b \cdot 10^3$	$c \cdot 10^6$	$d \cdot 10^9$
CH_3OH	-201.16	21.137	70.88	25.82	-28.50
O_2	0	28.087	-0.0042	17.447	-10.644
H_2O	-241.82	32.220	1.9225	10.548	-3.594
CO_2	-393.50	19.78	73.39	-55.98	17.14
H_2	0	27.124	9.267	-13.799	7.640

Table 4.2: Stoichiometric coefficients

	CH_3OH	O_2	H_2O	CO_2	H_2
$CH_3OH+0.5O_2 \rightarrow CO_2+2H_2$	-1.0	-0.5	0.0	1.0	2.0
$CH_3OH+1.5O_2 \rightarrow CO_2+2H_2O$	-1.0	-1.5	2.0	1.0	0

The heat of reaction at standard conditions can be calculated from the heat of formation of the participating species:

$$\Delta H_R^0(T_0) = \Delta H_R^0(25°C) = \sum_{i=1}^{nc} \nu_i \left(\Delta H_f\right)_{s,i}^0 \qquad (4.4)$$

The computed value of $\Delta H_R^0(T_0)$ is -192.34kJ/mol for the oxidative dehydrogenation of methanol and -675.98kJ/mol for the combustion of methanol. In order to determine the heat of reaction at other temperatures the following equation has to be used:

$$\Delta H_R(T) = \Delta H_R^0(T_0) + \int_{T_0}^{T} \sum_{i=1}^{nc} \nu_i c_{Pi}\, dT \qquad (4.5)$$

The temperature dependency of c_{pi} can be expressed by:

$$c_{pi}(T) = a_i + b_i T + c_i T^2 + d_i T^3 \qquad (4.6)$$

Figures 4.6 and 4.7 show the heats of reaction of the dehydrogenation and the combustion reaction as a function of temperature, respectively. It is apparent from these figures that the reactions show exothermic behaviour in the region of interest.

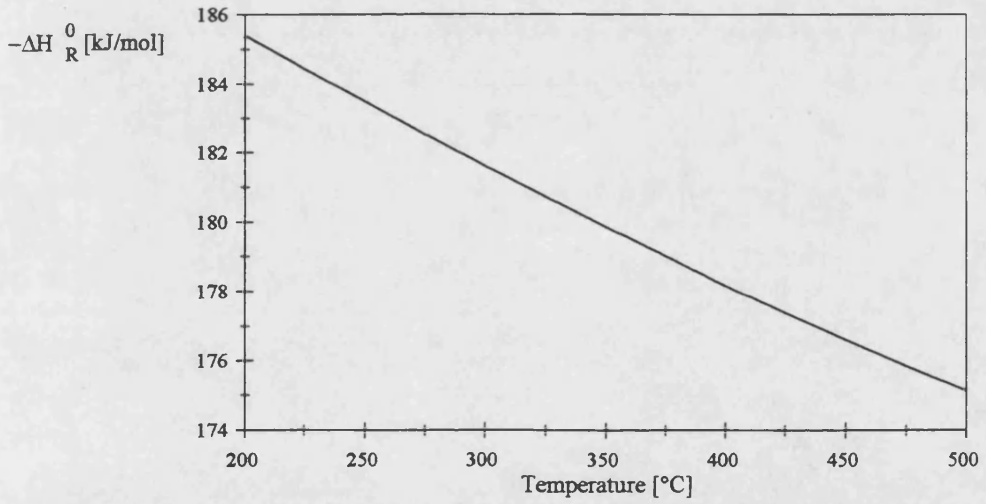

Figure 4.6: Heat of reaction vs temperature (reaction: $CH_3OH + 0.5\ O_2 \rightarrow CO_2 + 2\ H_2$)

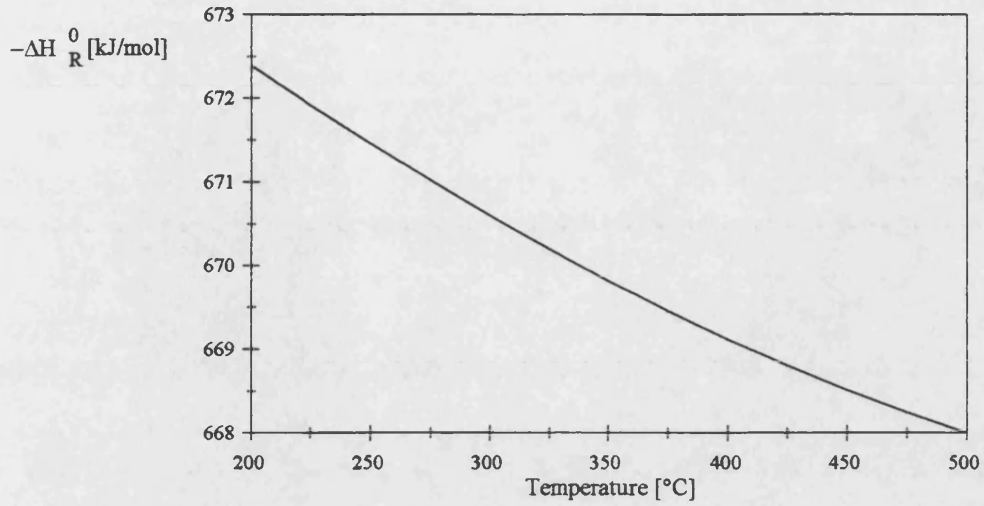

Figure 4.7: Heat of reaction vs temperature (reaction: $CH_3OH + 1.5\ O_2 \rightarrow CO_2 + 2\ H_20$)

The combustion reaction shows a higher heat of reaction than the oxidative dehydrogenation reaction. The aim of this study was produce hydrogen in as pure a form as possible. However, the thermodynamic equilibrium calculations suggested that water would be produced in parallel. Hence it was prudent to assess this reaction in terms of the energy it is likely to release.

CHAPTER 5

CATALYST SCREENING EXPERIMENTS

5.1 Experimental

Catalyst screening experiments were carried out using a packed bed reactor. The reactor as shown in Figure 3.5, consisted of 0.8" ID, 1" OD stainless steel tube of 250 mm length. The catalyst bed had an actual length of 50 mm. Wire mesh disks retained the catalyst particles in the bed. The remaining length of the reactor was filled with a stainless steel insert with a central hole of 1/4" diameter or an inert packing of 3 mm glass spheres. A 1/16" OD stainless steel tube, welded close at the end, was placed axially inside the reactor. Inside this tube a thermocouple could be moved in order to determine the axial temperature profile.

The oxidative dehydrogenation of methanol to hydrogen and carbon dioxide has not been investigated thoroughly, as reported in Chapter 2. Therefore a number of catalysts known for good oxidation and dehydrogenation performance were tested. Table 5.1 lists the catalysts used, which were all supplied by Strem Chemicals except the activated alumina which was obtained from UOP. The voidage of a packed bed of cylindrical particles of the size given in Table 5.1 inside a reactor as described above was determined to be 0.53 (see Appendix 6).

A total of 12 experiments was carried out. All but the first and last experiments were carried out at approximately the same molar feed flowrate and composition. Table 5.2 shows the parameters of these experiments. Experiments 5, 6 and 7 were carried out with a diluted catalyst bed. The initial reactor temperature was set between 25 and 75°C for the experiments carried out with a platinum catalyst. This catalyst was found to light-off independent of the temperature immediately after the methanol supply was switched on. All the other catalysts showed significant light-off temperatures. This light-off temperature was determined by setting the reactor initially to a low temperature. In case the catalyst did not light-off the

reaction, the temperature was increased stepwise until a sharp temperature increase indicated catalytic activity. Figure 5.1 explains this procedure for experiment 9.

Table 5.1 Investigated catalysts

Catalyst	Shape	Size [mm]	Surface area [m^2/g]
Pt (0.5 wt% on Al_2O_3)	cylinder	3.175x3.175	100
V2O5 (10 wt% on Al_2O_3)	cylinder	3.175x3.175	78
MoO_3 (10-12 wt% on Al_2O_3)	cylinder	3.175x3.175	64
NiO (10 wt% on Al_2O_3)	cylinder	3.175x3.175	65
CuO (10-12 wt% on Al_2O_3)	cylinder	3.175x3.175	187
γ-Al_2O_3	sphere	3.175	

The light-off temperatures for the individual experiments as well as the other results are listed in Table 5.3. The Reynolds number for the channels of a packed bed can be calculated according to (Bird *et. al.* 1960):

$$Re = \frac{v\rho d_h}{\mu} \tag{5.1}$$

Where v is the interstitial velocity in a channel of the packing, ρ the mass density and μ the viscosity. The characteristic length of the Reynolds number is defined by the hydraulic diameter of the channels making up the void spaces of the packing:

$$d_h = \frac{\text{Volume Channel}}{\text{Surface Channel}} = \frac{V_{bed}\varepsilon}{V_{bed}(1-\varepsilon)a_p\psi} \tag{5.2}$$

Here ε is the voidage of the packing and a_p is the particle surface area per unit apparent particle volume. It is related to the particle surface area per unit bed volume by:

$$a = \frac{A_p}{V_p}(1-\varepsilon) = a_p(1-\varepsilon) \tag{5.3}$$

The shape factor ψ is an empirical coefficient that depends on the particle shape. It was given as 0.91 for packed of cylinders by Bird *et. al.* (1960) without additional information regarding the aspect ratio of the cylinder.

The mass flowrate $\dot{m}$ per unit crossectional area A_T of the reactor tube, *i. e.* the superficial mass velocity, can be defined as:

$$\frac{\dot{m}}{A_T} = \frac{u\rho}{A_T} = \frac{\varepsilon v\rho}{A_T} \tag{5.4}$$

Inserting Equations 5.2, 5.3 and 5.4 into Equation 5.1 renders:

$$Re = \frac{\dot{m}}{A_T\, a\, \mu\, \psi} \tag{5.5}$$

Equation 5.5 gives the definition of the Reynolds number used in Table 5.3.

Table 5.2 Experimental conditions

Exp. No.	Catalyst	Catalyst weight [g]	Molar feed flowrate [mol/min]	Feed composition		
				O_2	N_2	CH_3OH
1	Pt	17.12	0.022039	0.1537	0.5784	0.2679
2	Pt		0.030701	0.1476	0.5554	0.2969
3	Pt		0.030373	0.1479	0.5566	0.2955
4	Pt		0.030484	0.1463	0.5503	0.3035
5	Pt	8.348	0.030131	0.1449	0.5452	0.3098
6	V_2O_5	10.5284	0.03040	0.1474	0.5545	0.2981
7	V_2O_5		0.030182	0.1475	0.5548	0.2978
8	MoO_3	17.1873	0.029614	0.1491	0.5611	0.2898
9	NiO	18.1224	0.029721	0.1486	0.5590	0.2924
10	NiO		0.029551	0.1487	0.5594	0.2919
11	CuO	15.4206	0.030273	0.1469	0.5524	0.3007
12	γ-Al_2O_3	8.8828	0.14440	0.0617	0.815	0.1233

The space-time was evaluated according to Equation 5.6:

$$\tau = \frac{m_{cat}}{N_F} \qquad (5.6)$$

where m_{cat} is the mass of catalyst in the bed and N_F is the total molar feed flowrate.

The average reactor pressure was, for all experiments, in the region of 1.01 to 1.02 bar. In the product mixtures of experiments 6, 7 and 8 a substantial amount of formaldehyde was detected in addition to expected components. In experiment 12 dimethylether was detected as well as formaldehyde. These two components were identified by taking samples and analysing those with a mass spectrometer and subsequently comparing the results with a database. Due to calibration complications as described in Appendix 3, it was not possible to quantify the amount of formaldehyde or dimethylether but the estimated mole fractions of these components were only about 1%.

Chromatograms resulting from the analysis of typical gas and liquid phase products encountered in this study are presented in Appendix 3. These chromatograms were produced for one of the spinning basket reactor experiments described in detail in Chapter 7. Pt/γ-Al_2O_3 was used as a catalyst. It is apparent from these chromatograms that only H_2, O_2, N_2, CH_4, CO, CO_2 and CH_3OH were present in the product in any quantifiable amounts.

The catalysts used in experiments six to eight were subject to severe carbon deposition. Visual inspection of the used vanadium(V)oxide catalyst showed that the initially yellow particles turned black whilst in operation. This effect was even more emphasized in case of molybdenum(VI)oxide. The colour of the used platinum catalyst remained the initial dark grey. Nickel oxide showed a slight darkening of the first sub-layers of the pellet. Activated alumina did not show any signs of coking, but it was only subjected to reaction conditions for approximately four hours.

Another indication for the occurrence of coking was the decrease in catalytic activity indicated by a decrease in reaction temperature for V_2O_5 and MoO_3 after approximately 13 and 5 hours respectively. The same platinum catalyst was used for all 5 listed experiments as well as for several test experiments carried out previously. Its total operation time was about

70 hours at least with no apparent loss in activity. Nickel oxide did not lose catalytic activity either. However, this catalyst was only in operation for about 12 hours. Furthermore the first signs of coking were observed.

The overall mass balances of experiments six to eight appear to be fulfilled more satisfactorily than those of the other experiments. However, it can be seen from the mass balances of the individual atomic species that the content of nitrogen in the product is larger than in the feed whilst all the other atomic species were underrepresented. Hence the overall mass balance appeared to be closed.

Other results of the catalyst screening experiments are the measured axial temperature profiles. Figure 5.2 shows one of these profiles.

Table 5.3: Results of the catalyst screening experiments

Exp No	Cat	Temperatures [°C]		Product									X (CH_3OH) [%]	S_{H2} [%]	Re	τ [g min/ mol]	Mass bal. Close [%]
		Light-off	Steady state (z=5mm)	Flowrate [mol/min]	Composition [%]												
					H_2	O_2	N_2	CH_4	CH_3OH	CO	CO_2	H_2O					
1	Pt	75	368.59	0.027246	26.3	1.43	44.5	1.06	2.56	6.78	11.8	5.61	87.41	74.1	1.6	742.8	6.26
2	Pt	75	365.48	0.037865	26.4	1.78	41.7	1.14	6.12	4.47	11.5	7.01	72.40	82.2	2.6	533.2	6.96
3	Pt	50	362.2	0.03648	27.1	2.05	45.2	1.21	4.20	4.50	11.4	4.39	81.77	71.9	2.3	529.0	9.45
4	Pt	25	342.71	0.038093	28.9	2.21	43.2	1.24	4.40	3.89	12.2	3.98	80.96	77.1	2.3	537.0	7.08
5	Pt	25	348.43	0.035638	25.9	1.53	42.5	0.76	8.04	2.75	11.4	7.21	66.44	81.4	2.3	277.1	10.11
6	V_2O_5	183	453.29	0.035502	5.51	0.93	61.0	3.75	2.58	15.2	3.07	8.03	89.47	12.6	2.0	346.3	1.74
7	V_2O_5	183	436.80	0.034630	5.23	1.09	64.5	3.04	2.74	14.2	2.50	6.65	89.44	11.3	2.0	348.8	0.78
8	MoO_3	230	476.24	0.035384	3.79	1.51	53.0	2.95	6.67	8.32	3.23	19.6	64.66	15.5	1.9	580.4	1.47
9	NiO	266	507.37	0.039526	30.0	1.14	40.2	1.23	1.56	4.91	12.2	8.79	92.42	78.6	1.9	609.8	5.06
10	NiO	267	500.4	0.039773	30.5	1.31	40.3	1.55	1.59	4.64	12.5	7.64	92.37	79.2	1.9	613.3	4.0
11	CuO	170	489.95	0.039827	29.5	0.86	42.8	0.36	3.26	5.33	11.1	6.80	85.28	78.2	2.0	509.4	4.94
12	γ-Al_2O_3	-	294.68	0.14513	-	6.17	81.5	-	12.333	-	trace	trace	-	-	0.2	61.26	-

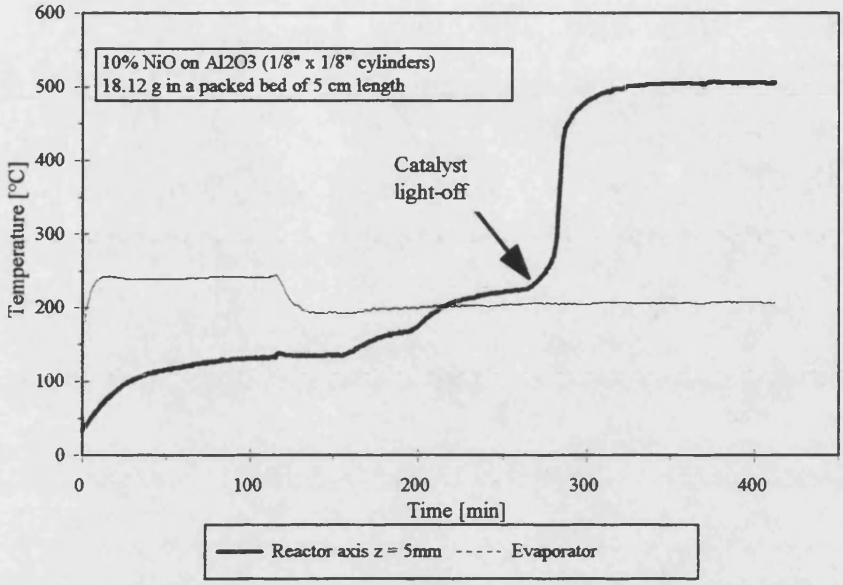

Figure 5.1: Determination of catalyst light off temperature (Experiment 9)

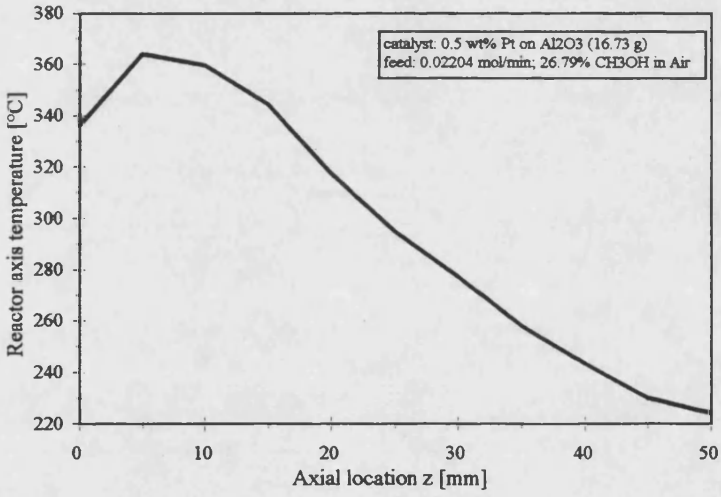

Figure 5.2: Axial temperature profile experiment 1; catalyst: Pt

5.2 Theoretical

In general the rate of heterogeneously catalysed reactions is dependent on three effects. These are:

- the mass transfer from the bulk of the gas to the surface of the catalyst particle (external mass transfer),
- the diffusive phenomena inside the porous catalyst structure (internal mass transfer) and
- the catalytic reaction taking place on the particle surface, consisting of three sub-steps: surface reaction, adsorption and desorption, which can be combined to give an intrinsic reaction rate.

The rate of each of the three effects listed above can be so small that the others are very large in comparison and hence can be neglected. The slowest step was then said to become the rate controlling step. In order to determine whether external mass transfer is the rate controlling step for the experiments carried out, a one-dimensional reactor model was used to simulate the reaction occurring.

A one-dimensional model simulating a packed bed reactor has been described by Froment and Bischoff (1990). This model takes into account interfacial gradients from the bulk of the gas to the particle surface. The catalyst is considered to be at a uniform temperature and concentration and hence the reaction rate in the following equations combines surface reaction and intraparticle mass transfer. It is assumed that no radial gradients occur.

$$-u\frac{dc_i}{dz} = k_{g,i}a\left(c_i - c_{s,i}\right) \tag{5.7}$$

$$u\,c_{tot}\,c_p\frac{dT}{dz} = h_g a\left(T_s - T\right) - 4\frac{U}{d_T}\left(T - T_{amb}\right) \tag{5.8}$$

$$\rho_{cat,b} r_i = k_{g,i} a(c_i - c_{s,i}) \tag{5.9}$$

$$(-\Delta H)\rho_{cat,b} r_i = h_g a(T_s - T) \tag{5.10}$$

The first two equations are the mass and energy balances for the fluid whilst the latter two describe the solid. The reaction rate r_i for a reactant in a non-reversible reaction can be expressed by:

$$r_i = k_i f(\underline{c}^s_{j,Reactants}) \tag{5.11}$$

If external mass transfer is rate controlling, the rate constant k_i would be much larger than the gas phase mass transfer coefficient $k_{g,i}$. This in turn means that the surface concentration $c_{s,i}$ would be small compared with the bulk concentration c_i (Equation 5.11). If these assumptions are introduced into Equation 5.7 one obtains:

$$-u\frac{dc_i}{dz} = k_{g,i} a c_i \tag{5.12}$$

The energy balances given by Equations 5.8 and 5.10 were completely neglected and thus the reactor was assumed to operate isothermally even though this was not actually the case (as described in Section 5.1). However, this simplification together with the use of average concentrations makes it possible to determine mean physical properties valid throughout the reactor. This in turn renders it possible to solve Equation 5.12 analytically. Applying the boundary condition $z = 0$: $c_i = c_{F,i}$ yields:

$$c_{z,i} = c_{F,i} \exp\left(-\frac{k_{g,i,m} a}{u} z\right) \tag{5.13}$$

The mean mass transfer coefficient was evaluated using the following correlation given by Bird *et. al.* (1960):

$$j_D = \frac{k_{g,i,m} M_m}{G} Sc_{i,m}^{2/3} = 0.91 Re^{-0.41} \psi \qquad (5.14\ a)$$

$$Sc_{i,m} = \frac{\mu_m}{\rho_m D_{i,m}} \qquad (5.14\ b)$$

The Reynolds number used in this equation is defined in Equation 5.5.

As already mentioned the physical properties were evaluated at average temperatures and mole fractions. The calculation of the viscosity is described in Appendix 7. The average, total concentration was evaluated from the ideal gas law. Subsequent multiplication with the mean molecular weight gives the mean density. Applying the arithmetic average of the molar feed and product flowrate to the ideal gas law results in a mean volumetric flowrate from which the superficial velocity, u, may be derived by dividing by the crossectional tube area.

The diffusion coefficient $D_{i,m}$ in Equation 5.14 b is the mean effective binary diffusion coefficient. Its evaluation is described in Appendix 7.

The model described above was evaluated using the results of experiment 4 in order to obtain the axial methanol concentration profile. For this purpose it was assumed that only the reaction $CH_3OH + 0.5\ O_2 \rightarrow 2\ H_2 + CO_2$ takes place. The products carbon monoxide, water and methane were neglected. This could be justified as these components account for less than 10% of the product mixture (Table 5.3). A further assumption was that the reaction is non-reversible. The equilibrium calculations of Chapter 4 show the latter assumption to be justified. The input data was:

Mole fractions (corrected for the exclusion of CO, CH_4 and H_2O):

Component	Feed	Product	Average
O_2	0.1463	0.0243	0.0853
N_2	0.5503	0.4756	0.5129
CH_3OH	0.3035	0.0484	0.1760
H_2	0.0	0.3176	0.1588
CO_2	0.0	0.1341	0.0671

Average temperature:	324.911°C
Average pressure:	1.003158 bar
Mean binary diffusion coefficient (CH_3OH):	0.72114 cm^2/s
Total concentration:	0.02018 $kmol/m^3$
Density:	0.5246 kg/m^3
Viscosity:	$2.6937 \cdot 10^{-5}$ Pa s
Schmidt number (CH_3OH):	0.7121
Reynolds number:	2.1459
Mass transfer coefficient (CH_3OH):	0.0676 m/s
Superficial velocity:	0.0873 m/s

The results of this simulation are shown Figure 5.3. According to the simulation all the methanol should have been consumed in the first 10 mm of the reactor. This is not reflected by the experimental observations for which, for this particular experiment, an exit methanol concentration of 0.0011 $kmol/m^3$ was determined.

One cause for the lack in conformity between the results obtained using this model and the experimental results could be the assumption of constant physical properties and temperature. An attempt was made to solve Equation 5.12 numerically with variable physical properties. For this purpose, the superficial velocity was brought on the right hand side of Equation 5.12.

Hence, all parameters subject to change with temperature and composition were part of the mathematical expression for the derivative of the component concentration with respect to the axial coordinate *z*. The Runge-Kutta algorithm used here is described in detail by Press *et. al.* (1992). For each step the derivative expression had to be evaluated four times. This was done using the calculated concentrations and the measured axial temperature profile. This method was, also, unsuccessful in simulating the experimental results obtained. After only a few steps the reactant concentrations became negative. This was caused by very steep axial concentration gradients.

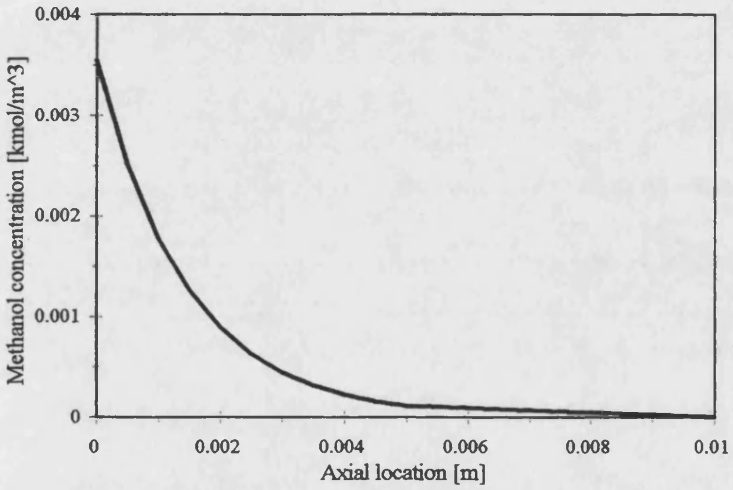

Figure 5.3: Calculated axial methanol concentration profile; experiment 4

5.3 Discussion of the results

The experimental results clearly show that platinum, nickel oxide and copper oxide favour the production of hydrogen and yield only a small amount of unwanted by-products. A further advantage of a platinum catalyst is that the reaction takes place at a lower temperature and

lights-off from almost ambient conditions. The reason for this behaviour is the known high catalytic activity of platinum.

The other two catalysts tested, vanadium(V)oxide and molybdenum(VI)oxide, were not very selective for hydrogen and subject to severe coking effects. Furthermore, the reaction temperature for these catalysts was considerably higher than for platinum.

The reason for the different behaviour of the metal oxide catalysts might be found in their structure. According to Hofmann (1972) metal oxides which posses relatively weak metal-oxygen bonds are very active in the homomolecular exchange of oxygen. Metal oxides of this type are oxidation catalysts. NiO and CuO fall into this category whilst the metal-oxygen bonds in V_2O_5 and MoO_3 are of a much stronger character. Metal oxides of this type have been described as very good dehydrogenation catalysts by Hofmann (1972). Thus, it can be concluded that oxidation catalysts such as NiO and CuO are clearly superior to dehydrogenation catalysts such as V_2O_5 and MoO_3 for the oxidative dehydrogenation of methanol.

Activated alumina is known to be a cracking catalyst (Froment and Bischoff 1990) and hence it appears plausible that it promotes the splitting of the hydroxyl group from the methanol molecule and subsequently the recombination of one or two methyl groups together with an oxygen atom to form formaldehyde or dimethylether. These two components were found as well by Zaspalis *et. al.* (1991a) in their methanol dehydrogenation experiments over an alumina membrane. However, the amounts of formaldehyde and dimethylether detected in experiment 12 were small and could only be detected by means of a mass spectrometer but did not show in the gas chromatography analysis. As only trace amounts of these two components were produced by using γ-alumina as a catalyst, it was decided to treat γ-alumina as inert in the scope of this study.

As expected the reaction showed exothermic behaviour, as determined from the heat of reaction calculation in Section 4.2.

As already indicated, platinum showed the best performance of all the catalysts tested in terms of product composition as well as steady state reaction temperature and light-off behaviour. Hence, it was decided to apply the results obtained with this catalyst to a theoretical analysis as described in Section 5.2. The methanol exit concentration obtained computationally did not reflect the experimental result. There are a number of probable causes for this behaviour. The model chosen was one-dimensional and thus it did not take any radial gradients into account. Nonhomogenously distributed packing leads to wall effects, channelling etc. These effects in turn cause a departure from the assumed plug flow behaviour of the bulk. In the first model the reactor was assumed to be operated isothermally which clearly did not reflect the experimental data. Further, constant mean physical properties were assumed. The second model involved the measured temperature profile and assumed adiabatic operation but was still one-dimensional. The physical properties were evaluated according to their temperature and composition dependence. Hence this model was a closer approach to the experimental conditions. However, the results still failed to reflect the experimental results.

The main conclusion that could be drawn from the theoretical analysis was that the assumption of a mass transfer controlled reaction mechanism was not valid. Hence the rate would be either determined by the surface reaction or by a combination of the effects given in Section 5.2. In order to simulate the results more successfully the Equations 5.7 to 5.10 would have to be solved simultaneously. This involves the knowledge of an expression for the reaction rate which is not yet known. Within the limits of our experimental design, it was not possible to determine this expression from the experiments carried out, as each catalyst was investigated at only one temperature and feed condition. For the derivation of an intrinsic rate expression it would have been necessary to cover a broad temperature and feed condition range with respect to composition and flowrate.

CHAPTER 6

CATALYST AND MEMBRANE PREPARATION AND CHARACTERISATION

6.1 Deposition of platinum on alumina catalyst supports

The deposition of metallic compounds on ceramic supports exhibiting a high internal surface area, as for example γ-alumina, is a well advanced science. A comprehensive review was compiled by Delmon *et. al.* (1979).

All catalysts investigated in this study were prepared using crystalline chloro platinic acid (hydrogen hexachloroplatinate, H_2PtCL_6, CPA) as source of the platinum. The chloro platinic acid was supplied by Johnson Matthey plc and had a platinum content of 40.52% by weight.

For the preparation of the pelleted catalysts and catalytic membranes, a stock solution of chloro platinic acid was prepared using water purified by means of reverse osmosis. 1.5543g of crystalline CPA were mixed with purified water in a 500ml volumetric flask. The total solution volume was 500ml. The flask was then wrapped in aluminium foil in order to shut out any light. A PTFE coated magnetic stirrer element was placed into the flask and the solution was stirred for 24h. The achieved molar platinum concentration of the solution was 6.231×10^{-3}mol/l, corresponding to a partial density of 1215.59μg/ml.

6.2 Preparation and characterisation of pelleted catalyst

The support for all pelleted catalysts was γ-alumina supplied by UOP Ltd. Two diameters of support were supplied: 1.6mm and 3.2mm. The internal UOP classification for these supports was CCS-2 and CCS-2L, respectively. In order to investigate the influence of intraparticle mass and heat transfer effects, the use of particle sizes smaller than the two standard diameters was necessary. In order to obtain smaller particle

diameters, an amount of CCS-2L catalyst was crushed by means of a mortar. The crushed catalyst support was sieved overnight in an agitated sieve set in order to obtain particles of the size ranges: 0.355mm to 0.650mm, 0.650mm to 0.850mm and 0.850mm to 1.0mm.

Platinum was deposited onto the γ-alumina catalyst support using the following procedure:

1. The γ-alumina was dried in a furnace under a nitrogen atmosphere at atmospheric pressure. The furnace was heated up from a starting temperature of 50°C to 250°C following a ramp of 5°C/min. Subsequently the temperature was held at 250°C for 8h. The nitrogen was supplied at a constant flowrate of 100ml/min.
2. A CPA solution was prepared by diluting an amount from the stock solution. The concentration of the solution was determined according to the desired Pt loading on the catalyst. The mass of platinum required can be calculated according to:

$$m_{Pt} = \frac{m_{Al_2O_3}}{\frac{1}{w_{Pt}} - 1} \tag{6.1}$$

where m_{Pt} is the mass of catalyst, m_{Al2O3} is the mass of alumina and w_{Pt} is the platinum massfraction. The volume of the required solution was determined according to the amount of catalyst to be prepared, *e. g.* a sufficient amount to completely immerse the γ-alumina. The required amounts of stock solution and reverse osmosis purified water required could be determined from a total volume balance and a platinum component balance.
3. Two different methods were used for impregnating the catalyst support with CPA solution, depending on the particle size. The 3.2mm and 1.6mm particles were placed inside a stainless steel wire mesh basket. The wire mesh basket was then inserted into

the CPA solution contained within a 150ml glass beaker. The beaker contained a PTFE coated magnetic stirrer element and was also placed upon a magnetic stirrer device. Figure 6.1 shows the assembly. Catalysts of smaller particle sizes were prepared by placing the γ-alumina into 30ml sample vials and then topping the vials up with CPA solution of the required concentration. The sample vials were then clipped onto a Stuart Scientific STR4 rotator, as shown in Figure 6.2. The impregnation time was 1h for both methods.

4. After the impregnation step, the impregnated catalyst support was carefully decanted from the remaining solution. The remaining solution was kept for further analysis. The impregnated catalyst support was dried in a furnace at 120°C under a flow of 100ml/min of nitrogen.
5. The dried catalyst precursor was then placed into a 20.32mm ID 316-stainless steel tube, acting as a reduction reactor. The catalyst precursor was placed in-between two sintered stainless steel disks. The reduction reactor was then placed into the furnace of the experimental apparatus and connected via Swagelok reduction fittings to the stainless steel linework of the experimental apparatus. Figures 6.3 shows the reactor. A thermocouple was placed into the reactor and the reactor was heated up to 350°C under nitrogen at a flowrate of 500ml/min fed through one of the mass flow controllers. Once the temperature had been achieved, the feed gas supply was switched to a mixture of 40% hydrogen and 60% nitrogen. The flowrate was 100ml/min. The reduction time was between 4 and 8h, depending on the amount of prepared catalyst. The reactor was cooled down with nitrogen at a flowrate of 300ml/min.
6. The amount of platinum deposited was evaluated by means of Atomic Absorption Spectroscopy. This method determines the amount of metal in solution and was used on the remaining solutions after the impregnation step. The following material balance can then be used to determine the amount of platinum deposited:

$$m_{Pt} = V_{Solution}\left(\rho_{Pt,Start} - \rho_{Pt,AAS}\right) \tag{6.2}$$

where $V_{Solution}$ is the volume of the solution, $\rho_{Pt,Start}$ the platinum mass density of the precursor solution at the beginning of the preparation procedure and $\rho_{Pt,AAS}$ the platinum mass density measured by Atomic Absorption Spectroscopy after the impregnation procedure was finished.

The amounts of γ-alumina catalyst support and of prepared catalysts were weighed using a precision balance. Solution volumes were measured using volumetric flasks and Gilson pipettes.

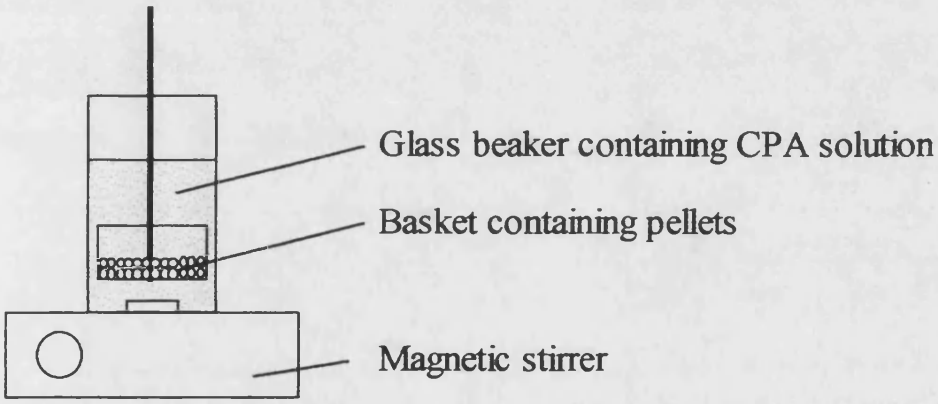

Figure 6.1: CPA impregnation of 1.6mm and 3.2mm γ-alumina particles

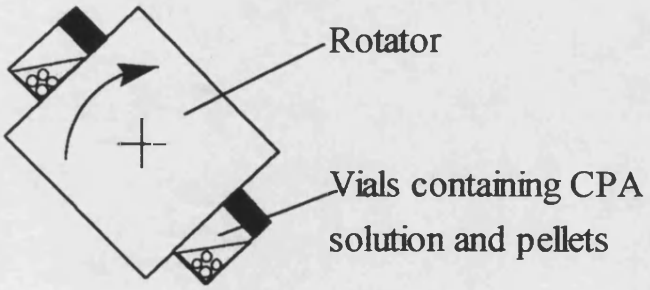

Figure 6.2: CPA impregnation of γ-alumina particles smaller than 1.6mm

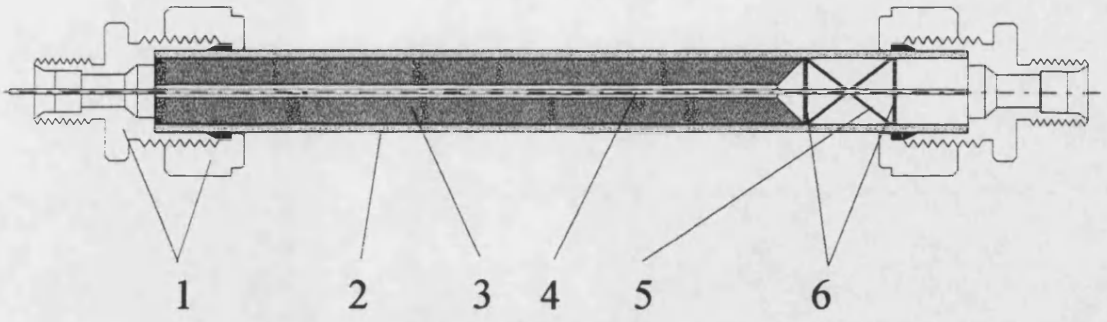

1: Swagelok compression fitting
2: 1" Stainless steel tube
3: Stainless steel insert
4: Thermocouple well
5: CPA Impregnated γ-alumina particles
6: Sintered stainless steel disk

Figure 6.3: Reduction reactor

Table 6.1 summarises the pelleted catalysts prepared. In this table, $w_{Pt,max}$ is the maximum achievable platinum loading, if all Pt in the solution were adsorbed whilst $w_{Pt,AAS}$ is the loading calculated according to Equation 6.2 on the basis of the Atomic Absorption Spectroscopy analysis.

Table 6.1: Pelleted catalysts

d_p [mm]	m_{Al2O3} [g]	$V_{Solution}$ [ml]	$\rho_{Pt,Start}$ [µg/ml]	$w_{Pt,max}$	$w_{Pt,AAS}$
3.2	15.0	75	1215.56	0.671	0.5906
1.6	11.75	65	1215.56	0.671	0.6669
0.850 to 1.0	1.0	23.56	286.86	0.671	0.6666
0.850 to 0.650	1.0	23.56	286.86	0.671	0.6665
0.650 to 0.355	1.0	23.56	286.86	0.671	0.6667

Delmon *et. al.* (1979) reported that $Pt/\gamma\text{-}Al_2O_3$ catalysts prepared by impregnation of γ-alumina with chloro platinic acid often exhibit an "egg shell" distribution of platinum. This behaviour is characterised by the deposition of the majority of the platinum in the region closest to the external particle surface. In order to investigate the platinum distribution in the particles prepared according to the method described above, an Electron Probe Micro Analysis (EPMA) was carried out. Catalyst particles of 1.6mm diameter and from the 1.0mm to 0.850mm and 0.850mm to 0.650mm particle ranges were embedded in epoxy resin which was then hardened. Subsequently, the resin was ground down, so that a cut along the particle axis was established. Then the samples were polished and subjected to the EPMA analysis.

Electron Probe Micro Analysis works by sending an electron beam onto the specimen. The electron beam is reflected with a wavelength dependent on the chemical element exposed to the beam. A lithium crystal, located according to the wavelength of the element to be detected, reflects the beam again to a counter. The amount of counts is proportional to the concentration of the investigated element. The beam was moved along the axis of a sample at 1μm increments, so that a radial Pt concentration profile could be established. Figures 6.4 to 6.6 show the measured profiles for the 1.6mm, 1.0mm to 0.85mm and 0.85mm to 0.65mm particles, respectively. It is apparent that an egg shell distribution was established for the 1.6mm particle, whilst the particle from the 1.0mm to 0.85mm size fraction shows a more uniform concentration profile. The platinum distribution in the smallest particle investigated is almost uniform and shows only a small dip in the concentration profile in the particle centre.

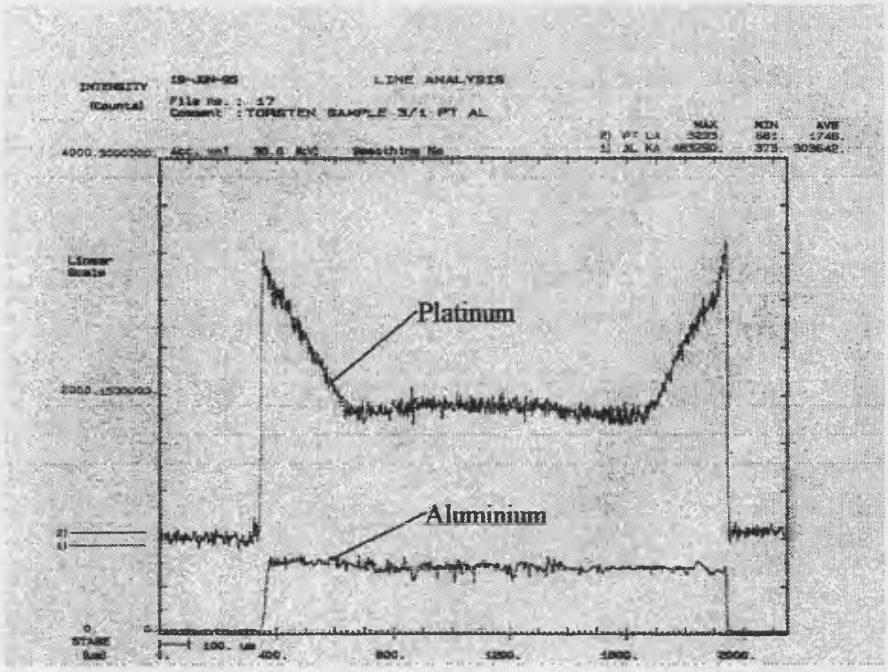

Figure 6.4: Platinum and γ-alumina distribution in 1.6mm pellet

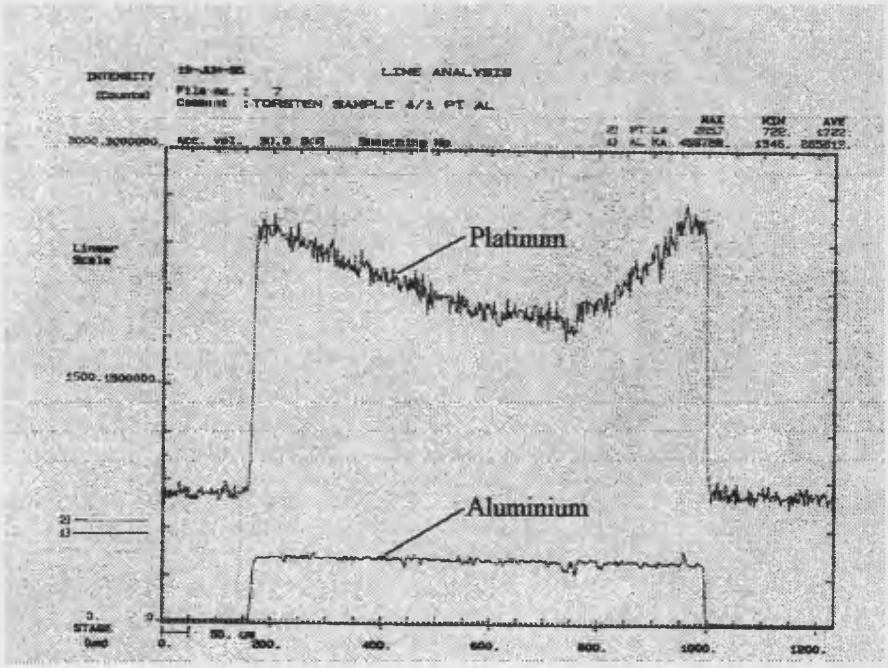

Figure 6.5: Platinum and γ-alumina distribution in pellet from 0.85mm to 1mm size fraction

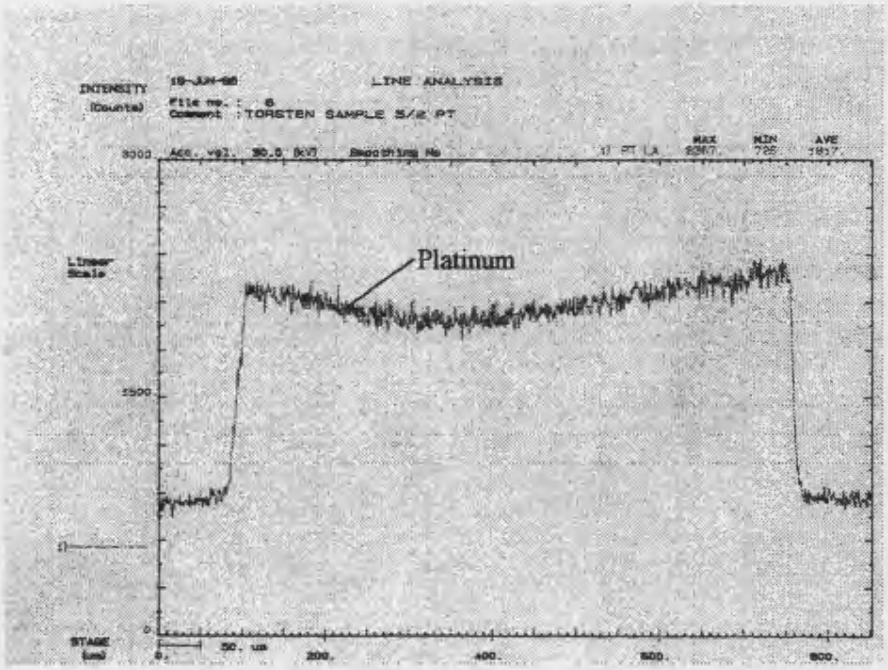

Figure 6.6: Platinum distribution in pellet from 0.65mm to 0.85mm size fraction

The internal catalyst structure was investigated using liquid nitrogen adsorption. The experiments were carried out in a Micorometrics ASAP 2000 instrument. The operation is described in detail by Bhardwaj (1998). Table 6.2 shows the results of the analysis.

The catalyst densities were determined by measuring the volume and the mass of 100 γ-alumina pellets of 3.2mm nominal diameter. As the particle shape was ellipsoid rather than spherical, the length of the main axes was determined and the volume of each ellipsoid was calculated. Dividing the sample mass by the sum of the individual particle volumes rendered the particle density.

Table 6.2: Pt/γ-Al_2O_3 catalyst structure

BET Surface area [m^2/g]	BJH Pore volume [cm^3/g]	BJH Pore diameter [nm]	Particle density [kg/m^3]
195.51	0.6349	13.7044	888.55

6.3 Preparation and classification of catalytic tube segments

Catalytic tube segments had to be prepared for use in the tubular wall reactor experiments. The catalytic tube segments consisted of a ceramic support tube with a catalytically active layer applied on the inside surface of the tube segment. The support was a Pormulite tube, consisting of 95% α-Al_2O_3 and 5% SiO_2. The external tube diameter was 20mm and the internal tube diameter was 15mm. Sections of 10mm, 20mm, 30mm and 40mm length were sawn off the tube to act as catalyst layer supports. These sections were dried in a furnace at 200°C overnight before use.

As previously, the catalyst to be deposited was platinum and γ-Al_2O_3. Alumina particles of a particle size smaller than 50μm were prepared by grinding 3.2mm CCS2-L UOP γ-Al_2O_3 catalyst support particles in a mortar and subsequently classifying the ground particles with a sieve set. The particles were dried overnight at 200°C in a furnace before using them for catalyst preparation purposes.

The first part of the preparation procedure consisted of preparing a slurry of γ-alumina particles and a ceramic binder. After measuring the weights carefully, binder and γ-alumina particles were well mixed in a glass petri dish in order to form a uniform slurry. After weighing the dried Pormulite tube section, a portion of the slurry was applied to the tube section. Subsequently, the tube section with applied slurry was weighed and placed into a fume cupboard for 4h in order to let the slurry dry. Using the measured

masses of the tube section before and after the application of the slurry, the amount of γ-Al_2O_3 could be determined.

The next step in the procedure was to prepare a small amount of chloro platinic acid solution of a concentration sufficient to achieve the desired platinum loading. The solution was prepared directly from CPA in crystalline form and mixed with reverse osmosis purified water in a glass beaker. The amounts of CPA and water were carefully measured. Subsequently, the solution was applied to the γ-alumina coating by means of a paint brush. The difference in the weight of the beaker before and after the CPA solution application and between the dry and the wetted paintbrush was used to determine the amount of CPA solution deposited.

After the application of the CPA solution the catalytic tube segment had to be submitted to a curing process in order to harden the binder. The curing was carried out in a furnace equipped with a Eurotherm temperature controller and consisted of the following steps:

- Heating to 121°C at a temperature ramp of 5°C/min and holding at 121°C for 60min
- Heating to 214°C at a temperature ramp of 5°C/min and holding at 214°C for 60min
- Heating to 307°C at a temperature ramp of 5°C/min and holding at 307°C for 60min
- Heating to 371°C at a temperature ramp of 5°C/min and holding at 371°C for 60min
- Cooling down to ambient temperature.

Subsequently the catalytic tube segments were placed into the reduction reactor shown in Figure 6.3. The reactor was connected to the experimental apparatus as described in Section 6.2. The system was purged and heated up to 350°C under nitrogen supplied at a flowrate of 500ml/min. The feed gas was then switched to a mixture of 40% hydrogen and 60% helium at a flowrate of 100ml/min. The time the prepared tube segment spent

under these reducing conditions was 7h. The reactor was then cooled down under flowing nitrogen.

Table 6.3 shows the conditions of the 10mm segment used in the tubular wall reactor experiments described in Chapter 7.

Table 6.3: Classification of catalytic tube segment

$m_{Pormulite,dry}$ [g]	m_{Al2O3} [g]	m_{Pt} [g]	m_{cat} [g]	W_{Pt} [%], on m_{cat} basis
2.9488	0.0133	2.2217×10-4	0.013522	1.643

Previous to the tube segment preparation, a sample of the γ-Al_2O_3 used was investigated by N_2 adsorption in the same way as described in section 6.2. The results of this analysis are shown in Table 6.4.

Table 6.4: γ-Al_2O_3 particle structure

BET Surface area [m^2/g]	BJH Pore volume [cm^3/g]	BJH Pore diameter [nm]
197.07	0.4912	10.8978

6.4 Preparation and classification of catalytic membranes

The membranes used in this study were supplied by SCT (Societé Ceramiques Techniques). The dimensions were 250mm length, 19mm external diameter and 14.9mm internal diameter. Impermeable ceramic glaze had been applied to a length of 10mm at either end of the membrane tube for sealing purposes. The structure of the membrane has been investigated by Uzio *et. al.* (1993 and 1994). The membrane consisted of four

layers. Three of these layers were manufactured from α-alumina, whilst the fourth, innermost layer was manufactured from γ-alumina. The γ-Al_2O_3 was deposited by means of a sol-gel process. The weight of γ-Al_2O_3 per unit membrane length was given to be 0.25g/m by Uzio *et. al.* (1993). In a later publication, Uzio *et. al.* (1994) give the thicknesses, pore sizes and porosities of the four layers, shown in Table 6.5. Figure 6.7 clarifies the layer numbering scheme.

Table 6.5: SCT membrane properties (Uzio *et. al.* 1994)

Layer	Thickness [μm]	Pore size [μm]	Porosity
1 α-Al_2O_3	2000	11	0.28
2 α-Al_2O_3	40	0.7	0.24
3 α-Al_2O_3	20	0.2	0.26
4 γ-Al_2O_3	4	0.004	0.45

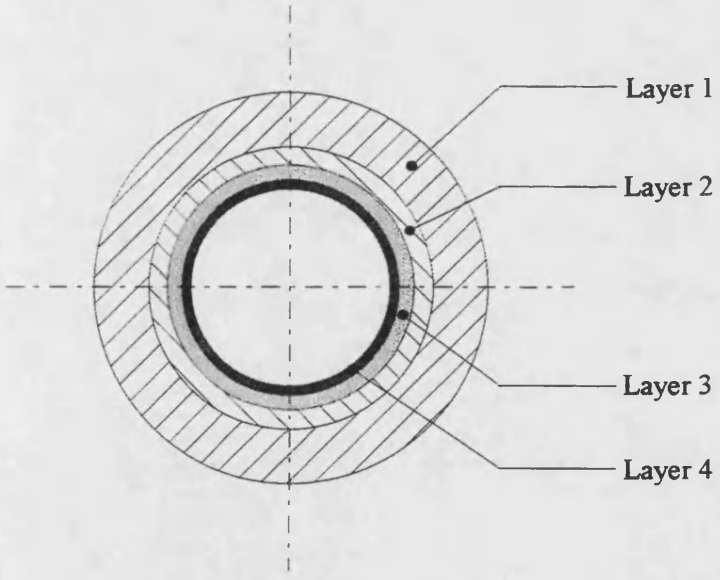

Figure 6.7: Crossection of SCT membrane

For the separation experiments carried out in the membrane reactor described in Chapter 8, these SCT membranes were used without any alteration.

The procedure for depositing platinum into the inner γ-alumina layer (Layer 4) is somewhat similar to the one described in Section 6.2 for the preparation of pelleted Pt/γ-Al_2O_3 catalyst. The procedure was developed on the basis of the method given by Uzio *et. al.* (1993).

The first step was to wash the SCT membrane with water, methanol and acetone in sequence. The membrane was then dried overnight at 250°C. After the membrane had cooled down, it was wrapped in PTFE tape and the tube was sealed at one end using a rubber stopper also wrapped in PTFE tape. Subsequently, the membrane was filled with reverse osmosis purified water in order to wet the membrane pore structure. The water was then removed out of the tube, leaving the membrane wetted.

A CPA solution sufficient to achieve a platinum loading of 6.54% by weight in the internal activated alumina layer was prepared. The strength of the solution was chosen to be this high as previous test experiments showed that the solution recovered after the impregnation step still had a high platinum concentration. Another reason was the porous, multilayered structure of the membrane, which made it possible for the precursor solution to penetrate into the outer layers. The internal volume of the membrane tube was calculated to be 43.59cm^3. The total volume of the solution prepared was 50.0cm^3, consisting of 43.87cm^3 of reverse osmosis purified water and 6.13cm^3 of diluted CPA stock solution at a platinum concentration of 816.15mg/l. The platinum concentration of the resulting CPA solution was 100.06mg/l. Solution was then poured into the prewetted membrane until full and the second tube end sealed with a PTFE coated rubber plug. 44.07g of the 54.79g of solution prepared was filled into the membrane. The CPA solution filled membrane was then placed onto a moving platform (Stuart Scientific Ltd) for 3h in order to agitate the solution inside the membrane and hence achieve a better

mass transfer of platinum from the solution to the pore surface.. Subsequently, the remaining solution was recovered from the impregnated membrane and the membrane was washed twice with purified water. The total amount of recovered solution and washwater was 120.46g. The volume of the recovered solution and wash water was 118.0cm^3. As in Section 6.2, Atomic Absorption Spectroscopy was employed to determine the content of platinum in the remaining solution. A platinum concentration of 22.63mg/l was determined.

The next step in the preparation procedure was to dry the CPA solution impregnated membrane for 15h at 120°C under nitrogen at a flowrate of 500ml/min. Subsequently, the temperature was increased at a rate of 1°C/min to 450°C and held for 2h. The membrane was then transferred to the reduction reactor (Figure 6.3), from which the stainless steel insert had been previously removed. The reactor was connected to the experimental apparatus and heated up to 385°C with nitrogen supplied at 500ml/min through a mass flow controller. Once the reduction temperature had been achieved, the feed gas supply was switched to hydrogen at 500ml/min. The duration of the reduction was 5h.

A material balance rendered the amount of platinum deposited into the porous structure:

$$m_{Pt} = \frac{m_{CPA,applied}}{m_{CPA,tot}} V_{CPA} \rho_{Pt} - \left(V_{CPA,recovered} + V_{Wash}\right) \rho_{Pt,AAS} \qquad (6.3)$$

The amount of platinum deposited was calculated and was 0.001354g. If it was assumed that the platinum was solely deposited within the innermost γ-alumina layer, a platinum loading of 2.3% would have been achieved.

The quantities given above are for the catalytic membrane prepared for the catalytic membrane reactor experiments. A second membrane was prepared using the same

procedure. This membrane was subsequently cut into 10mm long segments. One of these segments was again cut radially in order to produce eight segments for use in kinetic experiments carried out in a spinning basket reactor (Chapter 7). Another segment was used in an EPMA analysis in order to investigate the platinum distribution in the radial direction. The quantities used in the preparation procedure and the measured concentrations are given in Table 6.6.

Table 6.6: Catalytic membrane preparation

	Membrane 1 (used for catalytic membrane reactor experiments)	Membrane 2 (used for kinetic studies and classification)
Volume of precursor solution [cm^3]	50	50
Pt concentration of precursor solution [mg/l]	100.06	101
Used precursor solution [cm^3]	40.22	41.10
Theoretically achievable Pt loading [wt-%]	6.54	6.733
Volume of recovered precursor solution and washwater [cm^3]	118	109
Pt concentration of recovered solution and washwater [mg/l]	22.63	25.2
Achieved Pt loading [wt-%]	2.30	2.40

Visual inspection of the membrane after completed reduction showed had the inner membrane layer was grey as opposed to the original yellow-white colour, indicating that platinum had been deposited. However, grey areas appeared on the outer circumference as well. This was a sign that platinum penetrated into the outer α-alumina layers as well.

Figure 6.8 shows an EPMA analysis of a segment from Membrane 2 (Table 6.6). The analysis was carried out in the radial direction from the inside of the tube towards the outside. The increase in the aluminium signal shows the start of the internal γ-alumina layer. It is apparent that the platinum signal picks up as well. However, the signal strength appears to be fluctuating around a constant mean value inside the porous structure and does not indicate a high Pt concentration inside the first 5μm as desired. This indicates that platinum deposition occurred homogeneously throughout the pore structure instead of the γ-Al_2O_3 layer only. Another possible explanation for the lack of Pt detection in the internal layer, although its colouring indicated otherwise, is that the EPMA instrument emits electron beams in a minimum step size of 1μm. Considering that the inner layer is only 4μm thin (Table 6.5), Pt concentrated therein could have been missed owing to the relatively large increments.

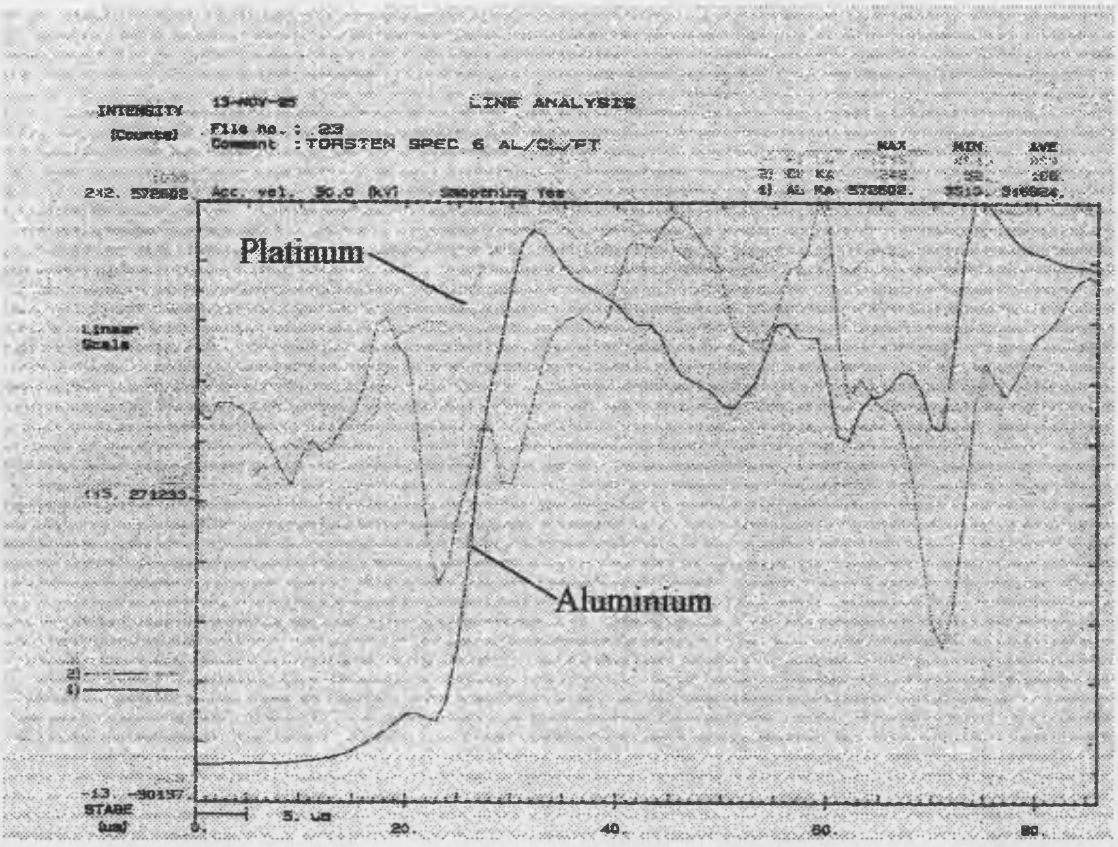

Figure 6.8: Radial EPMA investigation of catalytic membrane

CHAPTER 7

KINETIC EXPERIMENTS IN STANDARD KINETIC REACTORS

Kinetic experiments were conducted with the aim of establishing the intrinsic reaction kinetics of the oxidative dehydrogenation of methanol on a γ-alumina supported platinum catalyst. This type of catalyst emerged as the most promising one from the catalyst screening experiments described in Chapter 5. Kinetic experiments were carried out in two different types of reactor during the course of this study: a spinning basket reactor and a tubular wall reactor. Both types of reactor have distinct advantages and disadvantages, which will be discussed in detail in this chapter.

In general the observed reaction rate at the completion of an experiment following determination of the kinetics of the heterogeneously catalysed reaction contains the following information:

- Interparticle mass- and heat transfer resistances, *e. g.* the mass- and heat transfer resistances inside the boundary layer surrounding the catalyst particle
- Intraparticle mass- and heat transfer resistances inside the pore structure of the catalyst
- Intrinsic surface kinetics reaction consisting of the adsorption of reactants onto the catalytically active surface side, chemical reaction on the surface site and subsequent desorption of the products into the gas phase.

The occurrence of temperature gradients and hence heat transfer resistances can be avoided by ensuring isothermal operation of the reactor. This can be achieved by using only small quantities of catalyst and diluted reactant feeds.

Ensuring that mass transfer resistances do not obscure the observed reaction rate is somewhat more difficult. Tests, depending on the type of experimental reactor used,

have to be carried out prior to the kinetic experiments in order to determine an operating range in which only the intrinsic surface reaction rate is observed.

7.1 Spinning basket reactor experiments

The spinning basket reactor used was incorporated into the experimental apparatus. The experimental procedure employed is described in Chapter 3. The preparation of the catalyst is described in Chapter 6.

7.1.1 Determination of the spinning basket reactor operating range

Spinning basket reactors ensure gradientless operation by emulating Ideal Continuously Stirred Tank Reactor behaviour (Carberry 1964). The catalyst and any inert packing material is contained within a stainless steel wire mesh basket mounted on a rotating shaft. Basket and shaft are enclosed within the stainless steel reactor chamber. The shaft can be rotated at varying speeds of revolution by means of a magnetic clutch. External concentration and temperature gradients can be avoided by choosing a high enough speed of revolution. Once the speed of revolution had been determined, a series of experiments with decreasing particle sizes was carried out. When the observed reaction rate did not change on further decrease of particle size, intraparticle mass- and heat transfer resistances could be assumed to be excluded from the observed reaction rate.

Figure 7.1 shows the dependency of the methanol conversion and hence the observed reaction rate on the rotational speed of the basket. The catalyst used was prepared as described in Chapter 6. The particle diameter was 3.2mm. The amount of catalyst used was 0.168g. The remainder of the basket was packed with inert glass spheres of 3.0mm diameter. Extreme care was taken in order to distribute the catalyst particles at the outer circumference of the basket (see Figure 7.2). A total of six rotational speeds between 0 and 2500min^{-1} were investigated. Two experiments were carried out for each of these

speeds: one at 180°C and one at 312°C. The reactor pressure was 1.05 bar. These operating conditions closely matched those used for the catalytic membrane reactor operation. The experimental conditions are given in Table 7.1.

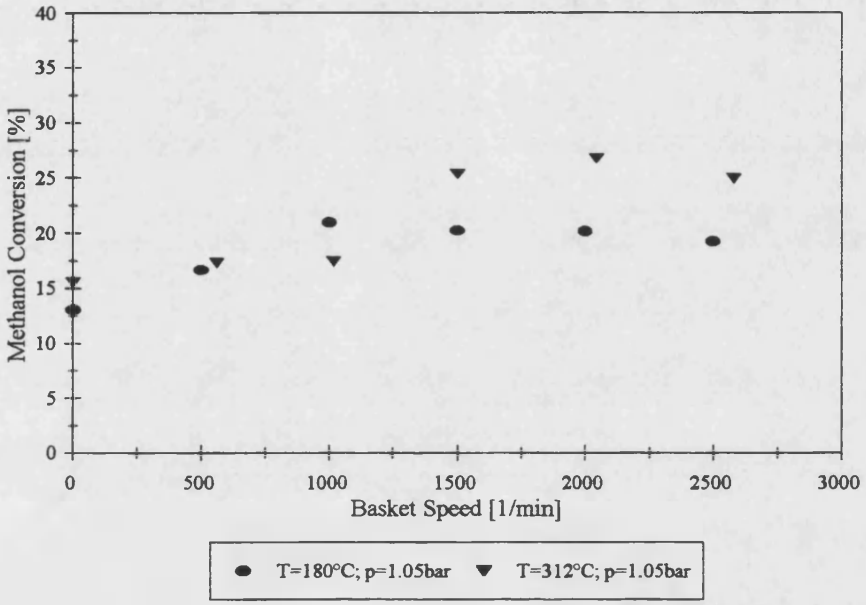

Figure 7.1: Dependency of observed methanol conversion on basket rotational speed

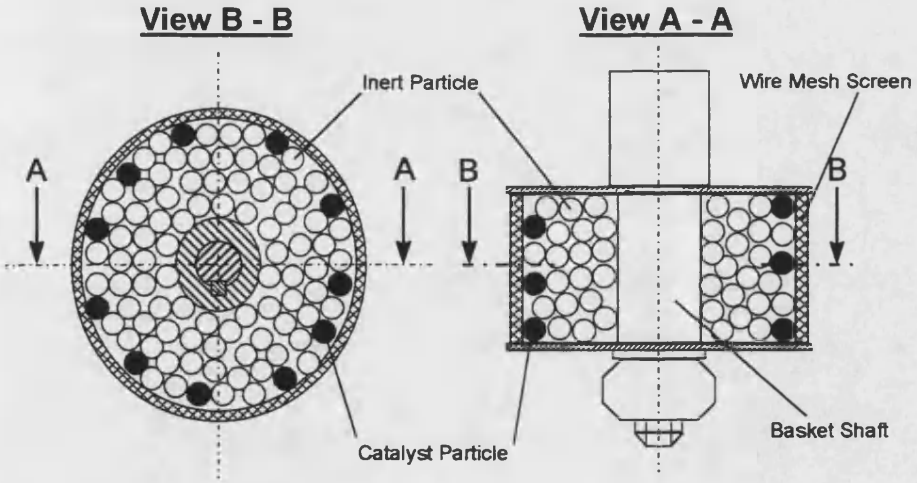

Figure 7.2: Catalyst particle arrangement

Table 7.1: Experimental conditions for the determination of the operating range not influenced by external mass transfer effects

Operating temperatures		180.0 and 312.0	°C
Operating pressure		1.05	bar
Catalyst mass		0.168	g
Platinum loading		0.67	% by weight
Catalyst particle diameter		3.2	mm
Catalyst bulk density		6.14	kg/m^3
Inert particle diameter		3.0	mm
Feed flowrate		0.0668	mol/min
Feed composition	Nitrogen	0.54	
	Oxygen	0.14	
	Methanol	0.32	
Basket rotational speeds		0, 500, 1000, 1500, 2000, 2500	min^{-1}

The catalyst bulk density was evaluated according to:

$$\rho_{cat,b} = \frac{\text{mass of catalyst}}{\text{volume of reaction chamber - volume of inert particles}} = \frac{m_{cat}}{V_{RC} - V_{inert}} \qquad (7.1)$$

$$V_{inert} = (1-\varepsilon)V_{basket} \qquad (7.2)$$

The Volume of the reactor chamber (V_{RC}) and the volume of the Basket (V_{Basket}) were calculated in Chapter 3.

The detailed experimental results are give in Table 7.2.

It can be seen in Figure 7.1 that the methanol conversion remained approximately constant for rotational speeds greater than 1500min^{-1}. A rotational speed of 2000min^{-1} was employed for the subsequent experiments.

An additional interesting observation could be made if the behaviour of hydrogen selectivity with changing rotational speed is considered. Figure 7.3 shows this behaviour.

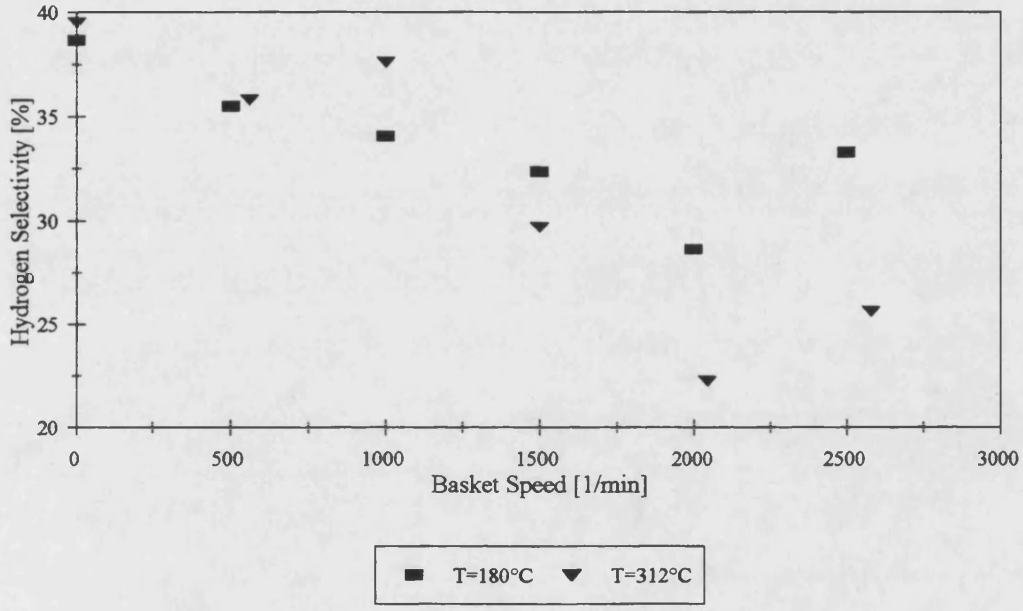

Figure 7.3: Hydrogen selectivity vs. rotational speed

It is apparent that the hydrogen selectivity decreases with increasing rotational speed up to 2000min^{-1} and then starts to increase again. This increase as well as the higher than expected selectivity at 1000min^{-1} and 312°C can be explained by experimental error as shown in Appendix 10.

The next set of experiments was carried out in order to determine the maximum particle size which could be used without internal mass transfer effects obscuring the observed

methanol conversion. Figure 7.4 shows the results. A total of five catalyst particle sizes were investigated. Other experimental conditions were as described in Table 7.1. The average pellet diameters were: 0.4775mm, 0.725mm, 1.0mm, 1.6mm and 3.2mm.

It can be seen from Figure 7.4 that particle sizes smaller than 1.0mm essentially result in the same conversion for both temperatures investigated. It was decided to use the smallest particle size investigated, 0.4775mm, for subsequent kinetic experiments. The detailed experimental results are shown in Table 7.3.

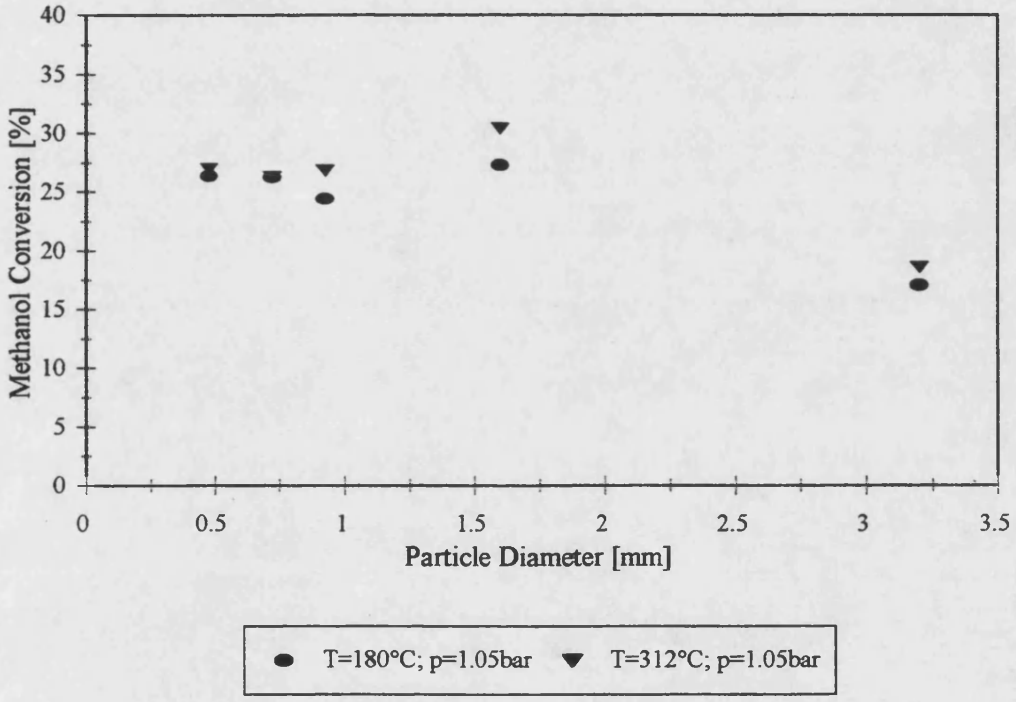

Figure 7.4: Dependency of observed methanol conversion on particle size

Table 7.2: Results of the experiments for the determination of the operating range not influenced by external mass transfer effects

		Exit Composition											
Exp No	T [°C]	n [min^{-1}]	O2	N_2	CH_3OH	H_2	CO	CO_2	CH_4	H_2O	X_M [%]	MB [%]	N_{Exit} [mol/min]
SBR 5	180.0	0	0.121	0.526	0.293	0.034	0.009	0.021	0.002	0.014	13.1	4.31	0.0653
SBR 6	180.0	500	0.127	0.550	0.279	0.039	0.010	0.021	0.002	0.014	16.7	2.09	0.0659
SBR 7	180.0	1000	0.120	0.524	0.271	0.037	0.009	0.024	0.003	0.018	21.0	6.54	0.0652
SBR 2	180.0	1500	0.110	0.518	0254	0.04	0.018	0.026	0.003	0.02	20.3	5.34	0.0669
SBR 3	180.0	2000	0.109	0.536	0.258	0.038	0.018	0.025	0.004	0.023	20.2	4.99	0.0654
SBR 4	180.0	2500	0.104	0.545	0.250	0.04	0.021	0.030	0.003	0.026	19.3	0.03	0.0684
SBR 10	312.0	0	0.101	0.501	0.272	0.039	0.020	0.025	0.002	0.029	15.6	6.42	0.0660
SBR 9	312.0	500	0.098	0.483	0.265	0.039	0.021	0.025	0.002	0.028	17.3	8.55	0.0664
SBR 13	312.0	1000	0.112	0.575	0.263	0.042	0.022	0.026	0.002	0.030	17.5	2.39	0.0670
SBR 12	312.0	1500	0.102	0.528	0.230	0.046	0.033	0.028	0.002	0.033	25.4	1.80	0.0693
SBR 15	312.0	2000	0.094	0.525	0.230	0.038	0.022	0.026	0.002	0.034	26.8	5.61	0.0685
SBR 14	312.0	2500	0.095	0.529	0.240	0.041	0.034	0.028	0.002	0.036	25.0	4.42	0.0672

Table 7.3: Results of the experiments for the determination of the operating range not influenced by internal mass transfer effects

		Exit Composition											
Exp No	T [°C]	d_p [mm]	O2	N_2	CH_3OH	H_2	CO	CO_2	CH_4	H_2O	X_M [%]	MB [%]	N_{Exit} [mol/min]
SBR 33	180.0	3.2	0.111	0.522	0.260	0.042	0.019	0.023	0.003	0.020	17.09	4.02	0.0674
SBR 35	180.0	1.6	0.103	0.539	0.227	0.045	0.021	0.036	0.004	0.025	27.27	4.06	0.0675
SBR 24	180.0	1.0	0.099	0.521	0.250	0.042	0.014	0.045	0.003	0.026	24.43	6.10	0.0677
SBR 37	180.0	0.725	0.110	0.518	0254	0.040	0.018	0.026	0.003	0.020	26.29	5.34	0.0669
SBR 32	180.0	0.4775	0.102	0.529	0.245	0.044	0.014	0.036	0.005	0.025	26.40	6.51	0.0666
SBR 34	312.0	3.2	0.108	0.525	0.248	0.045	0.025	0.023	0.002	0.025	18.59	1.73	0.0695
SBR 36	312.0	1.6	0.100	0.525	0.231	0.046	0.035	0.030	0.003	0.030	30.40	6.90	0.0676
SBR 25	312.0	1.0	0.090	0.514	0.237	0.038	0.037	0.040	0.004	0.040	26.79	4.55	0.0710
SBR 38	312.0	0.725	0.093	0.519	0.223	0.057	0.032	0.038	0.003	0.034	26.30	1.56	0.0703
SBR 31	312.0	0.4775	0.092	0.528	0.216	0.050	0.035	0.038	0.004	0.037	27.00	0.55	0.0695

7.1.2 Kinetic experiments carried out in the spinning basket reactor

Two series of kinetic experiments were carried out in the spinning basket reactor. For both series the feed oxygen partial pressure was varied whilst the other feed conditions were kept constant. The methanol partial pressure was kept constant by changing the partial pressure of the inert nitrogen diluent accordingly. The first series was carried out at 182°C using pelleted catalyst. In the second series segments of a catalytic membrane were used at 294°C. The reaction rates for each component detected in the effluent were calculated using an ideal CSTR component material balance:

$$y_{F,i}N_F - y_{P,i}N_P + r_i m_{cat} = 0 \qquad (7.3)$$

In Equation 7.3, r_i is the observed reaction rate of component i measured in mol/(min g_{cat}).

Table 7.4 gives the fixed experimental conditions employed in all of the experiments of the first series.

Table 7.4: Experimental conditions, spinning basket reactor experiments with pelleted catalyst

Temperature	182	°C
Total pressure	1.05	bar
Feed flowrate	0.0667	mol/min
Methanol feed partial pressure	0.3504	bar
Catalyst mass	0.1698	g
Catalyst particle diameter	0.4775	mm
Platinum loading	0.6	% by weight
Basket rotational speed	2000	min^{-1}

The nitrogen feed partial pressure was adjusted to allow for the variation of the oxygen feed partial pressure. Figures 7.5 to 7.11 show the measured rates as a function of oxygen partial pressure.

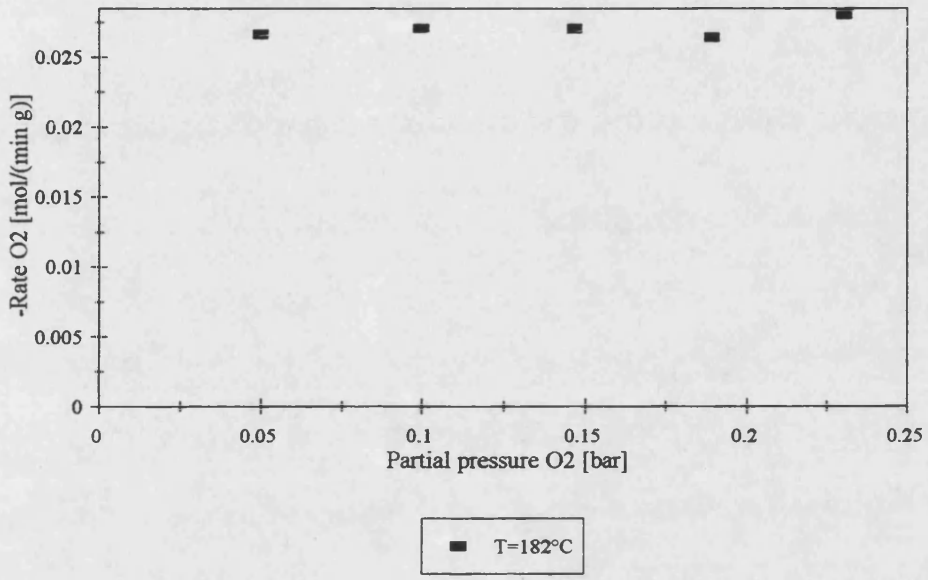

Figure 7.5: Rate of oxygen consumption vs. oxygen partial pressure

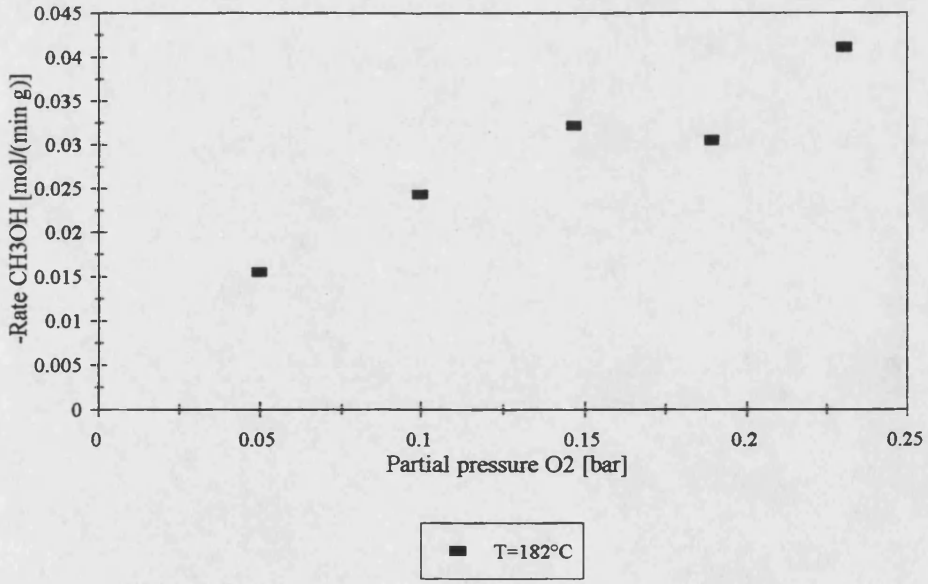

Figure 7.6: Rate of methanol consumption vs. oxygen partial pressure

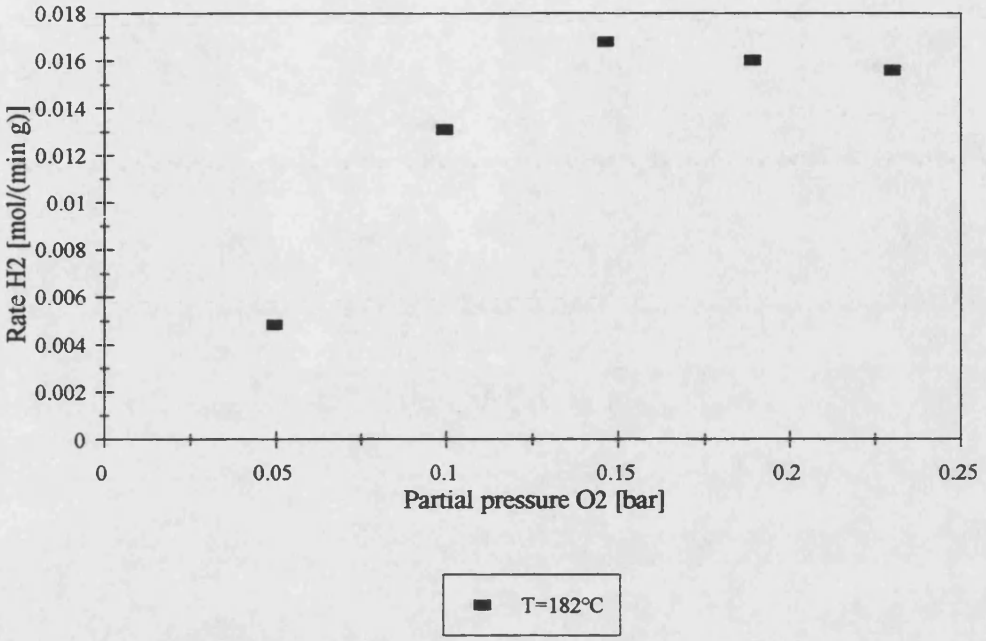

Figure 7.7: Rate of hydrogen formation vs. oxygen partial pressure

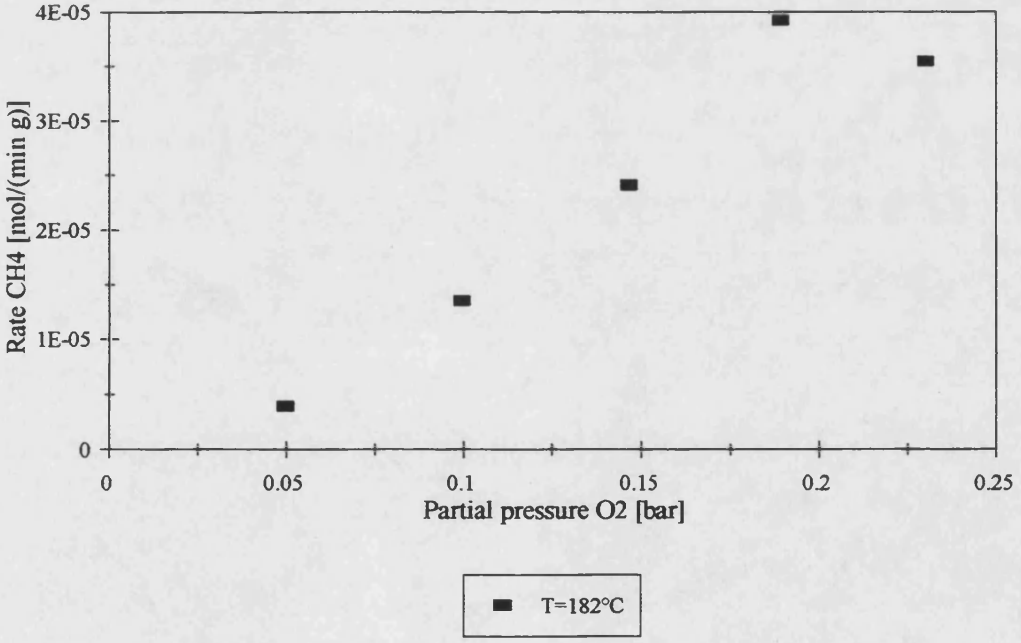

Figure 7.8: Rate of methane formation vs. oxygen partial pressure

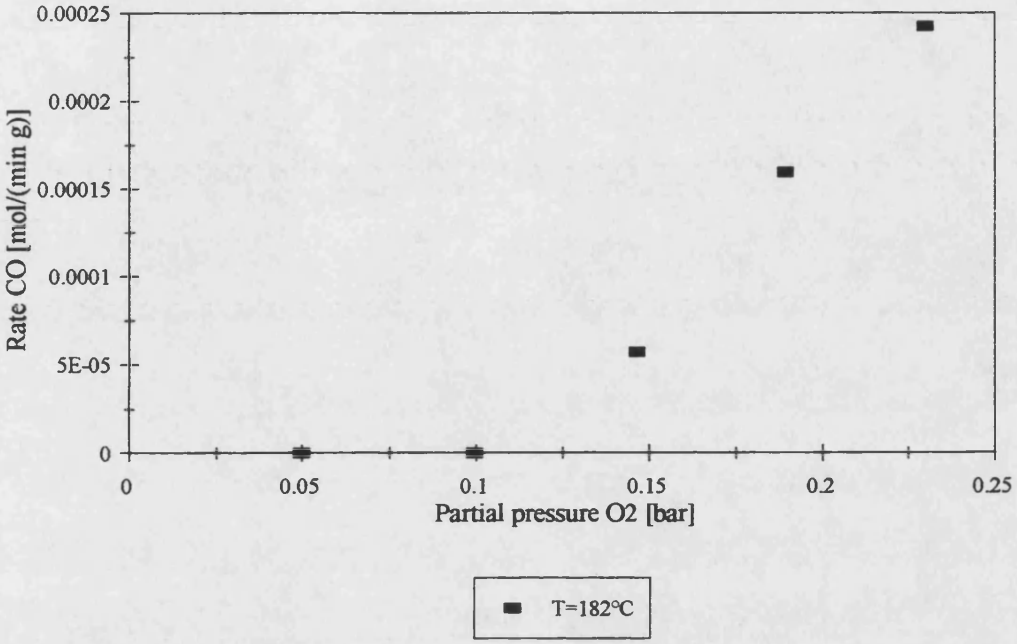

Figure 7.9: Rate of carbon monoxide formation vs. oxygen partial pressure

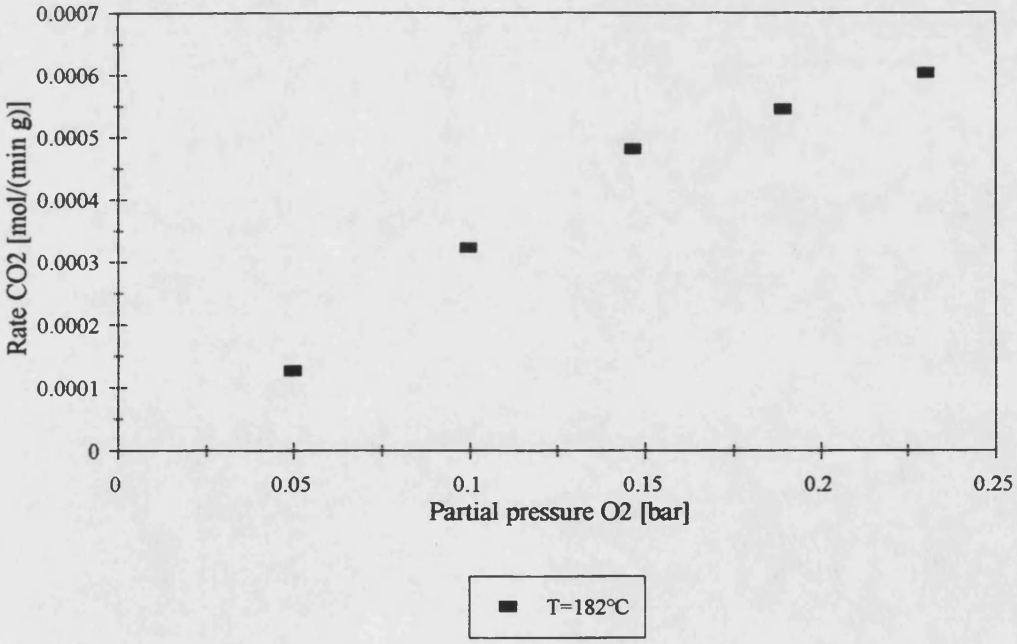

Figure 7.10: Rate of carbon dioxide formation rate vs. oxygen partial pressure

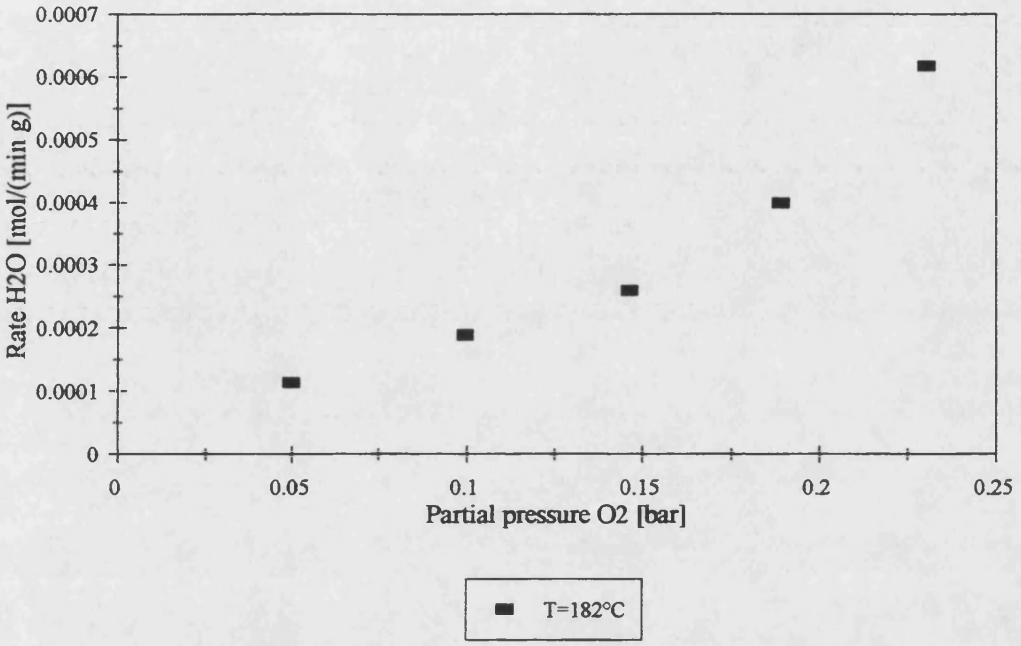

Figure 7.11: Rate of water formation vs. oxygen partial pressure

The second series of experiments was carried out using ten segments of a catalytic membrane tube. Platinum was deposited into the inner γ-alumina layer as described in Chapter 6. Subsequent to the platinum deposition, one 10mm long segment was cut off the tube. This segment was then cut radially into 8 segments, which were fastened into the reactor basket by means of stainless steel wire. Figure 7.12 shows the top view of the basket assembly.

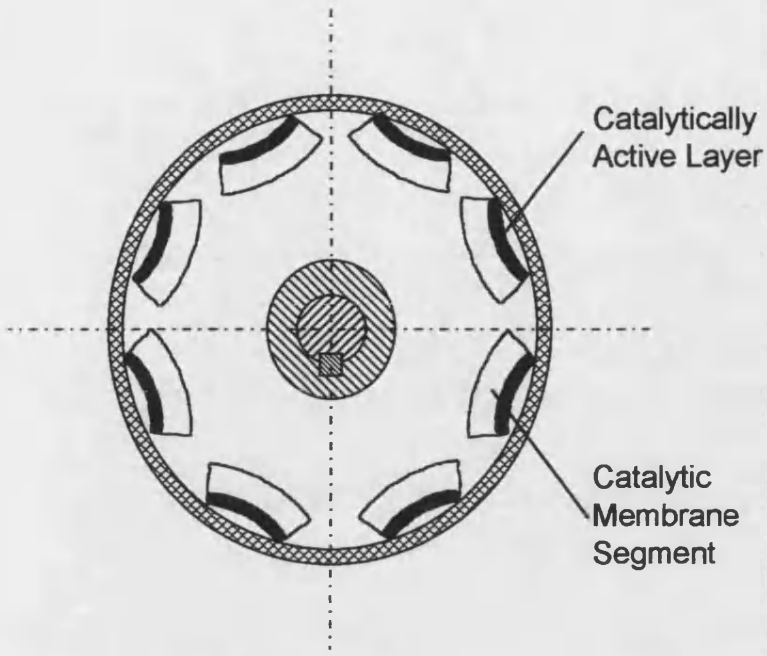

Figure 7.12: Catalytic membrane segment assembly

Figures 7.13 to 7.19 show the measured rates of the reaction participants. The rates were calculated according to Equation 7.3, where the catalyst mass was the mass of the active layer only. This mass was calculated as described in Appendix 8. The experimental conditions are given in Table 7.5.

Table 7.5: Experimental conditions, spinning basket reactor experiments with catalytic membrane segments

Temperature	294	°C
Total pressure	1.035	bar
Feed flowrate	0.09	mol/min
Methanol feed partial pressure	0.1097	bar
Catalyst mass	0.00252	g
Platinum loading	2.4	% by weight
Basket rotational speed	2000	min^{-1}

The feed flowrate was increased and the reactant feed partial pressures were decreased compared to the first series in order to prevent any inhibition of the observed reaction rates by reaction products.

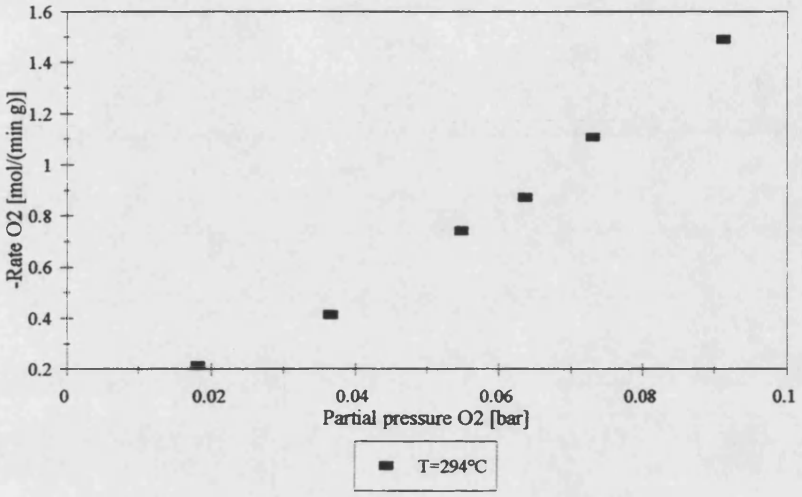

Figure 7.13: Rate of oxygen consumption vs. oxygen partial pressure

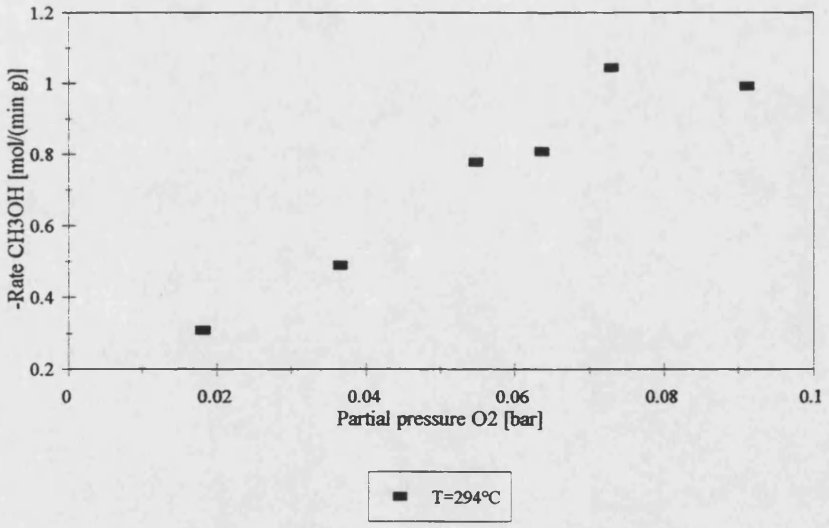

Figure 7.14: Rate of methanol consumption vs. oxygen partial pressure

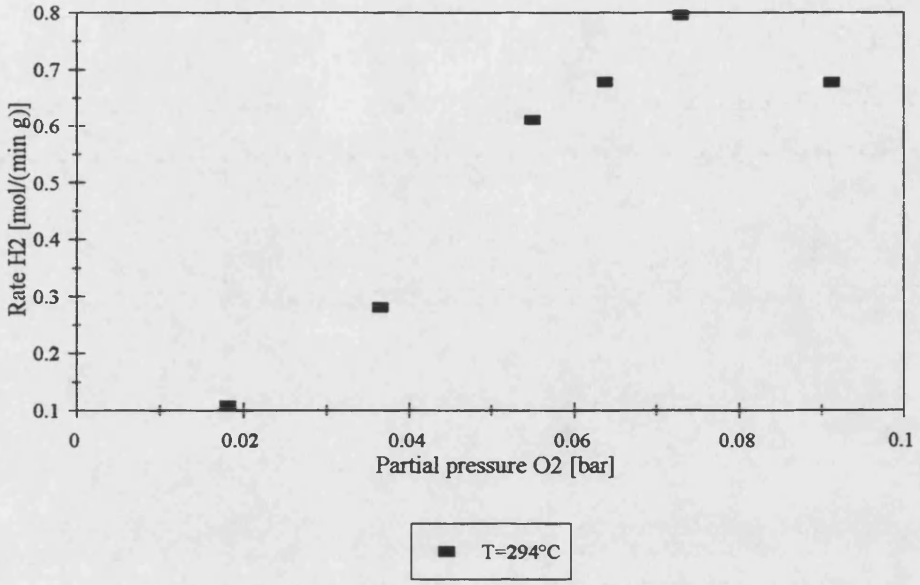

Figure 7.15: Rate of hydrogen formation vs. oxygen partial pressure

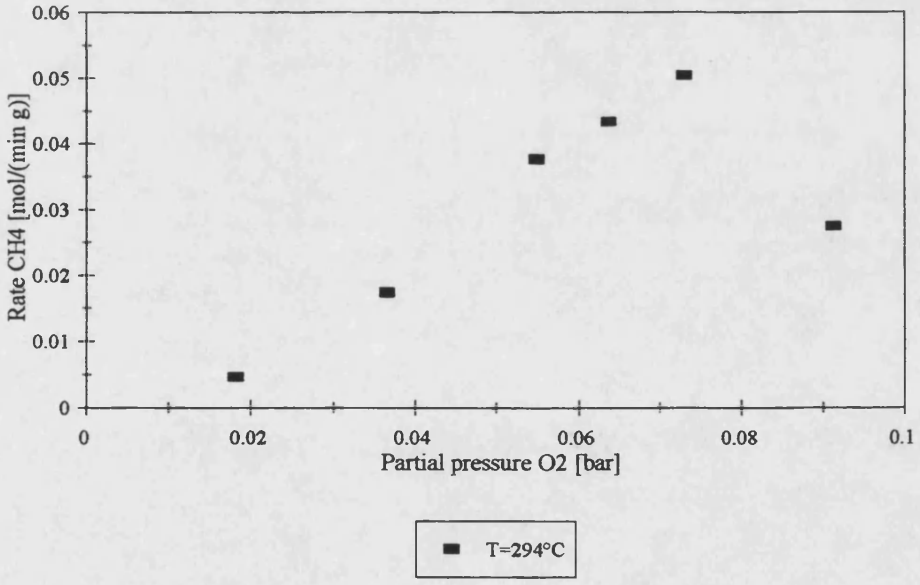

Figure 7.16: Rate of methane formation vs. oxygen partial pressure

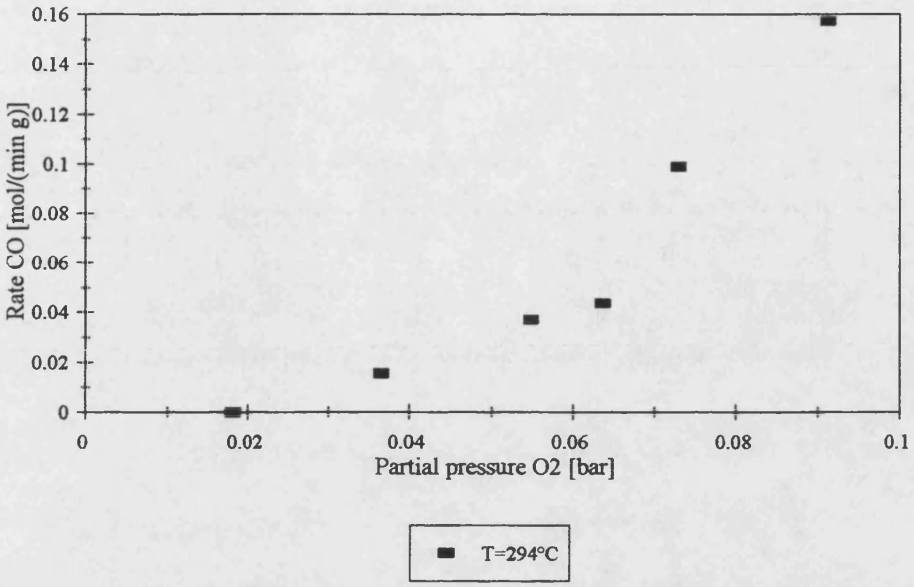

Figure 7.17: Rate of carbon monoxide formation vs. oxygen partial pressure

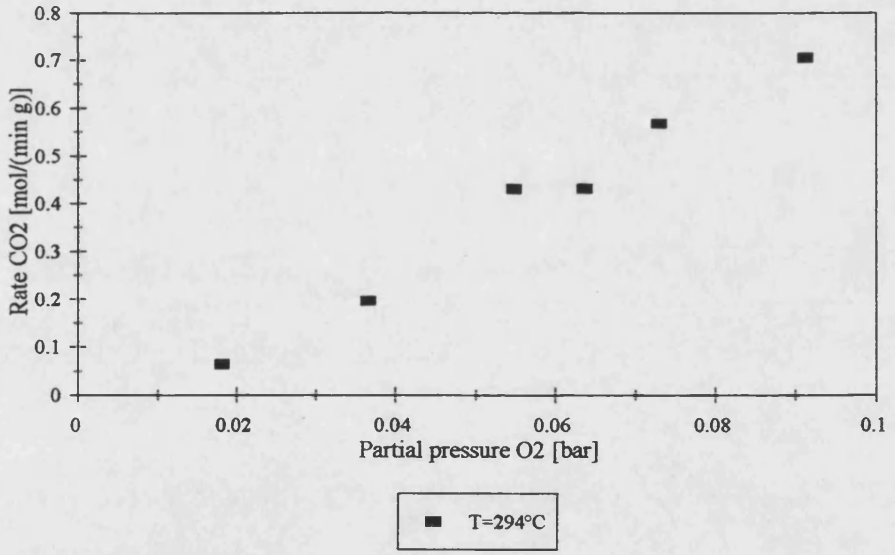

Figure 7.18: Rate of carbon dioxide formation vs. oxygen partial pressure

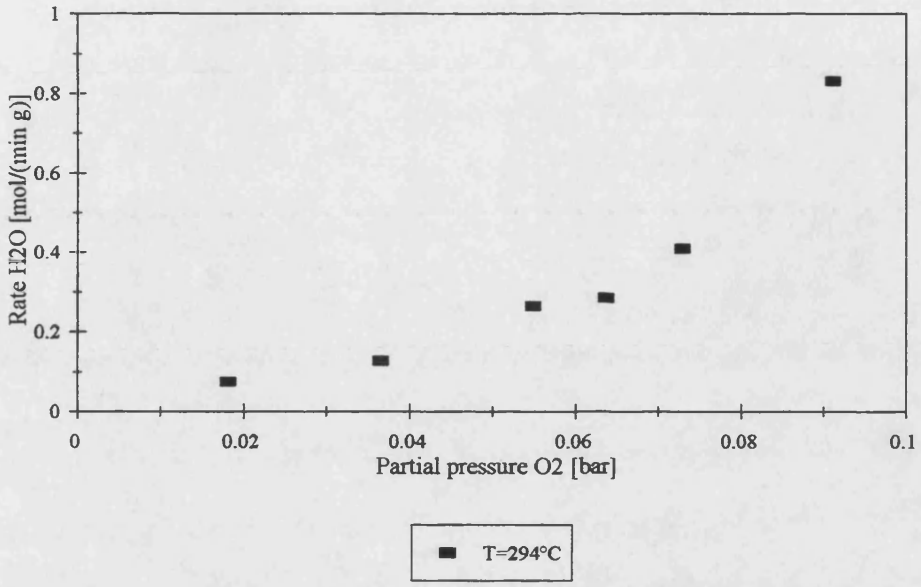

Figure 7.19: Rate of water formation vs. oxygen partial pressure

7.2 Tubular wall reactor experiments

The tubular wall reactor employed in this study was of the same design as described by Hayes *et. al.* (1995). It is described in detail in Chapter 3. The Pt/γ-Al_2O_3 catalyst was deposited on a Pormulite (mainly α-Al_2O_3) tube of 15mm internal diameter, 20mm external diameter and 10mm length. In order to increase the flow velocity, and hence radial mixing by means of increased turbulence, an insert of 12mm diameter was placed inside the tube close to the reactor entrance (see Figure 3.7). During the catalyst preparation, extreme care was taken to create a thin layer in order to prevent any influence of internal mass transfer resistances. The catalyst preparation is described in detail in Chapter 6. The temperature distribution inside the reactor was monitored by means of thermocouples placed in the bulk gas stream at the reactor inlet and outlet and close to the catalyst surface. The influence of external mass and heat transfer resistances on the experimentally observed rates was assessed using theoretical criteria given by Carberry (1976). The calculations are described in Section 7.2.2.

7.2.1 Tubular wall reactor kinetic experiments

A total of eight experimental series were carried out in the tubular wall reactor. Four temperatures (211°C, 251°C, 280°C and 305°C) were investigated. For each of these temperatures one series of experiments was conducted with the oxygen partial pressure held constant and the methanol partial pressure varying and one with the methanol partial pressure held constant and the oxygen partial pressure varying.

The tubular wall reactor was considered to operate as a differential, isothermal reactor. For this type of reactor the reaction rate for a reactant can be evaluated according to (Froment and Bischoff 1990):

$$\frac{N_F}{p}\left(p_{F,i} - p_{P,i}\right) + r_i m_{cat} = 0 \qquad (7.4)$$

where N_F is the molar feed flowrate of the reactor, p the total reactor pressure, $p_{F,i}$ the feed partial pressure of component i, $p_{P,i}$ the product partial pressure of component i, r_i the measured rate of consumption or formation of component i and m_{cat} the mass of Pt/γ-Al_2O_3 catalyst on the catalytic tube section.

The reactor geometrical data is given in Table 7.6 and in Chapter 3. The experimental conditions for the four series are given in Table 7.7.

Table 7.6: Tubular wall reactor data

Internal diameter catalyst tube [m]	0.015
Insert diameter [m]	0.012
Hydraulic diameter [m]	0.003
Reactor length [m]	0.01
Reactor Volume [m^3]	6.3617×10^{-07}
Catalyst mass [kg]	1.3522×10^{-05}
Catalyst bulk density [kg/m^3]	21.2556
Catalyst specific surface [1/m]	740.7407

Table 7.7: Tubular wall reactor experiments: experimental conditions

					Feed partial pressures [bar]		
	Experiment	Surface temperature [°C]	Pressure [bar]	Feed flowrate [mol/min]	CH_3OH	O_2	N_2
Series 1	TWR58	280	1.15500	0.25000	0.10240	0.01716	1.03544
	TWR56					0.03491	1.01770
	TWR57					0.05143	1.00117
	TWR55					0.06813	0.98447
	TWR59					0.08560	0.96700
Series 2	TWR66	280	1.15500	0.25000	0.04387	0.05100	1.06013
	TWR64				0.07311		1.03089
	TWR65				0.10236		1.00164
	TWR63				0.13162		0.97238
	TWR60				0.16083		0.94317
Series 3	TWR69	211	1.15500	0.25000	0.10240	0.01716	1.03544
	TWR70					0.03491	1.01770
	TWR67					0.05143	1.00117
	TWR71					0.06813	0.98447
	TWR68					0.08560	0.96700
Series 4	TWR72	211	1.15500	0.25000	0.04387	0.05100	1.06013
	TWR75				0.07311		1.03089
	TWR67				0.10236		1.00164
	TWR74				0.13162		0.97238
	TWR73				0.16083		0.94317

Table 7.7: Tubular wall reactor experiments: experimental conditions (continued)

					Feed partial pressures [bar]		
	Experiment	Surface temperature [°C]	Pressure [bar]	Feed flowrate [mol/min]	CH_3OH	O_2	N_2
Series 5	TWR78	305	1.15500	0.25000	0.04386	0.05100	1.06014
	TWR75				0.07378		1.03022
	TWR80				0.10282		1.00118
	TWR79				0.13164		0.97237
	TWR77				0.16083		0.94317
Series 6	TWR82	305	1.15500	0.25000	0.10240	0.01716	1.03544
	TWR84					0.03491	1.01770
	TWR80					0.05143	1.00117
	TWR85					0.06813	0.98447
	TWR83					0.08560	0.96700
Series 7	TWR87	251	1.15500	0.25000	0.04387	0.05100	1.06013
	TWR89				0.07311		1.03089
	TWR86				0.10236		1.00164
	TWR90				0.13162		0.97238
	TWR88				0.16083		0.94317
Series 8	TWR91	251	1.15500	0.25000	0.10240	0.01716	1.03544
	TWR93					0.03491	1.01770
	TWR86					0.05143	1.00117
	TWR94					0.06813	0.98447
	TWR92					0.08560	0.96700

The measured reaction rates are given in Table 7.8. In contrast to the experiments carried out in the spinning basket reactor, no methane and carbon monoxide were detected in the tubular wall reactor experiments.

Table 7.8: Measured reaction rates

		Measured reaction rates [mol/(g min)]				
	Experiment	H_2	O_2	CO_2	H_2O	CH_3OH
Series 1	TWR58	0.004809	-0.040520	0.007225	0.013948	-0.153337
	TWR56	0.005331	-0.069096	0.013350	0.014902	-0.173430
	TWR57	0.005279	-0.111030	0.023684	0.024270	-0.246260
	TWR55	0.005248	-0.124821	0.032018	0.024745	-0.126784
	TWR59	0.001084	-0.178860	0.035186	0.038975	-0.190617
Series 2	TWR66	0.000105	-0.080383	0.021955	0.019684	-0.093684
	TWR64	0.001751	-0.071410	0.019890	0.019532	-0.195430
	TWR65	0.003056	-0.072640	0.018925	0.021406	-0.136270
	TWR63	0.005135	-0.092090	0.019350	0.027187	-0.283720
	TWR60	0.007163	-0.121933	0.019683	0.027115	-0.287708
Series 3	TWR69	0.001389	-0.002100	0.004473	0.013064	-0.067384
	TWR70	0.001402	-0.017362	0.008430	0.017893	-0.145347
	TWR67	0.000362	-0.012871	0.012397	0.017021	-0.155845
	TWR71	0.000376	-0.014631	0.018984	0.024966	-0.026791
	TWR68	0.000000	-0.009320	0.025501	0.024336	-0.193775
Series 4	TWR72	0.000098	-0.001230	0.016242	0.013096	-0.085841
	TWR75	0.000130	-0.002539	0.013838	0.016508	-0.021350
	TWR67	0.000362	-0.012871	0.012397	0.017021	-0.155845
	TWR74	0.000376	-0.035680	0.013206	0.017063	-0.176016
	TWR73	0.000297	-0.054450	0.012088	0.002463	-0.269697
Series 5	TWR78	0.001297	-0.022520	0.024368	0.022877	-0.057228
	TWR75	0.005119	-0.012054	0.028264	0.024683	-0.119872
	TWR80	0.006580	-0.017454	0.023274	0.030221	-0.096900
	TWR79	0.009111	-0.036724	0.024241	0.033842	-0.199105
	TWR77	0.005281	-0.044833	0.024759	0.036345	-0.218060
Series 6	TWR82	0.007053	-0.021826	0.008433	0.031211	-0.106124
	TWR84	0.008800	-0.017270	0.015752	0.028409	-0.116269
	TWR80	0.006580	-0.017454	0.023274	0.030221	-0.096900
	TWR85	0.004600	-0.052991	0.027556	0.031563	-0.073330
	TWR83	0.001527	-0.004462	0.036542	0.035543	-0.154635
Series 7	TWR87	0.000114	-0.005169	0.017708	0.015915	-0.080791
	TWR89	0.001469	-0.021573	0.015717	0.013316	-0.127262
	TWR86	0.001794	-0.011650	0.016503	0.021627	-0.075427
	TWR90	0.002660	-0.026816	0.015473	0.022742	-0.167229
	TWR88	0.002022	-0.039116	0.014693	0.026098	-0.112612
Series 8	TWR91	0.004087	-0.006400	0.005416	0.017092	-0.106457
	TWR93	0.001261	-0.010522	0.010300	0.018100	-0.211732
	TWR86	0.001794	-0.011650	0.016503	0.021627	-0.075427
	TWR94	0.001405	-0.014774	0.019880	0.028904	-0.083977
	TWR92	0.000578	-0.016531	0.027510	0.028180	-0.121365

Figures 7.20 to 7.29 show the measured reaction rates reported in Table 7.8 as functions of the varied partial pressures.

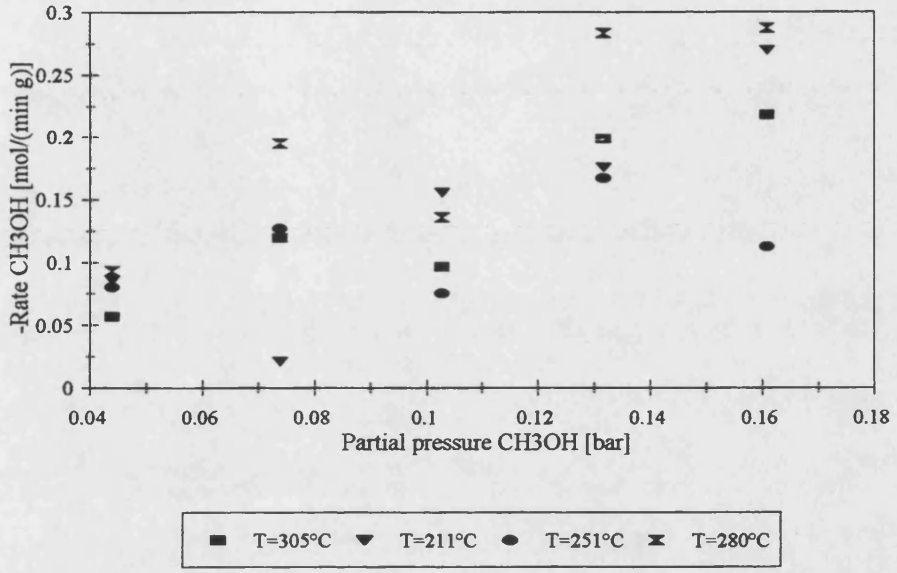

Figure 7.20: Rate of methanol consumption vs. methanol partial pressure

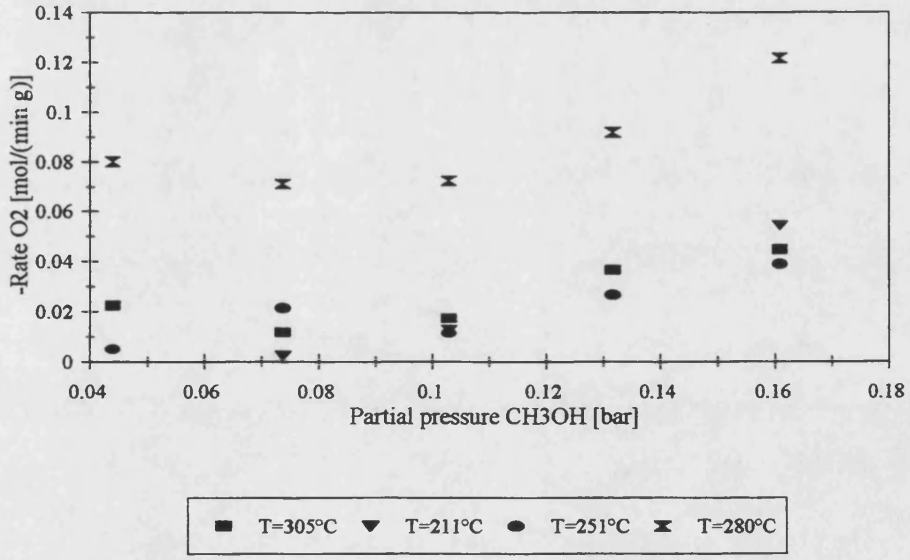

Figure 7.21: Rate of oxygen consumption vs. methanol partial pressure

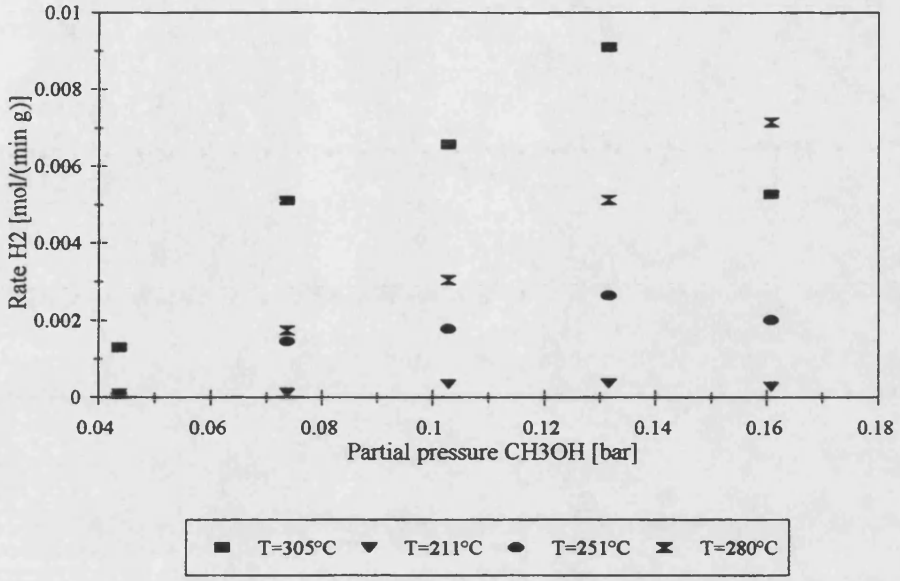

Figure 7.22: Rate of hydrogen formation vs. methanol partial pressure

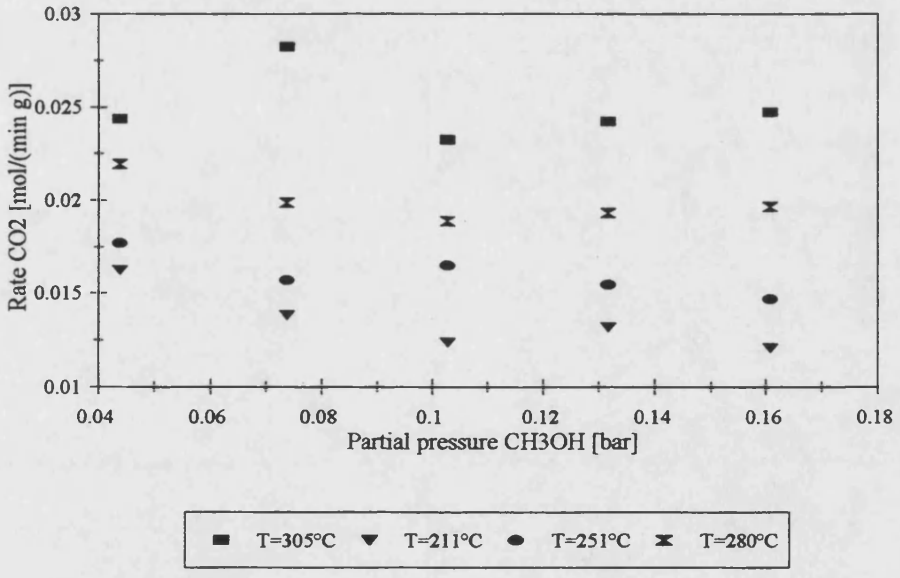

Figure 7.23: Rate of carbon dioxide formation vs. methanol partial pressure

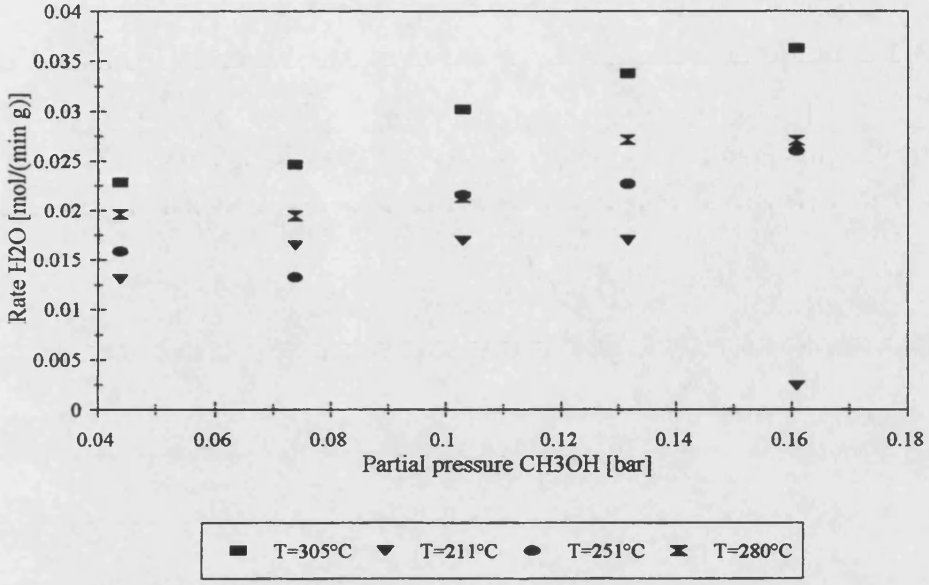

Figure 7.24: Rate of water formation vs. methanol partial pressure

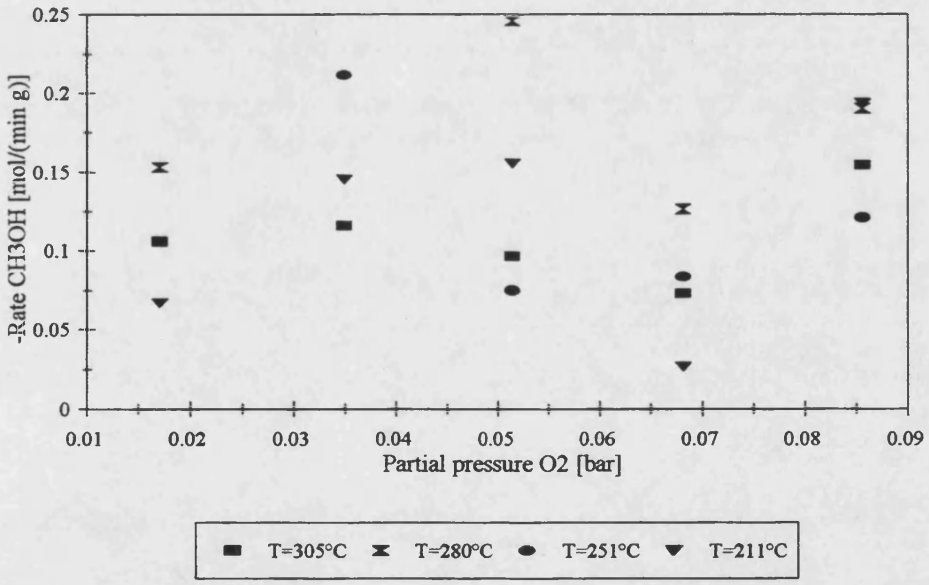

Figure 7.25: Rate of methanol consumption vs. oxygen partial pressure

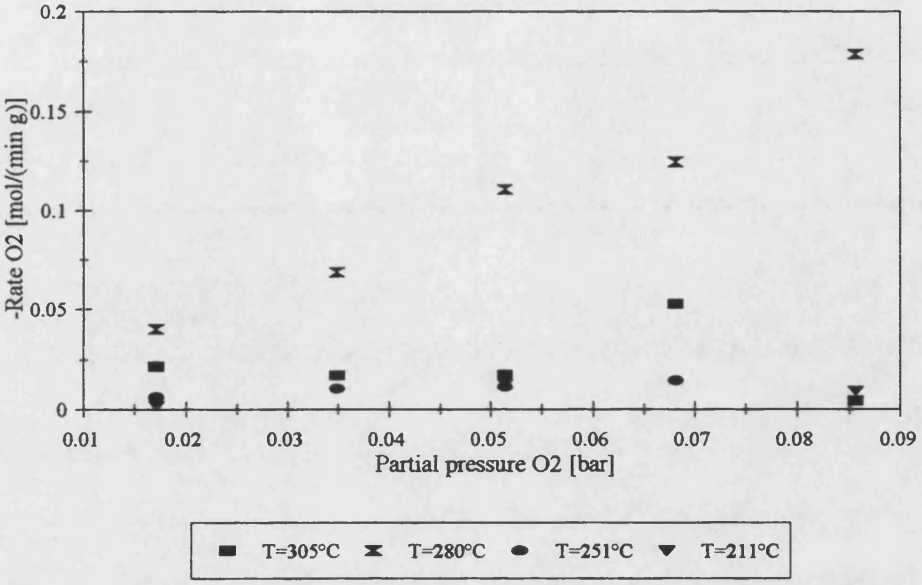

Figure 7.26: Rate of oxygen consumption vs. oxygen partial pressure

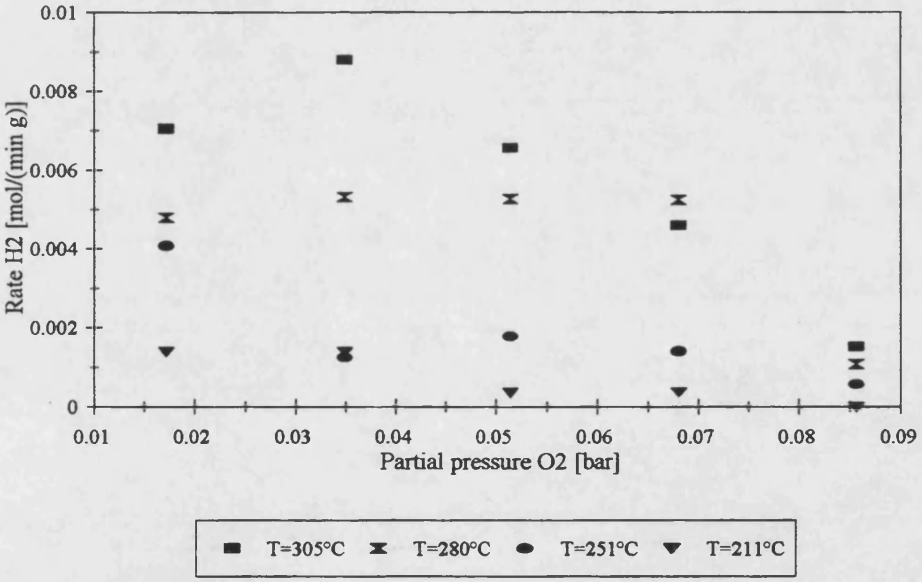

Figure 7.27: Rate of hydrogen formation vs. oxygen partial pressure

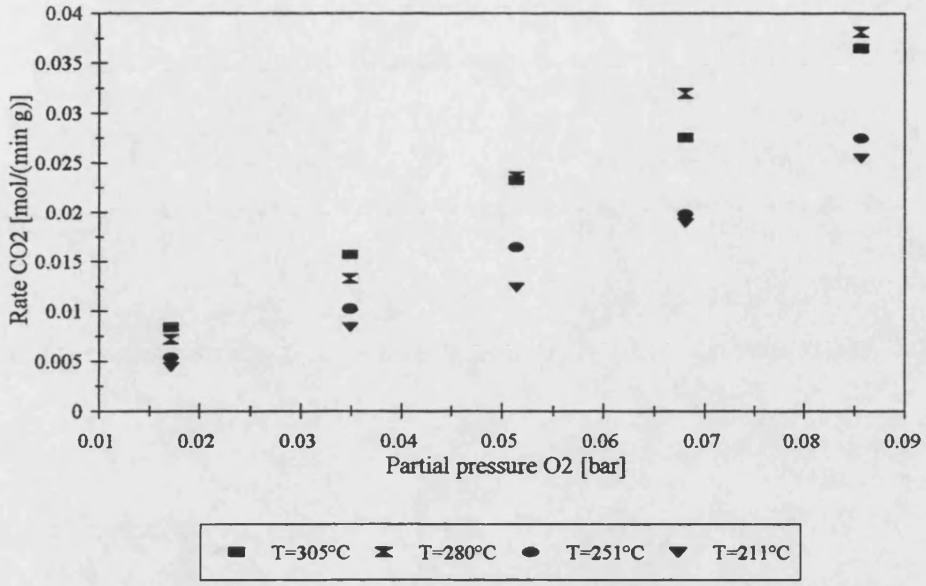

Figure 7.28: Rate of carbon dioxide formation vs. oxygen partial pressure

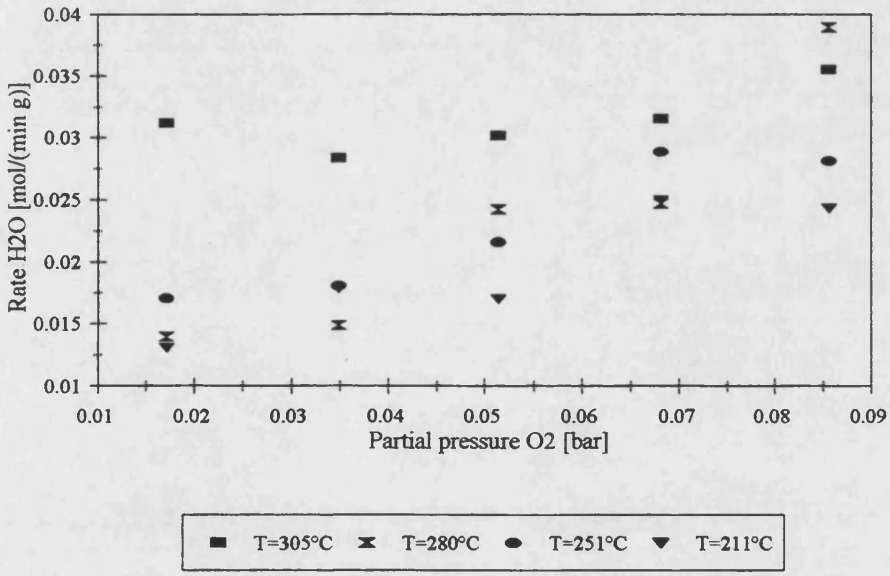

Figure 7.29: Rate of water formation vs. oxygen partial pressure

7.2.2 Validity of the tubular wall reactor experiments

The kinetic experiments reported in Section 7.2.1 can only be employed to determine intrinsic reaction rates if the reactor operation could be considered as isothermal and the measured conversions were differential. Furthermore should no external mass transfer resistance influence the observed reaction rate.

As carbon dioxide and methanol were the only carbon containing species involved in the reaction and the carbon dioxide composition could be measured with higher accuracy, stoichiometry (*i. e.* $r_{CH_3OH} = -r_{CO_2}$) was employed to determine the maximum methanol conversion on the basis of the rate of formation of carbon dioxide. Experiment TWR 83 exhibited the maximum rate of formation of carbon dioxide, from which the maximum methanol conversion was calculated to be 9%. This value is sufficiently low to regard the reactor operation as differential (Baerns *et. al.* 1987).

Figures 7.30 and 7.31 show the axial temperature profiles measured along the catalytic tube segment in experiments TWR 67 and 80, which were carried out at nominal temperatures of 211°C and 305°C, respectively. The figures show that the maximum temperature difference along the catalytic surface of the tube segment is approximately 6°C. The maximum temperature difference between gas phase and catalytic surface temperatures was measured to be approximately 7°C. These temperature differences were considered to be sufficiently low to assume isothermal behaviour of the tubular wall reactor.

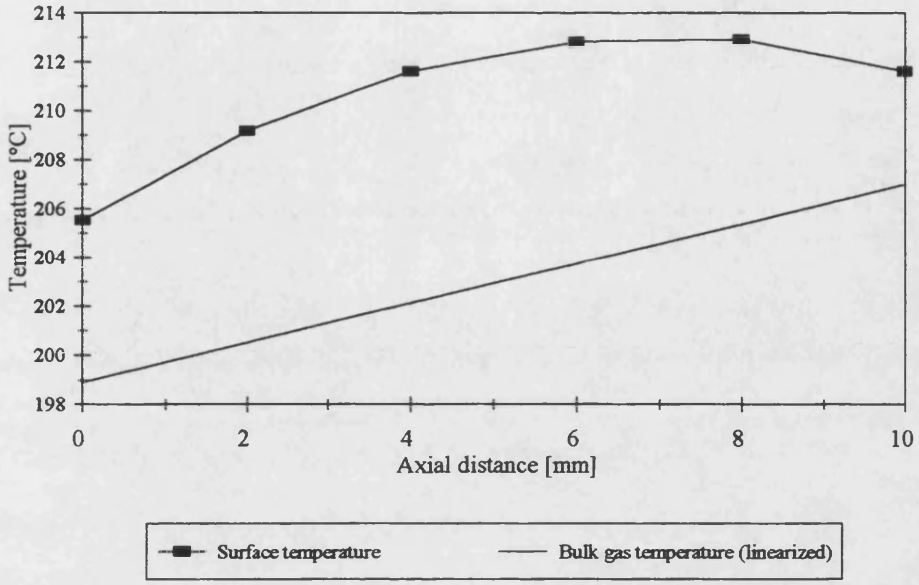

Figure 7.30: Axial reactor temperature profiles TWR67

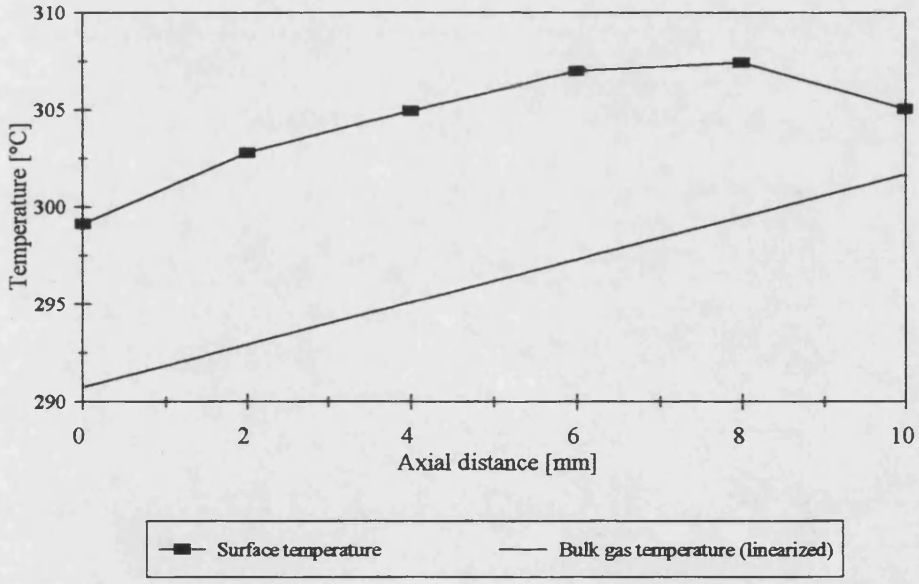

Figure 7.31: Axial reactor temperature profiles TWR80

In order to determine whether mass and heat transfer resistances between the bulk gas phase and the internal tube surface, *i. e.* the location of the catalyst, was likely to have any influence on the observed reaction rate, a theoretical analysis described by Carberry (1976) can be carried out. The criteria given in Equations 7.5 and 7.6 (Carberry 1976) should be fulfilled in order to ascertain the absence of external mass and heat transfer resistances, respectively. The inequalities are, respectively:

$$\overline{\eta} Da = \frac{r_{obs,i}\rho_{cat,b}}{k_{g,i} a c_{b,i}} < 0.01 \tag{7.5}$$

$$\frac{(-\Delta H) y_{b,i}}{c_p T_b}\left(\frac{\mathrm{Pr}}{Sc}\right)^{2/3} \frac{r_{obs,i}\rho_{cat,b}}{c_{b,i} k_{g,i} a} = \overline{\beta}\,\overline{\eta} Da < 0.01 \tag{7.6}$$

The external bulk to surface mass transfer coefficient $k_{g,i}$ was evaluated according to a Sherwood number correlation given by van Krevelen and Hoftijzer (1949):

$$Sh = const \times Re^{0.8} Sc^{1/3} \tag{7.7}$$

This correlation was developed for turbulent flow with *const*=0.03. However, van Krevelen and Hoftijzer (1949) showed that *Sh* is also proportional to $Re^{0.8}$ for incompletely developed laminar flow for ratios of *L/d* smaller than 20. In this case *const* becomes a function of the length to diameter ratio *L/d*, which is given in the same reference.

The hydraulic diameter (*e. g.* the characteristic length for *Re* and *Sh*) of the annulus can be calculated according to:

$$d_h = \frac{4A}{C} \tag{7.8}$$

Here A is the crossectional area and C the wetted circumference. Equation 7.8 gives a hydraulic diameter of 3mm for the investigated 10mm long tubular segment with insert. Hence the length to diameter ratio is 3.33, which is smaller than the diameter ratio of 20 for which developed profiles can be expected (van Krevelen and Hoftijzer 1949). For a ratio of 3.75, van Krevelen and Hoftijzer (1949) reported a value of 0.288 for *const.* This value was used in this study.

A further correlation to estimate the entrance length to be traversed prior to the development of laminar flow in a pipe was given by Bird *et. al.* (1960):

$$L_e = 0.035 \times d_h Re \tag{7.9}$$

L_e has a value of 21mm for a Reynolds number of 200. Applying the conditions of experiments TWR 67 and TWR 80 to calculate Reynolds numbers gives values for Re of 236.94 and 209.20, respectively (see Table 7.9). The length of the employed catalytic tube segment was 10mm (see Table 7.6). Thus it can be assumed that the flow through the annular tube is not fully developed.

Two of the kinetic experiments were subjected to the analysis (TWR 67 and TWR 80). Methanol was the component considered. As in the determination of the maximum methanol conversion, stoichiometry is employed to determine the rate of methanol consumption from the rate of carbon dioxide formation, *i. e.* $r_{CH_3OH} = -r_{CO_2}$. The required physical properties (density, viscosity, specific heat capacity, thermal conductivity and methanol mean diffusivity) were estimated as described in Appendix 7.

The required geometrical data and feed conditions for the calculations are given in Tables 7.6 and 7.7.

The results of the analysis according to Equations 7.5 and 7.6 for the two temperatures investigated as well as the physical, transport and reaction properties used to arrive at these values are shown in Table 7.9. It is shown in the subsequent section that the reaction mechanism observed experimentally in the tubular wall reactor can be described by a combination of an oxidative dehydrogenation reaction and an oxidation reaction. However, Equations 7.5 and 7.6 are only applicable to single reactions. For the purpose of the calculations, it was assumed that the rate of methanol consumption is solely due to the oxidation of methanol, as this reaction involves a higher heat of reaction than the oxidative dehydrogenation reaction and hence has a larger influence on thermal effects. The heat of reaction was evaluated as described in Chapter 4.

Table 7.9: Results of the mass and heat transfer resistance analysis

	TWR 67 T=211°C	TWR 80 T=305°C
Reaction rate [kmol/s/kg]	0.0002076	0.0003879
Re	236.94	209.20
Sc	0.90232	0.88123
Pr	0.74310	0.73872
Sh	22.092	19.84
Mass transfer coefficient [m/s]	0.2317	0.2870
CH_3OH concentration [kmol/m^3]	0.00262	0.00219
Heat of reaction [kJ/kmol]	-672455.18	-670771.67
Specific heat capacity [kJ/kmol/K]	31.9937	33.0335
$\overline{\eta}Da$	0.0097682	0.01773471
$\overline{\beta}\overline{\eta}Da$	0.0399133	0.05007045

According to the results in Table 7.9, the conditions given in Equations 7.5 and 7.6 are not strictly fulfilled. However, the resulting values for the mass transfer resistance

($\overline{\eta}Da$) are in close proximity. The values for the heat transfer resistance ($\overline{\beta}\overline{\eta}Da$) are clearly larger than 0.01 (Equation 7.6). However, it could be shown experimentally that the experiments carried out could be considered as isothermal (Figures 7.30 and 7.31). The experimental equipment employed did not allow a higher flowrate, which would have resulted in a higher Reynolds number and hence mass transfer coefficient. Another possibility of decreasing $\overline{\eta}Da$ would have been to increase the feed reactant concentrations. This route was also impractical as it would have resulted in an increase in conversion. In this case it would have been doubtful whether the reactor still could have been considered as differential and whether isothermal conditions could have been maintained. Hence it was decided to employ the reactor conditions outlined above.

7.2.3 Analysis of the tubular wall reactor experiments

The experimentally measured reaction rates for the species participating in the reactions shown in Table 7.8 and in Figures 7.20 to 7.29 show considerable experimental scatter. This behaviour is especially pronounced for the measured reactant reaction rates, rendering these rates useless for further analysis. The measured product rates show less scatter, especially for carbon dioxide and water. The following analysis of the experimental results will be based upon these two latter rates.

The experiments in the tubular wall reactor showed only three products (carbon dioxide, hydrogen and water) as opposed to the five products encountered in the spinning basket reactor experiments. This leads to the conclusion that the following three reactions took place:

- Oxidative dehydrogenation of methanol:

$$CH_3OH + \frac{1}{2}O_2 \rightarrow 2H_2 + CO_2 \qquad (7.10)$$

- Catalytic combustion of methanol:

$$CH_3OH + \frac{3}{2}O_2 \rightarrow 2H_2O + CO_2 \qquad (7.11)$$

- Hydrogen oxidation to form water, either heterogeneously catalysed or homogenous:

$$H_2 + \frac{1}{2}O_2 \rightarrow H_2O \qquad (7.12)$$

Because of time constraints, no experiments were carried out with hydrogen as a feed component. Experiments of this kind would have been required in order to access the third reaction (Equation 7.12). Instead, a reaction combination of the oxidative dehydrogenation of methanol and the catalytic combustion of methanol is proposed. The two reactions are assumed to take place in parallel. The matrix of stoichiometric coefficients is shown in Table 7.10.

Table 7.10: Stoichiometric coefficients

	CH_3OH	O_2	H_2	H_2O	CO_2
Equation 7.10 (Reaction 1)	-1.0	-0.5	2.0	0.0	1.0
Equation 7.11 (Reaction 2)	-1.0	-1.5	0.0	2.0	1.0

Relationships between rates of consumption or production of the components present and the reaction rates can be deducted from Table 7.10, employing Equation 7.13:

$$r_i = \sum_{j=1}^{nr} v_{i,j} R_j \qquad (7.13)$$

where i is the component, j the reaction, r_i the rate of consumption or production of i and R_j the rate of reaction j. Equations 7.14 to 7.18 show the relationships between the rates of the two reactions (Equations 7.10 and 7.11) according to Equation 7.13:

$$r_{CH_3OH} = -R_1 - R_2 \tag{7.14}$$

$$r_{O_2} = -0.5R_1 - 1.5R_2 \tag{7.15}$$

$$r_{H_2} = 2R_1 \tag{7.16}$$

$$r_{H_2O} = 2R_2 \tag{7.17}$$

$$r_{CO_2} = R_1 + R_2 \tag{7.18}$$

It is apparent from Equations 7.14 to 7.18 that the reaction mechanism can be sufficiently described if the rates of production of water and carbon dioxide are measured. Figures 23 and 28 and Figures 24 and 29 show the measured rates of production of carbon dioxide and water, respectively. The measurements of these two rates show the least scatter of all the measured rates.

The behaviour of the measured rates of formation of water and carbon dioxide with changing methanol or oxygen partial pressure suggest that a power law relationship might be sufficient to express the reaction rates R_j:

$$R_j = k_{0,j} \exp\left(\frac{-E_{act,j}}{R_G T}\right) p_{CH_3OH}^{m_{CH_3OH,j}} p_{O_2}^{m_{O_2,j}} \tag{7.19}$$

Using Equation 7.19, the measured rates of production of carbon dioxide and water (given in Table 7.8 and Equations 7.17 and 7.18), a non-linear regression analysis was carried out. The estimated variables were k_j, $E_{act,j}$, $m_{CH3OH,j}$ and $m_{O2,j}$ of Equation 7.19 whereas the actual variables (*e. g.* the experimental conditions) were the temperature, the methanol feed partial pressure and the oxygen feed partial pressure (Table 7.7). The software package ADSIM 6.0-1 (Aspen Technology, 1997) was employed to carry out this analysis. The method implemented is based on the minimisation of the sum of least squares as for example described by Press *et. al.* (1992). Table 7.11 shows the estimated parameters for two reactions.

Table 7.11: Reaction parameters

	E_{act} [J/(mol)]	k_0 $\left[\frac{\text{mol}}{\text{g bar}^{m_{CH_3OH}+m_{O_2}} \text{ min}}\right]$	m_{O2}	m_{CH3OH}
Reaction 1 $CH_3OH+\frac{1}{2}O_2 \rightarrow 2H_2+CO_2$	10328.975	4.555	1.901	-0.631
Reaction 2 $CH_3OH+\frac{3}{2}O_2 \rightarrow 2H_2O+CO_2$	15693.037	2.773	0.442	0.285

Figures 7.32 to 7.35 show the comparison between measured carbon dioxide and water production rates and the ones calculated according to Equations 7.17, 7.18 and 7.19 with the parameters according to Table 7.11. Full lines are estimated, point values are experimental.

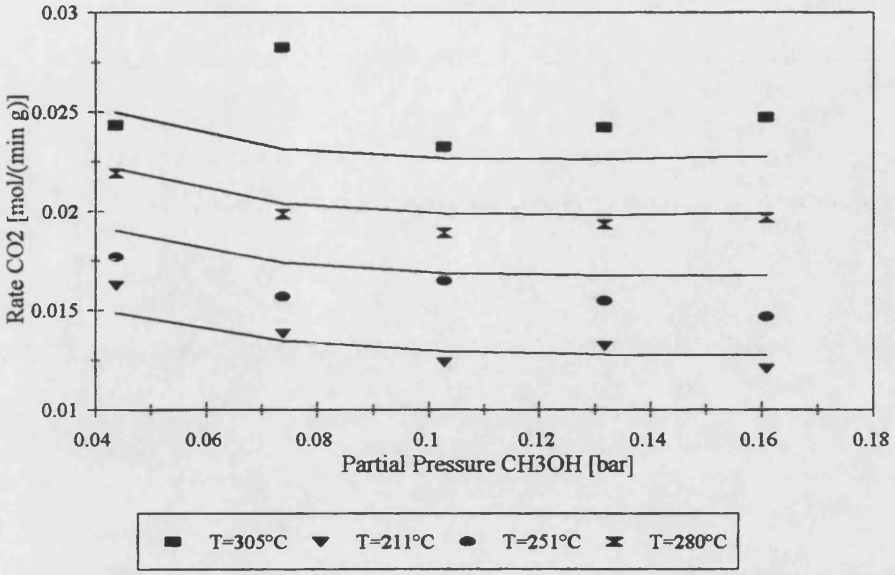

Figure 7.32: Comparison between estimated and measured rates of carbon dioxide formation vs. methanol partial pressure

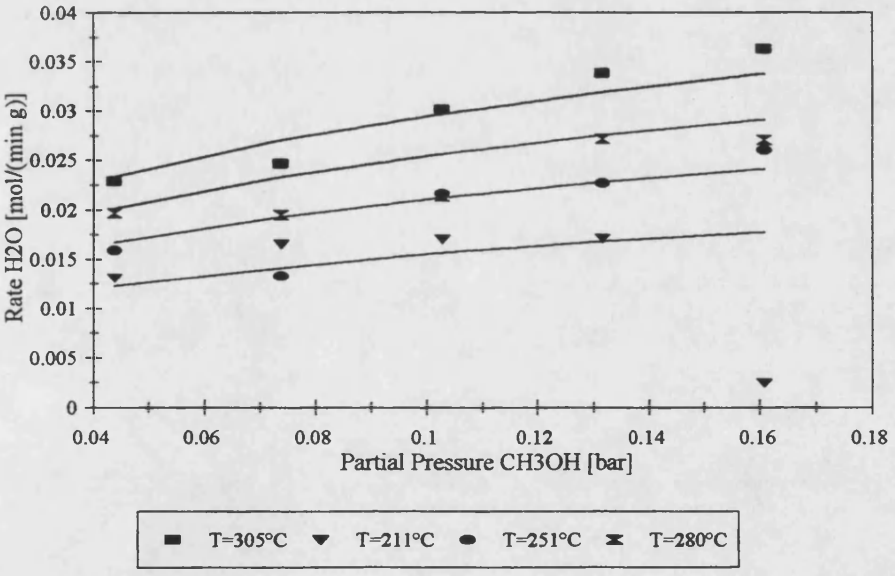

Figure 7.33: Comparison between estimated and measured rates of water formation vs. methanol partial pressure

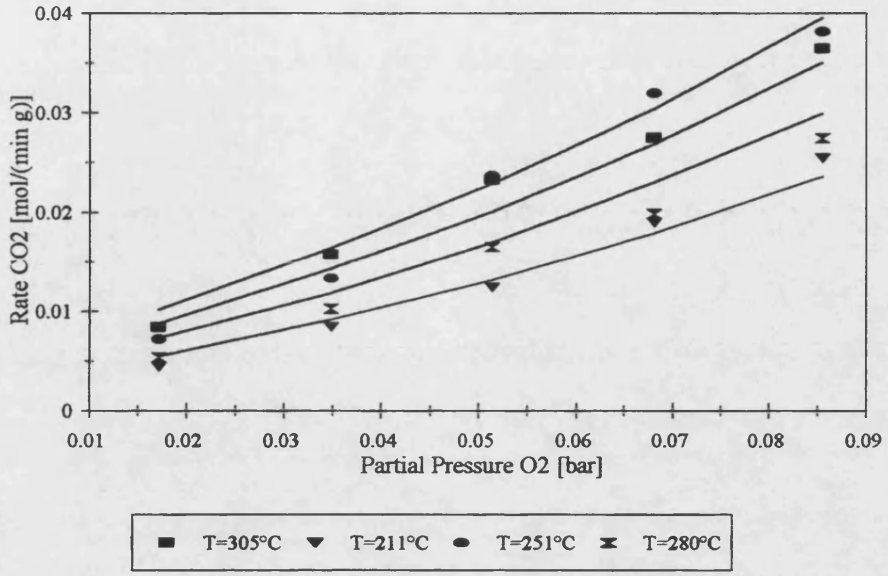

Figure 7.34: Comparison between estimated and measured rates of carbon dioxide formation vs. oxygen partial pressure

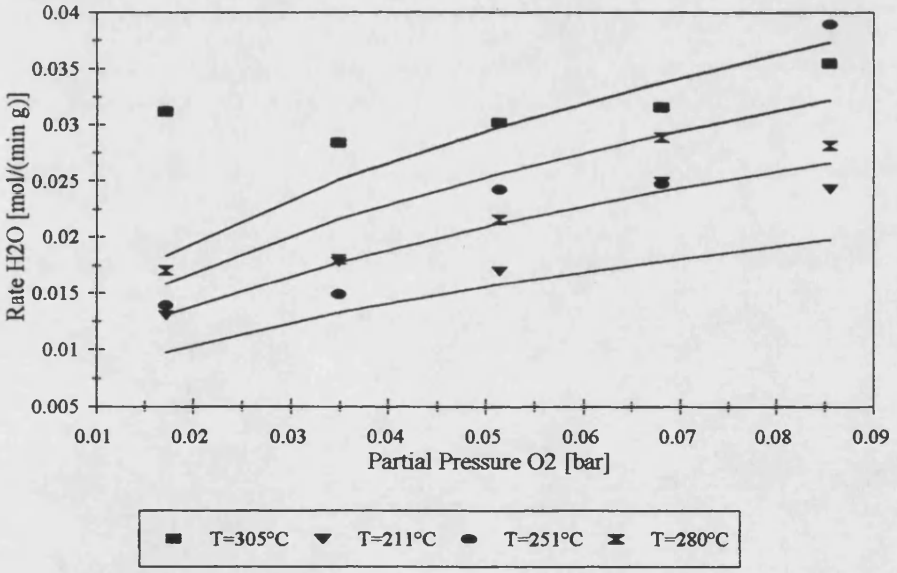

Figure 7.35: Comparison between estimated and measured rates of water formation vs. oxygen partial pressure

Except for the water production rate as a function of oxygen feed partial pressure, the rates calculated according to Equations 7.17 to 7.19 fit the experimental results reasonably well. Hence the proposed combination of reactions (Equations 7.10 and 7.11) was adopted for the remainder of this study.

7.3 Discussion of the results of the kinetic experiment

The spinning basket reactor experiments carried out to determine the speed of rotation clearly show that a rotational speed of 2000min^{-1} or higher is sufficient to ensure that external concentration and temperature gradients, and hence mass and heat transfer resistances, are of negligible influence on the observed reaction rate (Figure 7.1). The selectivity of the converted methanol towards hydrogen, the desired product, appears to be favoured by external gradients, as shown in Figure 7.3. This may well be caused by the high mass transfer rates of hydrogen compared to other components in the reaction. These high mass transfer rates are caused by the large diffusion coefficient of hydrogen compared with other components. For example the diffusion coefficient of the binary pair hydrogen-nitrogen is estimated to be 1.546cm^2/s at 180°C, whilst the water-nitrogen diffusion coefficient at 180°C has a value of 0.474cm^2/s. These values were calculated using the methods described by Reid *et. al.* (1977) and in Appendix 7. It can be concluded that a production scale reactor should be designed such that some external mass transfer resistance occurs.

The investigations regarding the intraparticle mass transfer resistances show that the observed reaction rate does not change once a particle size of smaller than approximately 1mm is employed (Figure 7.4). However, the measured methanol conversions at 180° and 312°C do not show the expected behaviour. A temperature increase of 10°C normally doubles the reaction rate (Rautenbach, 1990). This is clearly not the case for the experimental results shown in Figure 7.4. The temperature dependency of a reaction can normally be expressed by an Arrhenius relationship:

$$k(T) = k_0 \exp\left(\frac{-E_{act}}{R_G T}\right) \qquad (7.20)$$

where $k(T)$ is the reaction rate constant and k_0 is the reaction rate constant for $T \rightarrow \infty$. Froment and Bischoff (1990) showed that the presence of intraparticle mass transfer resistances reduces the observed activation energy by 50%. Hayes *et. al.* (1995) observed the same behaviour whilst studying the catalytic oxidation of carbon oxide at high temperatures, whilst at lower temperatures no mass transfer resistances were evident. This indicates that although the methanol conversion remained constant from particle sizes of 1mm downwards, the observed reaction rate still included intraparticle mass transfer effects.

As it was impossible to retain smaller particles than the smallest investigated size of 0.4775mm in the wire mesh enclosed basket, no smaller particles could be investigated. This was the reason for using catalytic membrane segments in the second series of kinetic experiments. The inner layer of the membrane consists of γ-alumina and has a thickness of 4μm. It was assumed that the platinum was deposited in this layer only. Hence this layer should pose only negligible diffusional resistance.

The results of the two experimental series investigating the change of the reaction rates with increasing oxygen partial pressure are shown in Figures 7.5 to 7.11 and 7.13 to 7.19. It is apparent that, apart from the rate of oxygen consumption, the reaction rates show the same qualitative behaviour. The rates of hydrogen formation, shown in Figures 7.7 and 7.15, appear to level off with increasing oxygen partial pressure. A similar behaviour, if not as pronounced, can be observed for carbon dioxide (Figures 7.10 and 7.18). At the same time the rates of formation of methane, carbon monoxide and water are increasing. This indicates the presence of other reactions apart from the oxidative

dehydrogenation of methanol and the direct catalytic oxidation of methanol as observed in the tubular wall reactor experiments (Equations 7.10 and 7.11). Probable reactions are:

- A water gas shift reaction, further converting the desired reaction products carbon dioxide and hydrogen to carbon monoxide and water

$$H_2 + CO_2 \rightarrow CO + H_2O \tag{7.21}$$

- A methanisation reaction converting part of the carbon monoxide and hydrogen to methane and water

$$3H_2 + CO \rightarrow CH_4 + H_2O \tag{7.22}$$

- Hydrogen oxidation to form water, either heterogeneously catalysed or homogenous

$$H_2 + \frac{1}{2}O_2 \rightarrow H_2O \tag{7.23}$$

- Catalytic methane oxidation

$$CH_4 + 2O_2 \rightarrow CO_2 + 2H_2O \tag{7.24}$$

The preceding discussion can only be qualitative as the experimental results are too scattered to allow for a rigorous quantitative analysis. The measured rates of formation of carbon containing molecules (*i. e.* carbon monoxide, carbon dioxide and methane) were too low compared to the rate measured for the consumption of methanol. The following example exemplifies this fact. The rates measured for the formation of

methane, carbon dioxide and carbon monoxide at a temperature of 294°C, a methanol pressure of 0.109728bar and an oxygen partial pressure of 0.06369bar add up to 0.50905mol/(min g), whilst the measured rate for the consumption of methanol is 0.80707mol/(min g).

The reason that these results are only of qualitative value can be found in the experimental evaluation of the methanol effluent composition (described in Appendix 4). Methanol in the effluent was only partly condensed out, which made it necessary to assess this component in both gas and liquid phases, introducing additional experimental error. Permanent gas compositions could be analysed more accurately.

Because of the qualitative experimental results and the uncertainty whether the measured rates were truly chemically controlled, it was decided to use a differential tubular wall reactor to gain further, quantitative insight into the reaction pathways.

The experiments carried out in the tubular wall reactor only paint a partial picture of the reaction pathway, as only the initial reaction rates were measured. Reaction inhibition by products was not assessed. In the spinning basket reactor experiments, methane and carbon monoxide were detected as additional products. These two components were not in evidence in the tubular wall reactor experiments carried out. The probable cause for this is that the tubular wall reactor can be considered as a differential reactor whereas the operation of the spinning basket reactor was akin to an integral reactor. In order to assess the influence of reaction products on the reaction mechanism, additional experimental series would have to be carried out. In these series, hydrogen, water carbon dioxide, carbon monoxide and methane need to be fed into the reactor separately at varying partial pressures and temperatures alongside with methanol and oxygen at fixed partial pressures. The results of these series would give the information required to quantify the influence of the reaction products on the reaction rates. Time constraints in the project schedule did not allow for these investigations to be carried out.

Experiments carried out in differential reactors require a high analytical accuracy, due to the low conversions required by this mode of operation. This high level of accuracy could not be met in the composition measurements of all components, especially the reactants. Carbon dioxide and water production rates could be measured with satisfactory accuracy. These two rates together with the stoichiometry of the proposed reaction mechanism allowed the description of the initial rates of this overall reaction (described by Equations 7.10 and 7.11) in terms of a power law according to Equation 7.19.

If the experiments carried out at increasing oxygen partial pressure in the spinning basket reactor and the tubular wall reactor are compared, a similar qualitative behaviour of the product rates for water, hydrogen and carbon dioxide can be observed. Consider the water production rates shown in Figures 7.11 and 7.29 for the spinning basket reactor and the tubular wall reactor, respectively. In both cases the rate increases with increasing oxygen partial pressure along a concave curve. This behaviour can be explained with the increasing amount of oxygen available so that the combustion reaction is favoured. As a result, the hydrogen production rates (Figures 7.7 and 7.27) decrease with increasing oxygen partial pressure. The carbon dioxide production rate shows a linear increase with increasing oxygen partial pressure in the tubular wall reactor (Figure 7.28) whilst a convex curve is observed in the spinning basket reactor. The rate increase is probably caused by the increase of oxygen reactant. The convex shape in the case of the spinning basket reactor is probably attributable to a water gas shift reaction (Equation 7.21).

The system behaviour for varying methanol partial pressure was only investigated in the tubular wall reactor. The carbon dioxide production rate (Figure 7.23) decreases with increasing methanol partial pressure, as less oxygen becomes available. Both hydrogen and water production rates (Figures 7.22 and 7.24) increase with increasing methanol partial pressure. This is caused by the increased hydrogen availability. The increase in

water production rate is less pronounced as less oxygen is present at high methanol partial pressures.

CHAPTER 8

MEMBRANE REACTOR EXPERIMENTS

8.1 Permeation characteristics of membranes used

The single component transport properties of the investigated membranes were assessed in terms of permeances which are defined according to:

$$P_i = \frac{N_i}{A\Delta p} \tag{8.1}$$

In Equation 8.1, A is the permeation area of the membrane, N_i the molar flowrate through the membrane and Δp the pressure drop across the membrane. The difference between permeance and permeability is that the latter contains the membrane thickness in its definition. Most permeation values in the literature are reported in terms of the permeance, hence this value is used in this study.

In order to carry out the permeation experiments, the membrane was mounted into the reactor in the usual manner (see Chapter 3). The shellside feed and the tubeside exit valves were then blocked. Thus all the gas entering the reactor through the tubeside feed was forced through the membrane and left the reactor by means of the shellside exit. For the permeation experiments carried out here only one gas was fed into the reactor by means of one of the mass flow controllers. Hence the flowrate was determined from the calibration data of this mass flow controller. The pressure in the system was altered using the needle valve in the shellside exit line.

8.1.1 Permeance of the commercial SCT membrane

The geometrical and structural data of the SCT T1-150 membranes used in this study are given in Section 6.3. Figure 8.1 shows the measured permeances for N_2, Ar, CO_2 and H_2 for this membrane as a function of the average pressure. The measurements were carried out at a temperature of 14.5°C, average pressures between 1.2 and 2bar and transmembrane pressure drops of 0.08 and 0.35bar. Table 8.1 compares the hydrogen and nitrogen permeances with those measured by Jia *et. al.* (1994).

Table 8.1: Measured and literature permeances

	Permeance [10^{-6} mol/(m^2 s Pa)]	
Component	This study (average value)	Jia *et al.* (1994)
N_2	6.78	6.73
H_2	20.70	21.70

As can be seen from Table 8.1, the H_2 and N_2 permeances measured in this study agree with those reported by Jia *et. al.* (1994) for the same membrane. This indicated that the membrane is sealed properly into the reactor.

Experiments were conducted over a range of pressures. It can be seen from Figure 8.1, that the permeance increases with an increase in pressure.

It is commonly assumed that the only transport mechanism in the type of membrane investigated is Knudsen diffusion. Equation 8.2 shows the relationship between the flux caused by Knudsen diffusion and the system parameters:

$$N''_{K,i} = -\frac{4}{3} d_P \sqrt{\frac{R_G T}{2\pi M_i}} \frac{1}{R_G T} \frac{\partial p_i}{\partial r} \qquad (8.2)$$

In Equation 8.2, N''_{Ki} is the Knudsen diffusion flux, d_P the pore diameter, R_G the gas constant, T the temperature, M_i the molecular weight, p_i the partial pressure and r the radial co-ordinate.

It is evident that Knudsen diffusion fluxes are only dependent on the pressure gradient but not on the absolute pressure.

The pressure dependence indicates that viscous flow is of importance. The flux of an ideal gas caused by viscous flow is given by:

$$N''_{visc} = -\left(\frac{p r_P^2}{8 \mu R_G T}\right) \frac{\partial p}{\partial r} \tag{8.3}$$

In Equation 8.3, N''_{visc} is the viscous flux, p the total pressure and r_p the pore radius.

Equation 8.3 shows that viscous flow is increasing with increasing absolute pressure. Thus, it can be concluded that viscous flow contributes to the transport phenomena inside the porous membrane structure.

Another result contradicting the Knudsen flow assumption is the high CO_2 permeance. Carbon dioxide has the highest molecular weight of the investigated gases and should consequently have the lowest permeance if Knudsen flow were the only transport mechanism, which is clearly not the case. One possible explanation for the high permeance of carbon dioxide is surface diffusion. This phenomenon occurs when molecules adsorbed on a surface "hop" from surface site to surface site along a gradient of unoccupied sites (Kast, 1988). As carbon dioxide is more strongly adsorbed on γ-alumina than the other species investigated and the temperature at which the experiments

were carried out was low (14.5°C), and hence favouring adsorption, surface diffusion is expected to have contributed to the observed high carbon dioxide permeance.

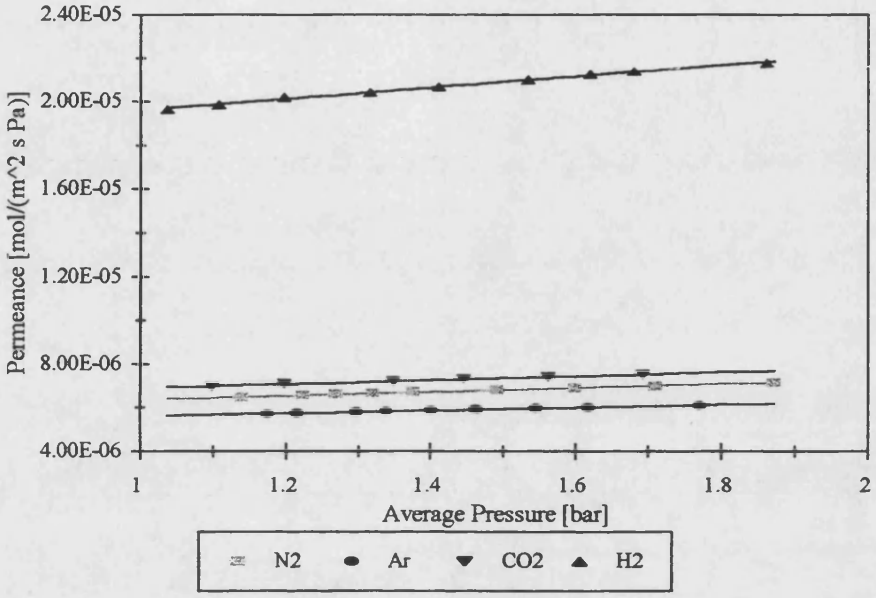

Figure 8.1: Permeances of different components in SCT membrane

8.2 Separation of multicomponent gas mixtures in porous membranes

The membrane used for the separation experiments was the commercial SCT membrane as described in Section 6.4. The membrane was mounted into the reactor housing as described in Chapter 3. Mixtures of hydrogen, nitrogen and either carbon dioxide or methane were fed by means of three mass flow controllers into the tubeside of the reactor. A fourth mass flow controller supplied the argon purge gas to the shellside. A total of 10 experiments was carried out, the feed conditions of which are listed in Table 8.2.

Table 8.2: Feed conditions of separation experiments

Exp	Tubeside						Shellside		
			Composition				pure Ar		
	$N_{F,t}$ [10^{-3} mol/s]	Re	H_2	N_2	CO_2	CH_4	$N_{F,s}$ [10^{-3} mol/s]	Re	$N_{F,s}/N_{F,t}$
Sep-1	1.3744	162	0.068	0.673	0.259	-	3.7107	143	2.693
Sep-2	2.0609	243	0.068	0.673	0.259	-	3.7107	143	1.796
Sep-3	2.7495	324	0.068	0.673	0.259	-	3.7107	143	1.346
Sep-4	4.1184	487	0.068	0.673	0.259	-	3.7107	143	0.899
Sep-5	5.4923	649	0.068	0.673	0.259	-	3.7107	143	0.676
Sep-6	1.3734	133	0.068	0.673	-	0.259	3.7107	143	2.702
Sep-7	2.0609	199	0.068	0.673	-	0.259	3.7107	143	1.801
Sep-8	2.7474	265	0.068	0.673	-	0.259	3.7107	143	1.351
Sep-9	4.1168	397	0.068	0.673	-	0.259	3.7107	143	0.901
Sep-10	5.4922	530	0.068	0.673	-	0.259	3.7107	143	0.676

All these experiments were carried out at a temperature of 150°C, a feed side pressure of 1.08 to 1.09bar, a transmembrane pressure drop of 0.025bar and using co-current mode of flow. The shellside needle valve was left fully open whilst the tubeside needle valve was used to control the transmembrane pressure. The Reynolds number in Table 8.2 was calculated according to Equation 8.4 at the physical properties of the feed streams.

$$Re = \frac{v\rho d_h}{\mu} \tag{8.4}$$

Here d_h is the hydraulic diameter which is, for the tubeside, the internal diameter of the membrane. For the shellside it was calculated according to (Renz 1989):

$$d_h = \frac{4 \text{ cross sectional area}}{\text{wetted circumference}} = d_{inner,shell} - d_{outer,tube} \tag{8.5}$$

The results are reported in terms of separation factors in Figures 8.2 and 8.3. The separation factors are defined with nitrogen as the reference component according to:

$$\alpha_{i,ref} = \frac{\left(y_i / y_{ref}\right)_{Shellside}}{\left(y_i / y_{ref}\right)_{Tubeside}} \tag{8.6}$$

In these figures the ideal Knudsen separation factor is also shown. It is defined as (Rautenbach, 1991):

$$\alpha_{K,i,ref} = \sqrt{M_{ref} / M_i} \tag{8.7}$$

The ideal separation factor is derived with the assumption that Knudsen diffusion is the only transport mechanism and that contributions to mass transfer behaviour by the boundary layers and by molecular diffusion and viscous flow in the membrane are of no influence. The results are given in terms of compositions in Table 8.3.

Figures 8.2 and 8.3 show that for both mixtures considered the hydrogen separation factor is approaching its ideal value for decreasing feed flowrates. The carbon dioxide separation factor has already reached its ideal value in experiments Sep-1 to 5, whilst the measured methane separation factor is consistently lower than the ideal value.

The deviation between the ideal Knudsen separation factor and the measured values show that the common assumption that Knudsen diffusion is the only transport mechanism of importance in membranes of the type investigated is clearly not justified. Other mass transfer resistances have to be considered in order to explain the experimentally observed behaviour. These consist of resistances in the boundary layers

between the bulk gas and the membrane surface on tube- and shellside of the membrane and the influences of molecular diffusion and viscous flow inside the porous structure. In Chapter 9, a model for the separation of multicomponent gas mixtures in porous membranes is developed. The model considers the different mass transfer resistances. The model allows a more detailed discussion and quantification of the different mass transport phenomena.

Table 8.3: Results of separation experiments

			Composition [Mole fractions]				
		N_P [10^{-3} mol/s]	H_2	N_2	CO_2	CH_4	Ar
Sep-1	Tubeside	1.1827	0.025	0.482	0.199	-	0.261
	Shellside	3.9473	0.019	0.099	0.033	-	0.833
Sep-2	Tubeside	1.9080	0.033	0.539	0.256	-	0.182
	Shellside	4.0491	0.023	0.105	0.050	-	0.821
Sep-3	Tubeside	2.6047	0.040	0.561	0.221	-	0.140
	Shellside	4.0039	0.026	0.108	0.035	-	0.812
Sep-4	Tubeside	4.0019	0.045	0.593	0.229	-	0.097
	Shellside	4.0480	0.029	0.111	0.035	-	0.807
Sep-5	Tubeside	5.3473	0.049	0.606	0.233	-	0.074
	Shellside	3.9890	0.031	0.112	0.035	-	0.796
Sep-6	Tubeside	1.1332	0.026	0.501	-	0.185	0.277
	Shellside	4.0570	0.020	0.105	-	0.043	0.838
Sep-7	Tubeside	1.8487	0.034	0.552	-	0.209	0.191
	Shellside	4.0510	0.024	0.111	-	0.047	0.822
Sep-8	Tubeside	2.5579	0.039	0.580	-	0.222	0.147
	Shellside	4.1153	0.027	0.115	-	0.049	0.818
Sep-9	Tubeside	3.9860	0.045	0.606	-	0.236	0.100
	Shellside	4.0955	0.029	0.118	-	0.050	0.809
Sep-10	Tubeside	5.3441	0.051	0.618	-	0.244	0.076
	Shellside	4.1208	0.030	0.119	-	0.052	0.805

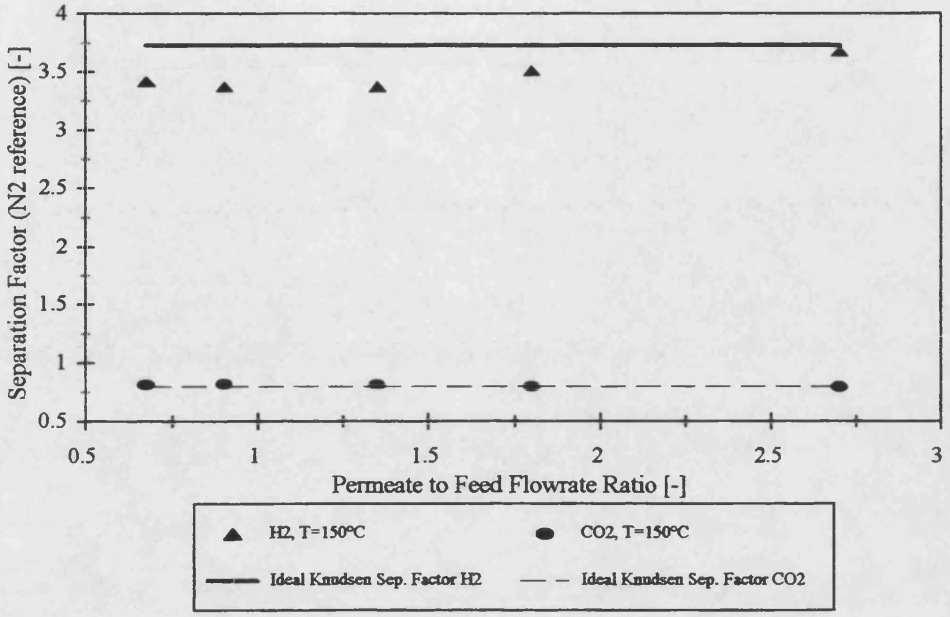

Figure 8.2: Separation factors experiments Sep-1 to 5

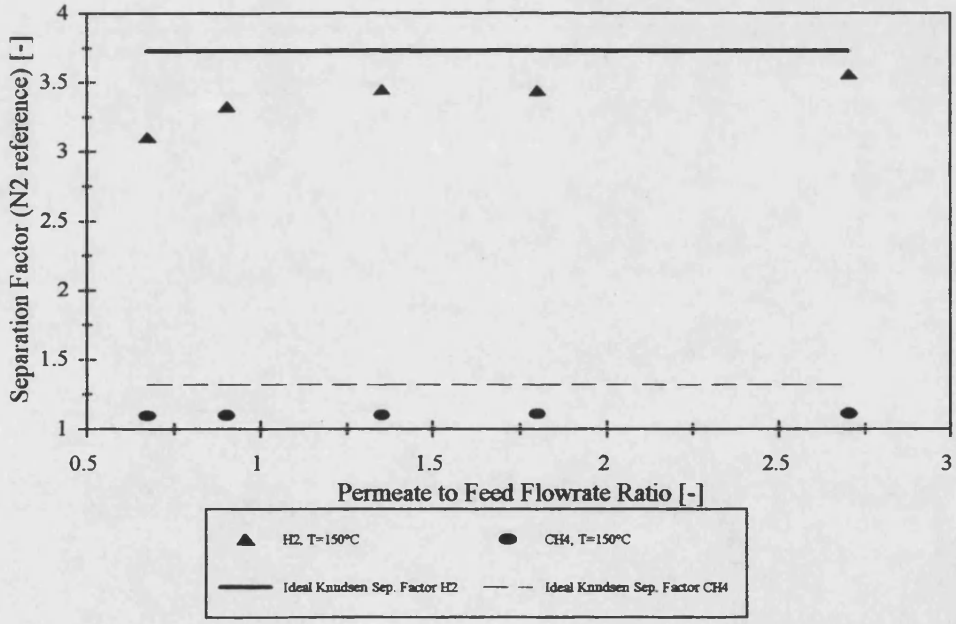

Figure 8.3: Separation factors experiments Sep-6 to 10

8.3 Membrane reactor experiments

For the membrane reactor experiments a platinum impregnated SCT T1-150 membrane was used. The preparation of the membrane was described in Chapter 6. The catalytic membrane was mounted into the membrane reactor as described in Chapter 3. The purpose of the experiments was to investigate the combined reaction and separation behaviour of the catalytic membrane reactor under varying operating conditions. The varied operation parameters chosen in this study were the purge to feed flowrate ratio and the transmembrane pressure drop. The reactions carried out in the reactor were the oxidative dehydrogenation of methanol as the principal reaction and associated parallel and consecutive reactions. The reaction pathway and the reaction kinetics are discussed in Chapter 7. The purpose of carrying out this reaction in a membrane reactor was to produce and separate hydrogen within one process unit in order to supply a hydrogen feedstock for possible use in a fuelcell.

As opposed to the flexible polymer based "O"-ring seals employed in the separation experiments described in Section 8.2, the catalytic membrane reactor experiments were carried out using graphite "O"-rings. It was necessary to use this type "O"-ring as it withstands temperatures in excess of 300°C as indeed observed in the catalytic membrane reactor experiments, whereas these temperatures exceed the upper operating temperature limit of the polymer based "O"-rings. Graphite based "O"-rings have a higher potential to leakage owing to its material structure. In order to test whether the seals had been compromised whilst the experiments were carried out, the nitrogen permeance through the membrane was measured in the same way as described in Section 8.1 before and after the use of the membrane in a reacting environment. Figure 8.4 shows the measured permeances. It is apparent that the nitrogen permeance is slowly increasing with an increasing number of experiments carried out. This indicates a deterioration of the seals or a widening of the membrane pore structure. The occurrence of the latter is unlikely, as the pore structure of γ-alumina is only affected by temperatures in excess of

600°C (Chanaud 1995). The experiments conducted during the course of this study never resulted in temperatures exceeding 600°C.

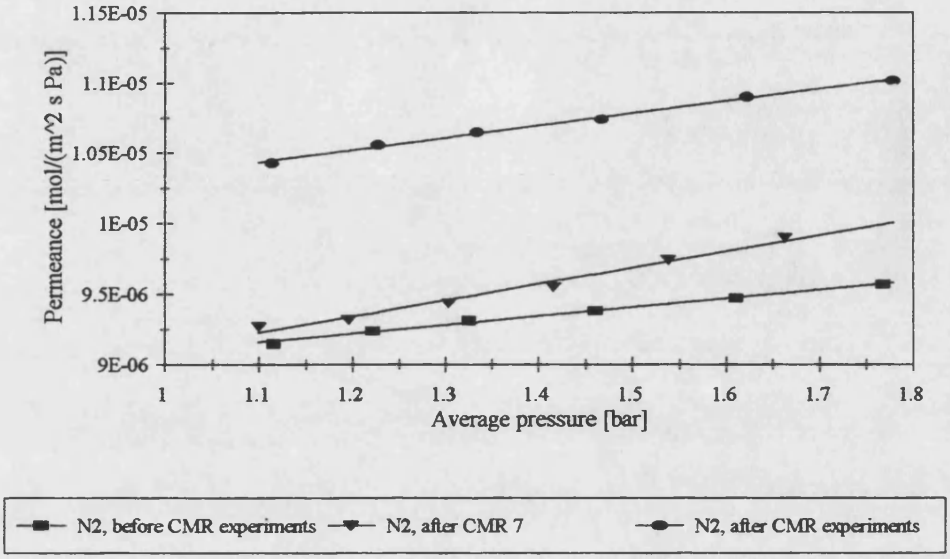

Figure 8.4: Change of catalytic membrane permeance as a function of catalytic experiments

All experiments were carried out in co-current mode, *e. g.* reactant and purge gas feed entered the membrane reactor from the same side. The reactants were supplied to the tubeside whilst the purge gas (argon) was supplied to the shellside.

Table 8.4 gives the feed parameters which were kept constant for all experiments whilst Table 8.5 lists the feed parameters that were varied.

Table 8.4: Constant feed parameters

Tubeside (Reactant feed)		
Molefractions	Methanol	0.1423
	Oxygen	0.0725
	Nitrogen	0.7852
Temperature [°C]		275.0000
Shellside (Purge gas feed)		
Flowrate [mol/min]		0.2229
Molefractions	Argon	1.0000
Temperature [°C]		275.0000
Pressure		atmospheric

Experiments CMR4 to CMR12 were carried out to investigate the influence of varying transmembrane pressure drop on measured methanol conversion, selectivity towards hydrogen and separation factor. The influence of changing purge to feed flowrate ratios was investigated with experiments CMR12 to CMR16. Figure 8.5 and 8.6 show, respectively, the changes in methanol conversion and in selectivity of the converted methanol towards hydrogen as a function of transmembrane pressure drop. Figure 8.7 shows the separation factors evaluated according to Equation 8.6.

Table 8.5: Varied feed parameters

Experiment	Tubeside pressure [bar]	Pressure difference [bar]	Tubeside flowrate [mol/min]
CMR4	1.08123	0.01177	0.22342
CMR5	1.24960	0.13575	0.22342
CMR7	1.07508	0.00648	0.22342
CMR8	1.16920	0.07370	0.22342
CMR9	1.07240	0.00653	0.22342
CMR11	1.21003	0.09901	0.22342
CMR12	1.11920	0.04466	0.22342
CMR14	1.13543	0.04653	0.15658
CMR15	1.13426	0.04918	0.20103
CMR16	1.13335	0.04690	0.17862

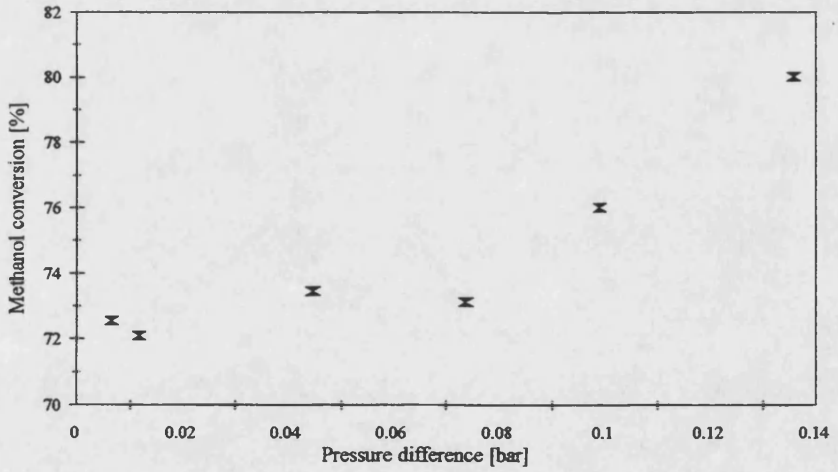

Figure 8.5: Methanol conversion as function of transmembrane pressure drop

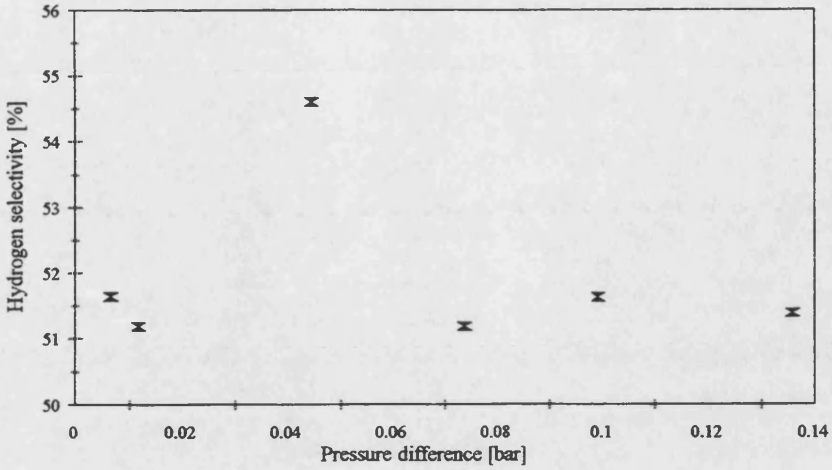

Figure 8.6: Selectivity towards hydrogen as function of transmembrane pressure drop

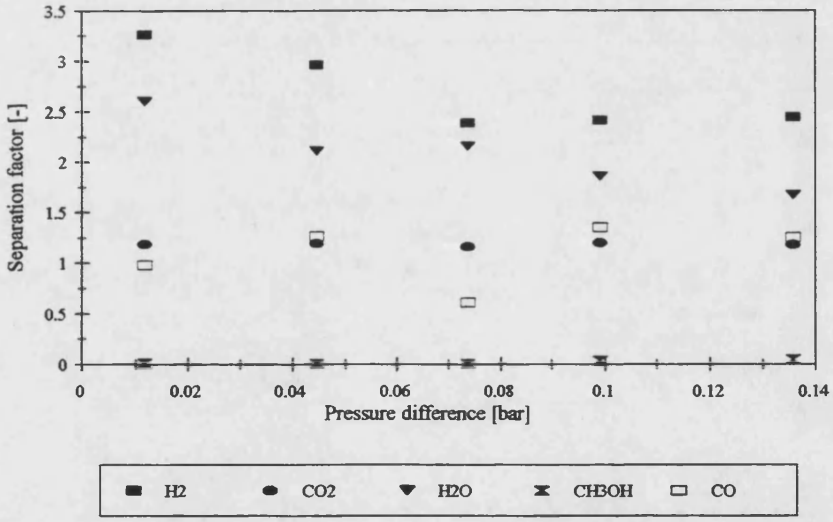

Figure 8.7: Separation factors as a function of the transmembrane pressure drop

Figure 8.8 shows the alteration of the measured axial temperature profiles with changing transmembrane pressure difference.

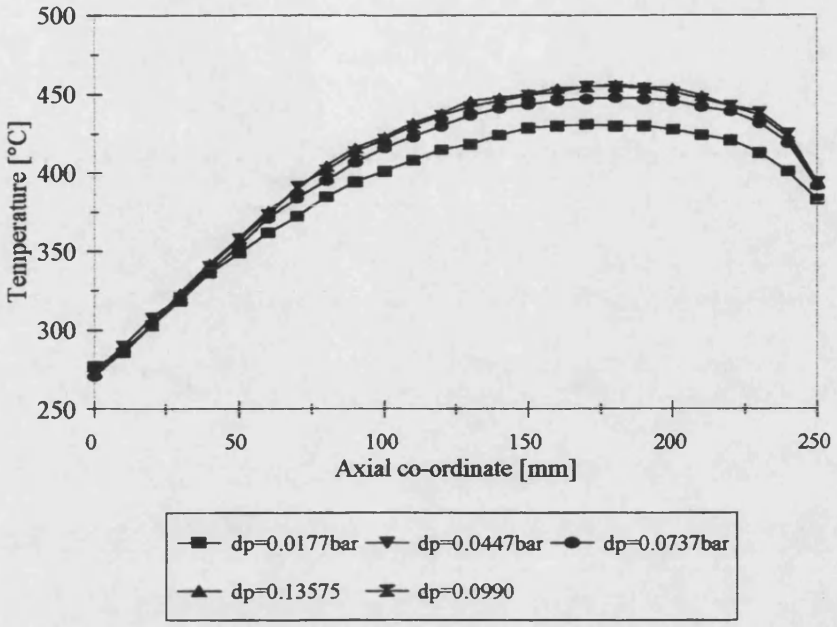

Figure 8.8: Axial temperature profiles as a function of varying transmembrane pressure difference

Figures 8.9 to 8.11 show the methanol conversion, selectivity towards hydrogen and separation factors as functions of the purge to reactant feed flowrate ratio, respectively. The measured temperature profiles of these experiments are shown in Figure 8.12.

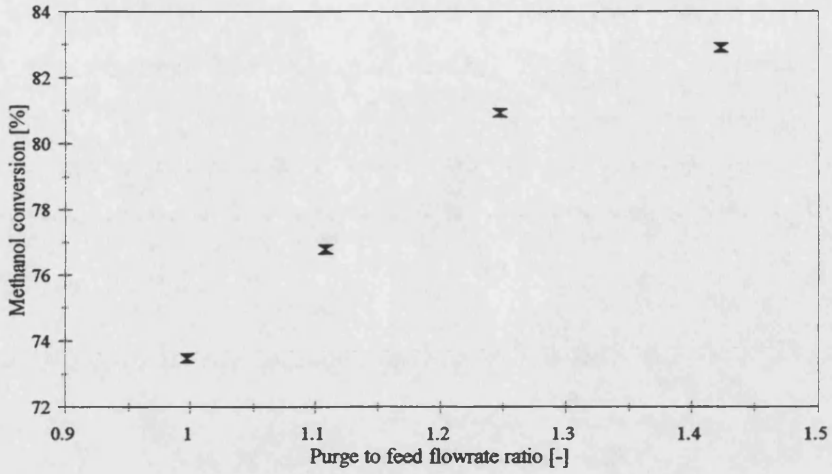

Figure 8.9: Methanol conversion as a function of purge to feed flowrate ratio

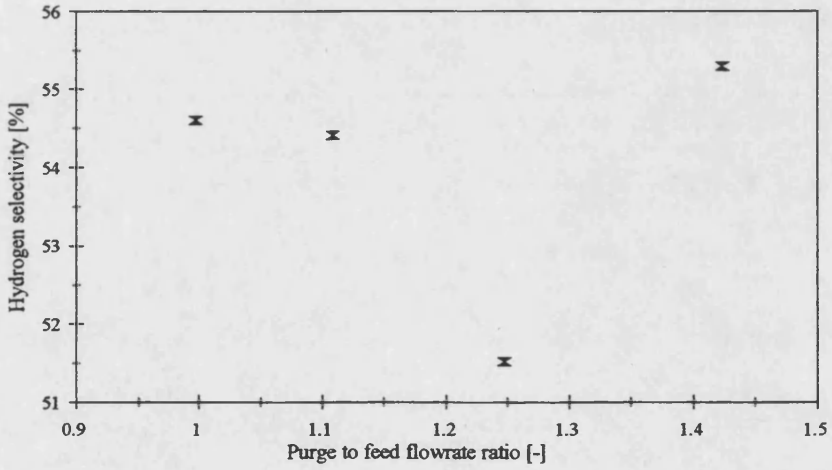

Figure 8.10: Selectivity towards hydrogen as a function of purge to feed flowrate ratio

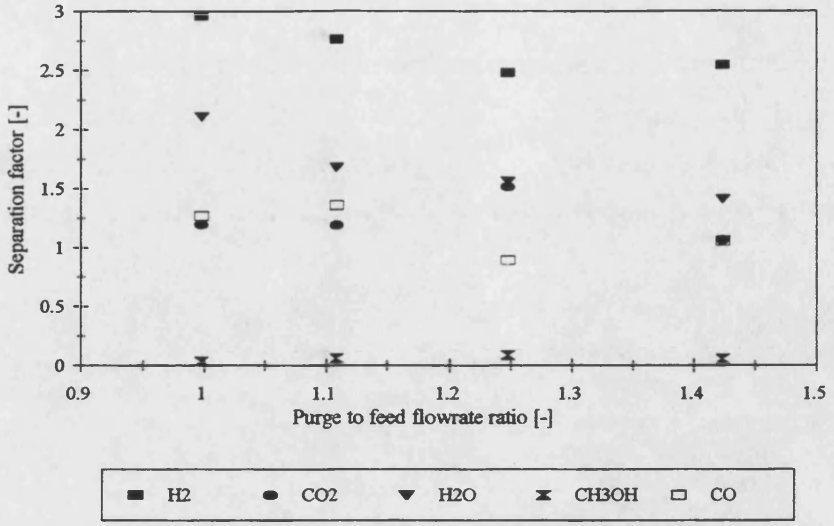

Figure 8.11: Separation factors as a function of purge to feed flowrate ratio

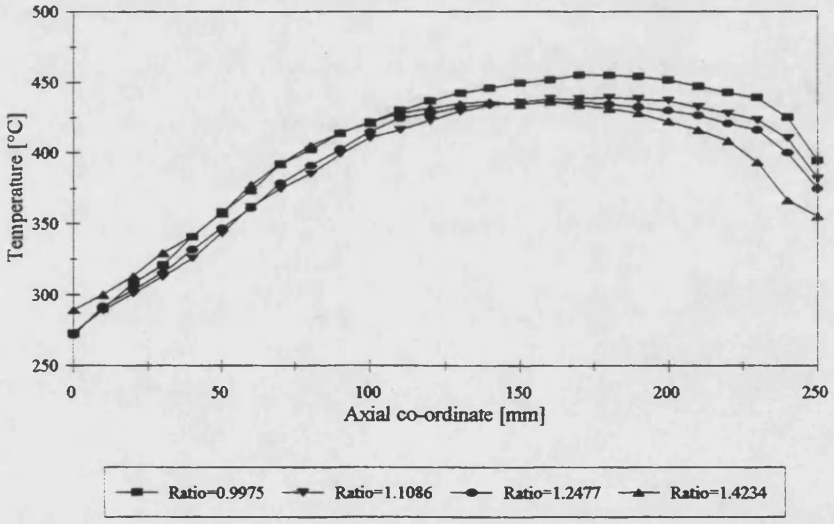

Figure 8.12: Axial temperature profiles as a function of purge to feed flowrate ratio

Table 8.6 shows the measured product molefractions for all components detected in the experiments as well as the product flowrates.

Table 8.6: Product molefractions and flowrates, T and S indicate tube- and shellside, respectively

Exp		N_P [mol/min]	Composition [Molefractions]							
			CH_3OH	O_2 and Ar	N_2	H_2	H_2O	CO_2	CO	CH_4
CMR4	T	0.2441	0.0360	0.2183	0.6042	0.0534	0.0200	0.0440	0.0227	0.0013
	S	0.2427	0.0003	0.7764	0.1490	0.0430	0.0128	0.0129	0.0055	0.0005
CMR5	T	0.1664	0.0346	0.1685	0.6299	0.0566	0.0296	0.0464	0.0328	0.0015
	S	0.3213	0.0018	0.6540	0.2371	0.0521	0.0187	0.0207	0.0156	0.0004
CMR7	T	0.2414	0.0342	0.2112	0.6052	0.0554	0.0254	0.0433	0.0239	0.0013
	S	0.2443	0.0004	0.7738	0.1490	0.0448	0.0120	0.0129	0.0072	0.0004
CMR8	T	0.1964	0.0410	0.1932	0.6108	0.0562	0.0229	0.0445	0.0299	0.0014
	S	0.2835	0.0017	0.7086	0.2045	0.0450	0.0166	0.0173	0.0062	0.0004
CMR9	T	0.2372	0.0364	0.2222	0.5898	0.0580	0.0229	0.0443	0.0254	0.0010
	S	0.2382	0.0003	0.7747	0.1509	0.0423	0.0130	0.0125	0.0063	0.0004
CMR11	T	0.1733	0.0395	0.1665	0.6378	0.0557	0.0264	0.0444	0.0284	0.0013
	S	0.3080	0.0025	0.6599	0.2357	0.0497	0.0182	0.0198	0.0143	0.0003
CMR12	T	0.2177	0.0373	0.2023	0.6042	0.0566	0.0250	0.0436	0.0298	0.0013
	S	0.2660	0.0012	0.7287	0.1784	0.0496	0.0156	0.0154	0.0112	0.0004
CMR14	T	0.1329	0.0262	0.2335	0.5774	0.0565	0.0319	0.0476	0.0255	0.0014
	S	0.2736	0.0012	0.7225	0.1889	0.0471	0.0147	0.0166	0.0089	0.0002
CMR15	T	0.1833	0.0336	0.1988	0.6097	0.0565	0.0292	0.0447	0.0262	0.0013
	S	0.2686	0.0018	0.7066	0.1966	0.0505	0.0158	0.0172	0.0115	0.0004
CMR16	T	0.1587	0.0273	0.2380	0.5856	0.0560	0.0298	0.0349	0.0270	0.0014
	S	0.2728	0.0019	0.7222	0.1904	0.0452	0.0152	0.0172	0.0079	0.0003

8.3.1 Discussion of membrane reactor experiment results

Figures 8.5 and 8.9 show that the conversion of methanol is increasing as a function of increased transmembrane pressure drop or purge to feed flowrate ratio, respectively. An increase of either of these operation parameters leads to an increase in the transmembrane driving force. In the case of an increased transmembrane pressure, viscous flow forces more reactants into the porous membrane structure and hence leads to an increase in conversion. An increase in purge to feed flowrate ratio results in increased partial pressure gradients for the reactants and hence higher Knudsen and Maxwellian diffusive fluxes. As in the case of increased transmembrane pressure drop, more reactants can enter the catalytically active region and hence cause an increase in conversion.

The selectivity of the converted methanol towards hydrogen does not change significantly as a function of increased transmembrane pressure drop or purge to feed flowrate ratio (Figures 8.6 and 8.10, respectively). As more reactants enter the catalytically active membrane structure, a decrease in hydrogen selectivity would be expected due to the increased amount of reactants inside the membrane structure. This increased amount of reactants would cause an increase in the extent of parallel reactions. The kinetic experiments reported in Chapter 7 showed that these additional reactions decreased the selectivity towards hydrogen. Examples of these reactions are the catalytic combustion of hydrogen and the water gas shift reaction. However, the diffusional transport rates of hydrogen inside the porous membrane structure and in the adjacent boundary layers are higher than those of all the other components present: hydrogen is transported away from the catalytically active zone more easily than other reactants. Thus it is not available as a reactant for any parallel reactions. An analogous behaviour was observed in the spinning basket reactor experiments carried out with a low speed of revolution.

The separation behaviour of the membrane reactor is shown in Figures 8.7 and 8.11 for increasing transmembrane pressure drop and increasing purge to feed flowrate ratio, respectively. In both cases the hydrogen and water separation factors decrease with increasing driving force, whilst those of other reaction components increase or remain approximately constant. In the case of increasing transmembrane pressure drop, this behaviour can be explained by an increased viscous flow contribution to the total transmembrane flux. As viscous flow is non-separative, heavier components are also forced through the membrane. An increase in purge to feed flowrate ratio results in increased driving forces for all components present and hence to a decrease of the separation factors for the lighter components. A further important result was that the carbon monoxide-nitrogen separation factor was greater than one for all the investigated cases. As carbon monoxide poisons fuelcell electrodes, an important operational requirement for a membrane reactor supplying the feedstock for such an unit is to ensure that only trace amounts of carbon monoxide are present.

The axial temperature profiles illustrated in Figures 8.8 and 8.12 show the profile expected for an exothermic reaction network. The temperature levels were not strongly influenced by any changes in operating conditions. However, an increase of temperature was observed with increasing transmembrane pressure drop (Figure 8.8). This can be explained by the increased conversion as depicted in Figure 8.5. The temperature behaviour observed with increasing purge to feed flowrate ratio is shown in Figure 8.12. With increase in flowrate the temperature level decreased. This behaviour appears to contradict any expected simultaneous increase in temperature due to conversion. It can be explained by an increased amount of energy transported out of the reactor by the increased purge gas flowrate.

8.4 Conclusions of the separation and reaction experiments

The separation experiments described in Section 8.2 clearly show that only a low degree of separation can be achieved using the type of membrane employed in this study. In order to obtain high purity hydrogen from a multicomponent gas stream, the membrane pore size would have to be smaller than used for the experiments reported herein. The membrane employed in this study had a pore size of 4nm. Smaller pore sizes could be achieved using silica or zeolite membranes. None of these membranes were commercially available in the course of this study. Additionally, zeolite membranes are likely to exhibit a pore blocking effect when used to separate hydrogen from hydrocarbon mixtures. This is caused by the affinity of many hydrocarbons for the active surface sites of zeolites and consequently leads to adsorption of the hydrocarbons and thus to a blocking of the hydrogen diffusion path. Another possibility is to employ a dense palladium or palladium alloy layer as the active membrane layer. Palladium and its alloys are known to be only permeable to hydrogen and not any other gases. However, this type of membrane is expensive and requires a high transmembrane pressure drop. Furthermore, the known catalytic activity of palladium might give rise to undesired reactions. In order to separate hydrogen from hydrocarbons, other processes, as for example pressure swing adsorption with product purities of higher than 99%, are superior to inorganic membrane processes.

The membrane reactor experiments showed a high conversion of methanol (72 to 84%) and a satisfactory selectivity of converted methanol towards hydrogen (52 to 55%), considering the complex reaction network. Mass transfer resistances in the porous membrane structure as well as in the adjacent boundary layers appear to increase the selectivity towards hydrogen. A similar behaviour was observed in the catalyst screening experiments reported in Chapter 5 and in the spinning basket reactor experiments reported in Chapter 7. In contrast the tubular wall reactor experiments described in Chapter 7 showed a higher selectivity towards water. In these experiments mass transfer resistances were minimised.

One of the detected reaction products was carbon monoxide. This component is known to deteriorate the electrodes of fuelcells. As the envisaged purpose of the membrane reactor is to supply a hydrogen feed stock for fuelcells, carbon monoxide has to be separated effectively from the product stream. This was not achieved in the experiments carried out.

The membrane reactor experiments carried out in this study showed that the oxidative dehydrogenation of methanol is a viable source of hydrogen. However, the separation behaviour of the membrane reactor is not sufficient to supply a high purity hydrogen feedstock. Further downstream processing is necessary to remove any undesired components.

CHAPTER 9

SIMULATION OF A CATALYTIC MEMBRANE REACTOR

9.1 Introduction

The membrane reactor considered is shown in Figure 9.1. The operating mode of the reactor is co-current, *e. g.* tube- and shellside streams flow in the same direction. In order to simulate such a unit, material and energy balances have to be solved for the tube- and the shellside. These balances are coupled by the mass and energy fluxes through the membrane and the adjacent boundary layers. Figure 9.2 shows these transport processes. The fluxes inside the membrane are governed by the heat- and mass transfer resistances of the different membrane layers as well as by the chemical reactions inside the catalytically active layer.

The following assumptions were made:

- Negligible pressure drop in axial direction in both tube- and shellside.
- Ideal thermodynamic behaviour, *e. g.* the ideal gas law is valid.
- Negligible axial dispersion.
- Transport processes from and to the membrane interfaces through the boundary layers can be expressed by appropriate heat and mass transfer correlations. It is also assumed that plug flow conditions prevail in the flow on the tube- and shellside of the membrane.
- The boundary layer thickness can be considered negligible in comparison with the tube diameters.

9.2 Axial model set-up

The transport processes taking place in every differential element *dz* of the axial co-ordinate are depicted in Figure 9.2. The following differential equations describe the mass and heat transfer in the axial direction.

Material balance tubeside:

$$\frac{dN_{i,t,z}}{dz} = -\pi D_1 N''_{i,t};\ i = 1,\ldots,nc \tag{9.1}$$

Material balance shellside:

$$\frac{dN_{i,s,z}}{dz} = \pi D_2 N''_{i,s};\ i = 1,\ldots,nc \tag{9.2}$$

Energy balance tubeside:

$$\frac{dQ_{t,z}}{dz} = \sum_{i=1}^{nc}\left(N_i c_{v,i}\right)_{t,z} \frac{dT_{t,z}}{dz} = -\pi D_1 Q''_t \tag{9.3}$$

Energy balance shellside:

$$\frac{dQ_{s,z}}{dz} = \sum_{i=1}^{nc}\left(N_i c_{v,i}\right)_{s,z} \frac{dT_{s,z}}{dz} = \pi D_2 Q''_s - \pi D_3 Q''_W \tag{9.4}$$

The specific heat capacity at constant volume, $c_{v,i}$, can be expressed by:

$$c_{v,i} = c_{p,i} - R_G \tag{9.5}$$

In the above equation R_G is the universal gas constant and $c_{p,i}$ is the heat capacity at constant pressure, evaluated according to Equation 4.6 (see Chapter 4).

The mass and energy fluxes on the right-hand-sides of these equations are governed by the transport processes and the chemical reactions inside the membrane as well as the mass and heat transfer resistances imposed by the boundary layers which will be discussed in Sections 9.3 to 9.5.

Equations 9.1 to 9.4 amount to $2nc+2$ ordinary differential equations with $2nc+2$ unknowns - the temperature and the component molar flowrates for tube- and shellside of the reactor. This system of differential equations constitutes an initial value problem with the feed temperatures and the feed molar flowrates of the tube- and shellside as initial conditions. The system can be solved numerically using the Runge-Kutta method (Press *et. al.* 1992).

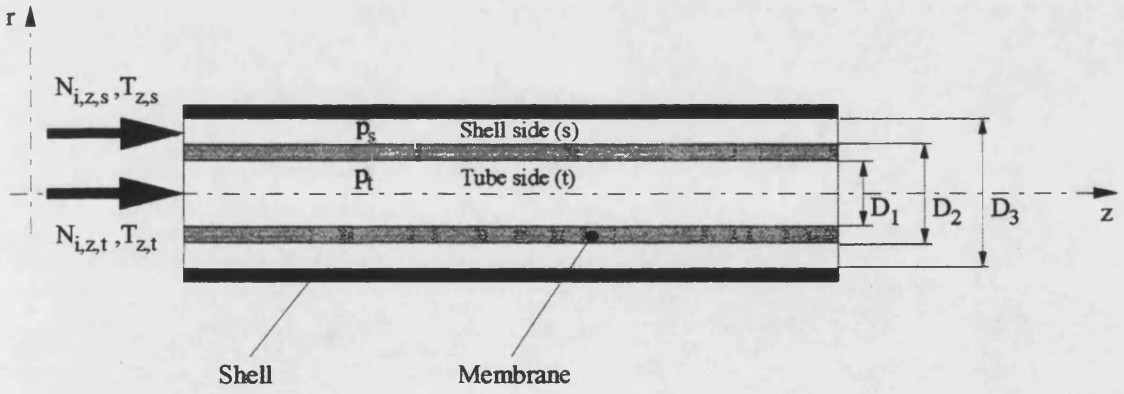

Figure 9.1: Catalytic membrane reactor

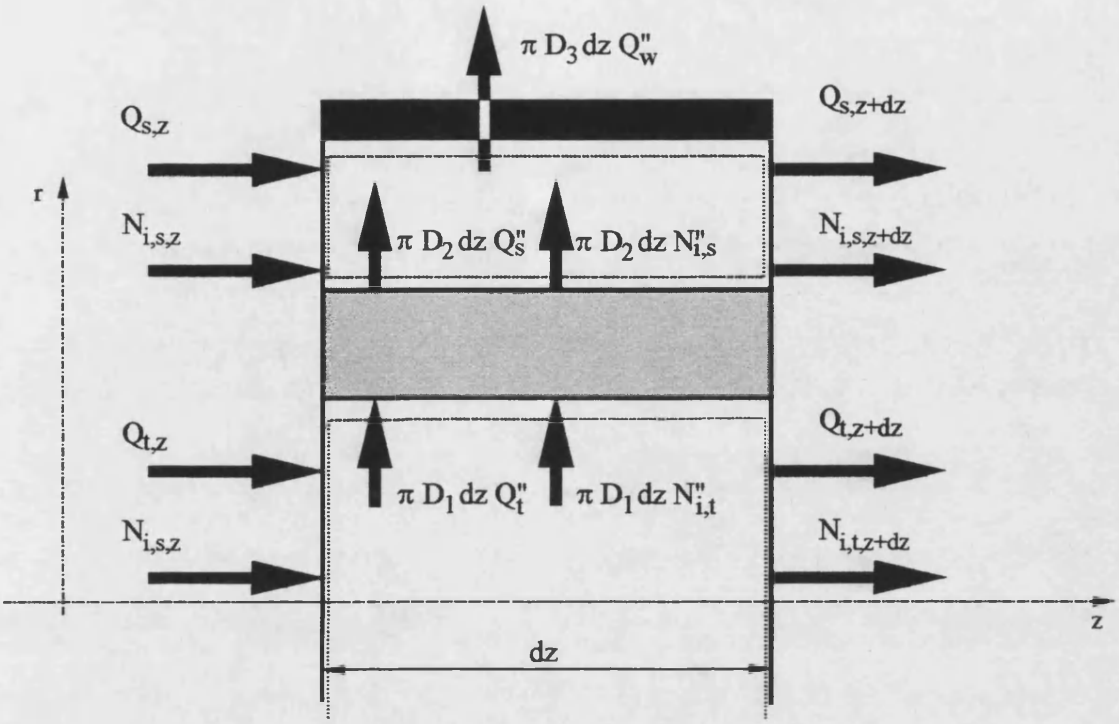

Figure 9.2: Radial and axial transport processes

9.3 Transport and reaction inside the membrane structure

Figure 9.3 shows the multilayered porous membrane structure considered in this study. The temperature profile shown is that for an exothermic reaction and the molefraction profile is that for a reactant fed from the shellside of the membrane. The reaction (or reactions) are assumed to take place only in the catalytically active layer. All the other layers are treated as inert. It is assumed that no homogenous chemical reactions occur. The three support layers increase in pore size towards the shellside. The commercial porous membrane used in this study has a structure of three support and one active layer as described in Section 6.4.

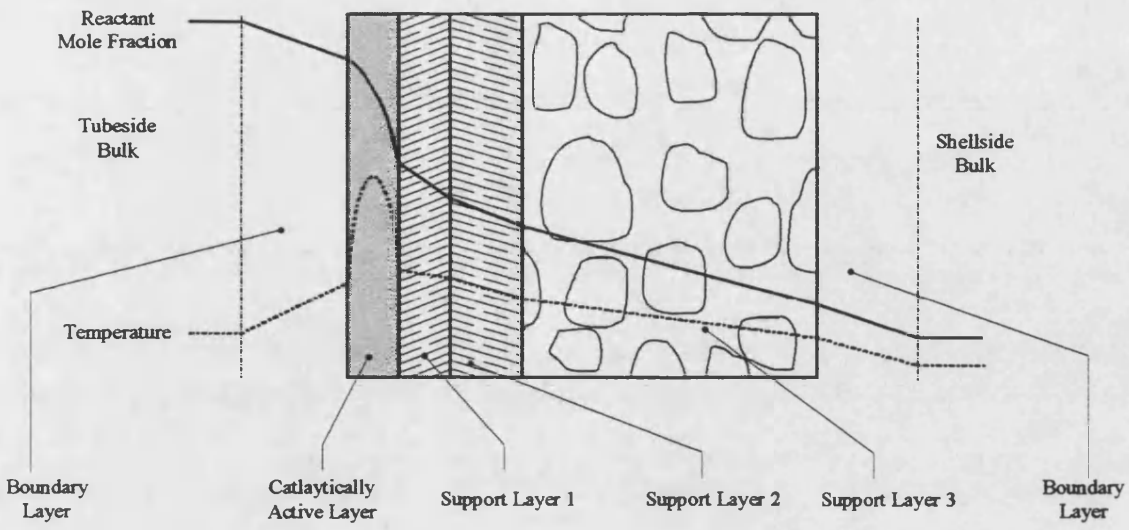

Figure 9.3: Supported catalytic membrane structure

In order to solve the axial mass and energy balances (Equations 9.1 to 9.4) the material and energy fluxes into the axial elements shown in Figure 9.2 have to be determined. They are governed by the transport resistances of the different membrane layers and the boundary layers adjacent to the membrane on the tube- and shellside as well as the chemical reactions inside the active layer. For non-adiabatic operation the heat transfer from the shellside through the reactor wall has to be considered as well. A rigorous model determining the required fluxes will be developed in the following sections.

9.3.1 Reaction and transport processes in the active membrane layer

The differential energy balance applicable to the catalytically active membrane layer written in radial co-ordinates given by Bird *et. al.* (1960):

$$\frac{1}{r}\frac{\partial}{\partial r}\left(r\lambda_{eff}\frac{\partial T}{\partial r}\right)+\sum_{j=1}^{nr}\left(-\Delta H_R\right)_j R_j = 0 \qquad (9.6)$$

In Equation 9.6 λ_{eff} is the effective thermal conductivity of the porous membrane material and the gas inside the pores. The summation term in Equation 9.6 adds up the heats of reactions generated by *nr* reactions. The temperature dependencies of the heats of reaction $\left(\Delta H_R\right)_j$ are given by Equation 4.5.

The material balances for all *nc* components written in radial co-ordinates (Bird *et. al.* 1960) are:

$$\frac{1}{r}\frac{\partial}{\partial r}\left(rN_i''\right) - \sum_{j=1}^{nr} v_{i,j} R_j = 0;\ i = 1,\ldots,nc \tag{9.7}$$

Here N_i'' is the flux of component i in the porous structure. The summation term accounts for the amount of i consumed or generated in each reaction j. A more convenient form for the numerical treatment of this equation is:

$$\frac{N_i''}{r} + \frac{\partial N_i''}{\partial r} - \sum_{j=1}^{nr} v_{i,j} R_j = 0;\ i = 1,\ldots,nc \tag{9.8}$$

The *nr* reaction rates R_j in Equations 9.7 and 9.8 are functions of temperature, pressure and composition. In this study only rate equations in the mass action law form according to Equation 9.9 were considered.

$$R_j = k_{0,j} \exp\left(\frac{E_{act,j}}{R_G T}\right) \prod_{i=1}^{nc} \left(y_i p\right)^{m_{i,j}} \tag{9.9}$$

A list of all the symobls used in the above equations together with their dimensions is given in the nomenclature.

The fluxes have to be determined by *nc* equations. The flux model used here is the Dusty Gas model (DGM), which is described in the next section.

9.3.2 Dusty Gas Model

The Dusty Gas Model describes the transport of a mixture of *nc* ideal gases through a porous medium. This porous medium is considered as the (*nc*+1) component of the mixture and whose molecules are fixed in space and hence have no velocity. The diffusional transport mechanisms are:

- Interactions between the molecule of species *i* and the pore wall: Knudsen diffusion (Figure 9.4)
- Interactions between molecules of species i and k: molecular or continuum diffusion (Figure 9.5)

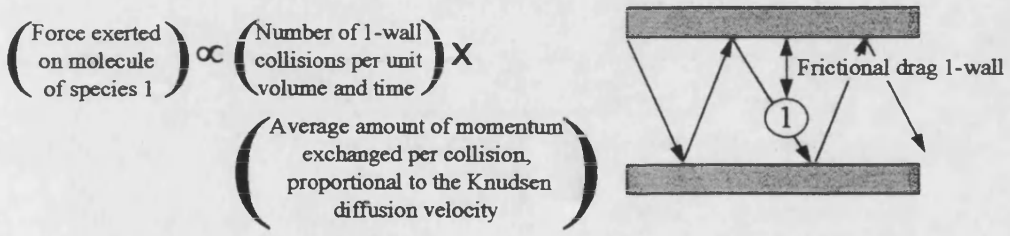

Figure 9.4: Derivation of the Dusty Gas Model: Knudsen diffusion

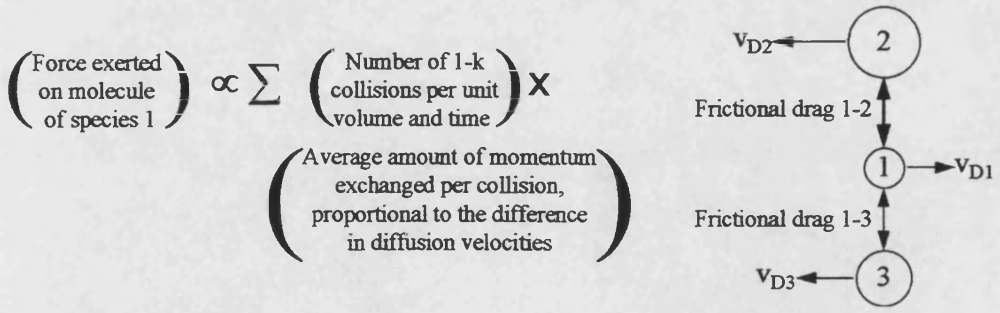

Figure 9.5: Derivation of the Dusty Gas Model: molecular diffusion (from Taylor and Krishna 1993)

Finally, the convective flow caused by a total pressure drop across the membrane is also considered.

The flux of component i in its conventional notation caused by Knudsen diffusion is (Kast 1988):

$$N''_{K,i} = -D_{K,i}\frac{1}{R_G T}\frac{\partial p_i}{\partial r} \tag{9.10}$$

A more convenient form than the above Equation 9.10 for use in the DGM is:

$$-\frac{1}{R_G T}\left(\frac{\partial p_i}{\partial r}\right)_{wall} = \frac{N''_{K,i}}{D_{K,i}} = \frac{c_i v_{K,i}}{D_{K,i}} \tag{9.11}$$

The partial pressure gradient in this equation represents the force exerted by the pore wall on a molecule of species i only.

The DGM is derived on the basis of the Maxwell-Stefan equations for multicomponent molecular diffusion. Taylor and Krishna (1993) give a sound derivation of the Maxwell-Stefan equations. Here, only the basic thoughts behind this derivation are given: the force exerted on a molecule of species i is proportional to the sum of collisions of molecules i with other molecules k of the mixture multiplied by the average amount of momentum exchanged in each of these collisions. Figure 9.5 depicts this behaviour graphically.

The partial pressure gradient caused by molecular diffusion can be expressed as:

$$-\frac{1}{R_G T}\left(\frac{\partial p_i}{\partial r}\right)_{molecule} = \frac{c_i c_2}{c_T D_{i,2}}\left(v_{D,i} - v_{D,2}\right) + \frac{c_i c_3}{c_T D_{i,3}}\left(v_{D,i} - v_{D,3}\right) + \frac{c_i c_4}{c_T D_{i,4}}\left(v_{D,i} - v_{D,4}\right) + \cdots \tag{9.12}$$

In Equation 9.12, the products $c_i c_k$ are proportional to the number of collisions between species i and k and the difference in diffusional velocity is proportional to the amount of momentum exchanged. The single terms of the summation on the right hand side of Equation 9.12 can be transformed into the more customary flux notation by:

$$\frac{c_i c_k}{c_T D_{i,k}}\left(v_{D,i}-v_{D,k}\right)=\frac{1}{D_{i,k}}\left(\frac{c_k}{c_T}c_i v_{D,i}-\frac{c_i}{c_T}c_k v_{D,k}\right)=\frac{1}{D_{i,k}}\left(y_k N''_{D,i}-y_i N''_{D,k}\right) \tag{9.13}$$

Comparing Equations 9.11 and 9.12 illustrates that the same thinking is behind both diffusional mechanisms described here. The two partial pressure gradients add up to the total partial pressure gradient exerted on component i whilst the two diffusional fluxes are the same (Mason and Malinauskas, 1983). This results in:

$$-\frac{1}{R_G T}\left(\frac{\partial p_i}{\partial r}\right)=\sum_{\substack{k=1\\k\neq i}}^{nc}\frac{\left(y_k N''_{D,i}-y_i N''_{D,k}\right)}{D_{i,k}}+\frac{N''_{D,i}}{D_{K,i}} \tag{9.14}$$

The total flux of component i is the sum of the diffusional flux and the viscous flux:

$$N''_i = N''_{D,i}+y_i N''_{visc} \tag{9.15}$$

The viscous flux can be expressed by the Poiseuille equation:

$$N''_{visc}=-\left(\frac{c_T B_0}{\mu}\right)\frac{\partial p}{\partial r} \tag{9.16}$$

Inserting

$$\frac{\partial p_i}{\partial r} = \frac{\partial (p y_i)}{\partial r} = y_i \frac{\partial p}{\partial r} + p \frac{\partial y_i}{\partial r} \tag{9.17}$$

as well as Equations 9.15 and 9.16 into Equation 9.14 produces:

$$\frac{p}{R_G T} \frac{\partial y_i}{\partial r} + \frac{y_i}{R_G T} \left(1 + \frac{B_0 p}{\mu D^e_{K,i}} \right) \frac{\partial p}{\partial r} = \sum_{\substack{k=1 \\ k \neq i}}^{nc} \frac{y_i N''_k - y_k N''_i}{D^e_{i,k}} - \frac{N''_i}{D^e_{K,i}} \tag{9.18}$$

Equation 9.18 is the Dusty Gas model in radial co-ordinates. Here, the Knudsen diffusion coefficient $D_{K,i}$ can be determined from either:

$$D_{K,i} = \frac{4}{3} d_P \sqrt{\frac{R_G T}{2\pi M_i}} \tag{9.19}$$

or single component permeation experiments. The molecular diffusion coefficient $D_{i,k}$ is determined from the kinetic theory of gases as described by Reid *et. al.* (1977) (see Appendix 7). The effective diffusion coefficients can be obtained using:

$$D^e_{K,i} = \frac{\varepsilon}{\tau} D_{K,i} \tag{9.20}$$

$$D^e_{i,k} = \frac{\varepsilon}{\tau} D_{i,k} \tag{9.21}$$

where ε and τ are the porosity and the tortuosity of the porous medium respectively. The porosities of the different layers of the SCT membrane used in this study are given in

Chapter 6. The tortuosity can be expressed according to the following assumption (Froment and Bischoff 1990):

$$\tau = \frac{1}{\varepsilon} \tag{9.22}$$

where ε is the porosity.

The Poiseuille constant B_0 can be evaluated from either:

$$B_0 = \frac{\varepsilon}{\tau} \frac{r_P^2}{8} \tag{9.23}$$

or from single component permeation experiments.

9.3.3 The system of equations

The energy balance Equation 9.6, the *nc* mass balances Equation 9.8 and the *nc* fluxes determined by the DGM Equation 9.18 constitute a system of $2nc+1$ ordinary differential equations. The equations introduced in sections 9.3.1 and 9.3.2 were derived from the general differential energy and material balances in radial co-ordinates (Bird *et. al.* 1960), which contain one time and three spatial dimensions and hence are expressed mathematically by partial differential equations. As only the radial direction is of interest in the context of this study and the developed model only considered steady state operation, the system of partial differential equations can be reduced to a system of ordinary differential equations. The number of variables sums up to $2nc+2$: temperature, pressure, *nc* molefractions and *nc* molar fluxes. Hence there is one equation missing before the system of equations can be solved. This equation is supplied by the summation of mole fractions:

$$\sum_{i=1}^{nc} y_i = 1 \tag{9.24}$$

In the above set of equations $2nc+1$ first order derivatives appear (pressure, nc fluxes and nc mole fractions) as well as one second order derivative (temperature). Hence $2nc+3$ boundary conditions are required. These boundary conditions are determined by mass and heat transfer resistances in the membrane layers adjacent to the catalytically active layer as well as in the gas phase boundary layers on the tube- and shellside. Figure 9.3 shows these resistances qualitatively. The equations describing the transport in these layers are introduced in the following sections.

9.4 Transport in the support layers

In order to rigorously describe the material and heat transfer behaviour in each support layer indicated in Figure 9.3, the energy balance (Equation 9.6), the nc material balances (Equation 9.8) in combination with the DGM (Equation 9.18) and the mole fraction summation have to be solved. As the support layers are considered to be inert, the reaction terms in the energy and material balance can be set to zero. However, Veldsink *et. al.* (1994) and Krishna (1987) proved that the error introduced by a linearisation of the DGM is small. The required fluxes can then be obtained directly from the DGM. The linearised form of Equation 9.18, given by Krishna (1987) for planar geometry, is:

$$-\frac{\overline{p}}{R_G \overline{T}}\frac{\Delta y_i}{\delta} - \frac{\overline{y}_i}{R_G \overline{T}}\left(1+\frac{B_0 \overline{p}}{\mu D^e_{K,i}}\right)\frac{\Delta p}{\delta} = \sum_{\substack{j=1 \\ j\neq i}}^{nc} \frac{\overline{y}_i N_j'' - \overline{y}_j N_i''}{D^e_{i,j}} - \frac{N_i''}{D^e_{K,i}} \tag{9.25}$$

Here Δy_i and Δp denote the mole fraction and pressure difference, respectively, across the membrane layer of thickness δ whilst $\overline{T}$, $\overline{y}_i$ and $\overline{p}$ stand for the average

temperature mole fraction and pressure. The viscosity and the diffusion coefficients are thus evaluated at average temperature, pressure and mole fractions.

For radial co-ordinates, the linearisation is somewhat more difficult, because the fluxes in the radial direction do not remain constant. However, the molar flowrates per unit length do remain constant. Equation 9.26 shows the approximation used:

$$N_i'(z,r) = \frac{N_i(z)}{2\pi r\, dz} = \frac{N_i'(z)}{2\pi r} \approx \frac{N_i'(z)}{2\pi \bar{r}} \tag{9.26}$$

In Equation 9.26, $\bar{r}$ is the average radius according to:

$$\bar{r} = 0.5\left(D + \delta\right) \tag{9.27}$$

where D is the internal diameter of the layer and δ is the layer thickness. Inserting Equation 9.26 into Equation 9.25 gives:

$$-2\pi\bar{r}\frac{\bar{p}}{R_G\bar{T}}\left(\frac{\Delta y_i}{\delta} + \bar{y}_i\left(1+\frac{B_0\bar{p}}{\mu D_{K,i}^e}\right)\frac{\Delta p}{\bar{p}\delta}\right) = \sum_{\substack{j=1\\ j\neq i}}^{nc}\frac{\bar{y}_i N_j' - \bar{y}_j N_i'}{D_{i,j}^e} - \frac{N_i'}{D_{K,i}^e} \tag{9.28}$$

Equation 9.28 can be rewritten into a *nc* dimensional vector notation and solved for the vector of molar flowrates per unit length:

$$\{N'\} = \frac{2\pi\bar{r}\bar{p}}{R_G\bar{T}}\left[\bar{B}\right]^{-1}\left(\frac{\{\Delta y\}}{\delta} + \{\bar{y}\}\left(1+\frac{B_0\bar{p}}{\mu D_{K,i}^e}\right)\frac{\Delta p}{\bar{p}\delta}\right) \tag{9.29}$$

the elements of the matrix $\left[\bar{B}\right]$ are given by:

$$B_{i,i} = \frac{1}{D^e_{K,i}} + \sum_{\substack{j=1 \\ j \neq i}}^{nc} \frac{\bar{y}_j}{D^e_{i,j}} \tag{9.30}$$

and

$$B_{i,j} = -\frac{\bar{y}_i}{D^e_{i,j}} \tag{9.31}$$

The energy transport in the support layers is described by Equation 9.6, which can be solved analytically, if no reaction and a constant effective heat conductivity λ_{eff} are assumed. This yields (Renz, 1989):

$$Q' = \frac{2\pi\lambda_{eff}\left(T_1 - T_2\right)}{\ln\left(D_2 / D_1\right)} \tag{9.32}$$

where Q' is the heat flow per unit length and the subscripts 1 and 2 denote the in- and outside of the layer respectively.

9.5 Mass and heat transfer through the boundary layers

9.5.1 Mass transfer

Multicomponent molecular diffusion in a gas of constant total pressure is described by the Maxwell-Stefan equations (Taylor and Krishna, 1993) and these are the foundation of the DGM (see Section 9.3.2 Equations 9.13 and 9.14):

$$\frac{p}{RT}\frac{\partial y_i}{\partial r} = \sum_{\substack{k=1 \\ k\neq i}}^{nc} \frac{y_i N''_{D,k} - y_k N''_{D,i}}{D_{i,k}} \tag{9.33}$$

The subscript D in this equation denotes diffusional flux only. Only nc-1 of the Equations 9.33 are independent. The flux $N''_{D,nc}$ is dependent on the *nc-1* other fluxes because the sum of all diffusional fluxes is zero (Bird *et. al.* 1960). Equation 9.33 can be rewritten into a (nc-1)×(nc-1) matrix in a similar way to Equation 9.28:

$$\left\{N''_D\right\} = -c_{tot}[B]^{-1}\left\{\frac{\partial y}{\partial r}\right\} \tag{9.34}$$

with the elements of the matrix $[B]$ defined by:

$$B_{i,i} = \frac{y_i}{D_{i,n}} + \sum_{\substack{k=1 \\ i\neq k}}^{nc} \frac{y_k}{D_{i,k}} \tag{9.35}$$

and

$$B_{i,k} = -y_i\left(\frac{1}{D_{i,k}} - \frac{1}{D_{i,n}}\right) \tag{9.36}$$

Equation 9.34 can be used to supply the diffusional fluxes to a system of nc-1 coupled differential material balances written in vector notation (Taylor and Krishna, 1993):

$$c_{tot}\frac{\partial\{y\}}{\partial t} + \nabla\cdot\left(N''_{tot}\{y\}\right) = c_{tot}[B]^{-1}\left\{\nabla^2 y\right\} \tag{9.37}$$

Equation 9.37 is written with the assumption that the total concentration c_T and the diffusion coefficient matrix $[B]^{-1}$ are constant along the diffusion path (*e. g.* they are to be evaluated at average temperature and composition). The system of *nc*-1 partial differential equations can be decoupled using the following procedure as described by Taylor and Krishna (1993):

$$[P]^{-1}[B]^{-1}[P]=[\hat{D}] \tag{9.38}$$

where $[\hat{D}]$ is a diagonal matrix whose elements are the eigenvalues of $[B]^{-1}$ and $[P]$ is a real, symmetric matrix. Its columns are the eigenvectors of $[B]^{-1}$. If Equation 9.37 is multiplied from the left by $[P]^{-1}$ and $[P][P]^{-1}$ is inserted into the right hand side between $[B]^{-1}$ and $\{\nabla^2 y\}$ one obtains:

$$c_{tot}\frac{\partial\{\hat{y}\}}{\partial t}+\nabla\cdot N''_{tot}\{\hat{y}\}=c_{tot}[\hat{D}]\{\nabla^2\hat{y}\} \tag{9.39}$$

with

$$\{\hat{y}\}=[P]^{-1}\{y\} \tag{9.40}$$

Equation 9.39 is a system of *nc*-1 decoupled partial differential equations taking the same form as in the case of a binary mixture:

$$c_{tot}\frac{\partial\hat{y}_i}{\partial t}+\nabla\cdot N''_{tot}\hat{y}_i=c_{tot}\hat{D}_i\nabla^2\hat{y}_i \tag{9.41}$$

Equation 9.41 makes it possible to apply binary case solutions to multicomponent systems. Examples are the film theory or the penetration theory as described for the binary case by Treybal (1980). Furthermore it is possible to use mass transfer correlations which were determined empirically in the form of:

$$\hat{Sh}_i = \frac{\hat{k}_i d}{\hat{D}_i} = f\left(Re, \hat{Sc}_i = \frac{\mu}{\hat{D}_i \rho}, geometry \right) \tag{9.42}$$

These correlations are generally determined for the vanishing flux case and where no convective fluxes are considered (Bird *et. al.* 1960):

$$\hat{k}_{i,b} = \lim_{N_i'' \to 0} \frac{N_{i,b}'' - y_{i,b} N_{tot}''}{c_{tot}\left(y_{i,b} - y_{i,I}\right)} \tag{9.43}$$

The subscripts b and I indicate the bulk and the membrane gas interface respectively. Equation 9.43 is written for a mass transfer coefficient giving the flux from the bulk into the boundary layer. For non-vanishing flow the defining equation is (Bird *et. al.* 1960):

$$\hat{k}_{i,b}^{\bullet} = \frac{N_{i,b}'' - y_{i,b} N_{tot}''}{c_{tot}\left(y_{i,b} - y_{i,I}\right)} \tag{9.44}$$

These two definitions are coupled by a finite flux correction factor $\hat{\Xi}_{i,b}$ as described by Taylor and Krishna (1993):

$$\hat{k}_{i,b}^{\bullet} = \hat{k}_{i,b} \hat{\Xi}_{i,b} \tag{9.45}$$

The definition for the finite flux correction factor evaluated at the bulk-boundary layer interface is (Taylor and Krishna 1993):

$$\hat{\Xi}_{i,b} = \frac{\hat{\Psi}_{i,b}}{\exp \hat{\Psi}_{i,b} - 1} \tag{9.46}$$

with

$$\hat{\Psi}_{i,b} = \frac{N''_{tot}}{c_T \hat{k}_{i,b}} \tag{9.47}$$

The correction factor results from the binary case solution of the Maxwell-Stefan equation under the assumptions used for the for the film theory and with the bulk gas phase as a reference state. Hence the subscript *b* in the above equations.

Once the mass transfer coefficients have been determined in the transformed domain according to Equations 9.42 and 9.45 to 47, the diffusional fluxes can be expressed by:

$$\hat{N}''_{D,i} = c_T \hat{k}^{\bullet}_{i,b} \left(\hat{y}_{i,b} - \hat{y}_{i,I} \right) \tag{9.48}$$

They can be re-transformed by:

$$\begin{aligned} [P]\left\{\hat{N}''_D\right\} &= c_T [P]\left[\hat{k}^{\bullet}_b\right][P]^{-1}[P]\left(\{\hat{y}_b\} - \{\hat{y}_I\}\right) \\ \{N''_D\} &= c_T \left[k^{\bullet}_b\right]\left(\{y_b\} - \{y_I\}\right) \end{aligned} \tag{9.49}$$

For the convective and diffusional flux of one component the following equation is finally obtained:

$$N''_i = N''_{D,i} + y_i N''_{tot} = c_T \sum_{j=1}^{nc-1} k^{\bullet}_{i,j,b} \left(y_{j,b} - y_{j,I} \right) + y_{i,b} N''_{tot};\ i = 1,\ldots,nc-1 \tag{9.50}$$

In order to solve the Equations 9.50 one additional condition is necessary. This equation is supplied by a summation of the molefractions $y_{j,I}$ at the interface.

9.5.2 Heat transfer

The heat transfer from the bulk of the shellside of the reactor to the reactor wall can be calculated by:

$$Q''_W = h_W\left(T_b - T_W\right) \tag{9.51}$$

Where the subscripts b and W indicate the bulk and the wall respectively. Alternatively an overall heat transfer coefficient U can be used, if the ambient temperature is defined.

For the heat transfer from the bulk on either the tube- or shellside of the membrane to the membrane-gas interface, the situation is somewhat different. Here the simultaneously occurring multicomponent mass transfer influences the heat transfer coefficient. The heat transfer coefficients require a finite flux correction just as the mass transfer coefficients did. Equation 9.52 gives the energy flow through the boundary layer:

$$Q'' = h^{\bullet}\left(T_b - T_I\right) \tag{9.52}$$

The finite flux heat transfer coefficient $h^{\bullet}$ is related to the vanishing flux heat transfer coefficient h determined from heat transfer coefficient correlations by:

$$h^{\bullet} = \Xi_{H,b} h \tag{9.53}$$

with

$$\Xi_{H,b} = \frac{\Phi_{H,b}}{\exp\left(\Phi_{H,b}\right) - 1} \tag{9.54}$$

and

$$\Phi_{H,b} = \frac{\sum_{i=1}^{nc} N_i' c_{p,i}}{h} \tag{9.55}$$

The specific heat capacity at constant pressure, $c_{p,i}$, is to be evaluated at the average temperature of the boundary layer.

The use of the correction factor is similar to the treatment of mass transfer coefficient described previously.

9.5.3 Mass and heat transfer correlations

The flow regimes in the tubular geometry investigated in this study can be either laminar (*i.e.* Re<2100) or turbulent. Furthermore, an entrance length has to be calculated which has to be passed before the flow profile can be considered as developed. The entrance length can be estimated using an equation given by Bird *et. al.* (1960):

$$L_e = 0.035 d_h Re \tag{9.56}$$

The mass transfer correlations used are given by van Krevelen and Hoftijzer (1949). These authors did not use the above equation to determine the entrance length but reported different correlations dependent on the length to diameter ratio. The equation for fully developed laminar flow is:

$$Sh = 2\sqrt{ReSc\frac{d_h}{L}} \tag{9.57}$$

where d_h is the hydraulic diameter and L is the length of the tubular section considered. For incompletely developed flow, the following correlation was recommended by van Krevelen and Hoftijzer (1949):

$$Sh = const \times Re^{0.8} Sc^{1/3} \tag{9.58}$$

The constant *const* is dependent on the ratio L/d_h. The values of *const* for the diameter to length ratios in the membrane reactor used (L/d_h is 15 for the tubeside and 31 for the shellside) in this study are 0.032 and 0.05 respectively.

The range of Reynolds numbers of interest in this study was 100 to 500. Figure 9.6 compares the Sherwood numbers calculated according to Equations 9.57 and 9.58 for both tube- and shellside of the membrane reactor. The shellside Sherwood numbers are not highly dependent on the correlation chosen. The difference on the tubeside is more pronounced.

The flow on the tubeside can be assumed as incompletely developed as L/d_h is less than 20 (van Krevelen and Hoftijzer 1949). Hence it was decided to employ Equation 9.58 for the simulations carried out in the study. Figure 9.7 compares the hydrogen separation factor calculated (see Section 9.6.1) using Equations 9.57 and 9.58 with those measured (see Section 8.2). It is apparent that the difference in calculated separation factors is not pronounced and that using Equation 9.58 represents the experimental results more closely.

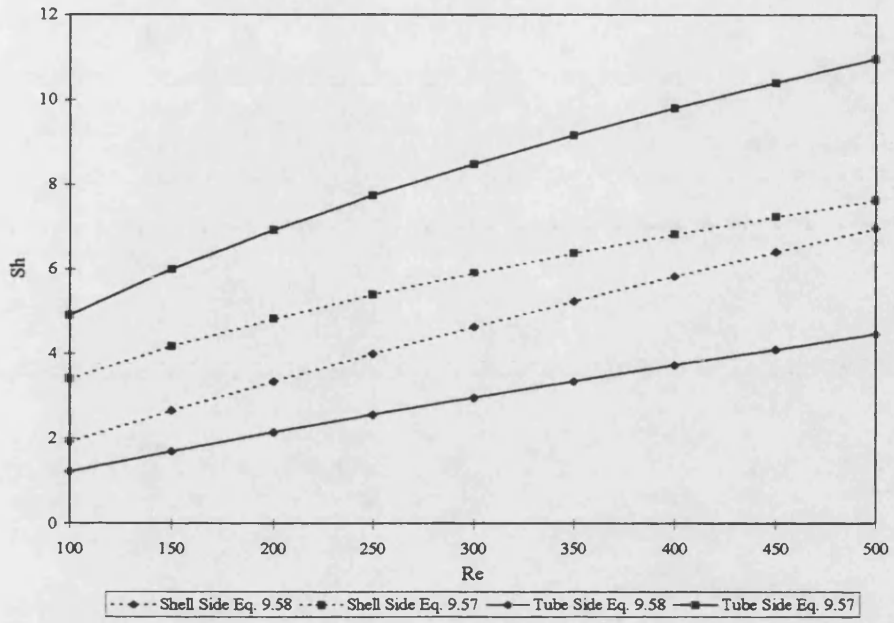

Figure 9.6: Comparison of mass transfer correlations

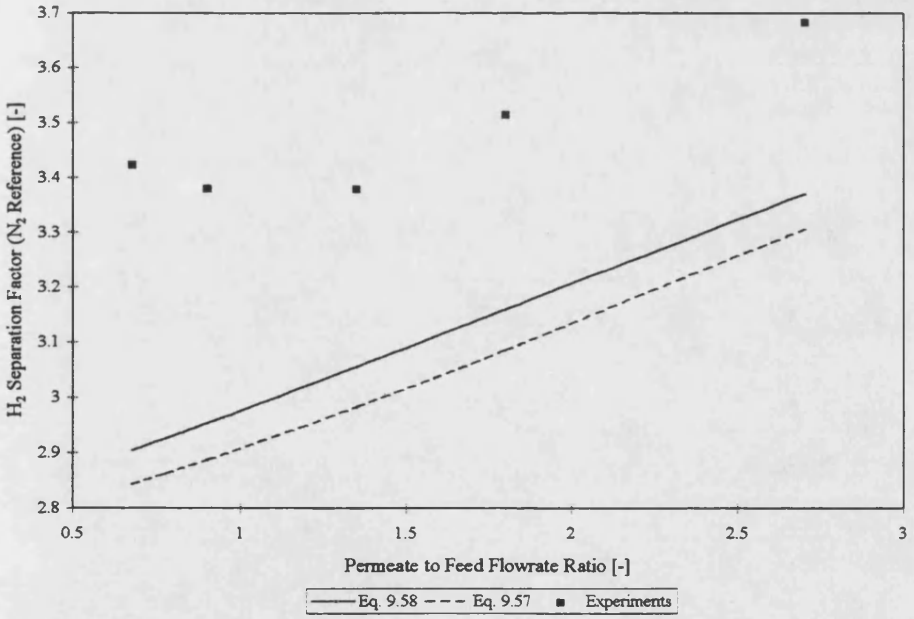

Figure 9.7: Calculated separation factors as a function of mass transfer correlations

The heat transfer coefficient was evaluated according to Equation 9.59 (Renz, 1989):

$$Nu = \left(49.028 + 4.173\, Re\, Pr \frac{d_h}{L}\right)^{1/3} \tag{9.59}$$

In all the transport correlations given above, the characteristic length is the hydraulic diameter evaluated according to Equation 8.5. The Reynolds number is to be evaluated according to Equation 8.4 at bulk flow conditions. The definitions for Sherwood, Schmidt, Nusselt and Prandl numbers are given in Equation 9.60 to 9.63. The physical properties used are evaluated at average boundary layer temperature and composition:

$$Sh = \frac{k d_h}{D} \tag{9.60}$$

$$Sc = \frac{\mu}{\rho D} \tag{9.61}$$

$$Nu = \frac{h d_h}{\lambda} \tag{9.62}$$

$$Pr = \frac{\mu c_p}{\lambda} \tag{9.63}$$

9.6 Isothermal separation model

If only isothermal separation is considered in a membrane reactor unit as depicted in Figure 9.1, only the axial material balances Equations 9.1 and 9.2 have to be solved. The fluxes on the right hand sides of these equations are governed by the mass transfer effects described in Sections 9.4 and 9.5.1. Furthermore, the assumption was made that

the mass transfer in the active layer could be described by the linearised form of the DGM given in Section 9.4, as no reactions were assumed to be present. Figure 9.8 shows the mass transfer resistances in the membrane and the adjacent boundary layers.

The required molar flowrate per unit length N_i' remains constant for a given axial location z as no reactions are assumed to occur. These flowrates are determined by the mole fraction and pressure gradients through the boundary layers and the different membrane layers.

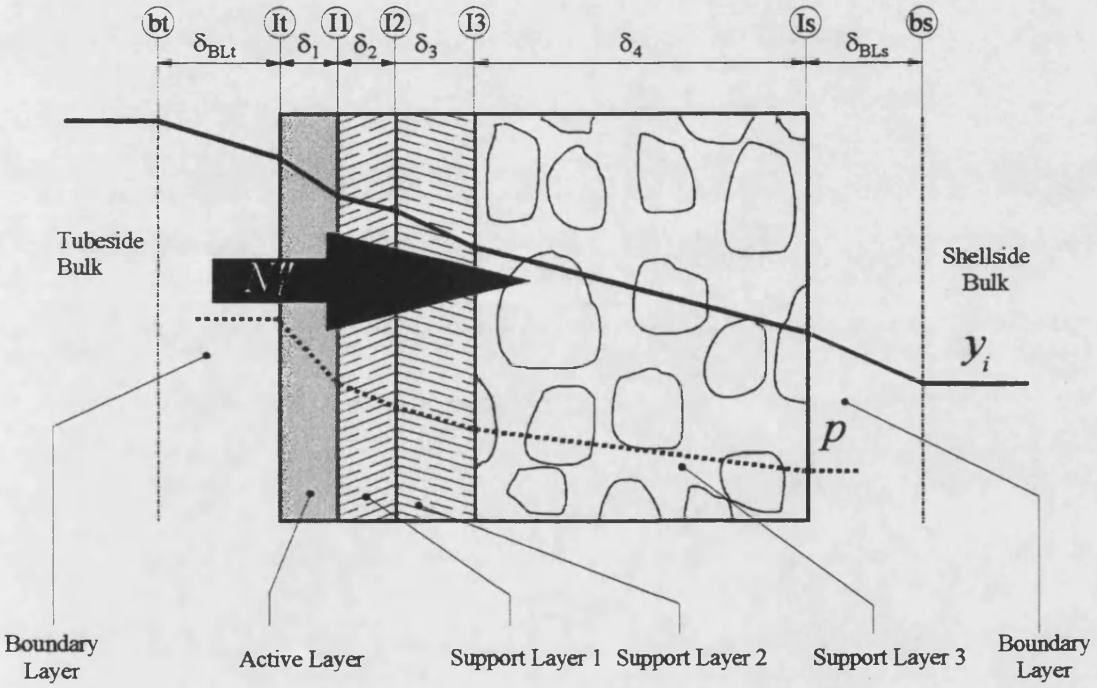

Figure 9.8: Gas separation in a multilayered porous membrane

Two different cases were investigated in this study:

1. The membrane is considered to be of uniform structure
2. The membrane consists of four layers as described in Section 6.4.

The unknowns in the first case are the *nc* molar flowrates per unit length N_i', the *nc* mole fractions $y_{i,It}$ at the tubeside-membrane interface and the *nc* mole fractions $y_{i,Is}$ at the shellside-membrane interface. In order to determine these 3*nc* unknowns, 3*nc* equations are required. The first *nc* equations are supplied by the DGM (Equations 9.28 to 30). There are *nc*-1 mass balances (Equation 9.50) per boundary layer. The remaining two equations are given by the mole fraction summations at the membrane-gas interfaces:

$$\sum_{i=1}^{nc} y_{i,I} = 1 \tag{9.64}$$

In the second case, the DGM is applicable to all of the four membrane layers which gives 4*nc* equations. Furthermore the 2*nc*-2 boundary layer mass balances and the 2 membrane-gas interface mole fraction summations are also valid. This gives a total of 6*nc* equations. However, there are 6*nc*+3 unknowns: *nc* molar flowrates per unit length, 2*nc* mole fractions at the membrane-gas interfaces, *nc* mole fractions and one total pressure at each of the three membrane layer interfaces. The three additional equations are given by the mole fraction summations in the form of Equation 9.64 at those interfaces. Table 9.1 gives the equations to be solved for the four-layered membrane and Figure 9.8 clarifies the subscripts used.

The equations in Table 9.1 can be solved using a Newton-Raphson method (Press *et. al.* 1992). For implementation of the set of equations, a finite difference approximation of the Jacobi matrix was used instead of evaluating the required partial derivatives analytically. For each evaluation of the boundary layer mass balances on tube- and shellside, the matrix of multicomponent mass transfer coefficients had to be evaluated. In order to carry out the necessary transformations (see Section 9.5.1), determination of the eigenvectors and values of the diffusion coefficient matrices in the boundary layers was necessary. This was achieved using the methods described by Smith *et. al.* (1976). A

computer program written in C was used to perform the calculations. A flowsheet of the program is given in Figure 9.9.

Table 9.1 Equations for a four-layered porous membrane

Equation	
Mass Balance Tubeside	$F_i = 0 = N_i' - c_{T,BLt}\pi D_t\left(\sum_{j=1}^{nc-1} k_{ijbt}^{*}\left(y_{jbt} - y_{j,B}\right)\right) - y_{i,bt}N_T'$
Mass Balance Shellside	$F_{nc-1+i} = 0 = N_i' - c_{T,BLs}\pi D_2\left(\sum_{j=1}^{nc-1} k_{ijbt}^{*}\left(y_{j,ls} - y_{jbs}\right)\right) - y_{i,bs}N_T'$
DGM Layer 1	$F_{2nc-2+i} = 0 = \pi\left(D_t + \delta_1\right)\frac{p_t + p_{f1}}{2R_GT}\left(\frac{y_{i,B} - y_{i,f1}}{\delta_1} + \frac{y_{i,B} + y_{i,f1}}{2}\left(1 + \frac{B_{0,1}\left(p_t + p_{f1}\right)}{2\mu D_{K,i,1}^{e}}\right)\frac{2\left(p_t - p_{f1}\right)}{\delta_1\left(p_t + p_{f1}\right)}\right) +$ $\frac{y_{i,B} + y_{i,f1}}{2D_{i1}^{e}}N_1' + \cdots - \left(\frac{y_{1,B} + y_{1,f1}}{2D_{i1}^{e}} + \cdots + \frac{y_{nc,B} + y_{nc,f1}}{2D_{inc}^{e}} + \frac{1}{D_{K,i,1}^{e}}\right)N_i' + \cdots + \frac{y_{i,B} + y_{i,f1}}{2D_{inc}^{e}}N_{nc}'$
DGM Layer 2	$F_{3nc-2+i} = 0 = \pi\left(D_t + \delta_1 + \delta_2\right)\frac{p_{f1} + p_{f2}}{2R_GT}\left(\frac{y_{i,f1} - y_{i,f2}}{\delta_2} + \frac{y_{i,f1} + y_{i,f2}}{2}\left(1 + \frac{B_{0,2}\left(p_{f1} + p_{f2}\right)}{2\mu D_{K,i,2}^{e}}\right)\frac{2\left(p_{f1} - p_{f2}\right)}{\delta_2\left(p_{f1} + p_{f2}\right)}\right) +$ $\frac{y_{i,f1} + y_{i,f2}}{2D_{i1}^{e}}N_1' + \cdots - \left(\frac{y_{1,f1} + y_{1,f2}}{2D_{i1}^{e}} + \cdots + \frac{y_{nc,f1} + y_{nc,f2}}{2D_{inc}^{e}} + \frac{1}{D_{K,i,2}^{e}}\right)N_i' + \cdots + \frac{y_{i,f1} + y_{i,f2}}{2D_{inc}^{e}}N_{nc}'$
DGM Layer 3	$F_{4nc-2+i} = 0 = \pi\left(D_t + \delta_1 + \delta_2 + \delta_3\right)\frac{p_{f2} + p_{f3}}{2R_GT}\left(\frac{y_{i,f2} - y_{i,f3}}{\delta_3} + \frac{y_{i,f2} + y_{i,f3}}{2}\left(1 + \frac{B_{0,3}\left(p_{f2} + p_{f3}\right)}{2\mu D_{K,i,3}^{e}}\right)\frac{2\left(p_{f2} - p_{f3}\right)}{\delta_3\left(p_{f2} + p_{f3}\right)}\right) +$ $\frac{y_{i,f2} + y_{i,f3}}{2D_{i1}^{e}}N_1' + \cdots - \left(\frac{y_{1,f2} + y_{1,f3}}{2D_{i1}^{e}} + \cdots + \frac{y_{nc,f2} + y_{nc,f3}}{2D_{inc}^{e}} + \frac{1}{D_{K,i,3}^{e}}\right)N_i' + \cdots + \frac{y_{i,f2} + y_{i,f3}}{2D_{inc}^{e}}N_{nc}'$
DGM Layer 4	$F_{5nc-2+i} = 0 = \pi\left(D_t + \delta_1 + \delta_2 + \delta_3 + \delta_4\right)\frac{p_{f3} + p_{ls}}{2R_GT}\left(\frac{y_{i,f3} - y_{i,ls}}{\delta_4} + \frac{y_{i,f3} + y_{i,ls}}{2}\left(1 + \frac{B_{0,4}\left(p_{f3} + p_{ls}\right)}{2\mu D_{K,i,4}^{e}}\right)\frac{2\left(p_{f3} - p_{ls}\right)}{\delta_4\left(p_{f3} + p_{ls}\right)}\right) +$ $\frac{y_{i,f3} + y_{i,ls}}{2D_{i1}^{e}}N_1' + \cdots - \left(\frac{y_{1,f3} + y_{1,ls}}{2D_{i1}^{e}} + \cdots + \frac{y_{nc,f3} + y_{nc,ls}}{2D_{inc}^{e}} + \frac{1}{D_{K,i,4}^{e}}\right)N_i' + \cdots + \frac{y_{i,f3} + y_{i,ls}}{2D_{inc}^{e}}N_{nc}'$
MFS Tubeside *)	$F_{6nc-1} = 0 = 1 - \sum_{i=1}^{nc} y_{i,B}$
MFS Shellside	$F_{6nc} = 0 = 1 - \sum_{i=1}^{nc} y_{i,ls}$
MFS Layer 1-Layer 2	$F_{6nc+1} = 0 = 1 - \sum_{i=1}^{nc} y_{i,f1}$
MFS Layer 2-Layer 3	$F_{6nc+2} = 0 = 1 - \sum_{i=1}^{nc} y_{i,f2}$
MFS Layer 3-Layer 4	$F_{6nc+3} = 0 = 1 - \sum_{i=1}^{nc} y_{i,f3}$

*) MFS: Mole fraction summation

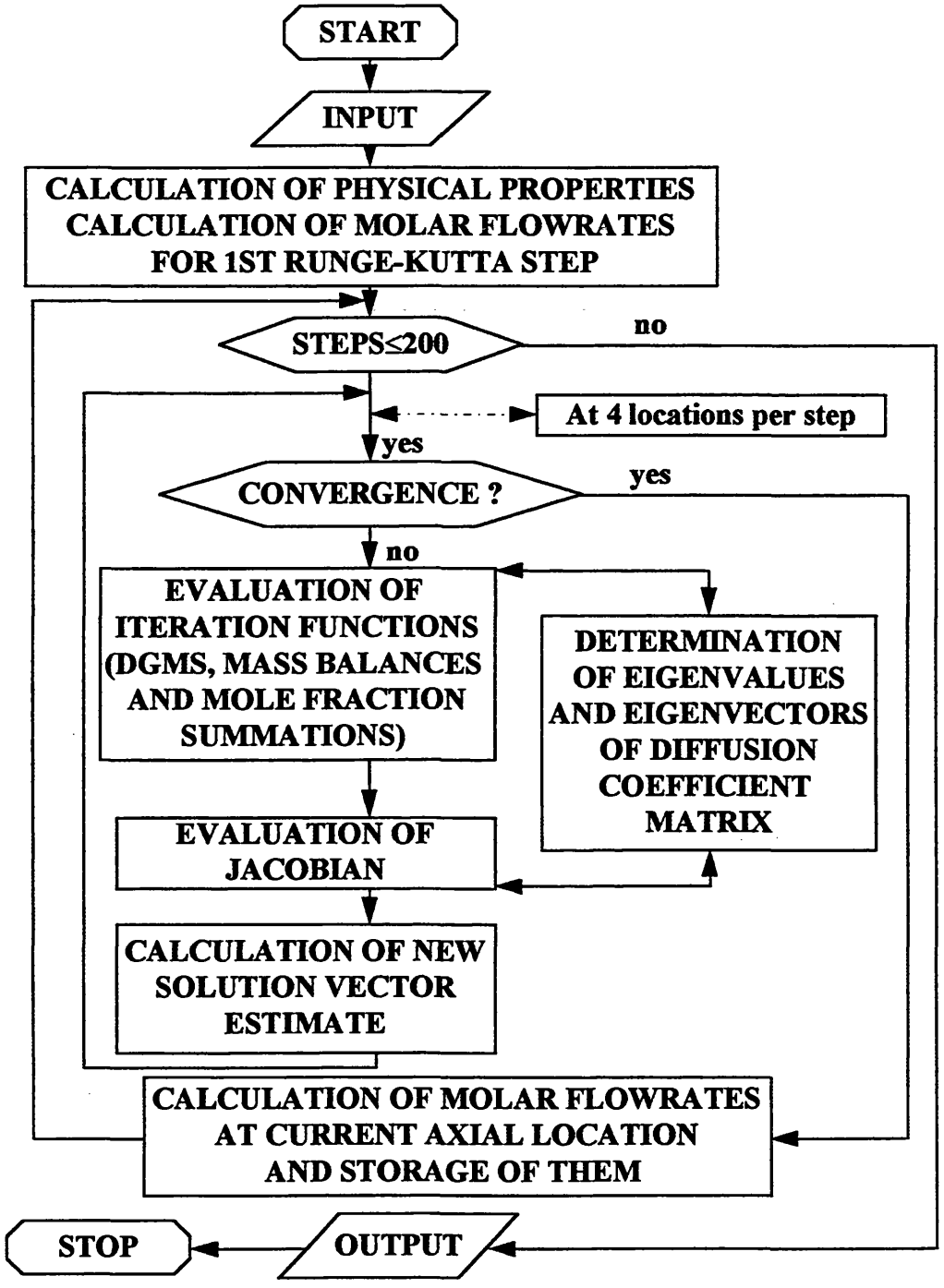

Figure 9.9: Flowsheet of the separation program

9.6.1 Comparison of the model with experimental results

In Section 8.2 a number of separation experiments are described. It can be seen from Table 8.2 that the maximum and minimum Reynolds Numbers for the tubeside were 649 and 133 respectively whilst it had a constant value of 143 for the shellside at feed conditions. This indicates operation within the laminar flow region. However, it is not likely that the flow was fully developed. The length of the entrance section after which the flow is developed can be estimated according to Equation 9.56, which gives a minimum value of 6.98cm for the shellside and 3.61cm for the tubeside. Hence it was unlikely that the flow profiles in tube- and shellside were fully developed in the experiments considered. For the estimation of the mass transfer coefficients the *Sh* correlation according to Equation 9.58 was used with the values for the constant *c* given in Section 9.5.3.

Figure 9.10 and Figure 9.11 compare the experimental results for multicomponent separation using the SCT membrane described in Section 8.2 with the model predictions using the program described above. The version considering all four membrane layers separately was used. It can be seen that the model predictions for both carbon dioxide and methane reflect the measured data very well. The hydrogen separation factors are consistently underestimated. The maximum deviation is about 19%.

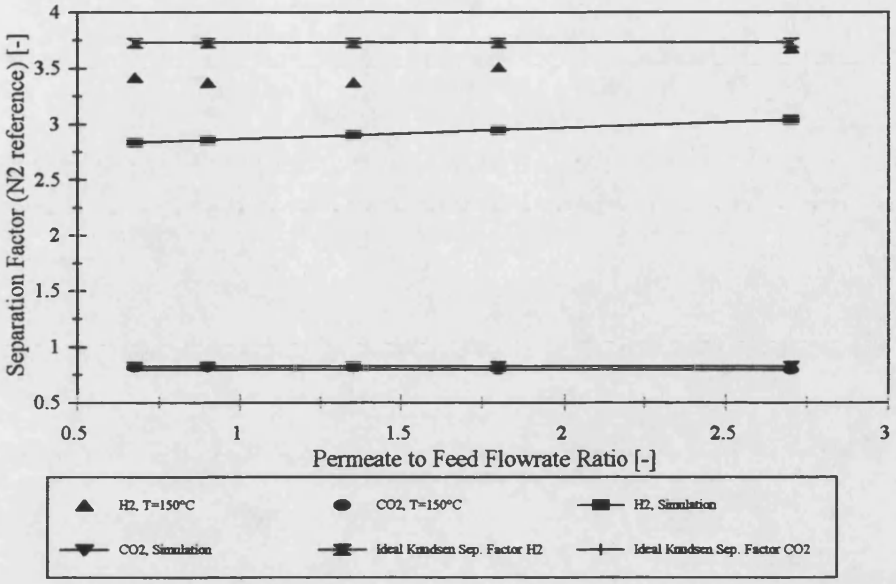

Figure 9.10: Comparison of experimental and simulation results of Sep-1 to 5

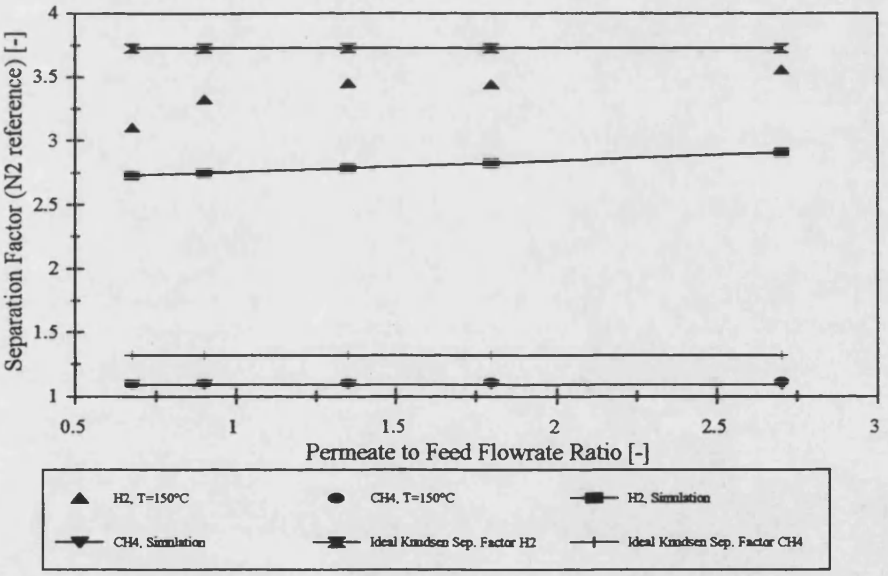

Figure 9.11: Comparison of experimental and simulation results of Sep-6 to 10

Figure 9.12 shows the comparison between the program versions. For the first program version, where only one layer was considered, the membrane was assumed to consist of the active layer only. The internal diameter of the shell was decreased accordingly in order to keep the crossectional area available to flow in the shellside constant. The calculated carbon dioxide separation factors are very close. However, the hydrogen separation factor calculated using the one layer version are lower than those obtained from the four layer program version.

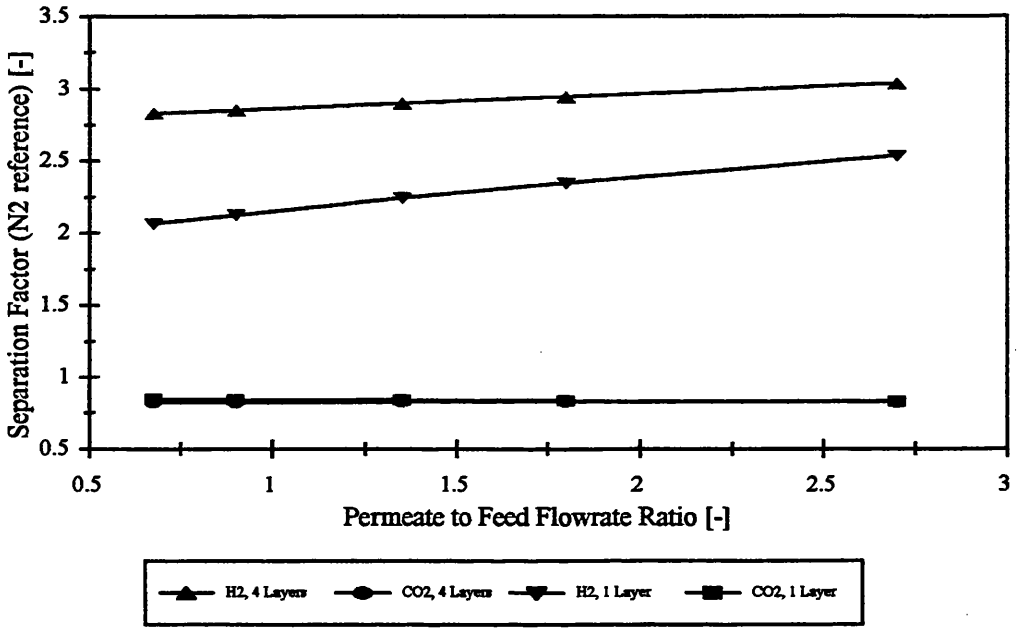

Figure 9.12: Comparison between one and four layered model

One reason for the underestimation of the hydrogen-nitrogen separation factor by the four-layered model could be the underestimation of the binary hydrogen diffusion coefficients. Reid *et. al.* (1977) quote deviations from experimentally observed binary diffusion coefficients of -5% for hydrogen-methane, -8% for hydrogen-nitrogen and -15% for hydrogen-argon whilst the deviation for the other binary pairs are generally

smaller. This causes an underestimation of the hydrogen mass transfer coefficients in the boundary layers and of the molecular diffusion part of the DGM.

Figure 9.13 shows the radial mole fraction and pressure profiles inside the membrane and the boundary layers of the membrane tube evaluated by the four layer program in the middle. It is apparent that the majority of the pressure drop occurs in the innermost layer with 4nm pores whilst the steepest mole fraction gradients are found in the thick but macroporous outer membrane layer. This effect is especially pronounced for nitrogen, the reference component of the reported separation factors, and carbon dioxide. Their mole fractions decreased by 80% and 81% respectively. In contrast, the decrease in hydrogen mole fraction across that layer was only 65.5%, leading to an increase in the separation factor. The prediction of a decrease of carbon dioxide and nitrogen by almost the same percentages explains the results obtained with the single layer model for the carbon dioxide-nitrogen separation factors. This is because the separation factor is calculated as a ratio of molefraction ratios (see Equation 8.7).

It is assumed that Knudsen diffusion governs the transport mechanism inside a porous structure if the mean free path of a molecule is larger than the pore size of the porous medium (Rautenbach 1991). The average pore sizes of the active γ-alumina and the three α-alumina support layers used in the experiments were 0.004μm, 0.7μm, 0.2μm and 11μm, respectively (see Table 6.5). The mean free path can evaluated according to (Bird *et. al.* 1960):

$$\lambda = 3\frac{\mu}{\rho}\sqrt{\frac{\pi M}{8R_G T}} \tag{9.65}$$

Table 9.2 compares the values calculated for the components present in the separation experiments and simulations at operating temperature (150°C) and pressure

(1.01325bar). It is apparent that only the innermost γ-alumina layer exhibits pure Knudsen diffusion behaviour, whilst a combination of the Knudsen and Maxwellian diffusion as well as viscous flow, as described by the Dusty Gas Model, can be expected to govern the transport behaviour in the other layers.

Table 9.2: Mean free path of components present in separation experiments and calculations

Component	Molecular weight [kg/kmol]	Viscosity [10^5×Pa s]	Density [kg/m3]	Mean free path [μm]
H_2	2.016	1.126	0.058	0.276
N_2	28.013	2.246	0.806	0.148
CO_2	44.010	2.049	1.269	0.107
CH_4	16.043	1.477	0.462	0.128
Ar	33.948	2.932	1.150	0.149

It is commonly assumed that the separation behaviour of the type of membranes used in this study is attributable to the layer with the smallest pore size only (Hsieh 1991) and hence Knudsen diffusion. However, the results of the simulations carried out in this study in combination with the experimental evidence presented in Chapter 8, indicate that this assumption is in error. Figure 9.13 suggests that innermost layer with the smallest pore size serves predominately to decrease the transmembrane pressure drop and hence cause viscous, non-separative flow contributions in the subsequent layers to decrease. The majority of the separation is then effected in these layers by means of a combination of Knudsen and Maxwellian diffusion.

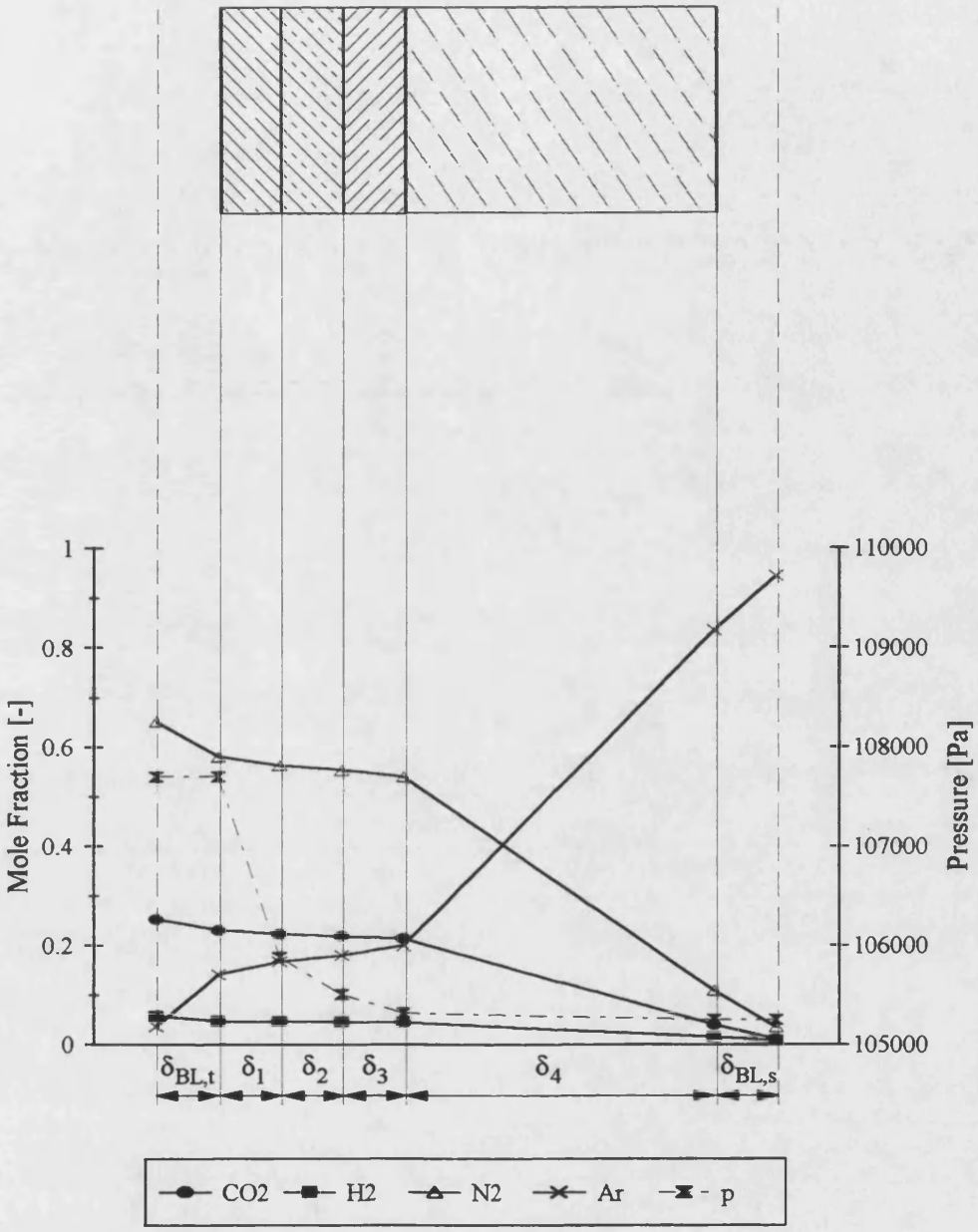

Figure 9.13: Molefraction and pressure profiles at z=110mm, experiment Sep-6

9.7 Non-isothermal reaction and separation model

In order to model a catalytic membrane reactor as depicted in Figure 9.1, the whole system of equations, detailed in sections 9.2 to 9.5 has to be solved. The material balances in the axial direction as well as the mass transfer resistances in the three support layers and the boundary layers adjacent to the membrane (Figure 9.3), are treated in the same way as for the isothermal separation model described in the previous section. Additionally, the axial energy balances, Equations 9.3 and 9.4, have to be solved. The heat transfer resistances in the boundary layers and the support layers are treated in Sections 9.4 and 9.5.2, respectively.

Apart from the non-isothermicity occasioned by the exothermic catalytic reactions, the main difference to the isothermal separation model is that the active layer cannot any longer be described by a set of linearised equation. The differential equations used to describe the transport phenomena have to be solved numerically. These equations are given in Sections 9.3.1 (energy and material balance) and in Section 9.3.2 (Dusty Gas Model for the determination of the component fluxes). The system of differential equations can be arranged for numerical solution by replacing the 1st and 2nd order differentials therein with finite difference approximations and subdividing the active layer into a grid with M nodes. Any of the first order derivatives appearing in Equations 9.6, 9.8 or 9.18 can be discretised using:

$$\left.\frac{\partial X}{\partial r}\right|_{r=\frac{1}{2}(r_j+r_{j-1})} \cong \frac{X_j - X_{j-1}}{r_j - r_{j-1}} = \frac{X_j - X_{j-1}}{\Delta r} \tag{9.66}$$

where X is any variable such as molar flux, pressure, molefraction or temperature. This discretisation scheme was suggested by Press *et. al.* (1992) for the numerical solution of

two point boundary value differential equation problems. Figure 9.14 shows the discretisation scheme used for the catalytically active membrane layer.

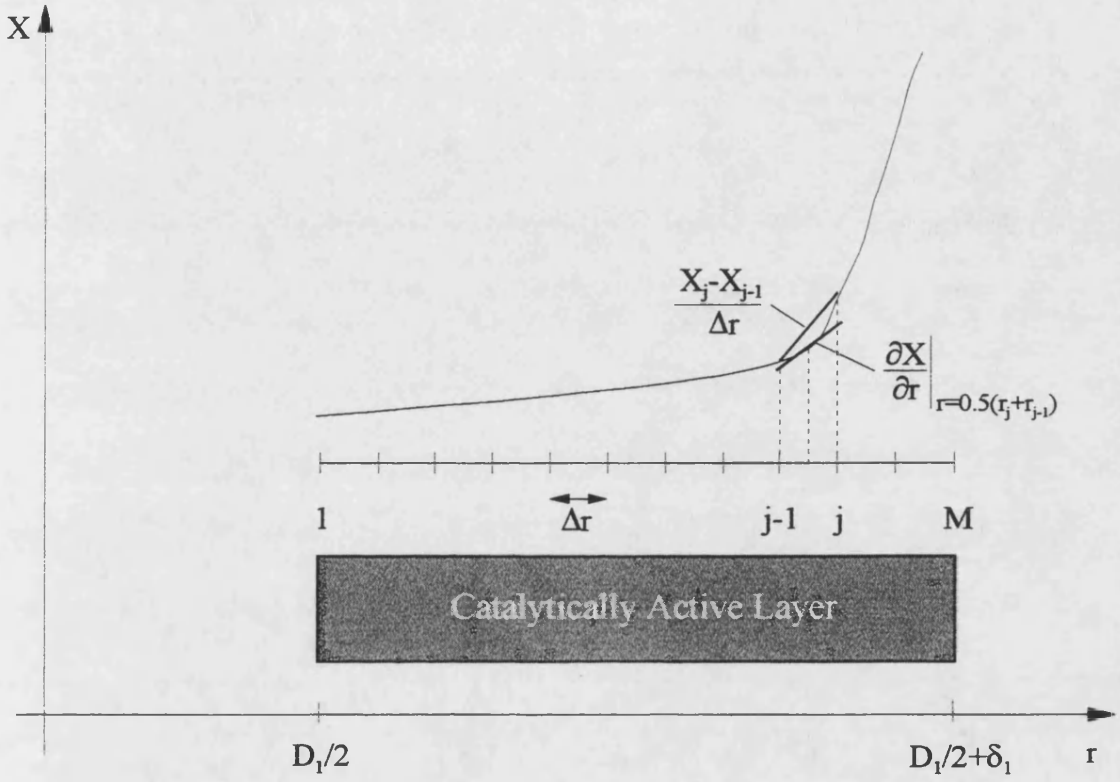

Figure 9.14: Discretisation of catalytically active layer

If the finite difference approximation given in Equation 9.66 is applied to the material balance, given in Equation 9.8, the resulting discretised form is:

$$\frac{N''_{i,j-1/2}}{r_{j-1/2}}+\frac{N''_{i,j}-N''_{i,j-1}}{\Delta r}-\left(\sum_{k=1}^{nr}\nu_{i,k}R_k\right)_{j-1/2}=0;i=1,\ldots,nc;j=2,\ldots,M \qquad (9.67)$$

In Equation 9.67 and the following discretisation equations, variables indexed with j-1/2 indicate the location r=0.5(r_j+r_{j-1}). Any values indexed this way are evaluated as the arithmetic mean of the same values at nodes j and j-1. The reaction rate R_k appearing in

Equation 9.67 is to be evaluated according to Equation 9.9 at each location $r=0.5(r_j+r_{j-1})$. The Dusty Gas Model (Equation 9.18), used to calculate the fluxes, can be discretised similarly:

$$\left(\frac{p}{R_G T}\right)_{j-1/2}\frac{y_{i,j}-y_{i,j-1}}{\Delta r}+\left[\frac{y_i}{R_G T}\left(1+\frac{B_0 p}{\mu D^e_{K,i}}\right)\right]_{j-1/2}\frac{p_j-p_{j-1}}{\Delta r}-$$
$$\left[\sum_{\substack{k=1\\k\neq i}}^{nc}\frac{y_i N''_k-y_k N''_i}{D^e_{i,k}}\right]_{j-1/2}+\left[\frac{N''_i}{D^e_{K,i}}\right]_{j-1/2}=0;i=1,\ldots,nc;j=2,\ldots,M \tag{9.68}$$

The energy balance, Equation 9.6, can be rewritten as:

$$\frac{\lambda_{eff}}{r}\left(\frac{\partial T}{\partial r}+r\frac{\partial^2 T}{\partial r^2}\right)+\sum_{k=1}^{nr}\left(-\Delta H_R\right)_k R_k=0 \tag{9.69}$$

with the assumption of a constant thermal conductivity, λ_{eff}. In order to simplify the numerical treatment of the above equation, it is advantageous to replace the derivative of the temperature with respect to the radial co-ordinate with an additional variable and so replace the 2nd order differential Equation 9.69 with two first order differential equations:

$$\frac{\lambda_{eff}}{r}\left(Z+r\frac{\partial Z}{\partial r}\right)+\sum_{k=1}^{nr}\left(-\Delta H_R\right)_k R_k=0 \tag{9.70}$$

and

$$Z=\frac{\partial T}{\partial r} \tag{9.71}$$

These equations can then be discretised on radial nodes 2 to M in the same fashion as the material balance and the Dusty Gas Model:

$$\frac{\lambda_{eff}}{r_{j-1/2}}\left(Z_{j-1/2}+r_{j-1/2}\frac{Z_j-Z_{j-1}}{\Delta r}\right)+\left[\sum_{k=1}^{nr}\left(-\Delta H_R\right)_k R_k\right]_{j-1/2}=0; j=2,\ldots,M \tag{9.72}$$

and:

$$Z_{j-1/2}-\frac{T_j-T_{j-1}}{\Delta r}=0; j=2,\ldots,M \tag{9.73}$$

As detailed in Section 9.3.3, an additional equation is required to satisfy the degrees of freedom of the set of equations describing energy and material transfer inside the membrane structure. This is the molefraction summation carried out at each r=0.5(r_j+r_{j-1}):

$$\left[\sum_{i=1}^{nc} y_i\right]_{j-1/2}-1=0; j=2.,..,M \tag{9.74}$$

The 2*nc*+3 boundary conditions required (see section 9.3.3) can be divided into *nc*+2 applicable at node j=1 and *nc*+1 at node j=M. The boundary conditions are:

$$p_t=p_{j=1} \tag{9.75}$$

Equation 9.50 supplies *nc*-1 fluxes through the tubeside boundary layer, hence:

$$N''_{i,t}=N''_{i,j=1}; i=1,\ldots,nc-1 \tag{9.76}$$

The heat transfer resistance through the boundary layer expressed by equation 9.52 supplies a further boundary condition:

$$\lambda_{eff} Z_{j=1} + h^{*}\left(T_{tb} - T_{j=1}\right) = 0 \tag{9.77}$$

The remaining tubeside boundary condition is the molefraction summation at the tubeside gas-membrane interface, Equation 9.64.

At the interface between the catalytically active layer and the first support layer the *nc* fluxes at node *M* are determined by Equation 9.28 for the first support layer. The flowrates per unit length used in Equation 9.28 are coupled to the fluxes at node *M* by:

$$N''_{i,j=M} = \frac{N'_i}{\pi\left(D_1 + 2\delta_1\right)}; i = 1,\ldots,nc \tag{9.78}$$

The final boundary condition is derived by equating the energy flows per unit length in the first support layer to that at node *M*. Equation 9.79 expresses this relationship:

$$\pi\lambda_{eff}\left(D_1 + 2\delta_1\right)Z_{j=M} + \frac{2\lambda_{eff}\left(T_M - T_{I2}\right)}{\ln\left[\frac{\left(D_1 + 2\delta_1 + 2\delta_2\right)}{\left(D_1 + 2\delta_1\right)}\right]} = 0 \tag{9.79}$$

The first term on the left hand side of Equation 9.79 expresses the thermal conduction at node *M*. Table 9.3 gives an overview of the equations and unknowns which have to be solved for each axial integration step.

Table 9.3: Radial transport equations and unknowns for catalytic membrane reactor simulation

Equations		Unknowns	
Equation	**Number**	**Unknown variable**	**Number**
Mass transfer, tubeside, 9.50	nc-1	Fluxes, active layer	M×nc
M.F.S. tubeside gas-membrane interface, 9.64	1	Molefractions, active layer	M×nc
		Temperature, active layer	M
Pressure, tubeside, 9.75	1	Temperature gradient, active	
Heat transfer, tubeside, 9.77	1	layer	M
Material balance, active layer, 9.67	nc×(M-1)	Pressure, active layer	M
DGM, active layer, 9.68	nc×(M-1)	Molefractions, interface	
Energy balance, active layer, 9.72	M-1	support layers 1 and 2	nc
Auxiliary energy balance, active layer,		Temperature, interface	
9.73	M-1	support layers 1 and 2	1
MFS, active layer, 9.74	M-1	Pressure, interface support	
DGM, support layer 1, 9.28, 9.78	nc	layers 1 and 2	1
Energy balance, support layer 1, 9.79	1	Molefractions, interface	
MFS, interface support layer 1 and 2,		support layers 2 and 3	nc
9.64	1	Temperature, interface	
DGM, support layer 2, 9.28	nc	support layers 2 and 3	1
Energy balance, support layer 2, 9.32	1	Pressure, interface support	
MFS, interface support layer 2 and 3,		layers 2 and 3	1
9.64	1	Molefractions, shellside	
DGM, support layer 3, 9.28	nc	membrane-gas interface	nc
Energy balance, support layer 3, 9.32	1	Temperature, shellside	
Mass transfer, shellside, 9.50	nc-1	membrane-gas interface	1
M.F.S. shellside gas-membrane			
interface, 9.64	1		
Heat transfer, shellside, 9.77	1		
Total number of equations	**2×M×nc+3×**	**Total number of variables**	**2×M×nc+3×**
	M+3×nc+5		**M+3×nc+5**

The discretisation of the differential equations into algebraic finite difference equations together with the boundary equations result in a system of non-linear algebraic equations. This system of equations has to be solved for each axial integration step in order to supply the right hand sides of the axial material and energy balances equations (Equations 9.1 to 9.4) on the tube- and shellside of the membrane reactor. The solution was achieved by employing a Newton-Raphson method as described by Press *et. al.* (1992).

9.7.1 Comparison with experimental results

The catalytic membrane reactor model outlined in the previous section was used to simulate the experimental investigation described in Section 8.3. The reaction rates were described by Equation 9.9 with values for the pre-exponential factor, the activation energy and the exponents for methanol and oxygen as given in Table 7.13 for the catalytic dehydrogenation of methanol and the catalytic oxidation of methanol. In order to express the calculated reaction rates with respect to unit apparent catalyst volume rather than per unit catalyst mass, the pre-exponential factors had to be multiplied by the apparent density of the catalytically active layer. Based upon a weight of γ-alumina per unit length of 0.25g/m (Uzio *et. al.* 1993), a platinum loading of 2.3wt%, a layer thickness of 4μm, an internal diameter of 15mm and tube length of 0.22m a value of 1357.15kg/m^3 was claculated for the apparent density (see Appendix 8).

In the experiments described in Chapter 8, carbon monoxide and methane were produced in addition to hydrogen, carbon dioxide and water. As the proposed reaction network did not account for these components, they were not considered in the following calculations.

Figure 9.15 and Figure 9.16 show the two-dimensional distribution of methanol (as an example for a reactant) and hydrogen (as an example for a product) under the conditions

of experiment CMR 12. The radial location in these figures is given in terms of 15 equidistant calculation nodes in order to portray the catalytically active layer visibly. This would not be possible if the actual distances were plotted, as the catalytically active layer is only 4μm thick compared to a total wall thickness of 2mm. It is apparent that the mass transfer restrictions imposed by the tube side - membrane interface boundary layer is very large. As in the separation model investigated in Section 9.6, the highest resistance to mass transfer inside the membrane lies in the outermost support layer for both components. Methanol, as a reactant, is partially used up whilst passing through the catalytically active layer. The unreacted remainder is transported through the inert membrane layers to the shellside of the reactor. However, this flux is restricted by the third support layer which serves as a barrier to prevent reactant loss commonly encountered in catalytic membrane reactors (Gokhale *et. al.* 1995). Simultaneously, hydrogen is produced and builds up in the catalytically active layer. Due to a composition dependent driving force exerted both in the direction of the tube and shellside (*e. g.* the chemical potential of hydrogen reaches its maximum inside the catalytically active membrane), hydrogen is enriched on either side of the membrane. This undesired effect cannot be prevented as the only means to force all the product hydrogen into the reactor shellside would be to increase the tubeside pressure. This would then increase not only the hydrogen flux directed towards the shellside, but also the fluxes of the other components. Furthermore, the flux would be of the non-separative, viscous type.

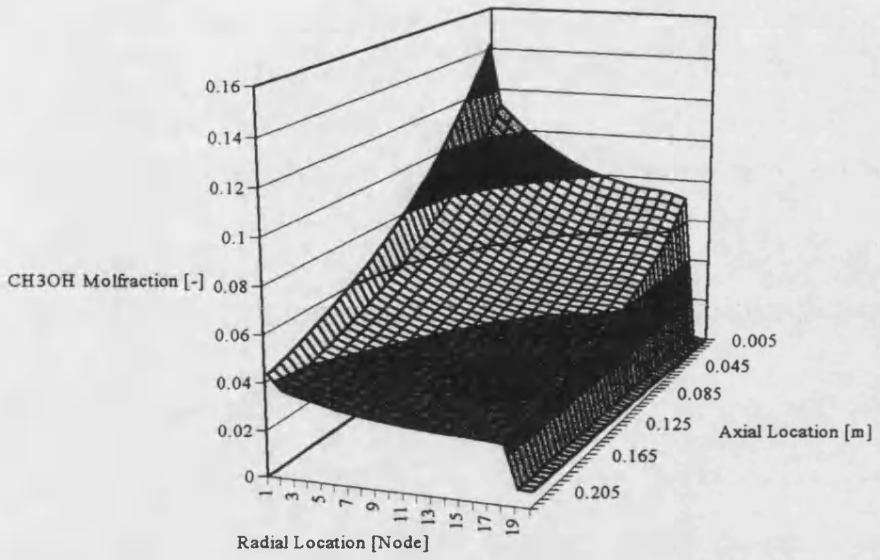

Figure 9.15: Calculated two-dimensional methanol distribution (parameters as in experiment CMR12)

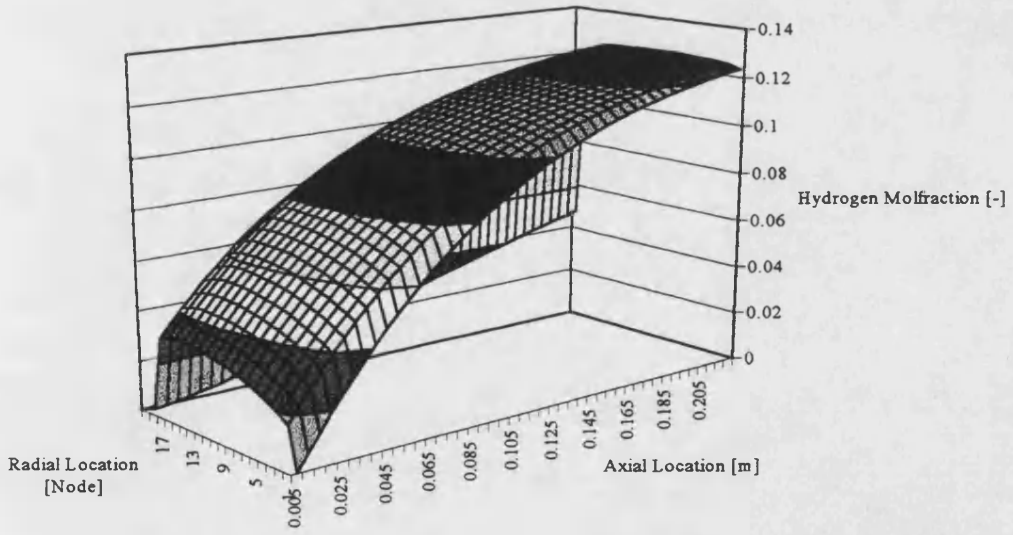

Figure 9.16: Calculated two-dimensional hydrogen distribution (parameters as in experiment CMR12)

Figure 9.17 shows the behaviour of argon, fed to the shellside as a purge gas. As expected, it is forced through the membrane by its driving force gradient. As for the two reaction components discussed previously, the 3rd membrane support layer poses the major mass transfer resistance.

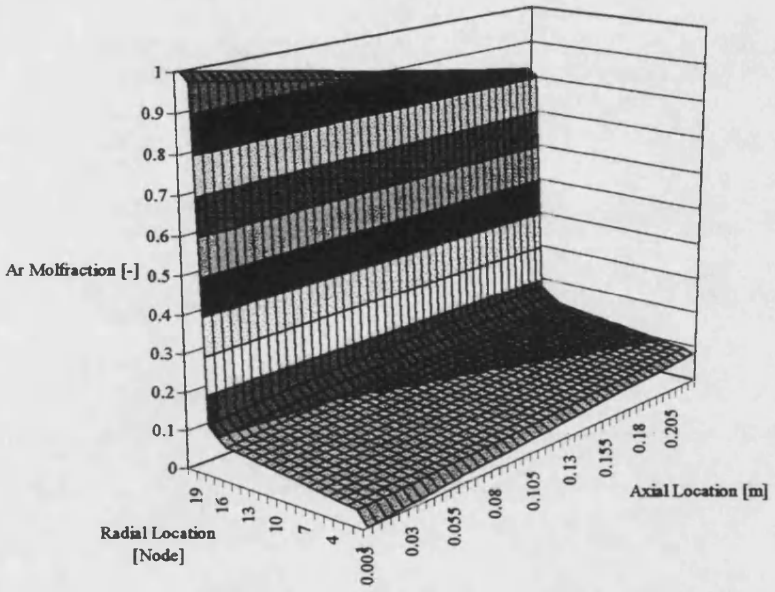

Figure 9.17: Calculated two-dimensional argon distribution (parameters as in experiment CMR12)

The two-dimensional temperature distribution shown in Figure 9.18 shows the behaviour expected from Figure 9.15 and Figure 9.16 for exothermic reactions. The main heat transfer resistance is posed by the boundary layers adjacent to the catalytic membrane, as commonly experienced in heterogeneous catalysis (Froment and Bischoff 1990)

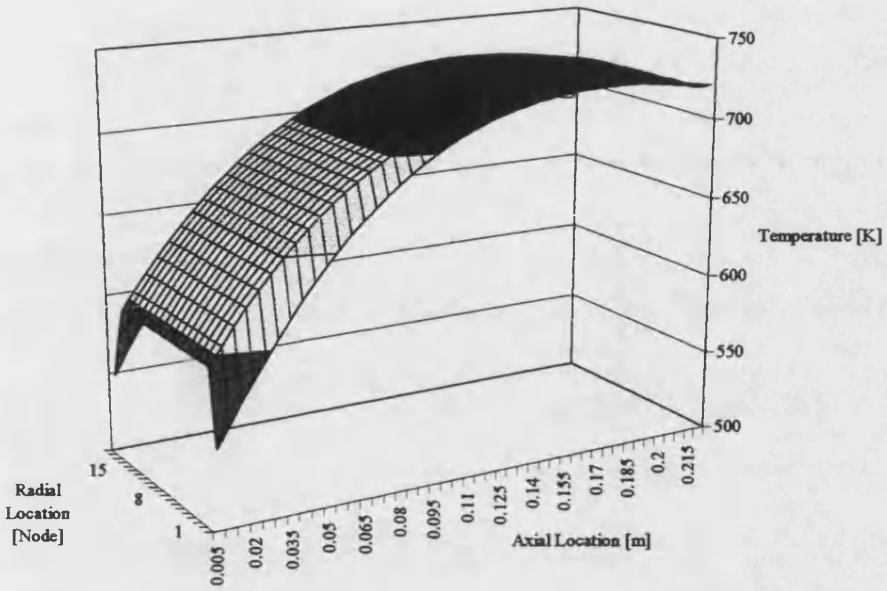

Figure 9.18: Calculated two-dimensional temperature distribution (parameters as in experiment CMR12)

The influence of changing the transmembrane pressure drop was investigated in experiments CMR 4 to 12 whilst experiments CMR 12 to 16 were carried out to investigate the reactor behaviour with changing purge to feed flowrate ratios. Figure 9.19 to Figure 9.22 show the comparison between the experimental results and the calculations.

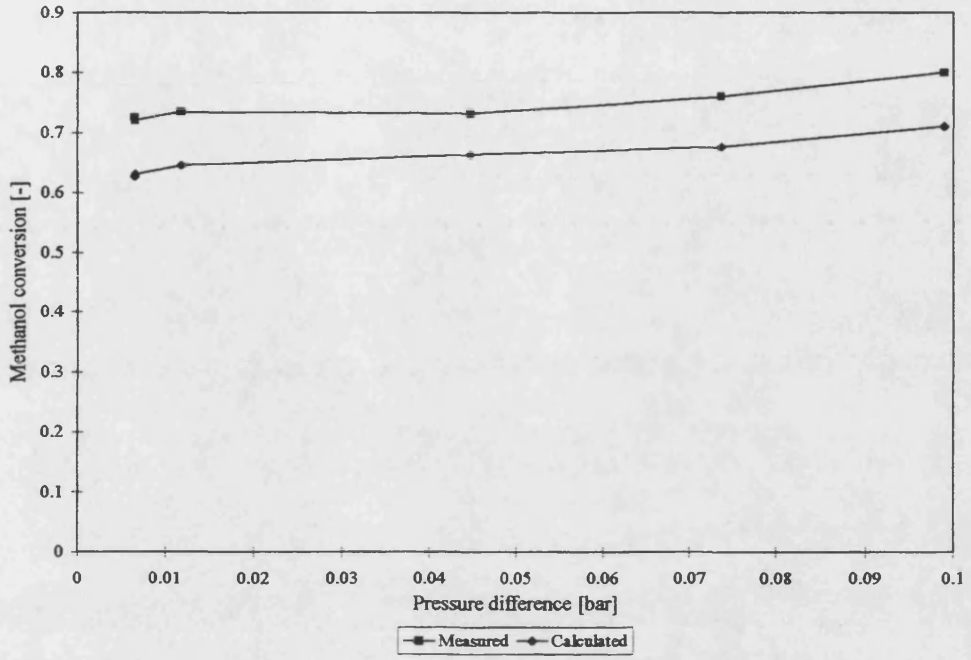

Figure 9.19: Measured and calculated methanol conversion as a function of transmembrane pressure drop

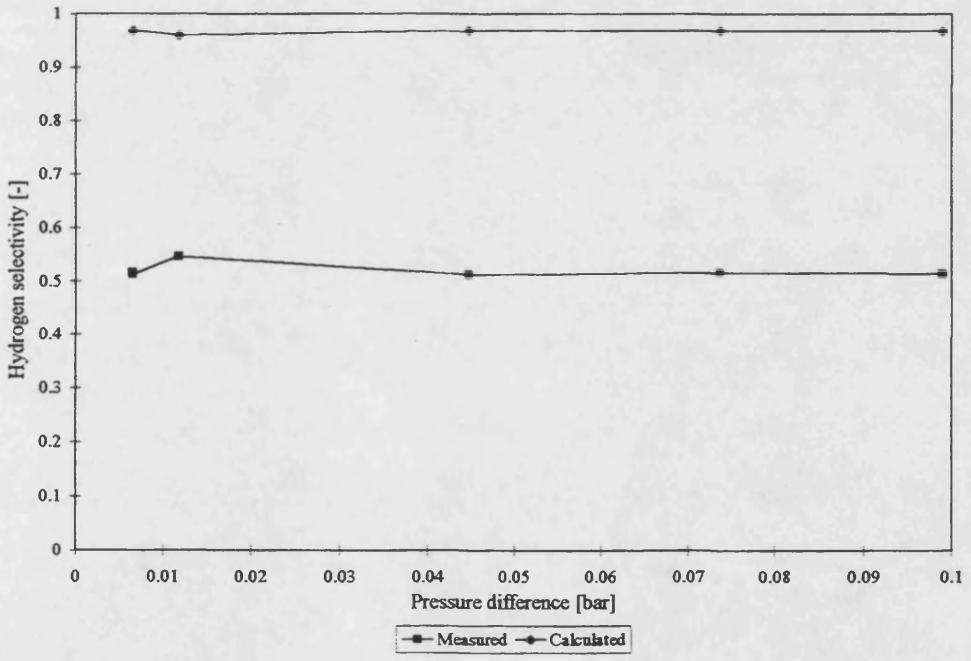

Figure 9.20: Measured and calculated selectivity towards hydrogen as a function of transmembrane pressure drop

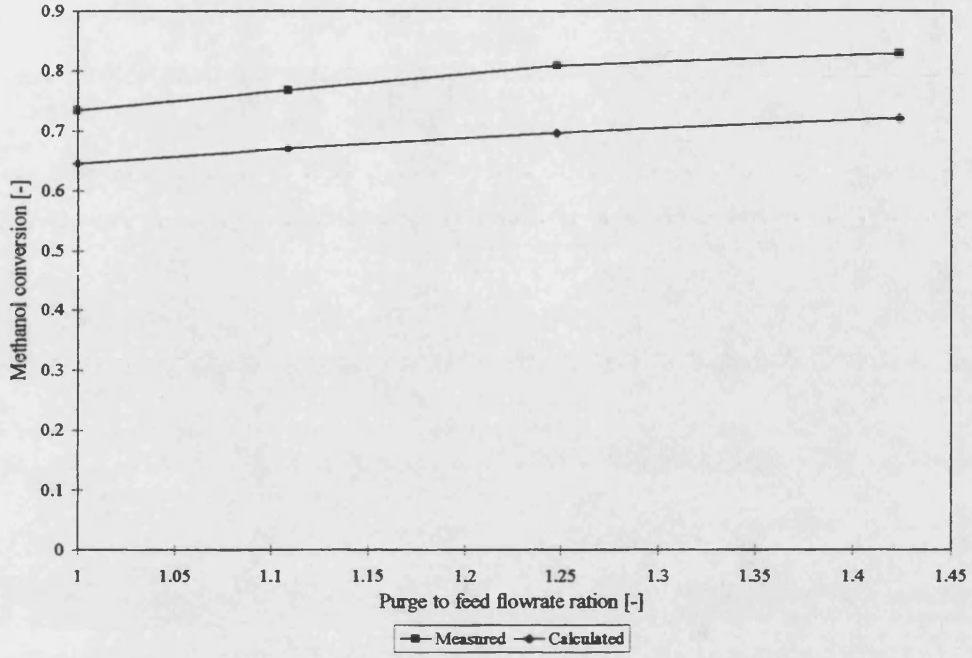

Figure 9.21: Measured and calculated methanol conversion as a function of purge to feed flowrate ratio

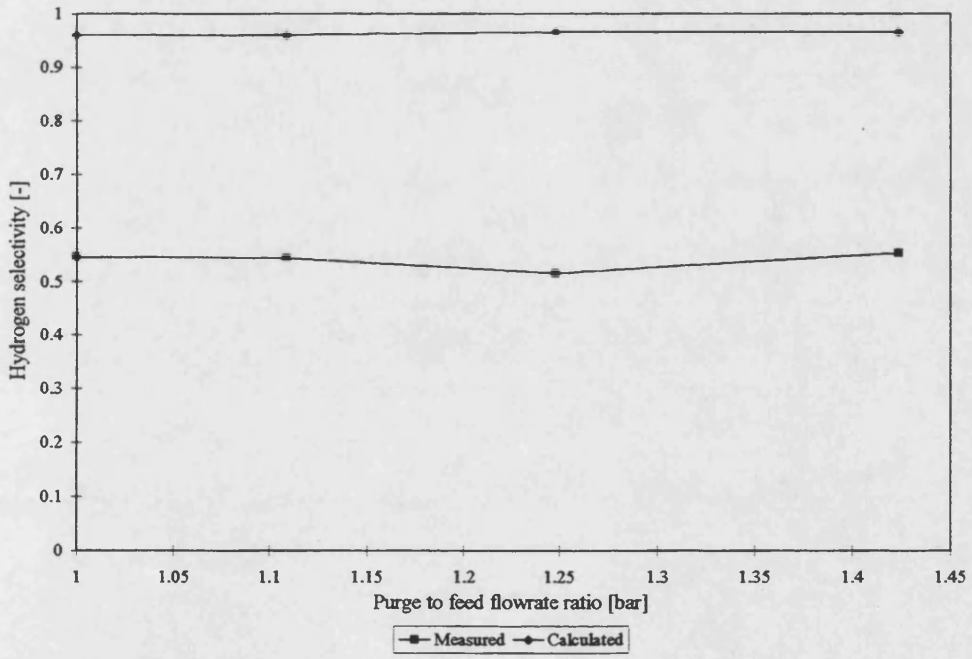

Figure 9.22: Measured and calculated selectivity towards hydrogen as a function of purge to feed flowrate ratio

It can be seen in Figure 9.19 that the calculated methanol conversion increases with increasing transmembrane pressure difference in a similar way to the measured conversion. However, the calculated extent of methanol conversion is consistently lower by a value of 10% compared to the experimentally measured value. The same behaviour can be seen for the calculated conversion as a function of purge to feed flowrate ratios (Figure 9.21). The calculated selectivities towards hydrogen for both varied transmembrane pressure drop and purge to feed flowrate ratio are approximately constant at a level of 96%, which is substantially higher than the experimental value.

The low conversions predicted by simulation when compared with experimental values are likely to be caused by an underestimation of the extent of the methanol oxidation. This would partly explain the rather high predicted selectivity towards hydrogen. Neglect of the methane and carbon monoxide producing reactions would also contribute to high calculated values.

Figure 9.23 compares the measured axial tubeside temperature profile with that calculated for experiment CMR 12. The simulated and experimental temperature profiles match well. However, from the low conversions measured, it would have been expected that the calculated axial temperatures were underestimated. That this was not the case could be caused by underestimating the shellside heat transfer to the environment.

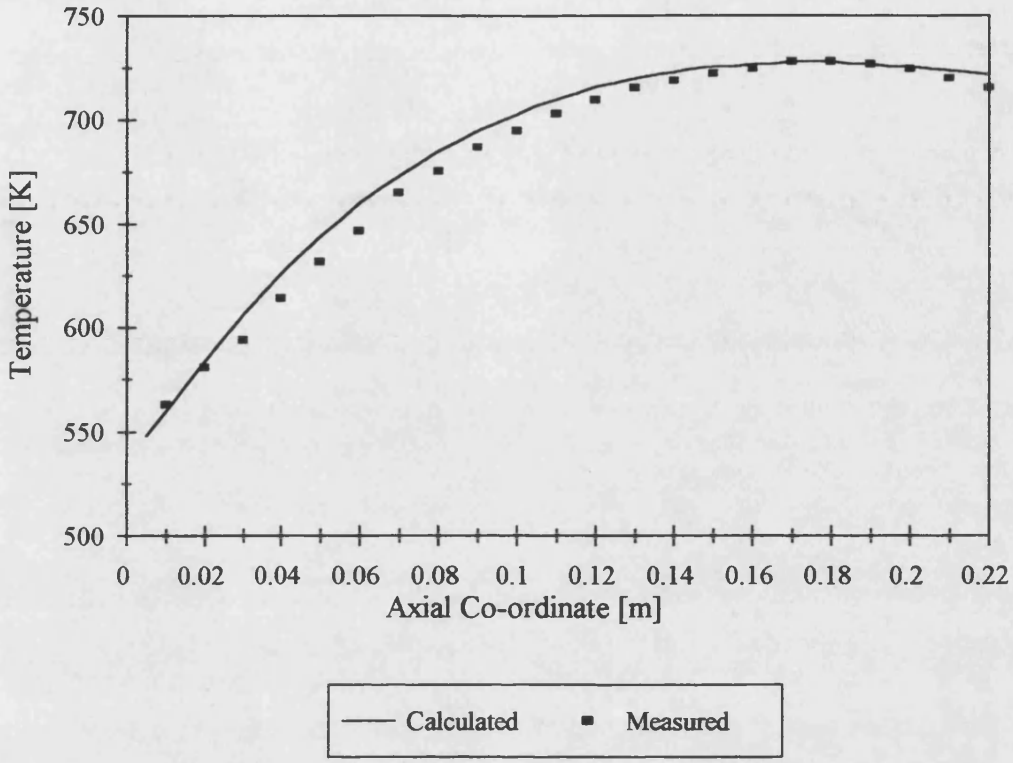

Figure 9.23: Measured and calculated axial temperature profile distribution (parameters as for experiment CMR12)

9.7.1.1 The catalytically active layer

In the following, the different transport and reaction phenomena inside the catalytic membrane and the adjacent boundary layers are investigated using the calculated radial profiles halfway through the reactor, *e. g.* at an axial length of 0.11m. The base case considered here is experiment CMR 9, which was carried out with equal feed and purge flowrates and the lowest transmembrane pressure drop. In contrast experiments CMR 11 and CMR 14 had the second highest transmembrane pressure drop and the highest purge to feed flowrate ratio, respectively.

Figure 9.24 shows the axial molefraction profiles for hydrogen, carbon dioxide and methanol for experiment CMR 9. It can be seen that the hydrogen molefraction remains almost constant throughout the catalytically active layer (nodes 2 to 16) whilst the methanol molefraction is decreasing. The carbon dioxide molefraction is increasing almost throughout the catalytically active layer. The hydrogen molefraction exhibits a maximum at node 11. Figure 9.25 shows the corresponding fluxes in the catalytically active layer. The methanol flux is positive throughout as expected from its driving force gradient as well as the fact that it is being used up by the reactions. Both hydrogen and carbon dioxide fluxes pass through zero and are directed at the tube as well as the shell side of the membrane reactor. The location at which these fluxes are reversed almost exactly coincides with the molefraction maxima shown in Figure 9.24. This, together with the pressure profile which exhibits a maximum at node 4 (shown in Figure 9.26), indicates that the flux in the catalytically active layer is governed by both Knudsen and molecular diffusion. The highest molefraction gradient is observed in the third support layer, in the same way as described in section 9.6 for the isothermal separation model.

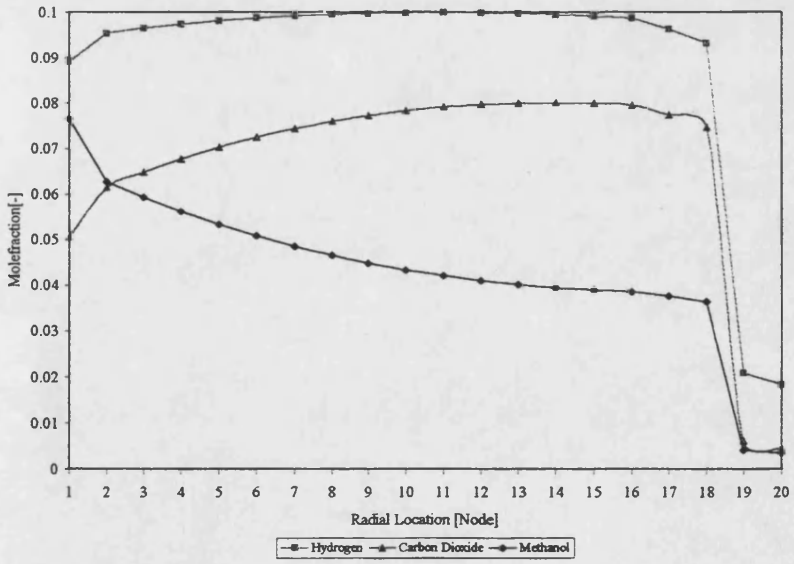

Figure 9.24: Calculated radial molefraction profiles at z=0.11m (parameters as for experiment CMR9)

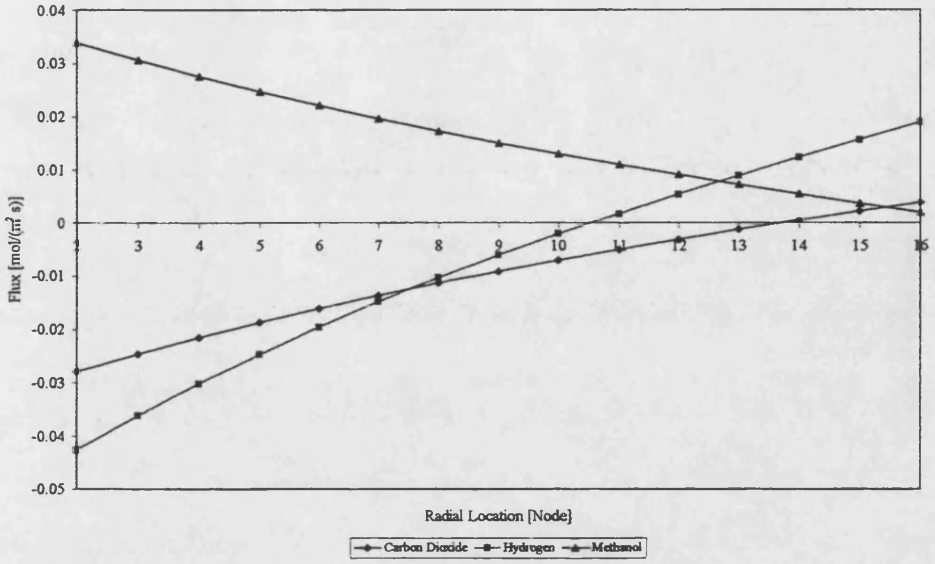

Figure 9.25: Calculated radial fluxes at z=0.11m (parameters as for experiment CMR9)

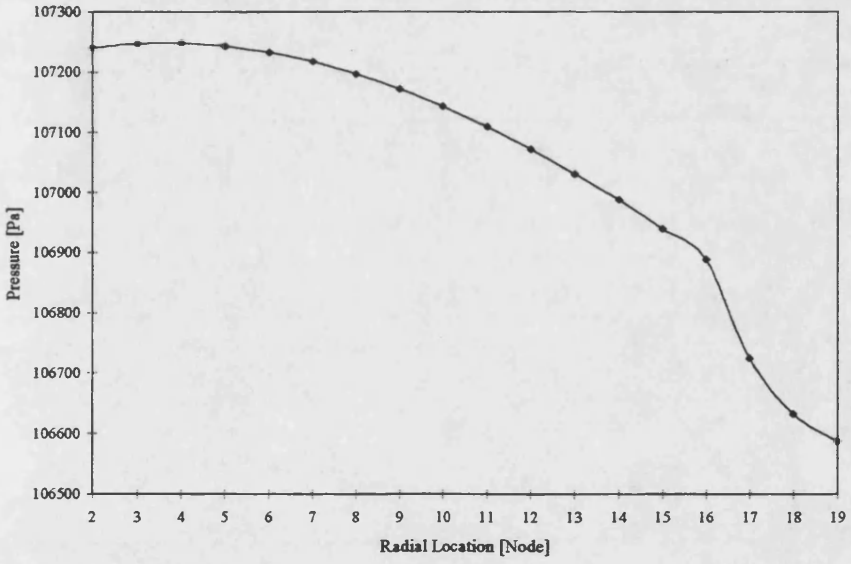

Figure 9.26: Calculated radial pressure profile at z=0.11m (parameters as for experiment CMR9)

Figure 9.27 and Figure 9.28 compare the calculated methanol compositions and fluxes of CMR 11, 9 and 14. The molefraction curve for CMR 11 does not exhibit a steeper slope than that of CMR 9. However, the calculated flux is higher, caused by the higher transmembrane pressure drop of CMR 11. The lowest methanol flux was calculated for the highest purge to feed flowrate ratio.

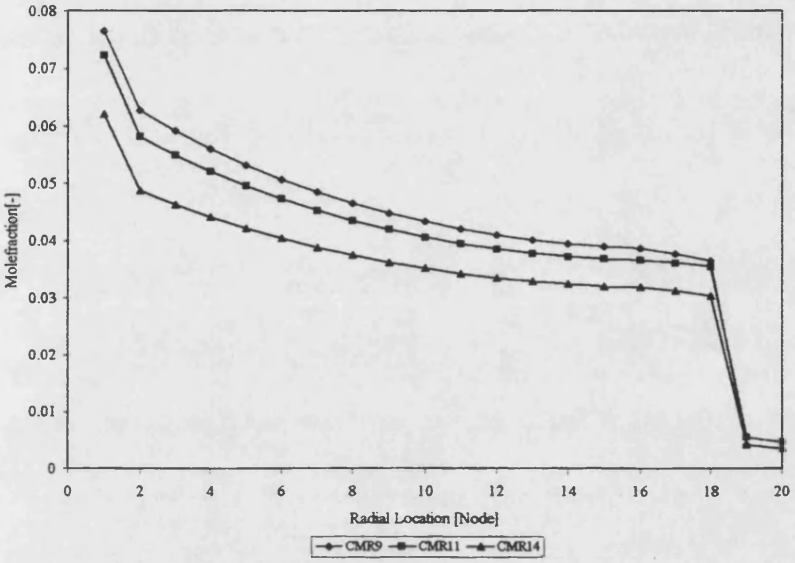

Figure 9.27: Calculated methanol molefraction profiles at z=0.11m

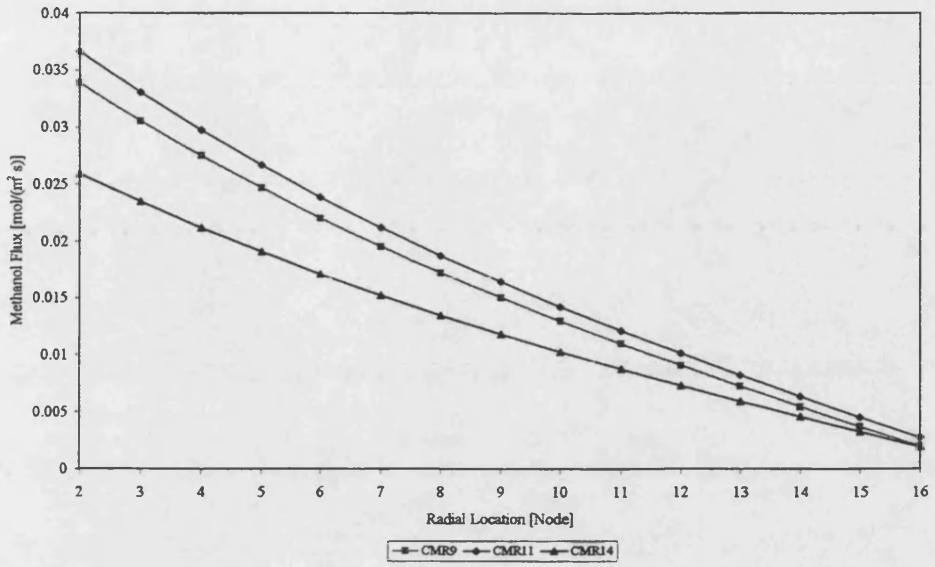

Figure 9.28: Calculated methanol fluxes at z=0.11m

Figure 9.29 and Figure 9.30 show the hydrogen molefraction profiles and fluxes for the three experiments. It is apparent that the hydrogen molefraction is increasing throughout the catalytically active layer for CMR 11. However the hydrogen flux again goes though zero and hydrogen leaves the catalytically active layer in both directions. The behaviour is similar but not as pronounced for the hydrogen molefraction profile of experiment CMR 14. Another important observation is that the hydrogen backflux into the tubeside of the membrane reactor is lowest for CMR 14 whilst the flux in the direction of the membrane shellside is in-between those of CMR 11 and 9. This indicates, in conjunction with the methanol fluxes given in Figure 9.27, that using a high purge to feed flowrate ratio is beneficial for separation efficiency.

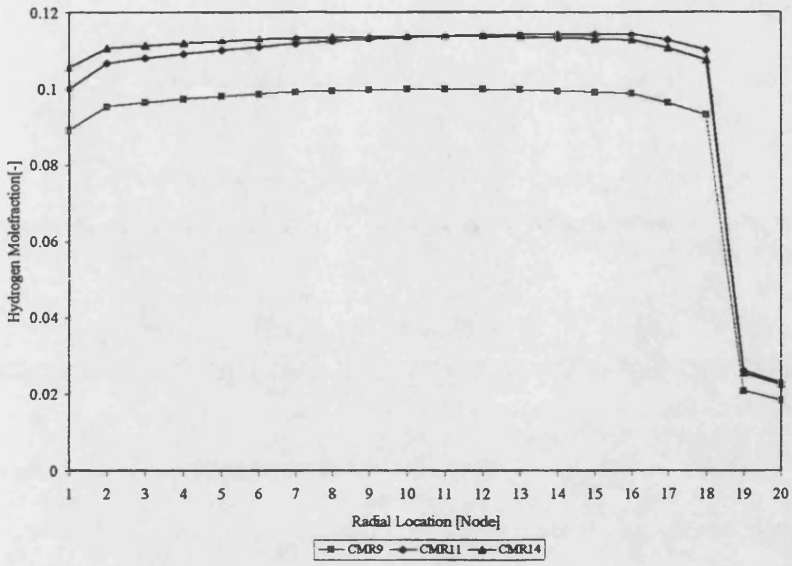

Figure 9.29: Calculated hydrogen molefraction profiles at z=0.11m

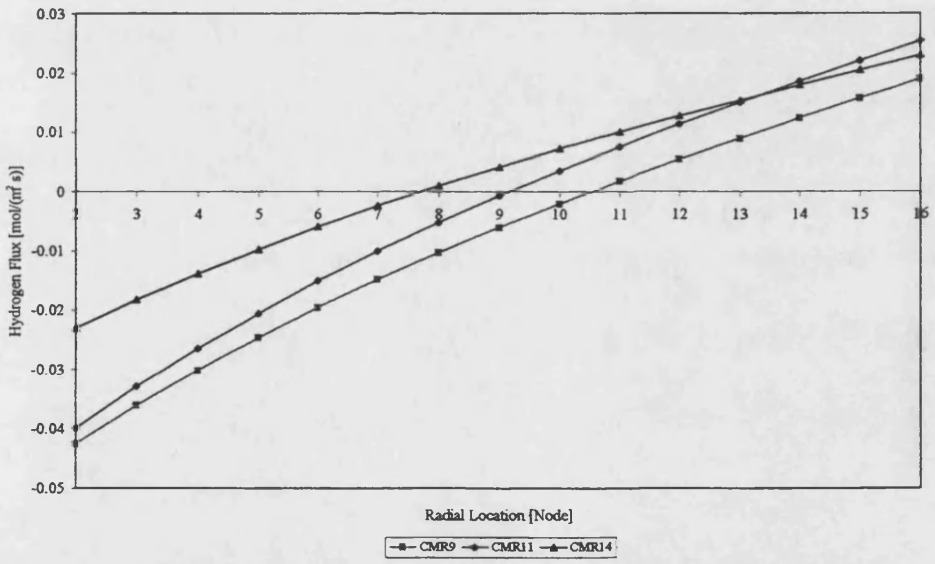

Figure 9.30: Calculated hydrogen fluxes at z=0.11m

The axial temperature profiles for the three experiments are shown in Figure 9.31. The highest and lowest temperatures throughout the reactor are calculated for CMR 11 and CMR 9, respectively. The temperature profile for CMR 14 initially increases due to the

high transmembrane driving force created by the high purge to feed flowrate ratio which thus increased the conversion. About halfway along the reactor length, an increased transport of energy out of the reactor causes the temperature to decrease more strongly than in the two other cases investigated. This higher energy transport is also due to the purge to feed gas flowrate ratio.

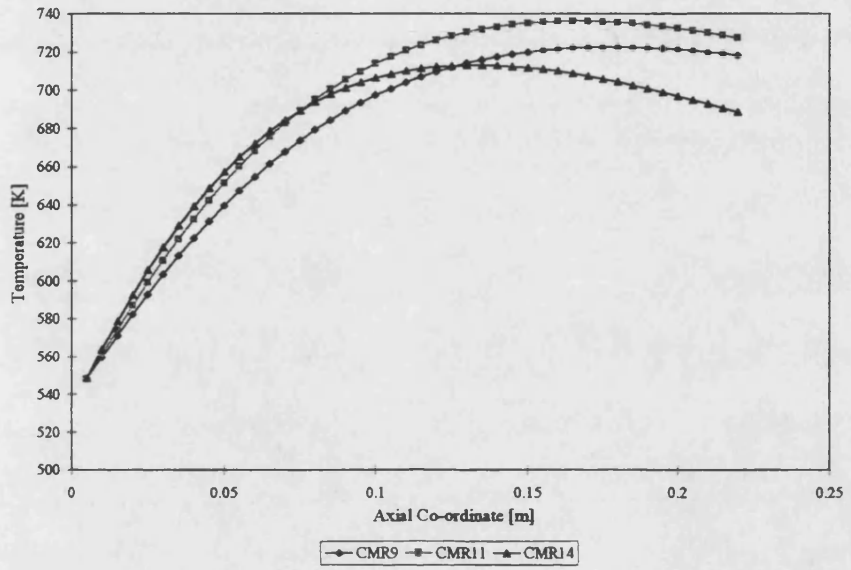

Figure 9.31: Calculated axial temperature profiles

All the transport and reaction phenomena expected inside a tubular catalytic membrane reactor are accounted for by the proposed model. The discrepancies between measured and calculated results are probably due to the following factors:

- Underestimation of the extent of the methanol oxidation reaction.
- Additional experimentally observed components methane and carbon monoxide were not accounted for in the model.
- Only the innermost membrane layer was assumed to be catalytically active. However, it was likely that platinum was also deposited into the outer support layers of the experimentally investigated membranes (see Chapter 6).

A further discrepancy could be that the mass and heat transfer coefficients on the tube- and shellside of the membrane reactor were estimated incorrectly, owing to the employed corellations used for their calculation. This would result in miscalculated component and energy fluxes to and from the catalytically active membrane layer.

Apart from the apparent discrepancies between the calculated and experimental results, the model provides a qualitative picture of the membrane reactor and can serve to explain some of the phenomena observed experimentally. The most important difference is that as the desired reaction product, *e. g.* hydrogen, is produced in the catalytically active layer, the driving force exerted upon this component changes sign in the catalytically active layer. Hence part of the products accumulate in the tube- and part in the shellside. The faster diffusion rate of hydrogen in the support layers and in the shellside boundary layer enhances separation compared with the other reaction products. However, this separation is too small to supply a hydrogen feedstock of the required purity for a fuelcell.

9.8 Computer code

The models described in this section were implemented by means of computer programs written in ANSI C.

The separation model was compiled under Borland Turbo C++ 3.0 on an IBM compatible PC with an Intel 486-66MHz processor and 16MB of RAM and under GNU CC 2.7 on different Sun Sparc workstations. The source code is contained on the attached floppy diskette under the directory "sepmod".

The reaction and separation model was compiled with Microsoft Visual C++ 4.0 and 5.0 on an IBM compatible PC with an Intel PentiumII 300 MHz processor and 128MB of

RAM. The execution of the program was also tested on an IBM RS6000/590 workstation equipped with IBM's proprietary C compiler and on Sun Sparc workstations equipped with GNU CC 2.7 compilers. The source code is contained on the attached floppy diskette under the directory "reacmod".

The numerical routines used in the programs were taken from Press *et. al.* (1992), except for the Eigensystem routines required for the mass transfer coefficient evaluation which came from Smith *et. al.* (1976).

CHAPTER 10
CONCLUSIONS AND FUTURE WORK

10.1 Conclusions

The subject of this study was to investigate the oxidative dehydrogenation of methanol to hydrogen in a catalytic membrane reactor in order to provide a feedstock for fuelcells. The purpose of the membrane reactor was twofold: production of hydrogen by means of the dehydrogenation reaction and separation of the hydrogen produced from other reaction products and unconverted reactant.

As no standard membrane reactor was commercially available during the course of this study, a membrane reactor was designed and manufactured. The most important design considerations were to ensure that the ends of the ceramic catalytic membrane were sealed gas-tight into the stainless steel housing and that the sealing mechanism allowed for the considerably different thermal expansion coefficients of stainless steel and alumina. The performance of the designed membrane reactor (Figure 3.8) was tested in separation and reaction environments (Chapter 8). It was shown by comparison with a previously published study, employing the same type of membrane (Jia *et. al.* 1994), that the designed membrane reactor fulfilled the expectations regarding the sealing mechanism (Table 8.1). The performance of the material from which the "O"-ring seals were manufactured emerged as an important factor in the separation and reaction studies (described in Chapter 8). Whilst the elastomer compound Kalrez (provided by DuPont) performed well in the separation experiments, this was not the case for the graphite seals employed in the reaction experiments. The seals appeared to deteriorate with increasing number of experiments carried out. Hence it appeared necessary to develop a new generation of high temperature seals which would be employed in situations where the relative movement of reactor parts occurs as in membrane reactors.

The thermodynamic calculations described in Chapter 4 suggest that the oxidative dehydrogenation of methanol yields high contents of water, carbon dioxide and methane at equilibrium. Furthermore the content of the desired product, hydrogen, was found to increase with increasing temperature. A rather large extent of carbon formation was also predicted. Other components commonly encountered in reactions involving methanol as a reactant, *e. g.* formaldehyde and dimethylether, were not predicted by the thermodynamic equilibrium calculations. The investigations into the reaction network, described in Chapter 7, showed that the reaction mechanism could be described by two reactions: the oxidative dehydrogenation of methanol and the total oxidation of methanol. The heats of reaction for these two reactions were also calculated in Chapter 4. The oxidation reaction showed a higher standard heat of reaction (-675.98kJ/mol) than the oxidative dehydrogenation reaction (-192.34kJ/mol).

A total of six catalysts was investigated in the catalyst screening experiments reported in Chapter 5. Platinum supported on activated alumina emerged as the best catalyst for the production of hydrogen from methanol in an oxidising environment. It exhibited a high selectivity (more than 70%) towards hydrogen at the lowest temperatures (approximately 360°C) and high methanol conversions (more than 80%) with no detectable degree of carbon deposition on the catalyst. Nickel oxide and copper oxide supported on activated alumina also showed a high selectivity towards hydrogen, although at a higher temperature level. The three aforementioned catalysts are typical oxidation catalysts whilst vanadium(V)oxide and molybdenum(VI)oxide are typical dehydrogenation catalysts. Experiments using these two catalysts showed a high extent of coking and also a low selectivity towards hydrogen (less than 20%). The molefractions of water, carbon monoxide and methane, *e. g.* undesired reaction products, detected in the experiments using the dehydrogenation catalysts exceeded those measured in the experiments using oxidation catalysts. The catalytic activity of activated alumina was tested also but no conversion could be detected. The conclusions of the catalyst screening investigation were that oxidation catalysts are best suited to promote the oxidative dehydrogenation of

methanol whilst dehydrogenation catalysts showed a poor performance. A simple isothermal model indicated that external mass transfer resistance was not the rate controlling step in the catalyst screening experiments. As the operating conditions made the occurrence of an external mass transfer gradient likely, it is probable that a combination of chemical reaction rate, internal and external mass transfer controlled the integral conversion. If the results of the screening experiments are compared with the thermodynamic equilibrium calculations, it is apparent that a careful choice of catalyst and operating conditions can deter unfavourable equilibrium.

As no catalytic membranes were commercially available during the course of this study, multilayered alumina membranes were used as the precursor for the catalytic membranes. Platinum was deposited into the pore structure of the membrane by means of impregnation with chloroplatinic acid and subsequent reduction. The method employed (Uzio *et. al.* 1993) ensured that platinum was distributed into the membrane. However, it was impossible to validate that the majority of the platinum was deposited within the inner, 4μm thick γ-alumina layer as desired. In fact, visual inspection of the prepared catalytic membranes showed grey coloured areas on the outer circumference of the membrane, and such colour is characteristic for platinum deposition.

The literature review (Chapter 2) shows that no publication regarding kinetics of the oxidative dehydrogenation of methanol was available prior to this study. Hence it was necessary to determine the reaction kinetics experimentally. As these reaction kinetics should also be applicable to the catalytic membrane, catalyst pellets were produced using a method closely related to the method used for the catalytic membrane. The support used was γ-alumina. The platinum distribution within the pellets showed typical "egg-shell" formation the extent of which decreased with decreasing particle size.

In order to minimise the extent of intraparticle mass transfer, finely ground γ-alumina particles were impregnated with chloroplatinic acid and applied to the inside of a ceramic tube section for use in the tubular wall reactor.

Two types of reactor were used to investigate the reaction kinetics: a spinning basket reactor and a tubular wall reactor. For the spinning basket reactor experiments, the pelleted catalyst was used. An important result of the experiments carried out to determine the speed of revolution at which external mass transfer was not influencing the observed reaction rate, was the decrease of selectivity towards hydrogen with increasing speeds of rotation (Figure 7.3). It can hence be concluded that the presence of external mass transfer resistances favours the production of the desired product. It was not possible to employ a small enough particle size in the spinning basket reactor to ensure the absence of internal gradients. However, two series of kinetic experiments were carried out in the spinning basket reactor, which gave some qualitative insight into the reaction mechanism. With increasing oxygen partial pressure, the production rates of hydrogen and carbon dioxide levelled off, accompanied by an increase in production of methane, carbon monoxide and water. This behaviour leads to the conclusion that apart from the oxidative dehydrogenation of methanol other reactions, as for example oxidation of methanol, combustion of hydrogen, methanisation and water gas shift were occurring.

External mass and heat transfer resistances could be assumed to be negligible in the tubular wall reactor as shown by theoretical calculations (Equations 7.5 and 7.6). Internal mass transfer was assumed not to influence the observed reaction rate because the $Pt/\gamma\text{-}Al_2O_3$ particles on the inside of the tubular segments had a particle size smaller than 50μm (Section 6.3). The reactor showed isothermal behaviour within the operation parameters employed in this study. As the conversion did not exceed 10%, the reactor could be considered as a differential reactor as opposed to the integral spinning basket reactor. A total of eight experimental series were investigated, determining the product

composition as a function of methanol and oxygen partial pressure at four different temperatures. The detected reaction products were hydrogen, carbon dioxide and water but no methane and carbon monoxide as in the spinning basket reactor and catalyst screening experiments. Hence it could be concluded that only initial reaction rates were measured. The proposed reaction combination consisted of the oxidative dehydrogenation of methanol (Equation 7.10) and the catalytic combustion of methanol (Equation 7.11). The measured production rates of carbon dioxide and water allowed this reaction mechanism to be fully described. A non-linear regression analysis of the measured carbon dioxide and water production rates provided power law descriptions of the two reaction rates (Equation 7.19) using the parameters given in Table 7.11. Thus it was possible for the first time (to the authors knowledge) to develop a partially quantitative description of the oxidative dehydrogenation of methanol and the accompanying oxidation of methanol.

The membrane reactor designed in this study was tested for single component permeation, separation and combined separation and reaction environments using the commercially obtained four-layered alumina membrane. The permeation experiments, carried out at a low temperature of 14.5°C, led to the conclusion that surface diffusion is of importance for readily adsorbed components such as carbon dioxide. The separation experiments were carried out at a constant temperature of 150°C and employed feed mixtures of nitrogen, hydrogen and carbon dioxide or methane. Argon was used as a purge gas. The transmembrane driving force was varied by increasing the permeate to feed flowrate ratio. For hydrogen, the ideal Knudsen separation factor with respect to nitrogen of 3.73 was approached with increasing transmembrane driving force. Carbon dioxide achieved its ideal Knudsen separation factor with respect to nitrogen for all investigated cases whilst the methane separation factor with respect to nitrogen was consistently lower. This lead to the conclusion that not only Knudsen diffusion was governing the material transport inside the membrane structure, but other effects as molecular diffusion, viscous flow and boundary layer resistances played an important role

as well. The overall hydrogen separation efficiency of the membrane assembly was poor, when compared with competing technologies such as pressure swing adsorption.

The separation model developed in Chapter 9 reflected the measured results well (Figures 9.10 and 9.11). It was shown that the treatment of the different membrane layers and the boundary layers between the membrane surfaces and the bulk gas on either side is important. Hence it is not sufficient to assume that the controlling mass transfer resistance lies in the layer with the smallest pore sizes, *e. g.* the γ-alumina layer with a pore size of 4nm, and to assume that mass transfer can be described by Knudsen diffusion alone. The Dusty Gas Model employed in this study allows for Knudsen and Maxwellian diffusion as well as viscous flow and hence is equally applicable to any of the porous membrane layers, whatever their pore size. Figure 9.13 shows the calculated radial composition and pressure profiles. It shows that the main effect of the layer with the smallest pore size is to decrease the pressure whilst changes in molefractions are small for all components considered. The separation effect occurs in the subsequent layers, which are characterised by a higher thickness and pore size. The separation is caused by a combination of Knudsen and Maxwellian diffusion.

For the reaction experiments, mixtures of methanol and oxygen diluted with nitrogen were fed into the tubeside of the membrane reactor whilst argon was employed as a purge gas to the shellside. The operation parameters which were varied were the transmembrane pressure drop and the purge to feed flowrate ratio. An increase of either of these parameters led to an increase in transmembrane driving force. The methanol conversion could be increased up to 84% by increasing this driving force and hence forcing more reactants into the catalytically active layer. The selectivity of the converted methanol towards hydrogen remained unaffected at a value between 50 and 55%. This is believed to be caused by a fast transport of hydrogen away from the reaction zone. The separation behaviour of the catalytic membrane reactor was poor. An increase in transmembrane driving force resulted in not only hydrogen, but also more heavy

components being forced through the membrane. Furthermore the reaction products were enriched on either side of the membrane as driving force gradients were present in both directions. This was caused by the production of these components in the catalytically active layer. Detrimental to the use of the shellside product as a feedstock for a fuelcell was the carbon monoxide present in this stream. This component acts as a poison for fuel cell electrodes and hence has to separated effectively.

The developed non-isothermal reaction and separation model introduced in Chapter 9 was based upon a non-isothermal separation model. The differential equations describing the material and energy balances in the active membrane layer were solved numerically. The two rate equations developed in Chapter 7 were used to describe the reaction combination. Using this model, it was possible to describe the two-dimensional composition and temperature distribution in the membrane reactor and thus provide an insight into the experimental behaviour observed in Chapter 8. The temperature behaviour could be described well (Figure 9.23). However, it was only possible to paint a qualitative picture with regard to the composition. This was because of the lack of information regarding the production of methane and carbon monoxide as well as a probable underestimation of the extent of the methanol combustion reaction. The result was an underestimation of the methanol conversion and an overestimation of the hydrogen selectivity. A further detrimental aspect was the uncertainty regarding the distribution of platinum in the porous structure as it was assumed that only the innermost layer was catalytically active. However, experimental evidence suggested that part of the platinum penetrated into the support layers, which were assumed to be catalytically inert in the mathematical model.

In summary it can be concluded that the oxidative dehydrogenation of methanol is a competitive candidate for the production of hydrogen if carried out in a reactor which is designed and operated with a degree of mass transfer resistance. As the mass transfer rates of hydrogen are higher than those of the other reaction participants, the mass

transfer resistances serve to transport the hydrogen product away from the catalytically active zones and so prevent it from further reacting to undesired products. A catalytic membrane reactor assembly is a good candidate for such a reactor, although the desired simultaneous separation was found to be negligible.

10.2 Future work

One important aspect of future work is to investigate the reaction mechanism further. The kinetic investigation reported in Chapter 7 can serve as a starting point. It would be necessary to investigate product inhibition and to account for the presence of carbon monoxide and methane in addition to hydrogen, carbon dioxide and water.

The membrane reactor operation has to be improved with respect to its separation efficiency. Novel membrane materials, as for example zeolite or silica, should be capable of separating hydrogen more effectively. One possible way would be to apply a layer of such material on the outer circumference of the type of membrane used in this study.

An alternative would be to employ a second process unit downstream of the reactor to facilitate the separation of hydrogen.

REFERENCES

Abdalla, B. K. and Elnashaie, 1993, S. E. H., *J. Membrane Sci.*, **85**, 229-239

Aspen Technology, 1997, *ADSIM 6.1-0 User Manual*, Aspen Technology, Cambridge Mass.

Bennet, C.J., 1990, Ph.D. Thesis, University of Bath

Bharadwaj, B., 1998, Ph.D. Thesis, University of Bath

Baerns, M., Hofmann, H. and Renken, A., 1987, *Chemische Reaktiontechnik*, Georg Thieme Verlag, Stuttgart

Bird, R. B., Stewart, W. E. and Lightfoot, E. N., 1960, *Transport Phenomena*, John Wiley and Sons, New York

Carberry, J. J., 1964, *Ind. Eng. Chem.*, **56**, 11, 39-46

Carberry, J. J., 1976, *Chemical and Catlytic Reaction Engineering*, McGraw-Hill, New York

Casanave, D., Giroir-Fendler, A., Sanchez, J., Loutay, R., Dalmon, J. A., 1995, *Catalysis Today*, **25**, 309-314

Champagnie, A. M., Tsotsis, T. T., Minet, R. G. and Webster, A., 1990, *Chem. Engng. Sci.*, **45**, 8, 2423-2429

Chanaud, P., 1995, Personal communication

Delmon, B., Grange, P., Jacobs, P. Ponclet, G., 1979, *Studies in Surface Science and Catalysis: Preparation of Catalysts II, Proceedings of the 2nd International Symposium on the Scientific Basis for the Preparation of Heterogenous Catalysts*, Elsevier Publishing Company, Amsterdam

Friedlander, J. and Bennet, C. O., 1965, *AIChE-IChemE Symp. Ser.*, 3, 34-40

Froment, G. F. and Bischoff, K. B., 1990, *Chemical Reactor Analysis and Design*, John Wiley and Sons, New York

Gmehling, J. and Kolbe, B., 1988, *Thermodynamik*, Georg Thieme Verlag, Stuttgart

Gobina, E. and Hughes, R., 1994, *J. Membrane Sci.*, **90**, 11-19

Gokhale, Y. V., Noble, R. D. and Falconer, J. L., 1995, *J. Membrane Sci.*, **105**, 63-70

Hayes, R. E., Kolaczkowski, S. T., Thomas, W. J. and Titiloye, J., 1995, *Proc. R. Soc. Lond.*, **448**, 321-334

Hofmann, H., 1972, *Kinetics of Catalytic Gas-Solid Reactions*, Proc. 5th Europ./2nd Int. Symp. Chem. Reac. Eng. Amsterdam, Elsevier Publishing Company, Amsterdam

Hsieh, H. P., 1991, *Catal. Rev.-Sci. Eng.*, **33 (1&2)**, 1-70

Jia, M-D., Baoshu, C., Noble. R. D., Falconer, J. L., 1994, *J. Membrane Sci.*, **90**, 1-10

Kast, W., 1988, *Adsorption aus der Gasphase*, VCH Verlagsgesellschaft, Weinheim

van Krevelen, D. W. and Hoftijzer P. J., 1949, *Recl. Trav. Chim. Pays-Bas*, **68**, 221-233

Krishna, R., 1987, *Chem. Eng. J.*, **35**, 75-81

Lender, Y. V., Krasnyanskaya, A. G., Leleka, V. E. and Nesterenko, 1985, N. T., *Khim. Prom.*, **2**, 76-77, translation: 1985, *The Soviet Chemical Industry*, **17:2**, 155-158

Lu, M., Xiong, G., Zhao, H. Cui, W, Gu, J. and Bauser, H., 1995, *Catalysis Today*, **25**, 339-344

Masakazu, S., 1985, *European Patent Application*, EP 0 130 068 A3

Mason, E. A. and Malinauskas, A. P., 1983, *Gas Transport in Porous Media: the Dusty Gas Model*, Elsevier Publishing Compnany, Amsterdam

Okubo, T., Harata, K., Kusakabe, K., Morooka, S., Auzai, H. and Akiyama, S., 1991, *Ind. Eng. Chem. Res.*, **30**, 614-616

Pantazidis, A., Dalmon, J. A. and Mirodatos, C., 1995, *Catalysis Today*, **25**, 403-408

Pereira J. R. and Calderbank P. H., 1975, *Chem. Eng. Sci*, 167-175

Perea, S. P., 1993, *Internal communcation University of Bath*

Perera, S. P., Howell, J. A., 1994, *Catalytic membrane reactors: state-of-the-art*, to be published

Press, W. H., Teukolsky, S. A., Vetterling, W. T. and Flannery, B. P., 1992, *Numerical Recipes in C*, Cambridge University Press, Cambridge

Rautenbach, R., 1990, *Vorlesungsumdruck Chemische Verfahrenstechnik*, RWTH Aachen

Rautenbach, R., 1991, *Vorlesungsumdruck Membranerfahren*, RWTH Aachen

Reid, C. R., Prausnitz, J. M. and Sherwood, T. K., 1997, *The Properties of Gases and Liquids*, McGraw-Hill, New York

Renz, U., 1989, *Vorlesungsumdruck Wärmeübertragung*, RWTH Aachen

Shu, J., Grandjean, B. P. A., van Neste and A., Kaliaguine, S., 1991, *Can. J. Chem. Eng.*, **69**, 1036-1060

Sloot, H. J., Smolders, C. A., van Swaaij, W. P. M. and Versteeg, G. F., 1992, *AIChE J.*, **38**, 6, 887-900

Smith, B. T., Boyle, J. M., Dongarra, J. J., Garbow, B. S., Ikebe, Y., Klema, V. C. and Moler, C. B., 1976, *Matrix eigensystem routines - Eispack guide*, Springer Verlag, Berlin

Sun, Y. M. and Khang, S. J., 1988, *Ind. Eng. Chem. Res.*, **27**, 1136-1142

Taylor, R. and Krishna, R., 1993, *Multicomponent Mass Transfer*, John Wiley and Sons, New York

Treybal, R. E., 1980, *Mass Transfer Operations*, McGraw-Hill, New York

Uemiya, S., Kajiwara, M. and Kojima, T., 1997, *AIChE J.*, **43**, 11A, 2715-2723

Uzio, D., Peureux, J. and Fendler, A. G., 1993, *Applied Catalysis*, **96**, 83

Uzio, D., Peureux, A., Giroir-Fendler, J. A., Dalmin, J. A. and Ramsay, J. D. F., 1994, *Studies in Surface Science and Catalysis*, **78**, 411-419

Veldsink, J. W., Versteeg, G. F., and van Swaaij, W. P. M., 1994, *J. Membrane Sci.*, **92**, 275-291

Walas, S. M., 1985, *Phase Equilibria in Chemical Engineering*, Butterworth Publishers, Boston

Wu, J. C. S., Gerdes, T. E., Pszczolkowski, J., L., Bhave, R. B. and Liu, P. K. T., 1990, *Separation Science & Technology*, **25**, 1489-1510

Yang, W. S., Wu, J. C. and Lin, L. W., 1995, *Catalysis Today*, **25**, 315-319

Zaka, Z. D., Minet, R. G., and Tsotsis, T. T., 1993, *J. Membrane Sci.*, **77**, 221-232

Zaman, J. and Chakna A., 1994, *J. Membrane Sci.*, **92**, 1-28

Zaspalis, V. T., van Prang, W., Keizer, K., van Ommen, J. G., Ross, J. R. H. and Burggraaf, A. J., 1991a, *Applied Catalysis*, **74**, 205-222

Zaspalis, V. T., van Prang, W., Keizer, K., van Ommen, J. G., Ross, J. R. H. and Burggraaf, A. J., 1991b, *Applied Catalysis*, **74**,223-234

Zaspalis, V. T., van Prang, W., Keizer, K., van Ommen, J. G., Ross, J. R. H. and Burggraaf, A. J., 1991c, *Applied Catalysis*, **74**,235-248

APPENDIX 1

CALIBRATION OF EXPERIMENTAL EQUIPMENT

A 1.1 Mass flow controllers

The four mass flow controllers used in this study were of the type Brooks 5850 TR with different maximum nitrogen flowrates at standard conditions (0.5l/min, 2.5l/min and twice 5l/min). The calibrations were carried out by the supplier of the mass flow controllers (Fisher-Rosemount, Prescal Technical Services, Oldham). If another gas than nitrogen was used with the mass flow controllers, conversion factors were used to adjust for this fact. The conversion factors are given in the mass flow controller operating manuals. The desired flowrate was controlled by supplying a voltage between 0 and 5V to the mass flow controller, where 5V was equivalent to the maximum flowrate. The voltage was controlled by a device manufactured at the University of Bath.

A 1.2 Calibration of peristaltic pump

The methanol was fed into the evaporator using a Watson-Marlow peristaltic pump. Calibration of the pump was carried out at three flowrates with the pump connected to the experimental apparatus in order to account for eventual effects of downstream pressure. Methanol was pumped into a system from a reservoir the weight of which had been determined beforehand. After an elapsed period of time, the weight of the reservoir was determined again. The difference between the weights was divided by the molar mass of methanol and the elapsed time. The results of this calibration are shown in Figure A 1.2.

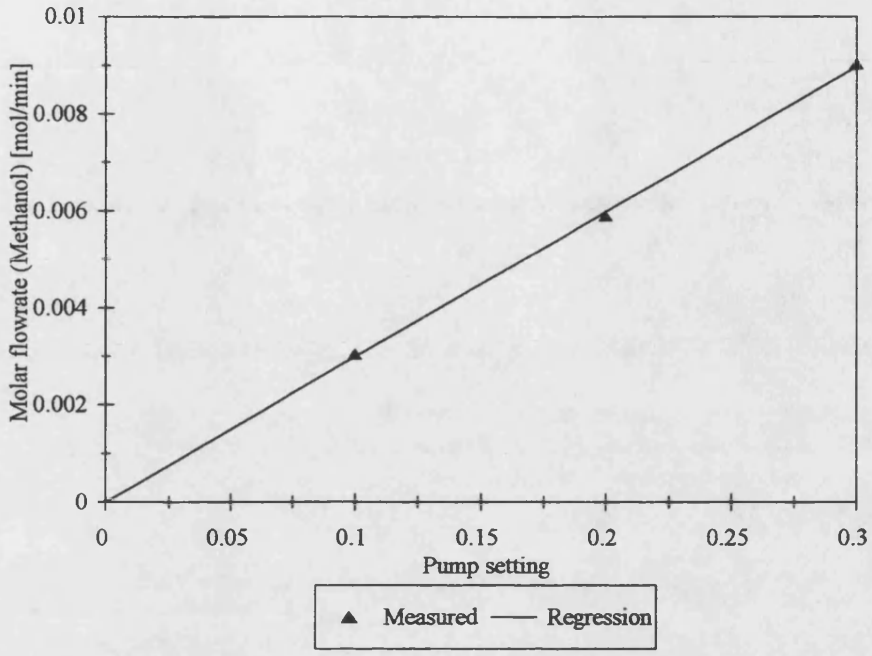

Figure A 1.2: Calibration of Watson-Marlow peristaltic pump

A 1.3 Pressure transducers

The pressure transducers used to measure the pressure up- and downstream the reactor were supplied by Druck Ltd and are of the type PDCR 10. They were calibrated by the supplier. The maximum pressure of 2 bara of the transducers is represented by an output voltage of 100.31 mV and 100.94 mV respectively. The output voltages of the pressure transducers is amplified by a factor of 50 by a amplifier circuit assembled in the department and subsequently fed to the data logging equipment. Hence the pressure detected by the transducers can be determined from the output voltage of the amplification circuit using Equation A 1.1:

$$p = P_{max} \frac{U_{out}}{50\ U_{max,in}} \qquad \text{(A 1.1)}$$

The subscripts in and out refer to the input and output of the amplification circuit, respectively.

The accuracy of the given calibration was checked by comparison with the barometric pressure which was determined using a barometer. The results are given in the following table.

Table A 1.1 Pressure transducer calibration

	Barometer	Pressure transducer 1	Pressure transducer 2
Pressure [bar]	0.997668	0.982306	0.990688
Error [%]	-	1.54	0.70

A 1.4 Differential pressure transducer

The differential pressure transducer was supplied by Druck Ltd. and of the type PDCR2161. The maximum difference pressure was 1bar, which was represented by a voltage of 99.69mV according to the calibration certificate. The differential pressure transducer was connected to the same amplifier circuit as described in Section A 1.3, so that the difference pressure could be calculated according to:

$$\Delta p = \Delta p_{max} \frac{U_{out}}{50\ U_{max,in}} \qquad \text{(A 1.2)}$$

A 1.5 Thermocouples

Temperatures were measured using BICC-Pyrotenax mineral insulated thermocouples (type K, CrAl-NiAl). The thermocouples were connected to a multiplexer board which in turn was connected to a analogue-digital conversion board. The digital signals were converted into the

respective temperature values according to the software delivered with the data-logging equipment (see Appendix 2). This conversion was to found to be correct within 1 °C when it was tested with two thermocouples by means of melting ice and boiling water.

APPENDIX 2
DATA LOGGING EQUIPMENT

As indicated in Chapter 3 and Appendix 1, the output signals of the pressure transducers, the differential pressure transducer and the thermocouples were processed electronically. The thermocouples were connected to a 16 channel multiplexer board (PCLD 789, supplied by Advantech Ltd). The thermocouple output signals were amplified according to a pre-selected gain and subsequently mutiplexed as an analogue signal to one input channel of the data acquisition card. For the used type K thermocouples, the recommended gain is 50. The board is equipped with a cold junction which supplies a reference temperature value needed for the calculation of the temperature from the output voltage of the thermocouple.

The output signals of the multiplexer board (the current thermocouple signal and the cold junction signal) as well as the amplified pressure transducer signals were fed in to four different analogue input channels of data acquisition card. This card is of the type PCL 812PG and supplied as well by Advantech Ltd. This card converts the analogue signals into digital ones which are fed into the computer. The computer used here is a Sperry PC equipped with 80286 processor.

The program included in the attached floppy diskette (directory "data")reads the data arriving from the different digital output channels of the data acquisition card and converts this digital data into real numbers. These numbers than can be processed in an usual manner. The temperatures and pressures are displayed on the computer screen. The reactor temperatures and the evaporator temperature are further plotted as a function of time. All the data is stored in an ASCII file, which can be loaded into spreadsheet programs for further processing of the data.

APPENDIX 3

CALIBRATION AND OPERATION OF THE GAS CHROMATOGRAPH

The gas chromatographic system was used for the determination of the composition of product streams. The gas chromatograph used was a Perkin-Elmer Autosystem GC. It was equipped with pneumatically driven gas sampling valve, enabling the injection of a defined amount ($1cm^3$) of gaseous sample into the system. Furthermore was it possible to inject liquid samples by means of a syringe into a packed injector. The samples were injected into a helium carrier gas stream. The gas stream was subsequently led into the column in order to separate the components. Two columns were used in this study: a Porapak S and a molecular sieve 5A column. The former was used for the analysis of methane, carbon dioxide, methanol and water whilst the latter separated hydrogen, oxygen, nitrogen, methane and carbon monoxide.

The GC was equipped with a Thermal Conductivity Detector (TCD) and a Flame Ionisation Detector (FID). On leaving the chromatographic column, the sample was first led to the TCD. This detector is non-destructive and compares the thermal conductivity of the sample gas stream with the one of a reference gas (the pure carrier gas). By means of this comparison, a measure of the concentration of the components could be obtained. This detector was used for the investigation of the permanent gases and water. The FID was used for the analysis of organic compounds. On entering the detector the sample is mixed with hydrogen and air and subsequently burned. This procedure generates ions. The concentration of ions is proportional to the amount of component present. The ions are collected by means of an electrical field and hence an electrical signal, proportional to the concentration, is produced.

The detector signals are led to a Perkin-Elmer model 1020 integrator and control computer. Here the signals were plotted as functions of time and the areas underneath the peaks representing the components were integrated. These areas were proportional to the concentration of the components in the investigated sample. The second function of the

integrator is to control the GC. The control parameters were set in the GC method. Here values as run time, injector, oven and injector temperatures, temperature ramps, gas flowrates, sample valve opening times, signal attenuation, detector sensitivity etc. were set.

The analysis of permanent gases with the molecular sieve column and the TCD was carried out using the following conditions:

Oven temperature:	50°C
Detector temperature:	200°C
Carrier and reference gas flowrate:	30 ml/min.

The method used for the Porapak S column consisted of the following basic parameters:

Oven temperature:	80 to 160°C at 16°C/min
Detector temperature:	250°C (FID), 200°C (TCD)
Carrier and reference gas flowrate:	30 ml/min.

In the latter method, both detectors were used according to the component which currently was analysed. Hence the signals supplied to the integrator were switched with respect to the retention time of the specific components.

All carried out calibrations resulted in a linear relationship between peak-area and concentration. Because hydrogen has a higher thermal conductivity than all the other components, including the carrier gas, its peak would have been negative. However, it is possible to reverse the TCD polarity, which results in a positive peak.

The calibrations can be expressed mathematically by:

$$y_i = b_i + s_i A_i \qquad \text{(A3.1)}$$

Table A3.1 shows the values for the different components in the gas phase analysis.

Table A3.1: Gas-phase calibration parameters

Component	Detector	Column	Retention time [min]	x-intercept b	Slope s
H_2	TCD	Mol-Sieve 5A	0.800	23.3098	2.1×10^{-6}
O_2	TCD	Mol-Sieve 5A	1.585	0	2.9×10^{-7}
N_2	TCD	Mol-Sieve 5A	2.890	0	2.8×10^{-7}
CH_4	TCD	Mol-Sieve 5A	4.915	0	3.4×10^{-7}
CH_4	FID	Porapak S	0.560	0	3.1×10^{-7}
CH_3OH	FID	Porapak S	5.811	0	1.3×10^{-7}
CO	TCD	Mol-Sieve 5A	12.028	0	2.8×10^{-7}
CO_2	TCD	Porapak S	0.770	0	4.7×10^{-7}

If the listed values for *b* and *s* are inserted into Equation A3.1 together with the measured peak area, the mole fraction in percent is obtained. The permanent gas calibrations were carried out using a Scotty II calibration gas mixture (supplied by Alltech Asc.), consisting of 4.22% H_2, 4.92% O_2, 4.99% N_2, 3.99% CH_4, 5% CO and 5% CO_2. Reliable gas phase calibration samples were found not to be available for methanol. Hence its calibration parameters were determined using the GC-analysis of the feed stream to the reactor. The methanol concentration in the feed stream could be evaluated as described in Appendix 4.

The contents of water and methanol in the liquid phase reaction product was analysed using a sample out of the cold trap content. A sample of 500 µl was mixed with 2000 µl iso-propanol. 0.1 µl of this sample was then injected by means of a syringe into the injector of the GC. The analysis was carried out using the Porapak S column and the TCD detector. This analysis yielded the molefractions of water and methanol in the liquid product from which the

gas phase molefractions prior to the cold trap could be calculated as described in Appendix 4.

The method used consisted of the following basic parameters:

Injector temperature:	200°C
Oven temperature:	132 to 160°C at 5°C/min
Detector temperature:	250°C (FID), 200°C (TCD)
Carrier and reference gas flowrate:	30 ml/min.

The calibration method used for this analysis was the internal standard method. Four liquid samples consisting of known amounts of water, methanol and iso-propanol were prepared and 0.1 μl of each sample was injected. The concentration ratios of water and methanol were then plotted versus the obtained respective area ratios and a linear least square fit was carried out. Figure A3.1 shows the measured data points and the best fit lines.

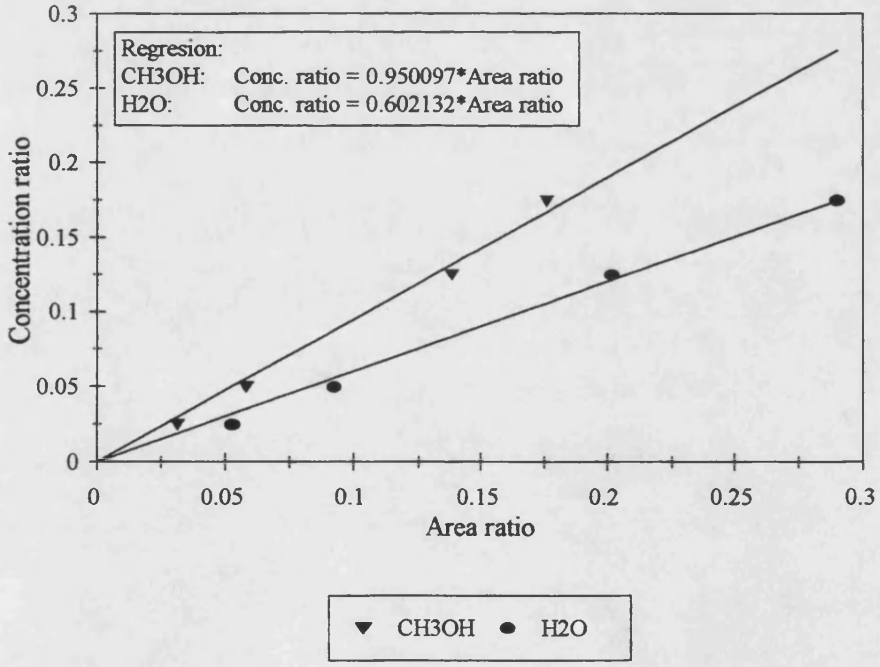

Figure A3.1: Internal standard calibration of methanol and water

The liquid samples taken from the cold trap after each experiment were prepared such that the iso-propanol concentration was known. Hence the methanol and water mole fraction in the sample could be determined using the peak areas obtained by the GC analysis in conjunction with the calibration lines depicted in Figure A3.1.

Figure A3.2 and Figure A3.3 show chromatograms using the molecular sieve 5A column and the Porapak S column for gas phase analysis, respectively. Figure A3.4 shows a chromatogram resulting from a liquid phase analysis using the Porapak S column. The chromatograms were created during one of the spinning basket reactor experiments reported in Chapter 7. It is apparent from Figure A3.2 that the TCD baseline suffers from high noise level during the first minute of elution time. This high noise level was caused by the high detector sensitivity required to detect hydrogen. For the detection of O_2, N_2 and CO lower sensitivities could be used. The noise at about 4.9min stems from CH_4. This component as well as CO_2 and the CH_3OH remaining in the gas phase downstream of the cold trap were analysed using the Porapak S column (Figure A3.3). Figure A3.4 shows the liquid phase analysis of the cold trap content with iso-propanoal as the internal standard.

The chromatograms presented in Figure A3.2 to Figure A3.4 are representative for the majority of experiments carried out in this study, *e.g.* oxidative dehydrogenation of methanol on $Pt/\gamma\text{-}Al_2O_3$ catalyst. Only the components H_2, O_2, N2, CH_4, CO, CO_2 and CH_3OH were detected by the chromatographic analysis. Other components commonly encountered in reacting systems involving CH_3OH as a reactant, such as formaldehyde, formic acid and dimethylether were not detected.

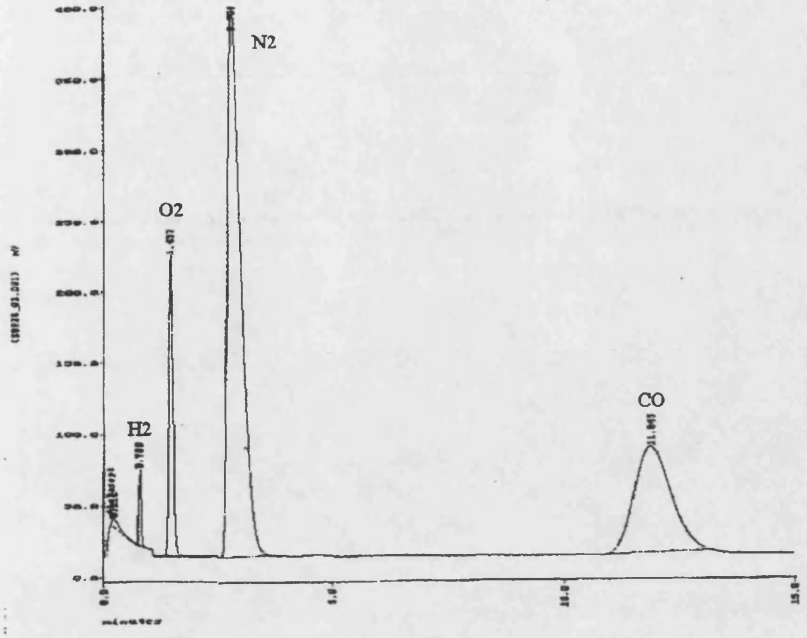

Figure A3.2: Molecular sieve 5A column chromatogram; analysis of H_2, O_2, N_2 and CO

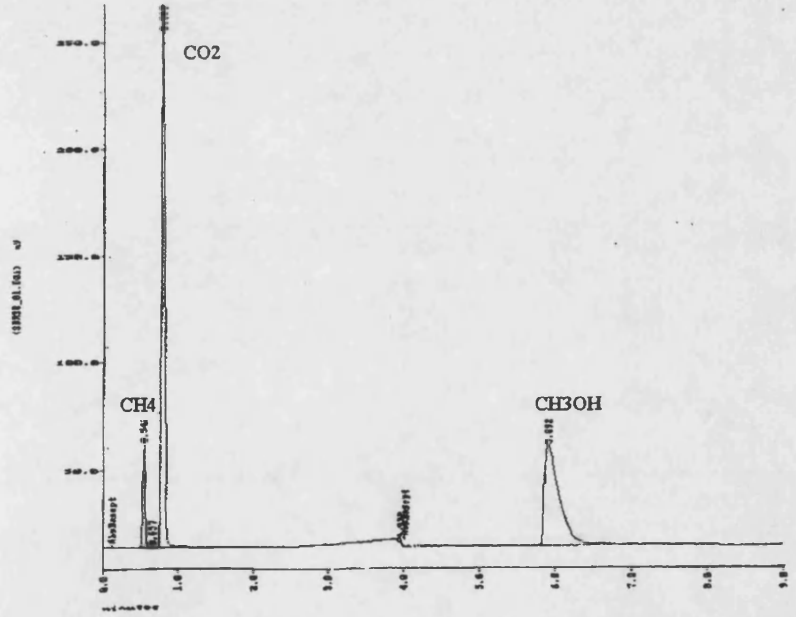

Figure A3.3: Porapak S column chromatogram; gas phase analysis of CH_4, CO_2 and CH_3OH

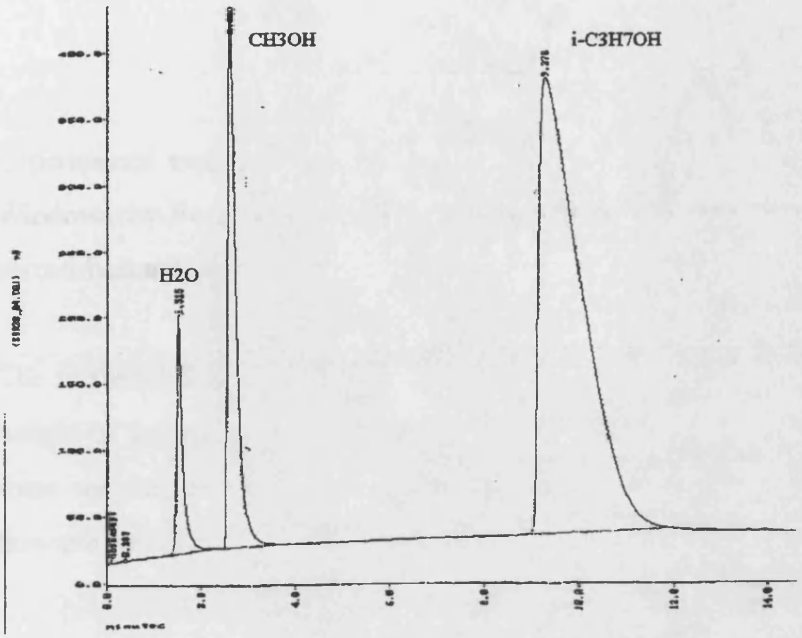

Figure A3.4: Porapak S column chromatogram; liquid phase analysis of H_2O and CH_3OH with iso-propanol as internal standard

APPENDIX 4

EXPERIMENT EVALUATION

Experimental evaluation was carried out using the spreadsheet software, Quattro Pro for Windows, by Borland Inc. In this section the procedure and equations implemented in this spreadsheet are described.

The methanol flowrate was set according to the calibration on the pump. Additionally the weight of the pump reservoir before and after the experimental run was determined. From these weights, the elapsed run time and the molar weight of methanol, the molar methanol flowrate was evaluated:

$$N_{CH_3OH} = \frac{1}{M_{CH_3OH}} \frac{m_{CH_3OH,start} - m_{CH_3OH,end}}{t_{run,pump}} \qquad \text{(A4.1)}$$

The molar flowrates of the gases fed into the experimental apparatus were determined by the mass flow controllers. As the mass flow controllers were calibrated in terms of volumetric flowrate at standard conditions (*i. e.*. 298.15K and 1.01325bar), the molar flowrates for each controller were determined according to:

$$N_{gas,MFC} = \frac{p_{std}\dot{V}_{gas,MFC}}{R_G\ T_{std}} \qquad \text{(A4.2)}$$

The total gas feed flowrate could be calculated by taking the sum over the single mass flow controller flowrates calculated according to Equation A4.2.

The mole fractions of the feed components were determined by:

$$y_{i,Feed} = \frac{N_{i,Feed}}{\sum_{j=i}^{ngas} N_{j,MFC,Feed} + N_{CH_3OH,Feed}} \qquad \text{(A4.3)}$$

where $y_{i,Feed}$ is the mole fraction of component i in the feed, $N_{i,Feed}$ is the feed flowrate of component i (either supplied by a mass flow controller or the peristaltic pump), *ngas* the number of permanent gases, $N_{j,MFC,Feed}$ is the mass flow controller supplied gas feed flowrate according to Equation A4.3 and $N_{CH3OH,Feed}$ is the methanol feed flowrate according to Equation A4.1. For membrane separation and reaction experiments, Equation A4.3 is applicable to the tubeside only. The feed flowrate of the shellside purge gas was evaluated according to Equation A4.1.

The concentrations of hydrogen, oxygen, carbon dioxide, carbon monoxide, methane, and methanol in the gas phase product after the cold trap were determined on-line by the GC according to Appendix 3. The compositions of methanol and water in the liquid sample were evaluated by means of gas chromatography using the internal standard method described in Appendix 3. In the case of membrane separation and reactor experiments, these steps were carried out for both the tube- and shellside products.

The volumetric flowrate of the permanent gases was measured using a bubble flowmeter and the molar flowrate evaluated by means of Equation A4.4:

$$N_{gas,Product} = \frac{p_{room}\dot{V}_{gas,Product}}{R_G\ T_{room}} \qquad \text{(A4.4)}$$

Again,. this evaluation was carried out for the tube-and shellside product in case of membrane operation.

The mass flowrate of the condensable components was calculated using following equation:

$$\dot{m}_{Cond} = \frac{m_{ColdTrap,end} - m_{ColdTrap,start}}{t_{ColdTrap,run}} \quad \text{(A4.5)}$$

Using the experimentally determined molar fractions in the liquid sample, the mean molecular weight of the condensed components was evaluated:

$$M_{av} = \sum_{i=1}^{nliq} y_{i,Liq} M_i \quad \text{(A4.6)}$$

Dividing the mass flowrate of the condensable components by the mean molecular weight gives the molar flowrate which can then be added to the molar flowrate of the permanent gases:

$$N_{Product} = N_{Gas} + N_{Liq} \quad \text{(A4.7)}$$

The total product mole fractions for permanent gases were evaluated according to:

$$y_{i,Product} = \frac{y_{i,Gas} N_{Gas}}{N_{Product}} \quad \text{(A4.8)}$$

As water could only be detected in the liquid phase, its total product mole fraction was calculated as:

$$y_{H_2O,Product} = \frac{y_{H_2O,Liq} N_{Liq}}{N_{Product}} \quad \text{(A4.9)}$$

Methanol appeared both in the liquid phase and in the gas phase product. Hence its product mole fraction was calculated as:

$$y_{CH_3OH,Product} = \frac{y_{CH_3OH,Gas} N_{Gas} + y_{CH_3OH,Liq} N_{Lig}}{N_{Product}} \quad \text{(A4.10)}$$

For experiments involving the membrane reactor, the calculations described by Equations A4.5 to A4.10 had to be carried out for the tube- and shellside product.

Using the feed (Equations A4.1 and A4.3) and the product (Equation A4.7) molar flowrates and the corresponding compositions, it was possible to carry out a mass balance for each of the atomic species present in the feed and product:

$$\left(N\sum_{i=1}^{nc} z_{ij} y_i\right)_{Feed} - \left(N\sum_{i=1}^{nc} z_{ij} y_i\right)_{Product} = \Delta N_j \quad \text{(A4.11)}$$

In Equation A4.11, z_{ij} is the number of atoms j in the molecule i. ΔN_j is the difference in the flowrate of atom j between feed and product. For membrane reactor operation, the appropriate for the shellside feed and product have to be added to Equation A4.11. Using ΔN_j, the closure of the mass balance for each atomic species present could be expressed by a percentage error:

$$\varepsilon_j = \frac{\Delta N_j}{\left(N\sum_{i=1}^{nc} z_{ij} y_i\right)_{Feed}} \times 100\% \quad \text{(A4.12)}$$

For membrane experiments, the appropriate term for the shellside feed had to be added to the denominator of Equation A4.12.

This error gave a means to decide whether an experiment had been conducted properly, if all important components had been taken into account or whether deposition of carbon had been

likely.

With the determined compositions and flowrates it was possible to evaluate the methanol conversion and the selectivity to hydrogen, the desired product:

$$X_M = \frac{N_{CH_3OH,Feed} - N_{CH_3OH,Product}}{N_{CH_3OH,Feed}} \quad \text{(A4.13)}$$

$$S_{H_2} = \frac{\Delta N_{CH_3OH,H_2}}{N_{CH_3OH,Feed} - N_{CH_3OH,Product}} \quad \text{(A4.14)}$$

In Equation A4.14, $\Delta N_{CH3OH,H2}$ is the amount of methanol consumed to produce hydrogen. For membrane reactor experiments both, tube- and shellside, had to be considered in Equations A4.13 and A4.14. The determined flowrates, compositions and temperatures made it possible to calculate hydrodynamical parameters, mass transfer coefficients etc. which were required for the analysis of the experiments carried out.

APPENDIX 5
REACTOR DESIGN DETAILS

The tubular wall reactor employed in this study was manufactured at the University of Bath. It is shown in Figure 3.7. Figure A5.1 shows the connection of the glass tube to the stainless steel flanges in more detail. In this figure, the positions of the baffles, the distributor disc, the thermocouples and the catalytic tube segment are detailed as well. Figure A.5.2 shows the detailed design of the flanges whilst Figure A5.3 shows the spacer design drawings. The spacer was placed into the reactor in order to reduce the crossectional flow area in the catalytically active region (see Figure 3.7).

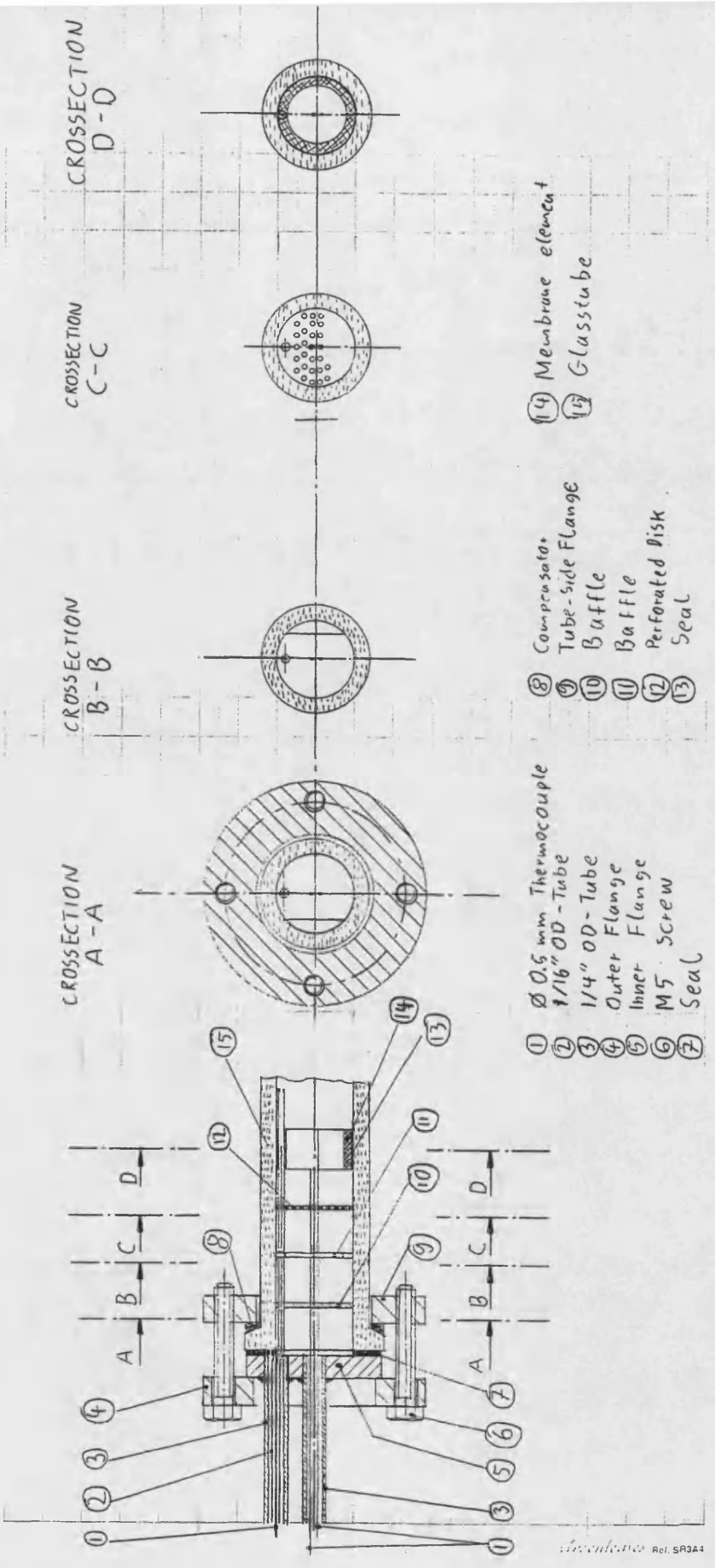

Figure A.5.1 Tubular wall reactor assembly

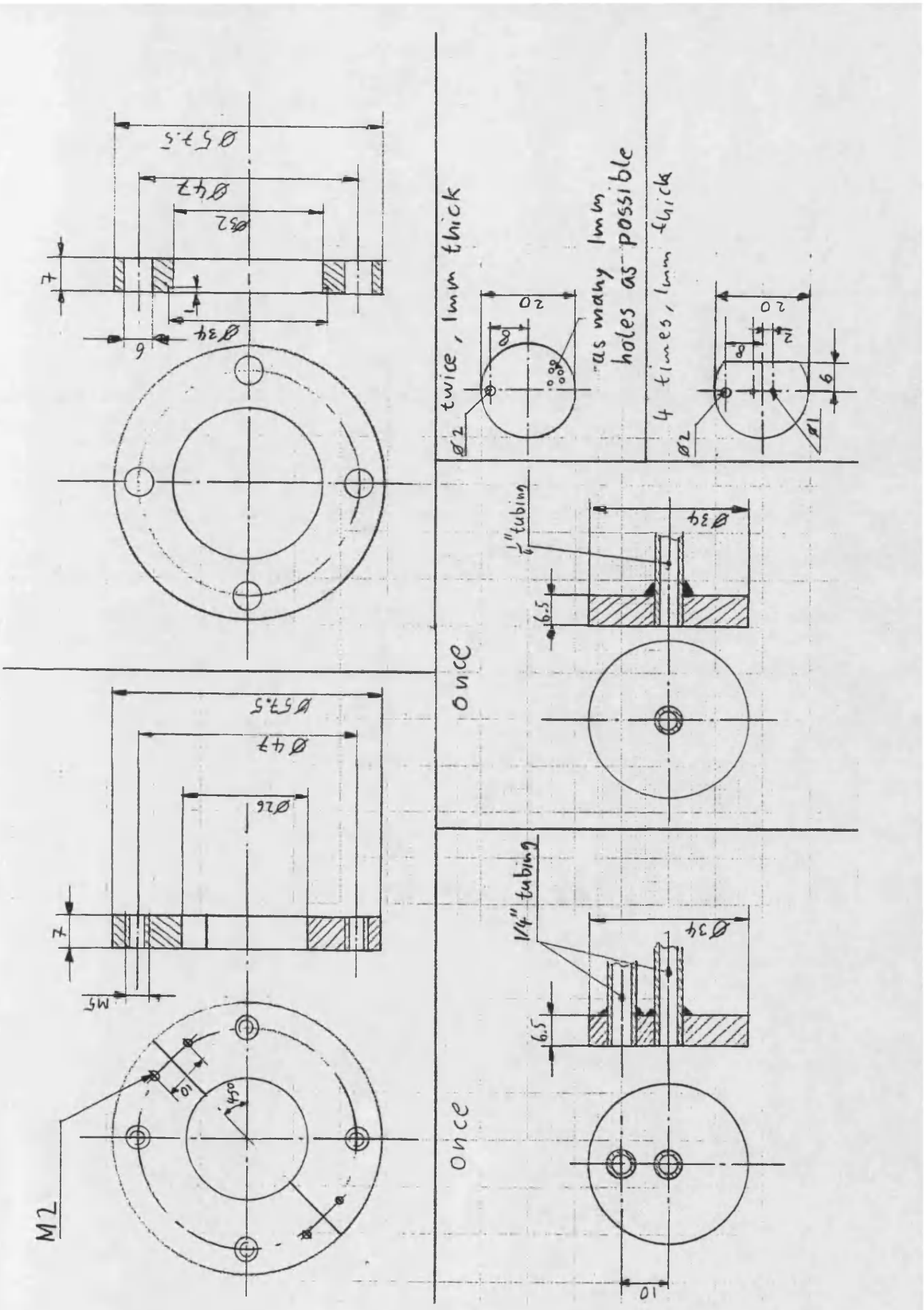

Figure A5.2: Tubular wall reactor flange design

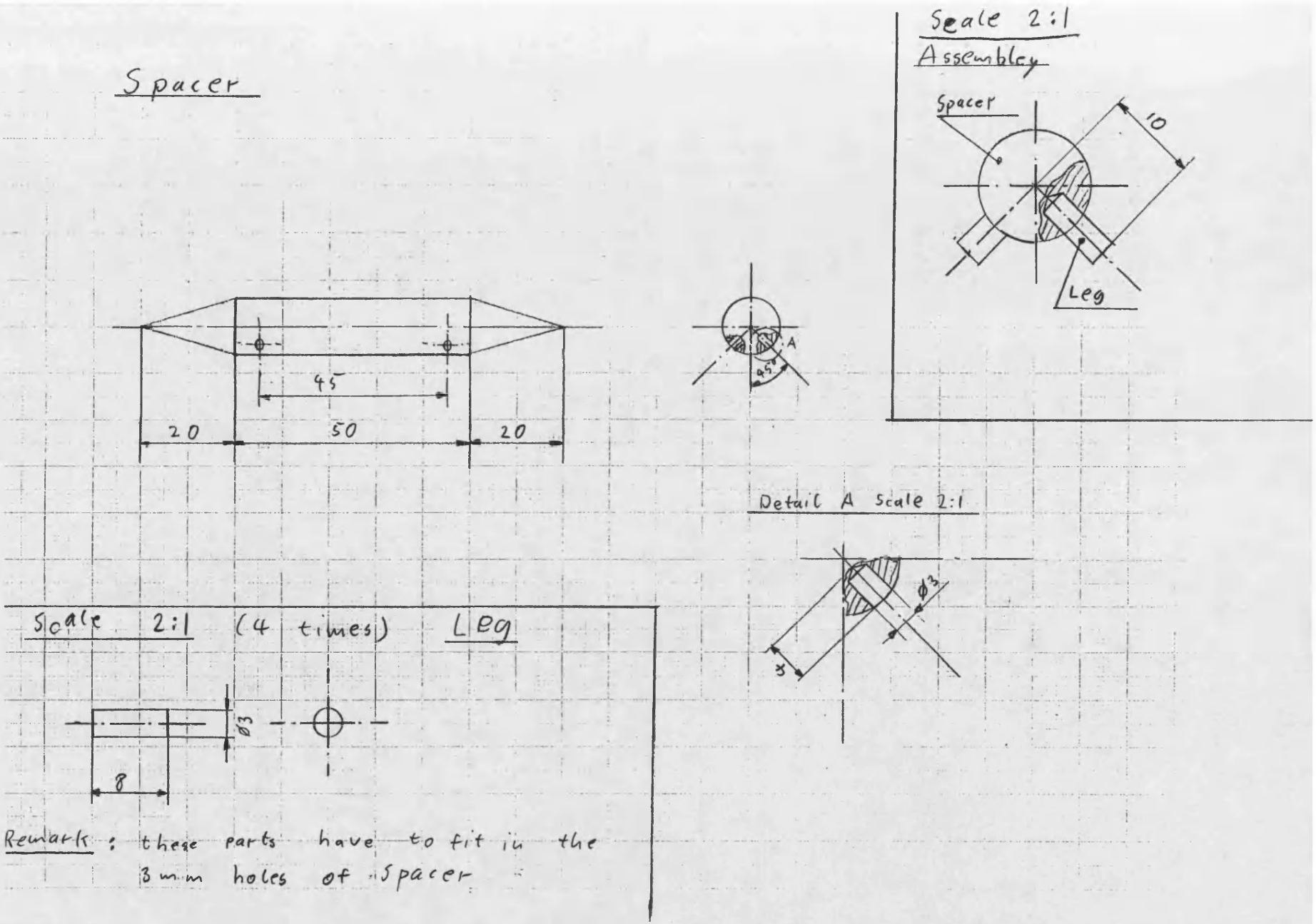

Figure A5.3: Tubular wall reactor flow insert

Figures A5.4 and A5.5 show the design drawings of the membrane reactor flanges annd shell. All parts are to be manufactured from 316 stainless steel. The most critical point of the reactor design is the sealing between the ceramic membrane tube and the flange shoulder (Figure 3.8). The sealing of the membrane tube against the reactor shell was achieved using a press disc (Figure A5.6). The application of the sealing meachnism is illustrated in Figure A.5.7. The "O"-ring material was either Kalrez (DuPont) or graphite, depending on the type of experimet (sparation or reaction) was carried out.

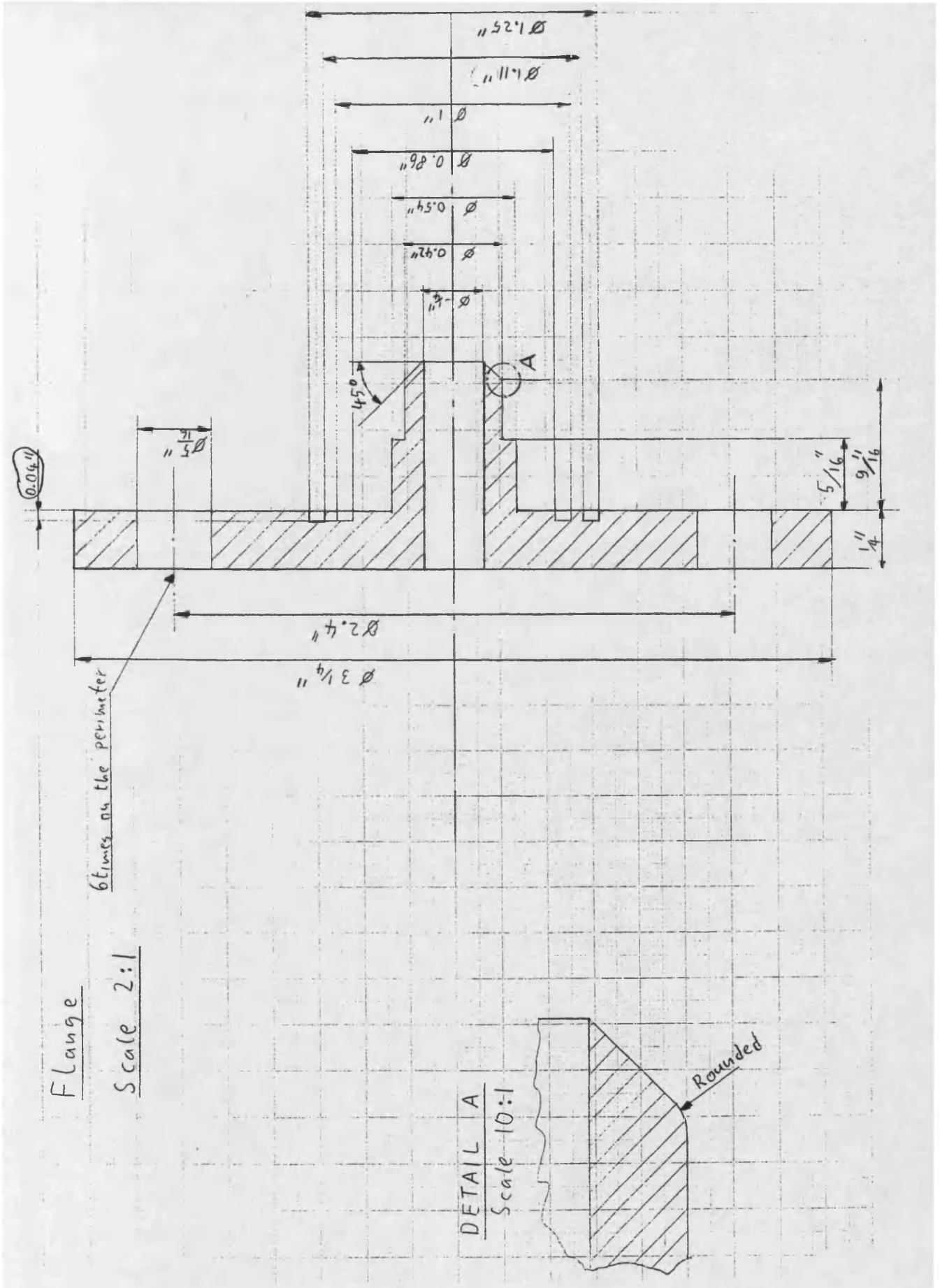

Figure A5.4: Flange design

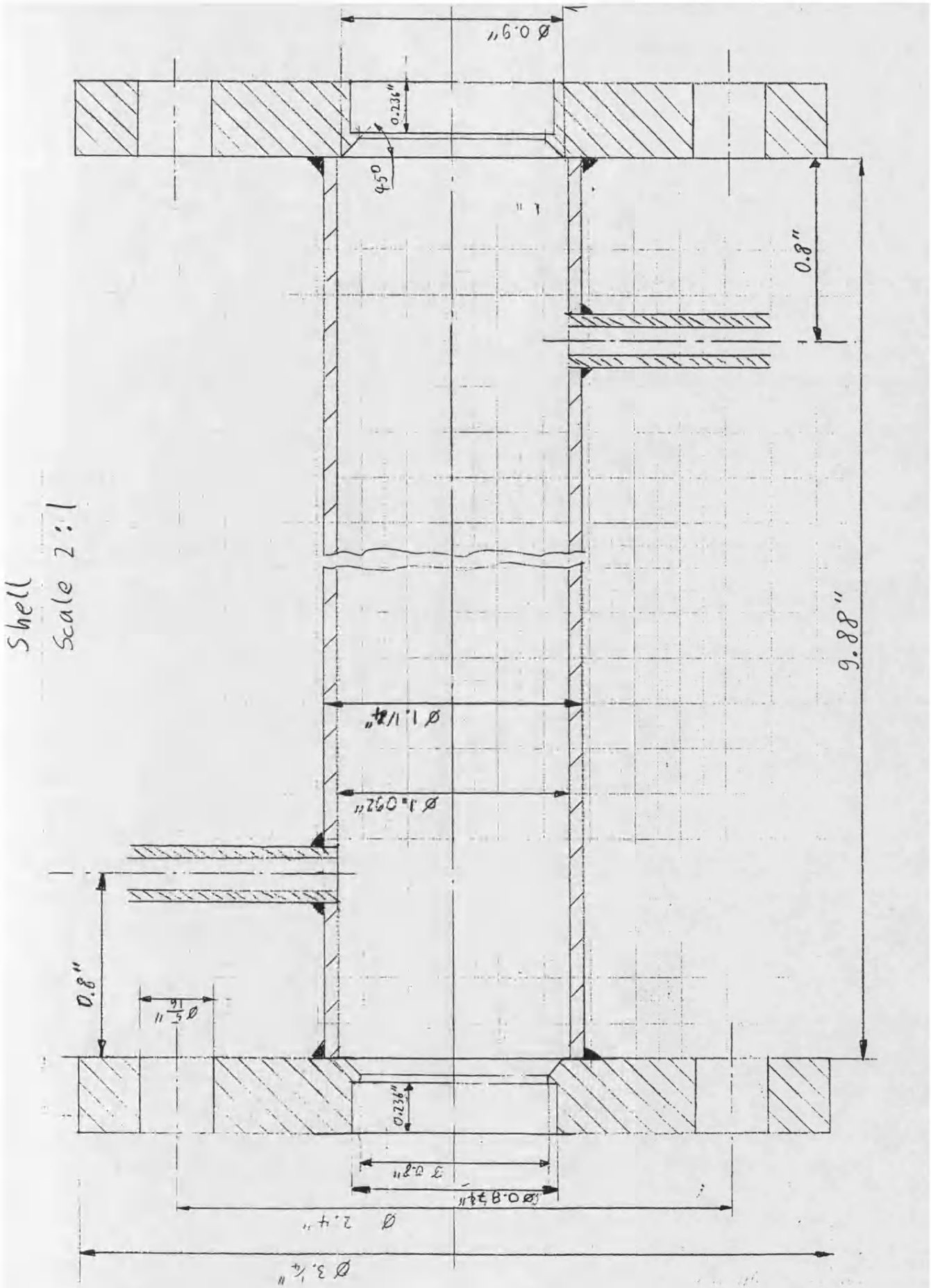

Figure A5.5: Shell design

PRESS DISK

Scale 2:1

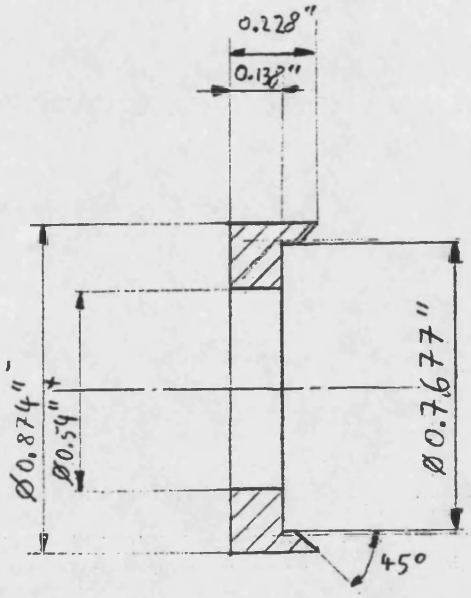

Figure A.5.6: Press disc

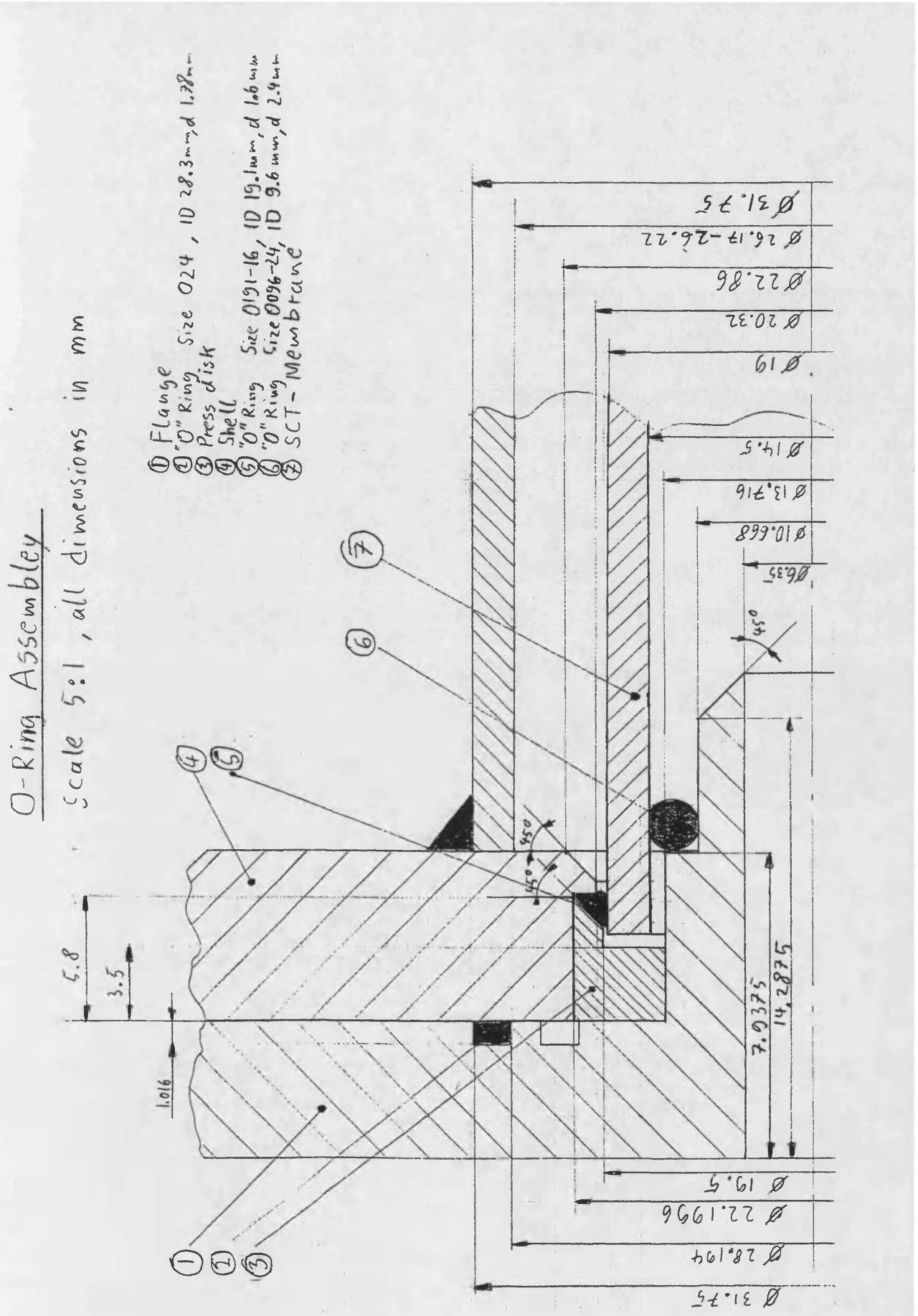

Figure A5.7: Sealing mechanism

APPENDIX 6

VOIDAGE OF THE PACKED BED REACTOR

The packed bed reactor used for the catalyst screening experiments reported in Chapter 5 consisted of a 1" OD and 0.8" ID stainless steel tube of 250mm length, 50mm of which were filled catalyst particles. All the examined catalysts, except γ-Al_2O_3 were of cylindrical shape with a diameter of 3.175 mm and a height of 3.175 mm. The voidage of the packed bed was determined in the following way: A 45.85mm long section of stainless steel tube of the above diameters was filled with 0.5 wt% Pt on γ-Al_2O_3 catalyst particles of the above dimensions. Subsequently, the mass of the pellets was determined by means of a balance (16.73g). By comparison with the weight of a known number of particles (20 particles have a weight of 1.2032g) the number of particles in the packing (n_p) was evaluated:

$$n_p = 16.73\,g \frac{20}{1.2032\,g} = 278 \qquad \text{(A6.1)}$$

With the known number of particles, the particle volume and the volume of the tube section it is then possible to calculate the voidage:

$$\varepsilon = 1 - \frac{n_p V_p}{V_T} = 1 - \frac{278 \times 25.1374 mm^3}{14868.82 mm^3} = 0.53 \qquad \text{(A6.2)}$$

APPENDIX 7

PHYSICAL PROPERTIES

A 7.1 Density

The temperature and pressure range encountered in this study justifies the use of the ideal gas law for the description of the temperature-pressure-specific molar volume relationship of a gaseous mixture:

$$p\,\overline{V} = R\,T \qquad \text{(A7.1)}$$

The density can then be calculated by dividing M_{av} by $\overline{V}$.

A 7.2 Viscosity

The viscosity was calculated as described by Reid *et. al.* (1977). For a monatomic gas at high temperatures and low pressures the viscosity can be derived as:

$$\mu = 26.69\,\frac{\sqrt{MT}}{\sigma^2\,\Omega_v} \qquad \text{(A7.2)}$$

This equation gives the viscosity in μP. It was found, that this equation is not only applicable to monatomic gases but to polyatomic ones as well. The parameter Ω_v is the collision integral. It can be calculated by means of the potential energy of interaction between two molecules. However, Reid *et. al.* (1977) recommended an empirical expression for Ω_v based on the Lennard-Jones potential:

$$\Omega_v = \frac{1.16145}{T^{*\,0.14874}} + \frac{0.52487}{\exp(0.77320\;T^*)} + \frac{2.16178}{\exp(2.43787\;T^*)} \qquad \text{(A7.3)}$$

In this equation T^* is a dimensionless temperature, defined by:

$$T^* = \frac{kT}{\varepsilon} \tag{A7.4}$$

The parameters ε and σ are the minimum of the potential energy between two molecules and the distance between two molecules where repulsion and attraction cancel each other respectively. They are tabulated in Reid *et. al.* (1977) for the most common gases.

In case the gas has a polar character, the collision integral has to be corrected. This can be done by adding the term

$$\frac{0.2\ \delta^2}{T^*} \tag{A7.5}$$

to the collision integral obtained by means of Equation A7.3. δ is a polar parameter given by:

$$\delta = \frac{\mu_p^2}{2\,\varepsilon\sigma^3} \tag{A7.6}$$

Here μ_p is the dipole moment which again is listed in Reid *et. al.* (1977).

In order to calculate the viscosity of a gas mixture the following mixing rule was recommended:

$$\mu_m = \sum_{i=1}^{N} \frac{x_i \mu_i}{\sum_{j=1} x_j \Phi_{ij}} \tag{A7.7}$$

The most reliable way of determining the binary parameter Φ_{ij} was found to be Brokaw approximation:

$$\Phi_{ij} = \left(\frac{\mu_i}{\mu_j}\right)^{0.5} S_{ij} A_{ij} \qquad \text{(A7.8)}$$

A_{ij} is determined by the molecular weight ratios:

$$A_{ij} = m_{ij} M_{ij}^{-0.5} \left[1 + \frac{M_{ij} - M_{ij}^{0.45}}{2\left(1+M_{ij}\right) + \frac{\left(1+M_{ij}^{0.45}\right) m_{ij}^{-0.5}}{1+m_{ij}}} \right] \qquad \text{(A7.9)}$$

The parameters m_{ij} and M_{ij} are defined by

$$m_{ij} = \left[\frac{4}{\left(1+M_{ij}^{-1}\right)\left(1+M_{ij}\right)} \right]^{0.25} \qquad \text{(A7.10)}$$

and

$$M_{ij} = \frac{M_i}{M_j} \qquad \text{(A7.11)}$$

The parameter S_{ij} equals 1.0 if both components are non-polar. If either δ_i or δ_j are larger than 0.1 , it has be calculated using the following equation:

$$S_{ij} = S_{ji} = \frac{1 + \left(T_i^* T_j^*\right)^{0.5} + \left(\delta_i \delta_j / 4\right)}{\left[1 + T_i^* + \left(\delta_i^2 / 4\right)\right]^{0.5} \left[1 + T_j^* + \left(\delta_j^2 / 4\right)\right]^{0.5}} \qquad \text{(A7.12)}$$

If the potential parameters ε and σ are not available for one component, they can be estimated according to Brokaw by the following equations:

$$\sigma = \left(\frac{1.585\ \overline{V}_b}{1 + 1.3\ \delta^2}\right)^{1/3} \qquad \text{(A7.13)}$$

$$\frac{\varepsilon}{k} = 1.18\left(1 + 1.3\ \delta^2\right) T_b \qquad \text{(A7.14)}$$

$$\delta = \frac{1940\ \mu_p^2}{\overline{V}_b\ T_b} \qquad \text{(A7.15)}$$

V_b and T_b in these equations are the molar liquid volume and the temperature at the normal boiling point.

Reid *et. al.* (1977) give as well a table comparing experimentally determined viscosities with the ones obtained using the different computational methods described by them. The difference between the method described here and experimental results lies in general within 5 %. However, for a 80 % H2 - 20% N2 mixture the computed mixture viscosity was 16 % higher than the experimentally determined one.

A 7.3 Binary diffusion coefficients

Binary diffusion coefficients for gases obeying the ideal gas law can be calculated in a similar manner as described in Section A 7.2 for pure component viscosities. Again, the calculation is described as recommended by Reid *et. al.* (1977). The diffusion coefficient of a binary gas

mixture consisting of components A and B can be written as:

$$D_{AB} = 1.858 \times 10^{-3} \; T^{3/2} \frac{\left[(M_A + M_B)/(M_A \; M_B)\right]^{1/2}}{p \; \sigma_{AB}^2 \; \Omega_D} \qquad \text{(A7.16)}$$

Ω_D in this equation is the diffusion collision integral. It can calculated in a similar manner as the viscosity collision integral (Equation A7.3):

$$\Omega_D = \frac{1.06036}{T^{*\,0.15610}} + \frac{0.19300}{\exp(0.47635 \; T^*)} + \frac{1.03587}{\exp(1.52996 \; T^*)} + \frac{1.76474}{\exp(3.89411 T^*)} \qquad \text{(A7.17)}$$

T^* is defined according to Equation A7.4, only that a binary parameter ε_{AB} is used. This binary parameter and σ_{AB} used in Equation A7.16 are calculated according to the mixing rules:

$$\frac{\varepsilon_{AB}}{k} = \left(\frac{\varepsilon_A}{k} \; \frac{\varepsilon_B}{k}\right)^{1/2} \qquad \text{(A7.18)}$$

$$\sigma_{AB} = \frac{\sigma_A + \sigma_B}{2} \qquad \text{(A7.19)}$$

In case either of the components A or B has a polar character, the collision integral according to Equation A7.17 has to be corrected by adding a correction term. This correction term has the same mathematical form as for the viscosity calculation (Equation A7.5):

$$\frac{0.19 \; \delta_{AB}^2}{T^*} \qquad \text{(A7.20)}$$

δ_{AB} can be calculated using the following mixing rule:

$$\delta_{AB} = (\delta_A \ \delta_B)^{1/2} \qquad \text{(A7.21)}$$

If σ, ε/k or δ are not available from tables as for example published by Reid *et. al.* (1977), they can be estimated using Equations A7.13 to A7.15.

As for the viscosity calculation Reid *et. al.* (1977) published tables in order to compare experimentally determined diffusion coefficients with those obtained from estimation methods. The maximum errors are again in the region of 15 %.

A 7.4 Mean effective binary diffusivity

In order to express multicomponent mass transfer, mean effective binary diffusivities are commonly used because otherwise the mathematically complex solution of the Maxwell-Stefan equations for multicomponent diffusion (see Chapter 9) would be necessary. This diffusivity is defined by the equation for the molar flux of a component j in a multicomponent mixture (Froment and Bischoff 1990):

$$N_j'' = -c_t \ D_{jm} \nabla y_j + y_j \sum_{k=1}^{nc} N_k'' \qquad \text{(A7.22)}$$

For ideal gases, the Maxwell-Stefan equations are given by:

$$-c_t \nabla y_j = \sum_{\substack{k=1 \\ k \neq j}}^{nc} \frac{y_k N_j'' - y_j N_k''}{D_{jk}} \qquad \text{(A7.23)}$$

By equating the driving force ∇y_j in Equations A7.22 and A7.23, the following expression for the mean effective diffusivity is obtained:

$$\frac{1}{D_{jm}} = \frac{\sum_{\substack{k=1 \\ k \neq j}}^{nc} \frac{1}{D_{jk}} \left(y_k - y_j \frac{N_k''}{N_j''} \right)}{1 - y_j \sum_{k=1}^{nc} \frac{N_k''}{N_j''}} \qquad \text{(A7.24)}$$

For a chemical reaction the molar flux ratios can be replaced by ratios of the stoichiometric coefficients:

$$\frac{1}{D_{jm}} = \frac{\sum_{\substack{k=1 \\ k \neq j}}^{nc} \frac{1}{D_{jk}} \left(y_k - y_j \frac{\nu_k}{\nu_j} \right)}{1 - \sum_{k=1}^{nc} y_j \frac{\nu_k}{\nu_j}} \qquad \text{(A7.25)}$$

This equation gives a mean diffusion coefficient for the diffusion of reactant or a product through a boundary layer towards or away from a reaction site.

APPENDIX 8

CALCULATION OF THE APPARENT DENSITY OF THE CATALYTICALLY ACTIVE MEMBRANE LAYER

The reaction rates for the oxidative dehydrogenation and the direct oxidation of methanol were measured and fitted to a power law expression ((Equation 7.19) in moles converted per unit catalyst mass and unit time in Chapter 7. In order to incorporate these rates into the material balance for the catalytically active membrane layer (Equations 9.7 and 9.9), which requires the reaction rates to be supplied in moles converted per unit catalyst volume and unit time, the apparent density of the catalytically active layer has to be employed. The SCT membrane employed in this study was investigated by Uzio *et. al.* (1993). This source quotes a mass of γ-Al_2O_3 per unit length of catalytically active layer of 0.25g/m. The length of the catalytically active layer of the membrane employed in Chapter 8 was 220mm with a thickness of 4μm. Hence the mass of γ-Al_2O_3 in the active layer and the apparent layer volume could be calculated to:

$$m_{\gamma-Al_2O_3} = L \times m'_{\gamma-Al_2O_3} = 0.22m \times 0.25g/m = 0.055g \tag{A8.1}$$

$$\begin{aligned} V_{\gamma-Al_2O_3,apparent} &= \frac{\pi}{4}\left(\left(D+2\times\delta_1\right)^2 - D^2\right)\times L \\ &= \frac{\pi}{4}\left(\left(0.015m+2\times4\times10^{-6}\right)^2 - (0.015m)^2\right)\times 0.22m \\ &= 4.148\times10^{-8}m^3 \end{aligned} \tag{A8.2}$$

The mass of platinum in the active layer could be calcullated according to:

$$m_{Pt} = \frac{m_{\gamma-Al_2O_3}}{\frac{1}{w_{Pt}}-1} = \frac{0.055g}{\frac{1}{0.023}-1} = 1.294\times10^{-3}g \tag{A8.3}$$

if it was assumed that all the platinum was deposited within the catalytically active layer and a loading of 2.3 wt% was achieved. The apparent density of the catalytically active layer can then be calculated as:

$$\rho_{apparent} = \frac{m_{Pt} + m_{\gamma-Al_2O_3}}{V_{\gamma-Al_2O_3,apparent}} = 1.35715 \times 10^6 \frac{g}{m^3} = 1357.15 \frac{kg}{m^3} \qquad \text{(A8.4)}$$

APPENDIX 9

SOURCE CODE

The source code of the computer programs developed in the course of this study is supplied in electronic form by means of the attached floppy diskette. The disk contains three directories:

- data: C program used in conjunction with the data logging equipment (see Appendix 2)
- sepmod: Isothermal separation model source code (see Chapter 9). The directory contains two subdirectories, src and input. The source code is stored in src whilst required input and physical property files are stored in input.
- reacmod: Combined, non-isothermal reaction and separation model (see Chapter 9). The directory is organised in the same way as described for the separation model.

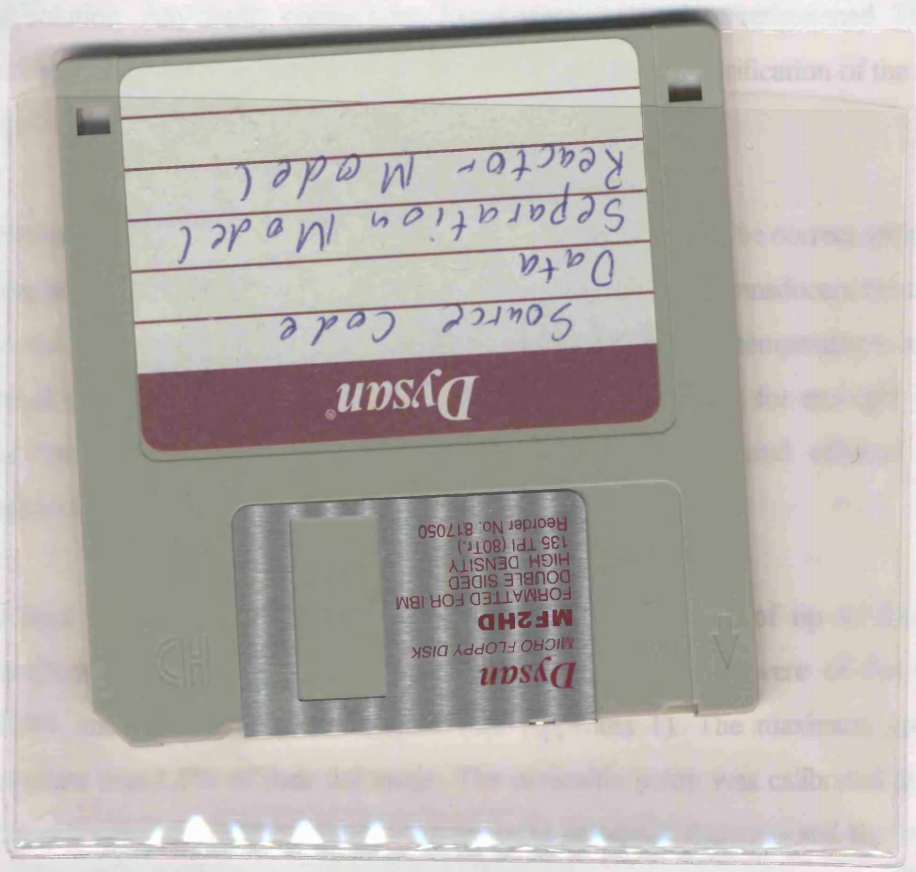

APPENDIX 10
ERROR ANALYSIS

Due to the complexity of the investigated system, the occurrence of experimental errors was likely. Two main areas can be identified by which these errors could have been introduced:

- The experimental apparatus employed to carry out the majority of experiments as shown in Figure 3.3.
- The analytical procedure used to determine effluent compositions and flowrates.

A 10.1 Experimental apparatus

A possible source for errors in a gas phase experimental apparatus is the occurrence of leaks through compression fittings and other pipework connections as for example welds. The pressurised apparatus was regularly checked for the occurrence of such leaks by means of soap solution. Any faulty connections found were replaced or retightened. However it is possible that an unquantifiable amount of leaked gas lead to a fallsification of the experimental results.

The thermocouples used throughout the apparatus were found to be correct within 1°C of the measured value (see Appendix 1). The readings of the pressure transducers were found to be accurate within 1.5% of the measured values. Both measured temperatures and pressures were of great importance in correlating the experimental data to, for example, reaction rate equations. However, their readings did not influence measured effluent flowrates or compositions.

The feed flowrate and composition was controlled by means of up to four mass flow controllers and a peristaltic pump. The mass flow controllers were of the type Brooks 5850TR and calibrated by the supplier (see Appendix 1). The maximum error for these controllers was 1.5% of their full range. The peristaltic pump was calibrated as described in Section A 1.2. The maximum error between the measured flowrate and the regression line was 3%.

A 10.2 Determination of product flowrates and compositions

One of the largest possible sources of experimental error was the measurement of the product flowrates. The reaction product gas consisted of permanent gases as well as methanol water vapour. Hence it was necessary to employ cold traps to decrease the dewpoint of the product gas. After an experimental run had achieved steady state conditions, one set of cold traps was exchanged for another one. A similar exchange was carried out after approximately 2 hours and the amount of condensate was determined by means of a balance. It is possible that these exchanges gave rise to perturbations, which were not quantified. The time a cold trap was on line was determined using a stop watch, introducing additional human error. Another possible error found in the cold trap operation, is the assumption of steady state behaviour. As methanol was only partially condensed repeatedly measuring the methanol composition in the gas exiting the cold trap was used to confirm the correct operation of the cold trap.

The flowrates of the gas exiting the cold traps was measured by means of soap bubble flowmeters. The time the soap bubble required to travel between two marks on the glass tube was stopped by hand. Hence human error was introduced at this point.

It was not possible to quantify the errors introduced into the flowrate measurements.

Gas and liquid phase compositions were determined using a gas. Two different methods were used to analyse the composition of the permanent gases leaving the experimental apparatus. The first method employed a molecular sieve 5A column for the determination of the H_2, O_2, N_2 and CO content. The second column was a Porapak S column for the quantification of CH_4, CO_2 and CH_3OH in the gas phase. The 5A zeolite used in the former column adsorbs CO_2 and CH_3OH strongly. Hence it was necessary to regenerate and recalibrate the column each day. Furthermore was it necessary to exchange the molecular sieve and the Porapak S column during a run in order to account for all the molecular species present. These operational requirements introduced additional inaccuracies (*e. g.* leakage, one point calibrations) into the GC operation. Before each run, the molecular sieve 5A column was calibrated twice as described in Appendix 3. The measured peak areas were within 1.5% of the average peak area. A possible source for error was that only one known gas composition

was used for this calibration as this assumes a linear response of the thermal conductivity detector of the GC. The linear behaviour could be proven for O_2, N_2, CO, CH_4, CH_3OH and H_2O, as shown in Figure A3.1 for water and methanol. For hydrogen a linear response could not be proven over an extended range. As the measured hydrogen compositions were close to the one of the calibration gas, a linear behaviour in this range was assumed. Another problem in H2 analysis was the high sensitivity with reversed polarity of the thermal conductivity detector required which caused a noisy TCD baseline (see Figure A3.2). This made the automated detection of the peak start and end error prone.

Figure A3.1 shows the internal standard calibration used to determine the composition of the condensate in the cold traps. The standard errors for the methanol and water slopes were 3% and 2.5% respectively. Apart from the GC specific sources of error, sample preparation might have caused additional error.

A 10.3 Example calculation

The following example calculation shows the possible effects the accumulation of different experimental errors can have on the reported results. The experiment considered was carried out to determine the operating range of the spinning basket reactor not influenced by external mass transfer resistances as reported in Section 7.1.1. The main results of these experiments were the methanol conversion and the selectivity of the converted methanol towards hydrogen. The compositions measured by GC were assumed to be accurate with 3% of the measured value, as this was the highest quantifiable error. Effluent flowrates were assumed to be measured accurately as no error quantification was carried out on these values. Table A.10.1 shows the results. The conversion was calculated as:

$$X_{CH_3OH} = \frac{N_{CH_3OH,Feed} - y_{CH_3OH,Product} N_{gas,Product} - x_{CH_3OH,Product} N_{liq,Product}}{N_{CH_3OH,Feed}} \qquad \text{(A10.1)}$$

The selectivity of converted methanol towards hydrogen was calculated as:

$$S_{H_2} = \frac{0.5 y_{H_2} N_{gas,Product}}{N_{CH_3OH,Feed} - y_{CH_3OH,Product} N_{gas,Product} - x_{CH_3OH,Product} N_{liq,Product}} \quad \text{(A10.2)}$$

Table A 10.1: Error calculation, data from experiment SBR4

	Measured	Error	Error Value
$N_{CH3OH,Feed}$	0.02117	+3%	0.02180
$N_{gas,Product}$ [mol/min]	0.05415		0.05415
$y_{H2,Product}$	0.05103	-3%	0.04950
$y_{CH3OH,Product}$	0.08535	-3%	0.08279
$N_{liq,Product}$ [mol/min]	0.01424		0.01424
$x_{CH3OH,Product}$	0.87528	-3%	0.84902
X_{CH3OH} [%]	19.287		23.988
S_{CH3OH} [%]	33.844		25.626

The table shows that even small errors can accumulate to large deviations, especially when combined as to give a worst case scenario as in the above example.